Queen Mary
University of London

Modelling of organic magnetoresitance in Aluminium tris(8-hydroxyquinolinate) Light Emitting Diodes

By

Zhang Sijie

School of Physics and Astronomy

Queen Mary, University of London

Supervisor – Dr. William Gillin

Dr. Theo Kreouzis

September 2011

Submitted for the degree of Doctor of Philosophy

Declaration

I declare that all the work contained within this thesis is accomplished by myself during my study at Queen Mary, University of London.

Zhang Sijie

Abstract

This thesis concerns itself with the scientific study of the modelling of organic magnetoresitance (OMR). This can be divided into two parts: the magnetic field effects on the intersystem crossing (ISC) in organic semiconductors, and the modelling of OMR, including triplet polaron interactions (TPI). In my studies of the magnetic field effect on photoluminescence (PL), the ISC rate, k_{ISC}, is estimated by modelling the dependence of the PL under high excitation intensity. Using a modified rate model, a k_{ISC} of $2.3 \times 10^4 s^{-1}$ is derived at a temperature of 80K in Alq_3. An excited state absorption (ESA) mechanism was also proposed to help understand how the ISC can occur from higher excited triplet states to the singlet state, rather than just from the singlet to a lower lying triplet state. This is necessary as the measured activation energy from the transfer from T_1 to S_1 is only 15 ± 5meV. In addition, the effect of a magnetic field on photoluminescence intensity for Alq_3 is reported, in order to explain the change in the k_{ISC} caused by an applied magnetic field. The magnetic field may affect the mixing of a pair state prior to exciton formation as well as the exciton itself. I then present the modelling of OMR as a function of device thickness. Here, a TPI model is proposed to fit the OMR data. For all Alq_3 devices of any thickness, the OMR data can be modelled using just three processes: triplet dissociation, polaron trapping and TPI. Both the sum of prefactors for dissociation and trapping $(a_{d+} a_t)$, and the prefactor for TPI, a_i, are proportional to the exciton concentration within the device, over the full range of operating conditions. This is the first time that a predictive model of OMR has been developed. This model is then extended to fit the OMR data as a function of temperature. In addition, I discuss some surprising phenomena at low temperature, such as a delay between the onset of light emission and the onset of OMR, and the decrease in the percentage efficiency change with the effect of a magnetic field.

Acknowledgements

First of all, I would like to express my sincere and deep gratitude to my supervisor Dr William Gillin. All the time he spent to supervise my work and care my life is deeply appreciated. I acquired my practical laboratory knowledge as well as theoretical background from him. This thesis would not have been completed without his patient guidance and support.

I would like to special thank and acknowledge my co-supervisor Dr Theo Kreouzis for devoting his valuable time for commenting and for helpful discussions on my PhD work. Specially, Dr Kreouzis's thoughtful comments and feedbacks on my thesis are also highly appreciated.

Special thanks go to Mr Geoff Gannaway and Dr Ignacio Hernandez for being available all the time when I met problems in my research works. I am also really appreciated friendly and talented academic and research staff in this School: Prof David Dunstan, Dr Alan Drew, Dr Mark Baxendale, Dr Kevin Donovan, Dr Andrei Sapelkin, Dr Ken Scott, Mr Jim Murphy, Dr George Anderson…

I would like to thank and acknowledge my colleague and close friend, Song jingyao, for his great help in my research and my daily life. Acknowledgements to all my colleagues and friends in our group: Pratik, Pabitra, Rendy, Nicola, Maureen, Kirsty, Shamim, Filippo, Zhe Li, Hongtao, Yu Peng, Huanqing, Carlos, Calum, Ali, Avi, Eva, Niranjeni, Rui, Chris, Steve, Seema, and Shima for making my stay in London very special. Last but not least, I would like to thank my beloved parents who have done so much to bring me up.

Contents

List of figures

List of Publications

1. **Sijie Zhang**, Jingyao Song, T. Kreouzis and W.P. Gillin, *Measurement of the intersystem crossing rate in Aluminium tris(8- Hydroxyquinoline) and its modulation by an applied magnetic field*, J. Appl. Phys. **106**, 043511 (2009).
2. W.P. Gillin, **Sijie Zhang**, P. Desai, P. Shakya, N.J. Rolfe, A.J. Drew and T. Kreouzis, *Determining the influence of excited states on current transport in OLEDs using magnetic perturbation*, Physical Review B, **82**, 195208 (2010).
3. **Sijie Zhang**, A.J. Drew ,T. Kreouzis and W.P. Gillin, *Modelling of organic magnetoresistance as a function of temperature using the triplet polaron interaction*, Synthetic Metals, **161**, 628 (2011).
4. Conference poster, *Modelling of organic magnetoresistance using the triplet polaron interactions*, SPINOS III, 3rd Topical Meeting on Spins in Organic Semiconductors, Amsterdam, The Netherlands
5. Conference poster, *The magnetic effect on the photoluminescence of* Alq_3, Physics Department poster presentation, Queen Mary university of London
6. **Sijie Zhang**, W.P. Gillin, P. Desai, P. Shakya, N.J. Rolfe, A.J. Drew and T. Kreouzis, *Modelling positive and negative organic magnetoresistance in organic light emitting diodes*, Submitted to PHYSICAL REVEIW B

Chapter 1:
Introduction

1.1 Properties of organic semiconductors

1.1.1 π-conjugated organic semiconductors

An organic material with semi-conducting properties is known as an organic semiconductor and consists of π-conjugated carbon compounds. An organic semiconductor is different to an inorganic semiconductor in that, in general, it is not doped. In this respect, an organic semiconductor is the perfect intrinsic semiconductor. Individual molecules are held together by the weak Van der Waals force, and the molecules interactively band by covalent bonds. Research on organic semiconductors has shown some promising applications and properties for electronic devices, such as flexible light sources and displays, low-cost production, and high electrical and electroluminescence efficiency. Organic semiconductors can be categorised into two groups: small molecules [1] and polymers [2]. Besides the molecular weight, there is also a difference in the fabrication processes between small molecule devices and the polymers. Small molecule devices are usually fabricated using a vacuum evaporation technique, while the polymers can be prepared using spin-coating, screen printing, inkjet printing, doctor blading, etc [3]. Both small molecule and polymer organic semiconductors have a common π-conjugated chemical structure, resulting in the delocalisation of their highest energy electrons (π-electrons) over the entire extent of the π-conjugation [4].

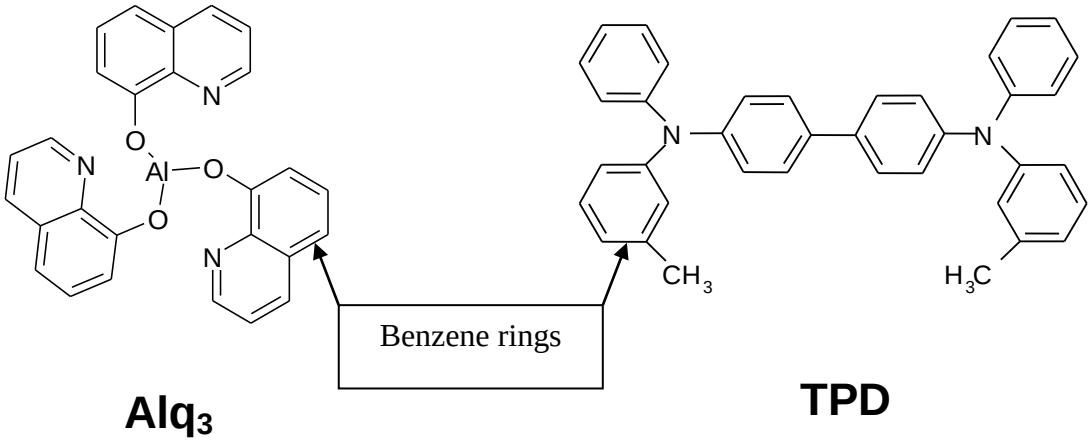

(a)

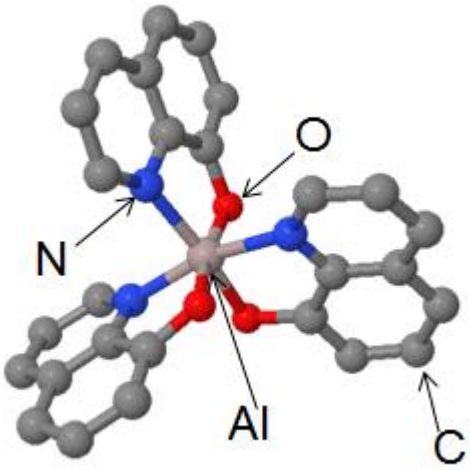

(b)

Figure 1.1: (a) A chemical structure of small molecule organics Alq_3 and TPD. (b) The 3-D Alq_3 structure.

It is important to introduce orbital hybridisation at the outset. The two main materials used in this study, Aluminium tris(8-hydroxyquinoline) (Alq_3) and N,N'-diphenyl-N,N'-bis(3-methylphenyl)-(1,1'-biphenyl)-4,4'-diamine (TPD), are constructed using benzene rings and benzene derivatives as shown in Figure 1.1.

Benzene can be used to explain the semi-conducting behaviour in the organic semiconductor. In order to understand the formation of the bonds between the carbon atoms in benzene, the sp^2 hybridised bonding has to be introduced. A

benzene ring is made up of six carbon atoms. The electrons in carbon atoms can be arranged in the following sequence: $1s^2$, $2s^2$, $2p^2$. The *s* orbitals are spherically symmetrical around the nucleus. The shape of an *s* orbital resembles a ball. In addition, a *p* orbital is present and has a shape similar to that of a dumbbell. The shapes of the *s* orbital and the p_x, p_y, p_z orbitals are shown in Figure 1.2, respectively.

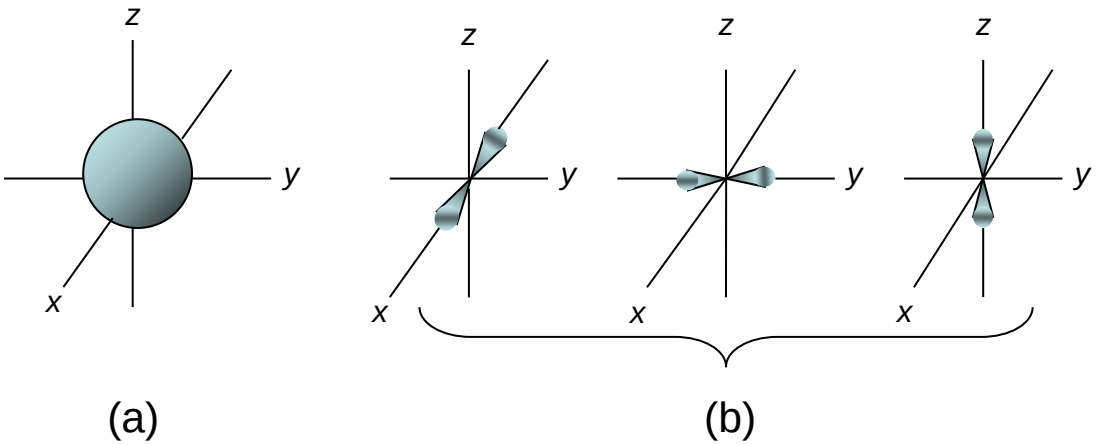

Figure 1.2: (a) The shape of an *s* orbital. (b) The shapes of p_x, p_y, p_z.

Electron filling takes place from low energy orbitals (closer to the nucleus) to the higher energy orbitals (furthest from the nucleus). This means that the 2*s* orbital will fill with electrons before the 2*p* orbitals. Unlike an *s* orbital, each *p* orbital has a distinct direction and hence at any one energy level, it is possible to have three absolutely equivalent *p* orbitals. Consequently, all the *p* orbitals have exactly the same energy. These three *p* orbitals are labelled p_x, p_y and p_z and are mutually at right angles to one another. The *p* orbitals at the second energy level are called $2p_x$, $2p_y$ and $2p_z$. The 2*s* orbital has a slightly lower energy than the 2*p* orbitals. Figure 1.3 shows the energies of the atomic orbitals up to the 2*p* level.

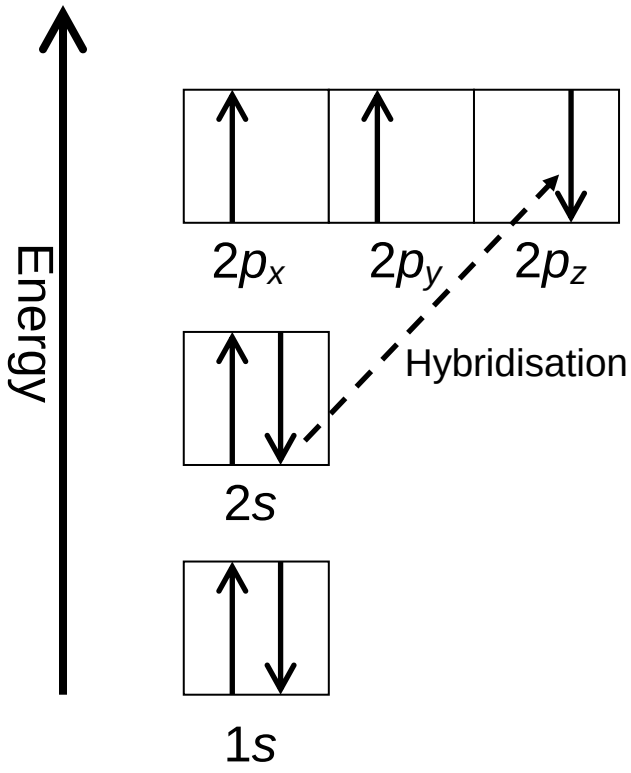

Figure 1.3: The energies and occupation of the carbon orbitals up to the 2*p* level.

It well known that a carbon atom has six electrons. According to the sequence of the electron filling, two electrons will firstly be assigned in the 1*s* orbital, which is close to the nucleus. The next two electrons will go into the 2*s* orbital and the remaining two electrons will be placed into two separate 2*p* orbitals.

Before orbital hybridisation, we needed to promote the configuration of each carbon atom from $1s^2 2s^2 2p_x^1 2p_y^1$ to $1s^2 2s^1 2p_x^1 2p_y^1 2p_z^1$, with four unpaired electrons in the separate orbitals. The three equivalent sp^2 orbitals are formed via the mixing of an *s* orbital with two *p* orbitals. The angle between neighbouring sp^2 orbitals is 120^o. These three equivalent sp^2 orbitals of each carbon atom overlap to form the σ bonds. These σ bonds lie in the same plane, while the remaining *p* orbital is perpendicular to it (see Figure 1.4). The σ bonds are the building blocks of the molecular skeleton. The excitation energy of the σ-bond is the σ-σ* transitions with an energy gap (E_g) in the UV spectral range (~8eV). Therefore, the σ-bond is so strong that its electronic property was believed to be insulating in nature.

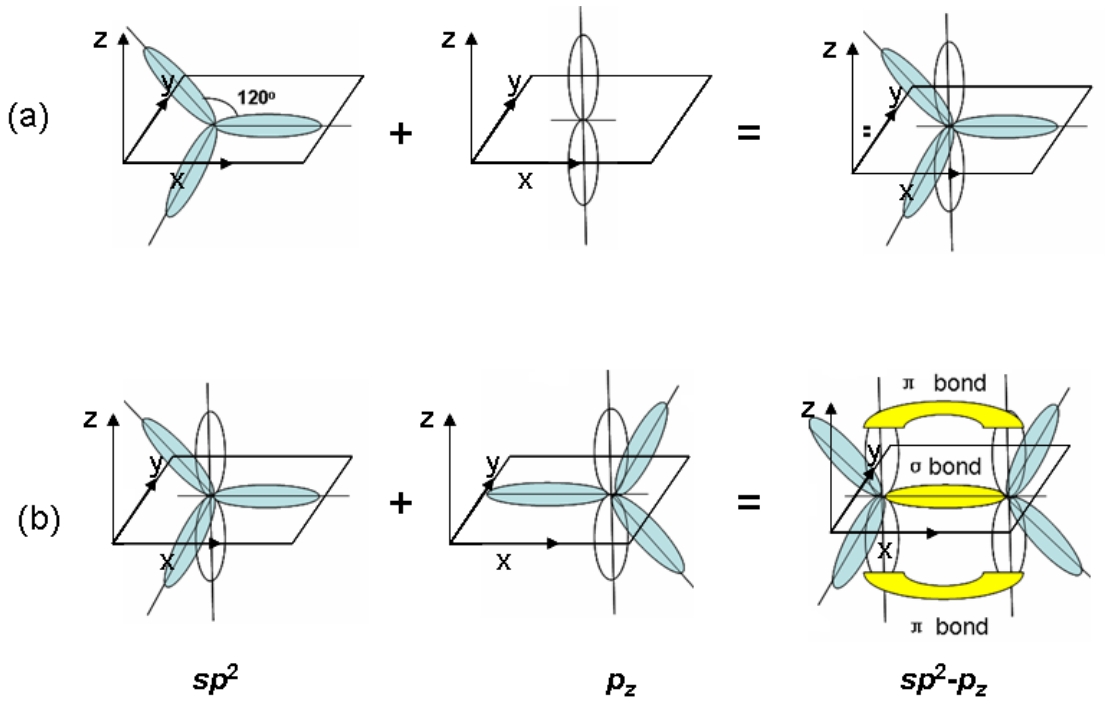

Figure 1.4: (a) A schematic representation of sp^2 orbitals and p_z orbital in a carbon atom. (b) Formation of σ and π-bonds combining with another carbon atom. Three sp^2 orbitals form σ-bonds, and p_z orbitals form π-bonds.

The p_z orbitals of each carbon atom overlap to form a π bond (see Figure 1.4). The excitation energy of the π-bond is the π-π* transitions with an E_g typically between 1.5 and 3 eV. With increasing conjugation length, then HOMO-LUMO gap is decreased, therefore, an E_g of 1.5 eV corresponds to long conjugation, and 3 eV to short. The delocalisation can be explained as electrons are spread across more than one atom. This kind of electron is known as a delocalised electron (π-electron). The delocalisation is recognised as taking place in a portion of the chain, in the case of polymers, or within an individual small molecule [5]. The semi-conducting behaviour in the nature of organic materials is attributed to the delocalised electrons (π-electrons).

It is well known that a π molecular orbital gives rise to the semi-conducting nature of organic molecules. When two atomic orbitals overlap, they interact in two ways to form two extremes of molecular orbitals: a bonding molecular orbital and an anti-bonding molecular orbital. If a molecular orbital is filled with electrons, it is called the Highest Occupied Molecular Orbital (HOMO), and if the molecular orbital is empty, it is called the Lowest Unoccupied Molecular Orbital (LUMO). The

HOMO and LUMO are roughly equivalent to the valence and conduction band in the case of an inorganic semiconductor, respectively. The energy difference between the HOMO and LUMO is regarded as the band gap (E_g) of the organic semiconductor. Electrons and holes can be injected into the HOMO and LUMO if the Fermi level of the contacts is at appropriate energies that the conduction is via a hopping mechanism between adjacent molecules.

1.1.2 Introduction to Alq_3 and TPD

The organic semi-conducting materials mainly used in this thesis are Alq_3 and TPD (see Figure 1.1), which are categorised as small molecule organic materials.

Alq_3 has been widely used in organic light-emitting diodes (OLEDs) as a cost-efficient green light-emitting material since the late 1980s [1]. Alq_3 is usually utilised as an electron transport and emissive layer, because the electron mobility in Alq_3 can achieve ~ 10^{-5} cm^2/Vs [6]. TPD is well known as a typical hole transport layer with the hole mobility ~$10^{-3}cm^2/Vs$ [7]. However, Song *et al.* have shown, using the time-of-flight (ToF) method, that the TPD can also transport electrons [8].

1.2 Luminescence

1.2.1 Excitons

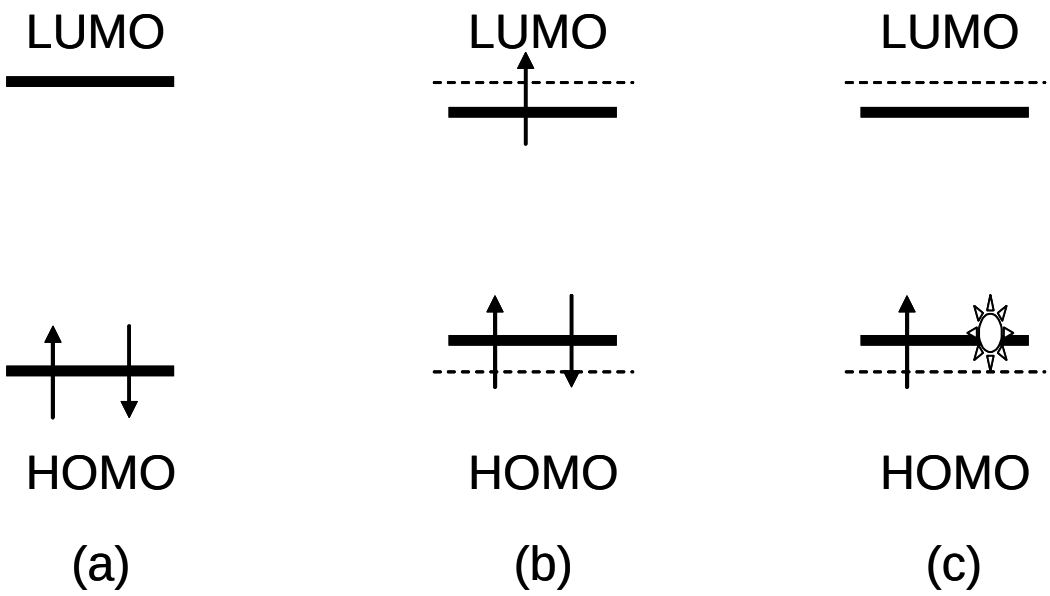

Figure 1.5: Schematics of the HOMO and LUMO of (a) a neutral molecule; (b) an electron polaron; (c) a hole polaron.

In Section 1.1.1, we introduced the formations of HOMO and LUMO. Figure 1.5(a) shows the HOMO and LUMO of a neutral molecule, which is regarded as a balanced state of this molecule. When an extra electron is added to the p_z orbital, it will disturb the balanced state of this molecule, resulting in the formation of an electron polaron. This is shown in Figure 1.5(b). Alternatively, when an electron is removed from the molecule, a hole polaron will be formed and the state of this molecule will become that in Figure 1.5(c).

If the hole and electron polarons meet each other, both inter- and intra-molecular electron-hole polarons can be formed in organic semi-conducting materials. This is

due to a coulombic attraction between the hole and electron polaron. If the electron-hole polarons are bound to different molecules over a large distance of many molecular units (typically greater than 1nm), then they are referred to as intermolecular electron-hole pairs (polaron pairs). Otherwise, if the electron-hole polarons are bound to a single molecule, with the distance between the electron and hole being smaller than 1nm, then Frenkel excitons can be formed. Usually, in organic semiconductors, the electron-hole pair interact to form Frenkel excitons [5]. The exciton is localised on a single repeat unit of the polymer or molecule [5].

Due to the spin combinations, the exciton can exist in four states. These states can be divided into two categories, namely singlet and triplet. A schematic diagram of the singlet and triplet is shown in Figure 1.6. A singlet state denotes that electrons with paired spins have zero resultant spin angular momentum (S=0). Where as a triplet state demands that the total spin angular momentum of paired electrons spins is non-zero (S=1). The triplet state can be divided into three orientations: firstly, both electron and hole have spins down (M_s=-1); secondly, the electron and hole spins are opposite but with a non-zero resultant spin and a zero Z component (M_s=0); and thirdly both have the spins up, the (M_s=+1) state.

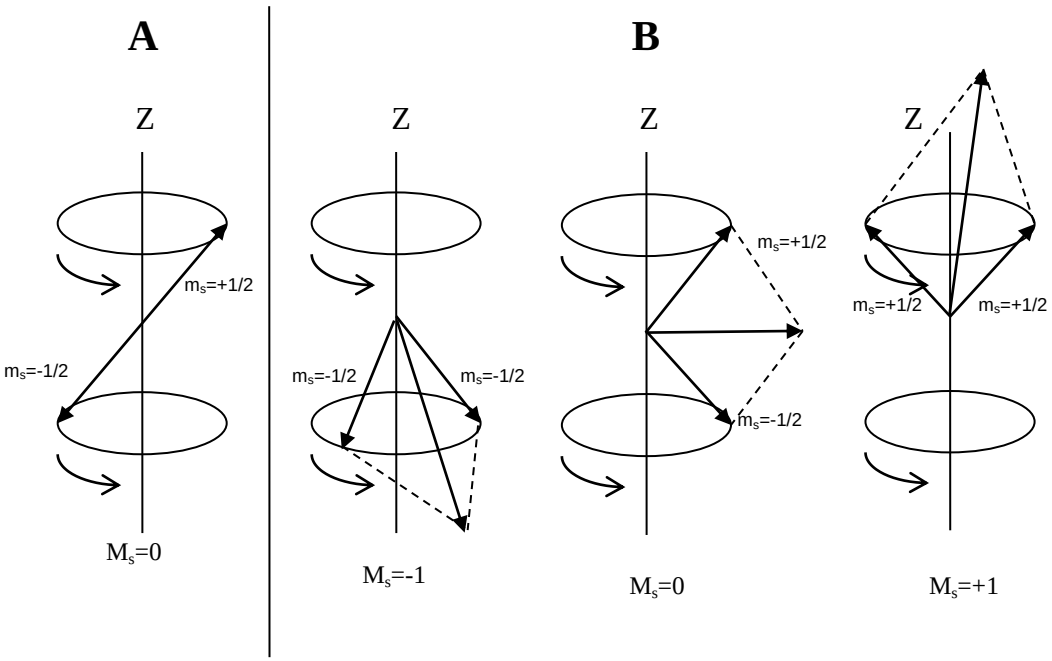

Figure 1.6: Schematic diagram of A) Singlet state and B) Triplet state

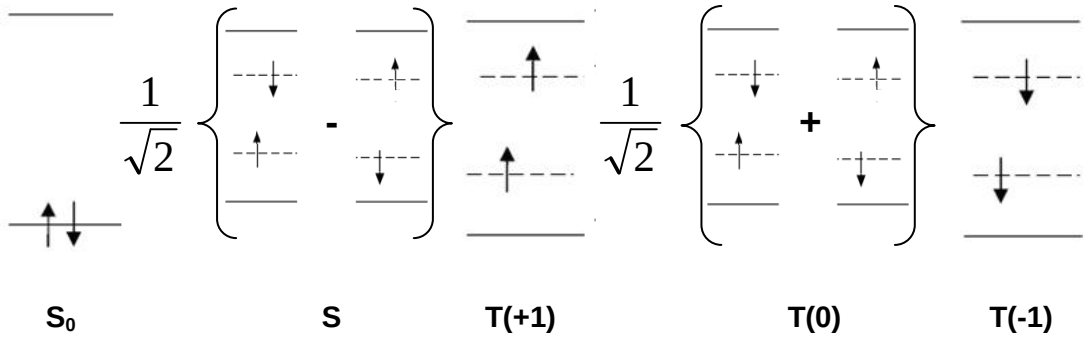

Figure 1.7: Representation of a ground state, singlet and triplet states.

Figure 1.7 demonstrates a representation of a ground state, singlet and triplet, respectively. The singlet is antisymmetric, and the triplet is symmetric and it is well known that there is an energy difference between antisymmetric and symmetric states. Besides the energy difference between the singlet and triplet states, the radiative recombination times of these differ by at least one factor of magnitude. It is also commonly known that the representative lifetime for a singlet in Alq_3 is 18ns [9], whilst that for triplets is of the order of 25μs-1ms [10].

In order to understand the schematic diagram of the singlet and triplet states seen in Figure 1.6, it is worthwhile reviewing the angular momentum. The electron possesses not only the spin angular momentum *S*, but also the orbital angular momentum *L*. The electron is attracted to the nucleus by a central force. This case is analogous to the Moon, which is attracted by the central gravitational force of the Earth, and thus possesses an orbital angular momentum. As mentioned above the electron in the atom has an orbital angular momentum *L*. $\vec{L}$ is the vector of an orbital angular momentum *L* and can be described by the equation $\left|\vec{L}\right| = \hbar[\ell(\ell+1)]^{1/2}$. In quantum mechanics, the orbital angular momentum of the electron is quantized by the quantum number ℓ, where ℓ=0, 1, 2…<n-1. The ℓ is called the orbital angular momentum quantum number. In the presence of an external field B_z, the component of the angular momentum along the z axis of the external field, L_z, is given by $L_z = m_\ell \hbar$. Therefore, the quantum number m_ℓ quantizes the component of angular momentum along the direction of an external field B_z. The m_ℓ is referred to as the

magnetic quantum number. For any given ℓ, the quantum number requires that m_ℓ must have values in the range of $-\ell, -(\ell-1), \ldots, -1, 0, 1, \ldots, (\ell-1), \ell$ or $|m_\ell| \leqslant \ell$.

In addition to the orbital angular momentum *L*, the electron possesses the spin angular momentum *S*. In the analogy previously discussed the spin of the electron around its own axis is equivalent to the 24-hour spin of the Earth around its axis. $\vec{S}$ is the vector of a spin angular momentum *S* and can be described by $|\vec{S}| = \hbar[s(s+1)]^{1/2}$. In quantum mechanics, the spin angular momentum of the electron is quantized by the quantum number *s* and $s = \frac{1}{2}$. In the presence of an external field B_z, the component of the spin momentum along the z-axis of the external field, S_z, is given by $S_z = m_s\hbar$, where $m_s = \pm\frac{1}{2}$. The $S_z = +\frac{1}{2}\hbar$ labels the spin of the electron as travelling in a clockwise direction, whereas $S_z = -\frac{1}{2}\hbar$ represents the spin of the electron as going counter clockwise. A total angular momentum *J* can be seen as a combination process between the orbital angular momentum *L* and the spin angular momentum *S*, namely *J*=*L*+*S* (see Figure 1.8).

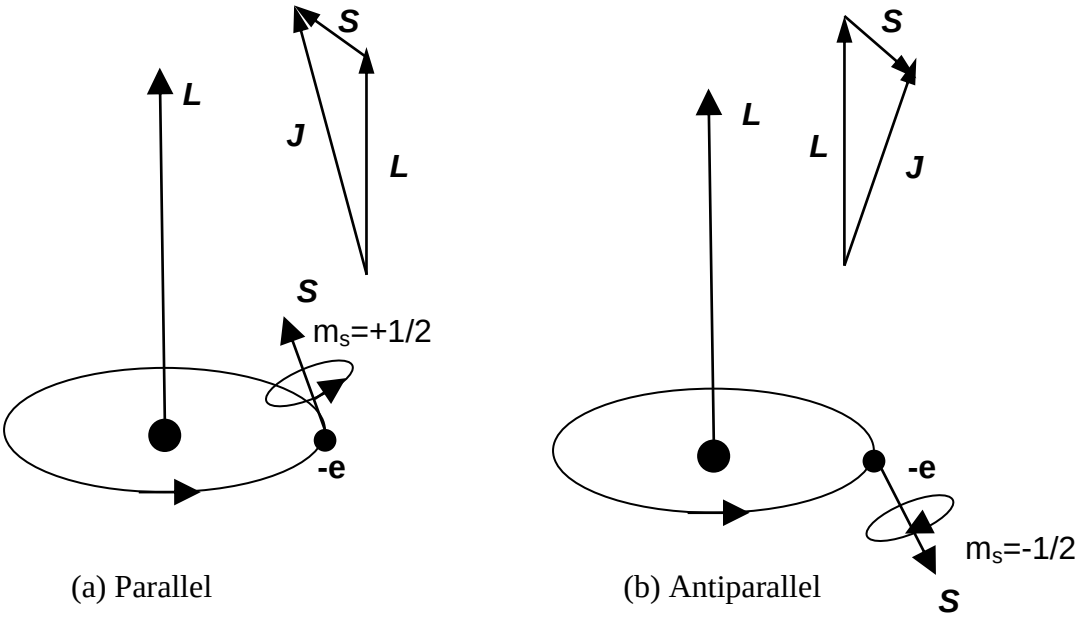

(a) Parallel (b) Antiparallel

Figure 1.8: Orbital angular momentum *L* and angular momentum *S* can add either in parallel, as in (a), or antiparallel, as in (b). The total angular momentum is *J*=*L*+*S*.

1.2.2 Photoluminescence

Photoluminescence is a well-known and widely used technique for studyng the optical properties in organic semiconductors. When the Alq_3 sample is excited by a laser, a photon with energy greater than the band gap (E_g) can excite the electrons from the HOMO to the LUMO. The electron then loses energy through phonon emission before an exciton is formed. The luminescence can be seen when electrons and holes recombine in the gap. This process is illustrated in Figure 1.9 and the luminescence is denoted photoluminescence.

In order to conserve angular momentum in the generation of excitons, the selection rules must be obeyed. In this case, the selection rules dictate that $\Delta L = \pm 1$, given that $\Delta S = 0$. The photon being absorbed has integer angular momentum, which would change the orbital angular momentum while maintaining the spin. The only possible transition is that to the singlet state, thus photon absorption can only generate singlet excitons by exciting electrons from HOMO to LUMO. When an electron interacts with a photon, the electron must obey the law of the conservation of angular momentum. Given that the photon has an intrinsic angular momentum with a constant magnitude, *h*, the orbital angular momentum of the electron must change when a photon of energy $hv=E_2-E_1$ is absorbed. E_2 is the emission energy and E_1 is the absorption energy. It could be suggested that, for photon absorption or emission, both the principle quantum number *n* and the orbital angular momentum quantum number *l* must change. Therefore, photon absorption can only generate singlet excitons.

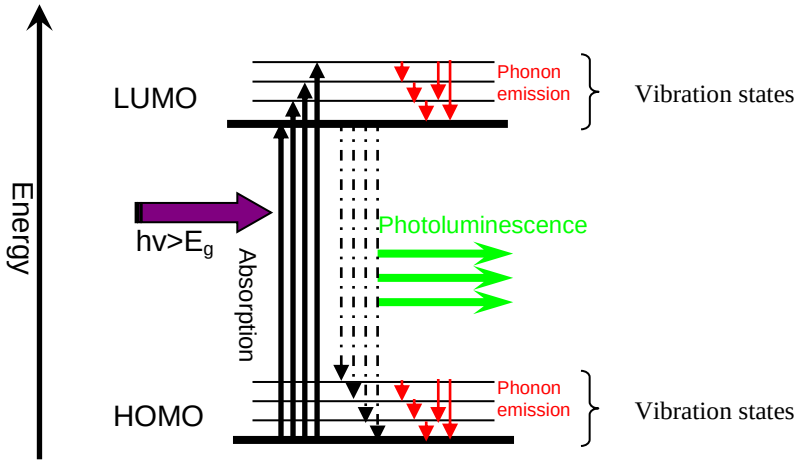

Figure 1.9: Schematic diagram of photoluminescence process.

1.2.3 Electroluminescence

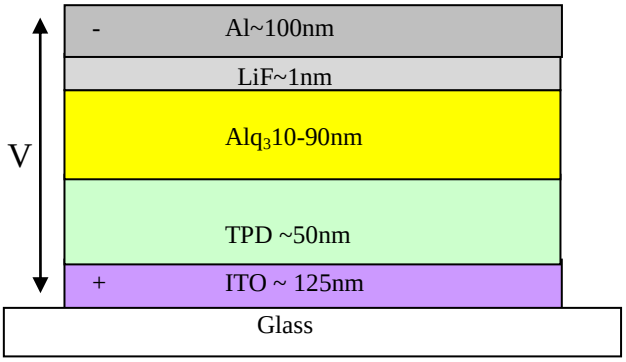

(a)

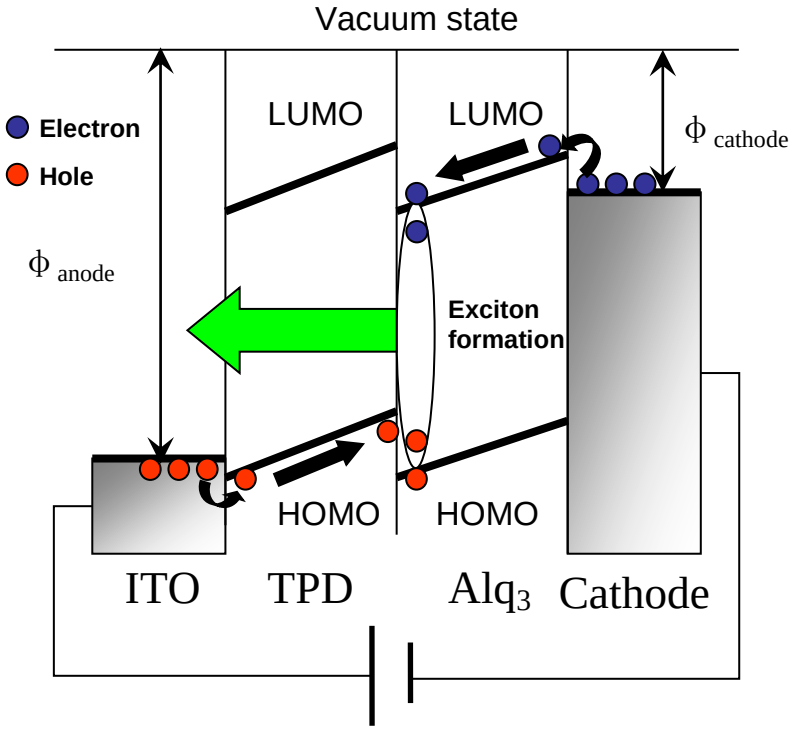

(b)

Figure 1.10: (a) A basic OLED device structure. (b) A typical OLED structure of the injection, transport, recombination and light emission.

Electroluminescence is the process responsible for light emission in an OLED. A basic structure of an OLED is shown in Figure 1.10(a). This basic structure was first proposed by Tang and Vanslyke [1]. Once a forward bias is applied to the device, electrons from the cathode have to overcome an energetic barrier and are injected into the LUMO of the electron transport emission layer (ETL), while holes from the anode have to overcome the hole barrier and are transferred into the HOMO of the hole

transport layer (HTL). At that moment, the electrons and holes can recombine in the interface between the ETL and HTL. Excitons can be formed and can decay with light emission in the ETL. A typical OLED structure with the injection, transport, recombination and light emission processes is shown in Figure 1.10(b). There are two kinds of electrodes: the cathode and the anode. The cathode is a low work function metal, which is capable of injecting electrons into the ETL. The anode is made of a transparent high work function material, through which light can pass. A typical material used for this electrode is indium tin oxide (ITO).

Some ideas for improving the charge injection have been suggested by different research groups. One of the general ideas is to use oxygen plasma treatment to increase the work function of the ITO anode up to 5.2 eV [11, 12]. Another is to use a thin insulating layer (LiF) to lower the work function of the cathode [13, 14]. Due to the spin statistics, electrical excitation can generate 25% singlet excitons and 75% triplets. Spin statistics state that the formation of singlet excitons and triplets is equal under this condition with no external influence. When the spin of the injected charge is random, only one singlet combination can be formed, and the triplet state is three-fold degenerate. This would result in the ratio of 25% singlets to 75% triplets under electronic excitation. This distribution of exciton populations has been confirmed in Alq_3 OLED devices [15] and is supported by the work of Baldo *et al.* who measure a singlet fraction that agrees within error with the expected value of 25%, after accounting for varying photoluminescence efficiencies. It was found that the ratio of singlets/triplets in a working device can be influenced by the effect of spin-orbit coupling in the absence of magnetic field [16-19] Due to the section rule, the emission to the singlet ground state (S_0) is allowed from excited singlet state (S_1) but forbidden from the excited triplet state (T_1). However, triplet emission can be observed if a perturbation, such as spin-orbital coupling, takes into account. Wilson *et.al* [16, 17] found that the spin-orbital coupling introduced by the platinum atom allows triplet state emission, resulting in the change of the ratio of singlets/triplets. Yang *et.al* [19] dopped the heavy metal atom material, $Ir(ppy)_3$, into OLEDs. They observed that the luminescence capabilities of devices are different when the concentration of $Ir(ppy)_3$ is different. This would confirm that the spin-orbital coupling affects the ratio of singlets/triplets.

1.3 Magnetic field effects in organic semi-conducting materials

1.3.1 Early B-field work on organic crystals

The role of magnetic fields on the optical and electrical performance of OLEDs has been developing for over 40 years. The history of the modern OLED can be traced back to studies conducted on the organic semi-conducting crystals in the 1960s.

A study of the magnetic field dependence of delayed fluorescence (DF) in anthracene was performed by Merrifield *et al.* (1967) [20]. Once the laser used to excite the sample is turned off, the spontaneous PL decreases within less than 1μs. DF is the fluorescence observed when the laser has been turned off for a few milliseconds. The emission spectrum of a DF is similar to a normal photoluminescence spectrum, as a singlet is involved in a recombination process. The DF emission occurs with a relatively longer time delay, compared with a normal fluorescence, and is attributed to the triplet-triplet annihilation (TTA). The TTA is described by the following equation:

$$T_1 + T_1 \leftrightarrow (T_1 T_1) \leftrightarrow S_1^* + S_0 \rightarrow S_0 + \gamma \qquad \text{Equation (1.1)}$$

where, T_1 is the first excited triplet state, S_1^* is the first excited singlet state, S_0 is the ground state singlet, and γ is the energy lost through photon emission.

When this process emits a photon from S_1^*, the decay time is dominated by the long-lived T_1 that went on to form S_1^*. This corresponds to a long time decay of fluorescence, called DF. Merrifield's group observed a small increase in DF at low field between 0 and 35 mT, followed by a decrease as the magnitude of the field increases to 80% of its null field value. The DF is saturated by the effect of a magnetic field above 200 mT. This phenomenon was attributed to the magnetic field effect on the triplet-triplet annihilation (TTA) process. In light of this, the low field

effect on the TTA is significantly more efficient than the that of high field effect on the TTA.

A year later, Merrifield's group proposed that triplets could interact with paramagnetic centres [21], namely through triplet polaron interaction (TPI). The reaction can be described by:

$$T_1 + D_{\pm 1/2} \overset{k_1}{\longleftrightarrow} (T_1 \cdots D_{\pm 1/2}) \overset{k_2}{\longrightarrow} D_{\pm 1/2} + S_0^{\,*} \qquad \text{Equation (1.2)}$$

where, T_1 is the triplet state, $D_{\pm 1/2}$ is the spin ±1/2 paramagnetic centre, ($T_1 \ldots D_{\pm 1/2}$) is a pair state, $S_0^{\,*}$ is an excited vibrational level of the ground state, and k_1 and k_2 are the rate constants for back scattering and quenching, respectively.

The left side of this equation describes a scattering event with a rate constant of k_1 between a free carrier and a triplet. This process results in a decrease in the carrier mobility with a rate constant of k_1. The right side of the equation refers to the quenching of triplets by paramagnetic centres with a rate constant of k_2. The quenching process indicates that the pair state can dissociate into a free carrier and an excited ground state singlet. Therefore, it can be imagined that any process that increased the concentration of triplets would have the effect of decreasing the mobility of free carriers, due to scattering of the free carrier and the quenching of the triplet state. Ern and Merrifield also studied the effect of the magnetic field on the DF. In the quenching process (right side of Equation (1.2)), the lifetime of the DF should be decreased. However, Merrifield's group found that the lifetime of DF is increased by applying a magnetic field. Therefore, it was suggested that the quenching process is diminished with increasing magnetic field.

1.3.2 Magnetic field effects on modern devices

The early research studies described in the previous section provide some basic ideas about how to study experimentally the magnetic field effect on exciton populations and exciton/charge-carrier interactions within organic crystals. During the 1990s, the development of modern OLEDs had generated research interest in modern organic semiconductors and electronic devices. This has motivated various research groups to explore the effect of a magnetic field on modern organic semiconductors.

In 1992, Frankevich *et al*. [22] observed the effect of a magnetic field on the PPV derivatives that were configured with both contacts on one surface. This group observed that the photocurrent experienced a sharp increase of 3% with an applied field at about 4mT, followed by a saturation when the magnetic field was greater than 4mT. This experiment is an early example of magnetic field effects on a modern organic semiconductor. Frankevich *et al*. proposed a model for explaining this phenomenon, which is shown in Figure 1.11. In this model, $^1M_0$ is the ground state, and the excited states $^1M_1$ and $^3M_3$ are equivalent to singlet and triplet states. It was assumed that $^1M_1$ and $^3M_3$ are characterised by the rate constants of recombination (K_S and K_T, respectively) and by the spin-independent dissociation rate (K_{-1}). Separate to the excited states ($^1M_1$ and $^3M_3$), there are short-range polaron pairs $^1(P^+.P^-)$ and $^3(P^+.P^-)$. Above $^1(P^+.P^-)$ and $^3(P^+.P^-)$ there are long-range polaron pairs $^1(P^+\ldots P^-)$ and $^3(P^+\ldots P^-)$. In addition to all of these states, there are well-separated polaron pairs P^+, P^-, which are known as dissociated polarons. Each of the previously mentioned excited states and polarons exhibit similar behaviours to singlet and triplet states. In addition, Frankevich's group suggested that the magnetic field modulation on ISC only occurs in the mixing between $^1(P^+\ldots P^-)$ and $^3(P^+\ldots P^-)$ states. The effect of an external field allows the long-range polaron pairs to finally recombine into a singlet and T_0 component of the triplet, resulting in a decrease in the population in T_{-1} and T_{+1}. This may increase the population of long-range pair states that can go on to dissociate, so that the photocurrent is raised with the magnetic field.

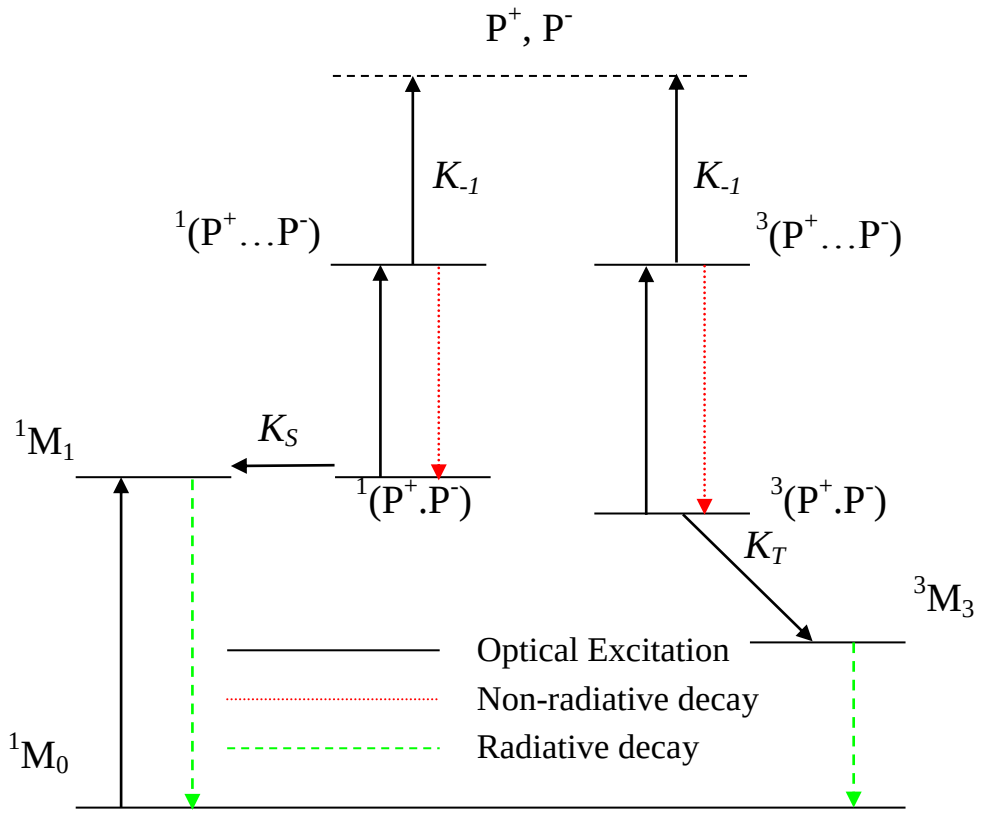

Figure 1.11: Schematic diagram of Frankevich's model.

The role of magnetic fields on the optical and electrical performance of OLEDs has received increasing attention in the last few years. This directly reflects on the large increases in efficiency and current through the device with applied field. Kalinowski *et al.* carried on the early work of Merrifield and proposed a mechanism in 2003 [23]. They reported magnetic field effects on emission and current in Alq_3 based electroluminescent diodes. Kalinowski's group was the first to report that the magnetic fields could modulate current in an OLED. They observed that, for Alq_3 OLED devices, increases in light output of ~5% could be obtained with the application of magnetic fields of ~500mT.

Kalinowski's group has explained that the increase of electroluminescence with magnetic field is caused by increasing the combination of electron-hole pair states prior to exciton formation. Kalinowski's model is summarised in the schematic diagram shown in Figure 1.12. In order to explain the observed increase of electroluminescence with magnetic field they used Zeeman effects and the hyperfine

interaction to explain an increase in singlet population and hence the electroluminescence. Without the magnetic field affects on the device, the singlet mixes with the triplets through the hyperfine interaction (HFI), which is an interaction between the magnetic moments of the unpaired electron and the nuclei. The HFI has two main parts to it, the Fermi Contact Term (FCT) and the Dipolar Term (DT). In some cases there are higher order terms but in most cases they are negligible. The Hamiltonian for the HFI is derived below using the method given in reference[24].

The ratio between the magnetic moment and angular momentum is given by the gyromagnetic ratio (γ) and is defined for a particle of charge q to be[25]

$$\gamma_i = \frac{qg}{2m} \qquad \text{Equation (1.3)}$$

where g and m are the g-factor and mass of the particle respectively. Knowing this the relationship can be derived between the magnetic moment of a particle ($\overrightarrow{\mu_i}$) and its spin ($\overrightarrow{S_i}$).

$$\overrightarrow{\mu_i} = \gamma_i \overrightarrow{S_i} = \frac{qg}{2m} \overrightarrow{S_i} \qquad \text{Equation (1.4)}$$

It can therefore be shown that

$$A \propto \overrightarrow{\mu_i} \qquad \text{Equation (1.5)}$$

The two key terms that arise the deviation is a contact term that describes the coupling when the wave function of the electron is non-zero at the nucleus and the anisotropic term which in where a majority of the spin mixing comes from. The HFI can be simplified to the relation,

$$H = -\overrightarrow{\mu_e} \cdot \vec{B} = H_{FCT} + H_{DT} \qquad \text{Equation (1.6)}$$

As there are many nuclei in the system the HFI couplings can be incorporated into a single HFI tensor and hence the relation becomes,

$$H = \overrightarrow{S_e} \cdot A \cdot \overrightarrow{S_i} \qquad \text{Equation (1.7)}$$

It is worth noting that if the hydrogen is changed to a Deuteron as in the case of deuteration of Alq_3 the spin is also changing in addition to the magnetic moment. Therefore, this can affect the spin orbit interaction as well as the HFI, so one must be

cautious when considering deuteration results. At moment, three triplet components T(+1), T(0), and T(-1) are degenerated. With the application of an external magnetic field to the device, the triplet state splits due to the Zeeman Effect, resulting in three triplet components T(+1), T(0) and T(-1) removing the degeneracy. For a strong field, the hyperfine mixing is reduced to transfer rates from singlet pair states to triplet pair states. This results in an increase of the singlet pair states and hence increases the singlet exciton population and the electroluminescence. However, Kalinowski's group didn't explain why the transfer only occurs between singlet pair states and triplet pair states, rather than at the excitonic levels. Kalinowski's group also proposed that the increase in current was attributed to the singlets dissociation, corresponding to the rise of the singlet excitons population with applied field. However, they ignored the fact that the triplet dissociation can also contribute to the current in the device. Since the lifetime of triple states is at least a thousand times longer than singlets, their concentration will be considerably higher in a working device. Therefore, it appears doubtful that the singlet dissociation rate at the cathode is more favourable than the singlet excitons.

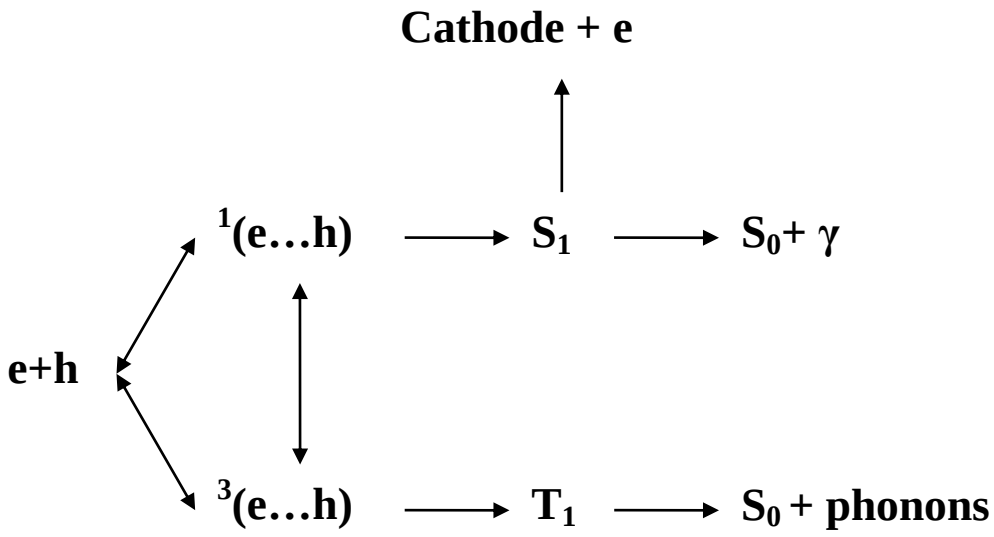

Figure 1.12: Schematic diagram of Kalinowski's model.

In 2006, Prigodin *et al.* published a paper about the role of spin-orbit coupling on organic magnetoresistance(OMR) [26]. The OMR indicates the change of current in the organic semiconductor with a magnetic field. Spin-orbit coupling is a magnetic interaction between the spin and orbital magnetic moments. They described how the OMR is changed with doping PtOEP and $Ir(ppy)_3$, in which the spin-orbit coupling is enhanced. They also proposed a model to explain why the large spin-orbit coupling in the semiconductor should diminish the OMR effect. It is true that doping changes the spin-orbit coupling, however, the population of excitons has also been changed through doping. In this case, the author has ignored the fact that the population of excitons could influence the change of current through the OLED devices.

In addition, Prigodin's group proposed a model to explain the OMR by calculating the electron-hole recombination rate. Similarly to Kalinowski's model, Prigodin's group suggested a magnetic field controls the spin interconversion of pair states. Without the influence of a magnetic field, the singlet pair states mix with the triplet pair states through the hyperfine interaction. When an external field is applied to the device, the magnetic field causes the triplet pair states to split into three triplet components T(+1), T(0), and T(-1) as previously mentioned. For a strong field, the ISC between singlet excitons and the triplet T(0) component decreases in the presence of the magnetic field. Therefore, the electron–hole recombination rate is changed and hence the current is increased based on Prigodin's model.

In 2007, Hu and Wu observed that the OMR can be switched between positive and negative values by adjusting the dissociation and charge reaction in excited states. This is achieved by shifting the bipolar charge injection in the OLEDs [27]. They extended Kalinowski's model in which the external magnetic field makes the change in the singlet and triplet ratios with ISC. It was proposed by Hu's group that there are two conditions that must be satisfied for the ISC to be field dependent. Firstly, the magnetic splitting caused by the external field must be larger than the intrinsic one induced by the spin orbital coupling. Secondly, the magnetic splitting energy, $\triangle E_B$, of the three triplet sublevels should be larger than the singlet–triplet energy difference, $\triangle E_{ST}$, caused by spin-exchange interaction. Hu's group revealed that an external magnetic field can affect the generation of secondary charge carriers from the

dissociation and charge reaction, therefore the electrical injection current can be changed by varying the singlet and triplet ratios. The ratios between the singlet and triplet are adjusted through field dependent ISC.

Furthermore, Hu's group observed both negative and positive OMR. The opposite signs of OMR were attributed to the fact that the dissociation and charge reaction have reverse dependencies on magnetic field in the generation of secondary charge carriers. In light of this observation, they proposed an idea on how to modify the OMR. A schematic of Hu's model is shown in Figure 1.13. However, they still did not explain why they were only concerned with the singlet dissociation, and ignored triplet dissociation. Given the fact that the lifetimes of triplets are at least a factor of one thousand larger than that of singlet excitons, their concentration will be considerably higher in a working device. Therefore, the triplet dissociation would be expected to dominate.

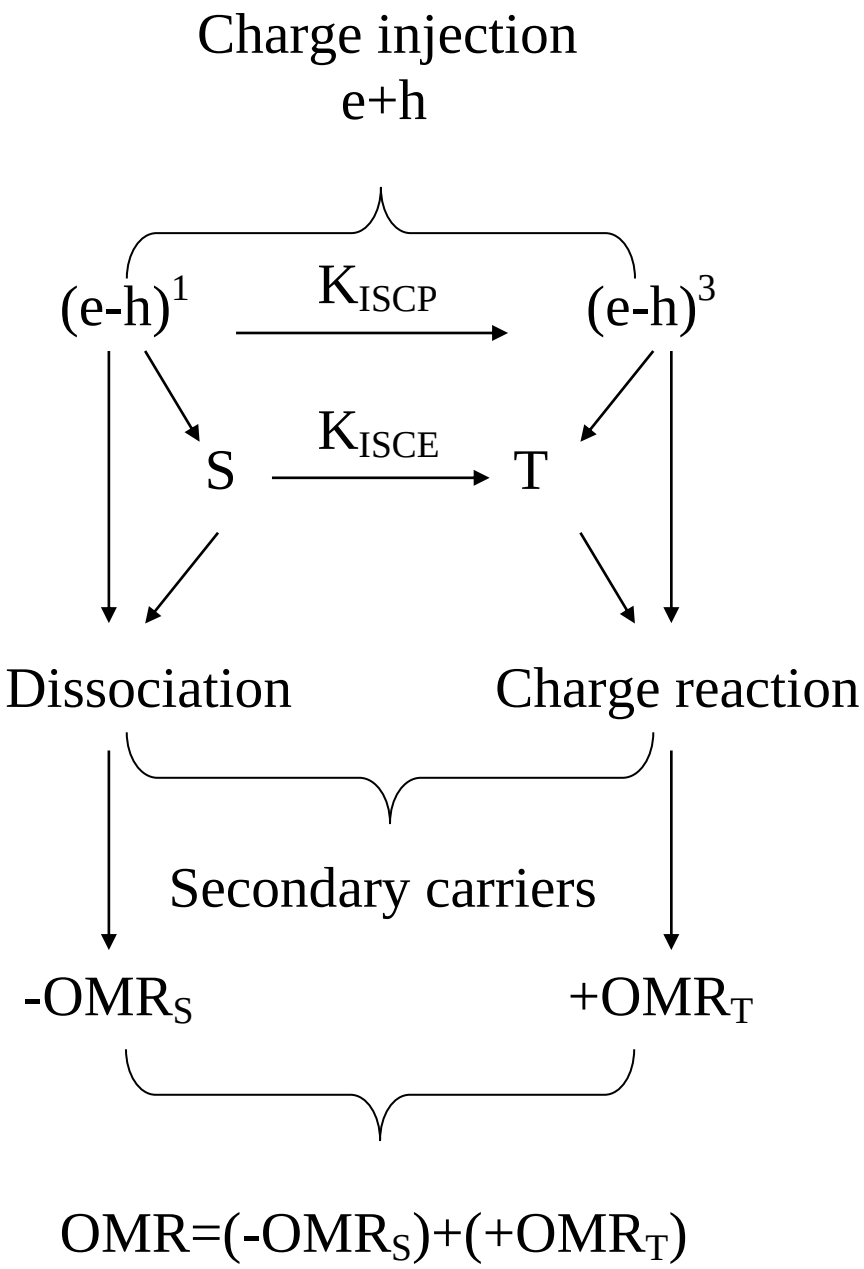

Figure 1.13: Schematic diagram of Hu's model.

Despite the discussion about the details of the mechanism responsible for OMR, some groups have proposed theoretical models based on the hyperfine interaction [23, 26, 28]. In 2007, Tho Duc Nguyen *et al.* in Iowa tried to experimentally probe the role of the hyperfine interaction in OMR [29, 30]. They found that devices consisting of ITO/C_{60}/Ca/Al or Au/C_{60}/Ca/Al do not exhibit an OMR effect. The existence of hydrogen atoms is usually regarded as the required condition for causing hyperfine

interaction. However, C_{60} is a material without hydrogen atoms, so its hyperfine interaction strength should be very weak. Nguyen's group also found a definite positive OMR, based on a PEDOT/C_{60}/Ca/Al device. They suggested that this OMR might originate from the PEDOT layer, since an OMR had been found in the PEDOT-only device, albeit with a negative sign. This OMR was attributed to the hydrogen atoms in PEDOT. It was concluded that the interactions of the hydrogen are a necessary prerequisite for the observation of OMR. However, it was not clear from this work why opposite signs were found for OMR between the PEDOT/C_{60}/Ca/Al device and the PEDOT-only device. Some debate has occurred between the different groups in the community in proving the role of the hyperfine interaction in OMR. Rolfe *et al.* (2009) produced OLEDs based on fully deuterated Alq_3, where the hydrogen atoms inside the Alq_3 sample are replaced with deuterium [31]. For the deuterated Alq_3, the strength of the hyperfine interaction should be considerably reduced [32]. They demonstrated that OMR can still be observed in these deuterated Alq_3 OLED devices, and found no consistent differences between the deuterated and non-deuterated devices, including in the magnitude or line shape of the magnetic field effect on current and efficiency. They concluded that the hyperfine interaction is not the cause of the intrinsic OMR [31]. A year later, Nguyen *et al.* (2010) [33] observed a clear difference between the deuterated and non-deuterated DOO-PPV polymer in the optically detected magnetic resonance, magneto-electroluminescence and giant magnetoresistance. They proposed that all of the above phenomena relating to magnetic field effects are due to the hyperfine interaction. Rolfe *et al.* (2011) [34] went on to research the deuterated Alq_3 OLED devices and proposed that three spin interaction processes affect the efficiency data of OLEDs, including the ISC between the polaron pair state, the ISC between excitons, and the interaction of polarons with triplets. They found that only the ISC between the polaron pair state is affected by deuteration, hence the hyperfine interaction may have some effect on OMR.

The effect of spin-orbit coupling on OMR has also been studied by this Iowa group [29, 35]. They compared the OMR effects between Alq_3 and $Ir(ppy)_3$ devices. These two materials have similar chemical structures, but the $Ir(ppy)_3$ contains a heavier atom to enhance spin-orbit coupling. They observed that the magnitude of OMR in $Ir(ppy)_3$ is roughly two orders of magnitude smaller than that in Alq_3.

Hence, the OMR trace of the $Ir(ppy)_3$ device showed a much weaker OMR characteristic than in the Alq_3 device, which corresponds to strong spin–orbit coupling strength. In light of this, Tho Duc Nguyen *et al.* concluded that the OMR is caused by the spin–orbit coupling in the organic semiconductor material. In addition, Prigodin *et al.* [26] and Wu *et al.* [36] also observed that the magnitude of OMR decreases dramatically in materials with strong spin–orbit coupling. However, Shakya *et al.* (2007) found that virtually no change in the efficiency of OLEDs, upon the application of a magnetic field, can be seen when changing the atomic mass of the central ion in the quinolate system from aluminum to indium [37, 38]. Shakya's group concluded that spin–orbit coupling is not responsible for the mixing between triplet and singlet states under the influence of a magnetic field.

In the same year, Desai *et al.* observed an increase in OLED efficiency with applied magnetic field. It was suggested that the magnetic field was acting directly on the excitons, rather than the pair states, thus altering the intersystem crossing rate [39]. However, further to this work, it is now proposed that the magnetic field not only acts on the excitons, but also on the pair states[40]. In addition, a simple rate model was proposed to explain the positive change in efficiency. The schematic diagram of the simple rate model is shown in Figure 1.14. This model demonstrates the processes controlling the exciton population. In electrical pumping, due to spin statistics, one singlet, S_1, *is* formed for every three triplet states, T_0 (a=25% of total molecules and b=75% of total molecules). In this case, a magnetic field modulates the ISC to make the triplets transfer to singlets, therefore the change in efficiency increases. Alternatively, in optical pumping, the excitons are pumped solely to the singlet S_1 (a=100% of total molecules and b=0% of total molecules). The role of the magnetic field is to increase the ISC between the S_1 and T_0, resulting in an increase in the triplet concentration. The simple rate model can be used to explain related OMR phenomena, such as the positive change of efficiency and current. However, the simple rate model cannot physically explain the back transfer process from T_1 to S_1, because there is a large energy barrier between them. However, a revised ESA model was proposed to amend the default point of the simple rate model [40].

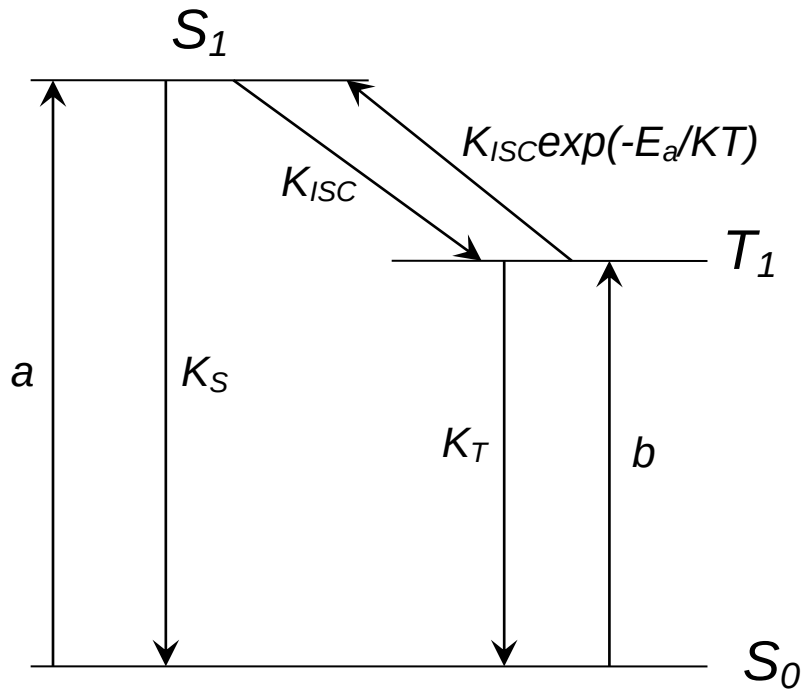

Figure 1.14: Schematic diagram of the simple rate model.

Meanwhile, it was proposed that no OMR can be observed before the onset of light emission, and it was concluded that OMR is due to exciton formation in the device. We found that the emission of light can be seen once the driving voltage has been reached and excitons are formed. Moreover, both the negative and positive OMR have been explained using the triplet-polaron interaction (TPI) and triplet dissociation mechanisms, respectively. In electrical excitation, fewer triplets, due to triplets transfer to singlets with magnetic field, can interact with free carriers, resulting in an increase of the mobilities of free carriers. The triplet-polaron interaction (TPI) and triplet dissociation mechanisms are described in detail in Chapter 4.

In late 2007, a collaborating group from the Universities of Iowa and Eindhoven proposed a bipolaron model for explaining OMR [41]. This group introduced the unipolar model. If two polarons have the same spin state, a bipolaron intermediate state cannot be formed (see Figure 1.15(a)). This process is known as spin-blocking in bipolaron formation. If the two polarons have different spin states, a bipolaron state can be formed (see Figure 1.15(b)).

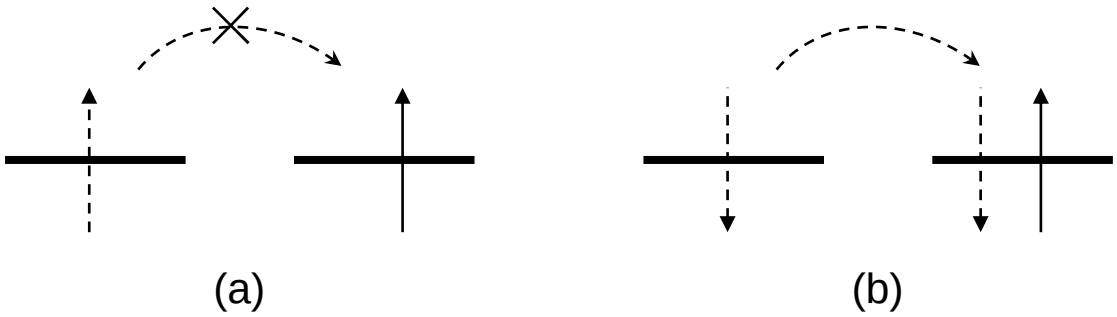

Figure 1.15: (a) Spin-blocking in bipolaron formation. (b) Bipolaron formation.

The hydrogen atoms generate a very small intrinsic field inside organic semiconductors, known as the hyperfine field. Each of the polarons experiencing with a small hyperfine field will hop throughout the bulk of the material. The hyperfine field is totally random, resulting in the random flips of these polarons. This means that the spin of polarons can flip in any possible direction. Without the magnetic field, the possibility of bipolaron formation is maximised. In the case of an external magnetic field being much greater than the hyperfine field, all the polarons should precess with the overall applied magnetic field, hence the possibility of spin random flipping can be reduced. It could be suggested that fewer bipolarons are formed under the influence of the external field compared to without the magnetic field. As a consequence, the total bipolaron density is dependent on the magnetic field. Because polarons and bipolarons have different mobilities, magnetically changing the polaron and bipolaron densities essentially leads to positive and negative OMR in organic semi-conducting materials. However, Song *et al.*'s experimental results [42] conflict with the bipolaron theory. In bipolaron theory, the mobility and current density change only depends on bipolaron formation, rather than the electrode choice. According to this theory, the magnetically mediated increase in mobility should be observed in both unipolar and ambipolar devices. However, Song *et al.* observed a significant increase in mobility and current density in the ambipolar sample, but not in the unipolar sample.

1.4. Summary

This introductory chapter has provided a theoretical background of the basic properties of the organic semiconductor. It also discusses excitons and PL/EL, and provides fundamental information on Alq_3 and TPD, both of which are used widely in this research. In addition, I have undertaken a chronological literature review of several previous studies about the magnetic field effect on organic semiconductors. Chapter 2 goes on to explain the methodology used in this research. Chapter 3 discusses the magnetic field effects on PL, while Chapters 4 and 5 investigate the magnetic field effects on EL.

Chapter 2:

Experimental and Measurement methodology

This chapter describes the experimental equipment and measurement methods used in this research. It is divided into two parts: magneto-luminescence (MPL) and magetoresistance (OMR). In this research, the MPL indicates the effect of a magnetic field on the percentage change in steady state PL intensity for Alq_3. OMR denotes the effect of a magnetic field on the percentage change in the current through an OLED device. The MPL experimental set-up is discussed in Chapter 3, where the device fabrication and OMR measurement are also described. Chapters 4 and 5 discuss the OMR results.

2.1 Purification of organic materials

Freshly purified organic materials (Alq_3 and TDP) are required for undertaking this research into MPL and OMR. Before purification, these organic materials contain impurities such as water, oxygen, salts, and hydroxides. The presence of such impurities can act as quenching centres and affect the distribution in lifetimes. In addition, these impurities can cause degradation of the OLED devices [43]. Therefore, purification of the organic materials is an essential step prior to further testing. The purification of Alq_3 and TDP was done using train sublimation in a Pyrex glass tube.

A purification column is composed of a glass boat and a Pyrex glass tube. 1 gram of Alq_3 or TDP was placed into the glass boat. The Pyrex glass tube was used as an inner tube to collect the pure, sublimed material. Some filter papers were placed between the glass boat and the Pyrex glass tube, in order to block the larger sized impurities. An additional Pyrex test tube was used as housing for the purification column. One end of the housing was inserted into the furnace tube of a Carbolite Furnace close to the centre. A thermocouple was also inserted inside the furnace to monitor the temperature in the purification column. A Turbotronik NT 10 turbo pump and Trivac rotary pump, attached at the other end of the housing column, maintain the vacuum in the system, while a combined Penning/Pirani gauge was used to measure the pressure inside. The vacuum in the system was kept at $<10^{-6}$ mbar during the evaporation.

In order to purify the Alq_3, the raw Alq_3 powder was initially heated at a fast rate of ~5 ℃/minute until the temperature reached ~120 ℃, maintaining a constant pressure of $<10^{-6}$ mbar in the system. Once the temperature reached ~120 ℃, the system was left at this temperature for about 3 hours for out-gassing. Afterwards the temperature was increased by 30 ℃ every three hours and the rate of heating was adjusted to 10~20 ℃/minute. The essential point in the sublimation process is to maintain a pressure of $<10^{-6}$ mbar in the system. When the temperature was increased to ~200 ℃, evaporation started to occur. This was then kept constant for the complete

sublimation process over several days. The equipment set-up and method for purifying the TPD is similar to that in the Alq_3 purification. After the completion of sublimation, the furnace was switched off and the system was left to cool for at least five hours. The pump was then switched off and the sublimation column was taken out. The pure material was harvested from the glass tube and stored in a screw top jar under vacuum.

2.2 Magneto-luminescence

2.2.1 Introduction

Figure 2.1 shows a schematic diagram for organic MPL measurements of the powdered Alq_3. Freshly purified Alq_3 powder was placed into a continuous flow cryostat in a nitrogen atmosphere. The temperature inside the cryostat can operate in the range of 300K to 80K. PL was excited using a 25mW, 405nm laser that was focused onto a <0.1mm spot, by a microscope objective (*Achro 4/0.1*) onto a relay. The laser was mechanically modulated by the switch of the relay at 5Hz with a rise time of ~100μs. The frequency of laser beam was mechanically modulated by the switch of the relay, which was controlled by a function generator (*JUPITER 500*).
This function generator not only provides a pulse signal to this relay but also feeds a reference frequency to a lock-in amplifier (PerkinElmer 7265 DSP Lock-in Amplifier). The use of such a reference signal ensures that the instrument will only track changes in the signal of the same frequency. A clean decay of the initial PL before it reaches a steady state value is important to the discussions in the section 3.2. The time response of the PL will be produced when the laser is switched on to excite the powdered Alq_3 sample. A fast laser, which has a short rise time, can make a decay in the initial PL before it reaches a steady state due to the ISC generation T_1 from the photoexcited S_1 states. This is results in a reduction in the number of molecules in the ground state that can then be subsequently photoexcited to give PL. The rise time of the laser is defined by the size of the laser when the speed of chopping the laser beam is constant. In order to produce the rise time as fast as possible, a microscope objective has to be used to reduce the size of the laser beam and focus it at the switch of the relay. In this experiment, the purpose of the mechanical modulation is to obtain several measurements to perform an average and the time scale of the measurement is that of a continuous wave steady state.

In order to modify the laser intensity, neutral density (ND) filters were placed before Lens 1. The modified laser beam was then focused onto the Alq_3 powder sample in

the cryostat using Lens 1, to produce the PL. The emitted PL was collimated by Lens 2 and then focused by Lens 3 onto the input slit of the spectrometer. The PL was dispersed in a spectrometer and detected using a S-20 photomultiplier. A digital oscilloscope was used to measure the output of a lock-in amplifier (*Model 7265 DSP*). To determine the effect of a magnetic field on the PL, the cryostat was placed between the poles of an electromagnet and the PL intensity was measured using the lock-in amplification. Measurements were made as a function of increasing magnetic field alternated with null field measurements. The electromagnet was controlled by a magnet power supply unit (PSU).

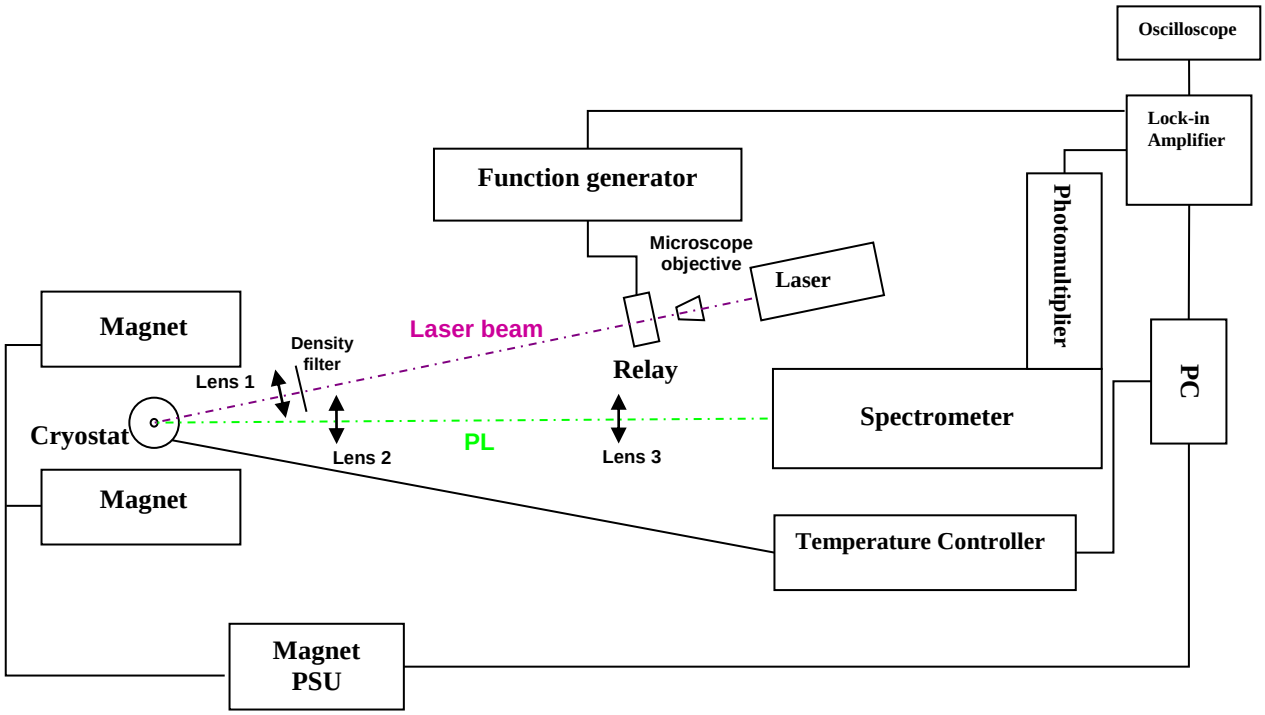

Figure 2.1: A schematic set up for the MPL measurement for the powdered Alq_3.

2.2.2 Experimental apparatus and set-up

Spectrometer

A spectrometer is used to disperse the luminescence. The characteristics of materials can be identified by measuring the wavelengths and intensity of the spectrum [44]. In the schematic diagram of a spectrometer (see Figure 2.2), the luminescence is aimed at an entrance slit (A). The intensity and resolution of the luminescence can be adjusted by the slit (A). This luminescence is then focused ino a curved mirror (B), which is called a collimator. In this case, the luminescence will be parallel. This process is denoted collimation. The collimated luminescence is diffracted by the Diffraction Grating (C) and then collected by another mirror (D). The mirror (D) refocuses the dispersed luminescence with individual wavelengths on the different positions of the exit slit (E). At the exit slit, the wavelengths of the luminescence are spread out spatially. Therefore, when the Diffraction Grating is

rotated, the intensity changes of a sample's spectrum can be seen at different wavelengths.

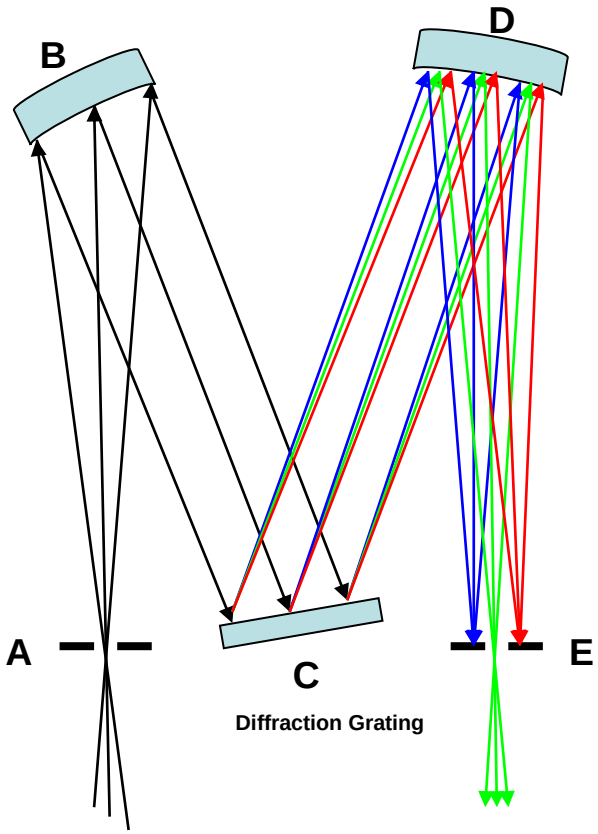

Figure 2.2: The schematic diagram of a spectrometer.

Photomultiplier

The dispersed luminescence is detected using a photomultiplier tube. The schematic diagram of a photomultiplier tube is shown in Figure 2.3. A photomultiplier tube is an apparatus that multiplies the electrical signals caused by light; these multiplied signals are then measured by a lock-in amplifier. It is constructed from a glass envelope with a high vacuum inside. This tube is constructed by a photocathode, several electrodes, and an anode. When the incident photons strike the photocathode material, electrons are produced as a consequence of the photoelectric effect. These electrons are directed by the focusing electrode toward the electron multiplier. The electron multiplier consists of a number of electrodes. There is a 1kV supply between electrode 1 and electrode 8. When the electrons move towards each electrode, they are accelerated by the electric field and arrive with much greater energy. Therefore, an increasing number of electrons are produced at each stage.

Finally, the electrons reach the anode, where the accumulation of charge results in a sharp current pulse, indicating the arrival of the photons at the photocathode.

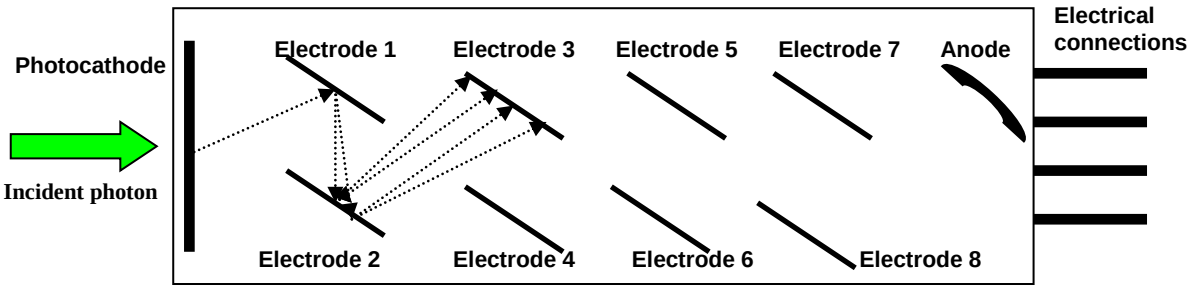

Figure 2.3: The schematic diagram of a photomultiplier tube.

Lock-in amplifier

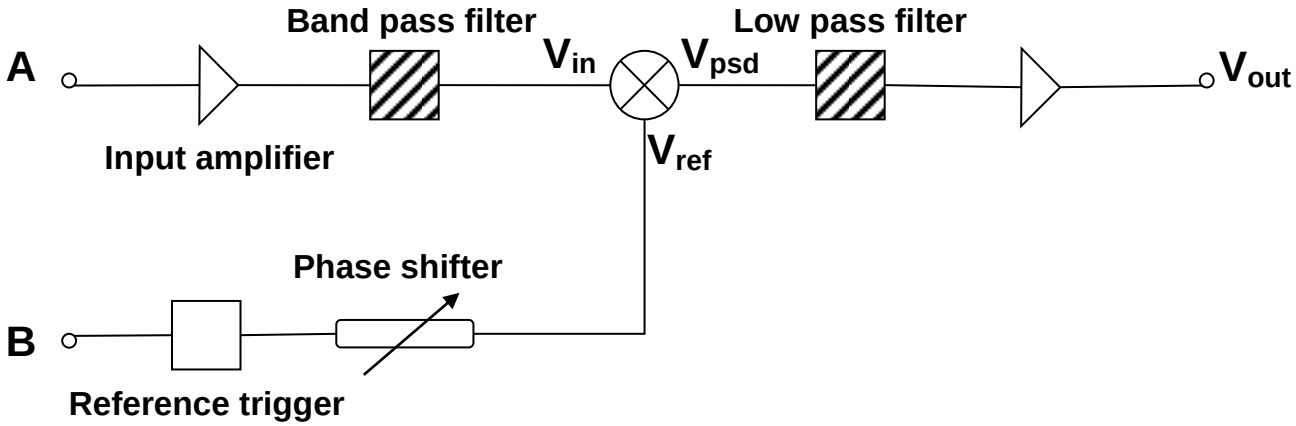

Figure 2.4: The schematic diagram of typical lock-in amplifier.

Figure 2.4 shows the schematic diagram of typical lock-in amplifier. The lock-in amplifier uses a technique known as PSD (phase-sensitive detection) to pick up the component of signals at a specific reference frequency and phase. A lock-in amplifier can not only recover signals from a noisy background, but also enhance the resolution of relatively clean signals over several orders of magnitude and frequency.

The output of PSD is simply the product of two cosine wave functions, as follows:

$$V_{in} = A \times Cos(\omega t)$$
$$V_{ref} = B \times Cos(\omega t + \theta)$$
$$\theta = (\theta_{sig} - \theta_{ref})$$

θ is the phase difference between signal and lock-in reference. It is a user-adjustable phase-shift introduced within the lock-in amplifier.

$$V_{psd} = V_{in} \times V_{ref} = ACos(\omega t) \times BCos(\omega t + \theta) = 1/2 \times AB\ Cos(\theta) + 1/2 \times AB\ Cos(2\omega t + \theta)$$

The output from the PSD then passes to a low-pass filter which removes the 2ω component. Consequently, the output of PSD is $V_{out} = AB \times Cos(\theta)$. Therefore, the largest output signal can be obtained when θ is 0, namely θ_{sig} is equal to $\theta_{ref.}$ This case can be called the "In-phase"[45].

Oscilloscope

An oscilloscope is an electronic test instrument used to observe the change in signal voltages. The display of an oscilloscope is a two-dimensional graph, composed of a horizontal or "X" axis and a vertical or "Y" axis. The horizontal or "X" axis indicates a function of time, and the vertical or "Y" axis shows one or more electrical potential differences. An oscilloscope is usually needed to observe the wave shape of an electrical signal. The amplitude of the signal can be read by the vertical or "Y" axis, and the time between two events (such as pulse width, period, or rise time) and relative timing of two related signals can be measured by the horizontal or "X" axis. In Chapter 3, we used an oscilloscope to observe the change of PL intensity as a function of time.

Continuous-flow cryostats

A continuous-flow cryostat was used to adjust the temperature changes for this experiment. When liquid nitrogen is consumed within the cryostat, it is continuously replenished by a steady flow of liquid nitrogen from the storage Dewar. Inside the cryostat, a manually controlled continuous-flow of liquid nitrogen enters a heat exchanger fitted with a heating coil and temperature sensor, which are connected to a temperature controller. This arrangement allows the cooling power to be optimised for the required temperature, minimising liquid nitrogen consumption and temperature gradients between sample and sensor. The thermal link between the heat exchanger and sample is made by exchanging the gaseous nitrogen.

2.2.3 Measurements in magnetic field

The magnetic field was generated by an electromagnet, which is combined with a variable PSU. The power supply varies the current through the electromagnet in order to change the magnitude of the magnetic field from 0 to ~200mT. A Hall-probe gaussmeter (GM 05 Gaussmeter) was placed close to the sample holder to measure the strength of the electromagnet. The PSU supplies a positive current for magnetic field measurement, and a negative current for null field in order to counteract the remnant field of the electromagnet.

A common problem with the Alq_3 powder is that the sample will degrade when the laser excites it for a long time. Degradation could occur for the following reasons. Firstly, the intense laser can damage some of the Alq_3 molecules. Secondly, the Alq_3 powder sample was exposed to contact with impurities such as water and oxygen (in the air), which can act as quenching centres. As a result, this degradation of the Alq_3 powder sample will lead to a decrease in the PL. Since the drift in the PL is not necessarily constant between successive measurements, it is necessary to account for this drift when taking measurements. In order to resolve the drift problem in the PL, the adjacent raw null field data was taken and averaged as one MPL null field data point,

PL_{nul}. Table 2.1 shows the magnetic field values for each MPL measurement. The raw data with null fields, $PL\ (B_{n-1})$ and $PL\ (B_{n+1})$, are given as odd number measurements. The raw data with magnetic filed, $PL\ (B_n)$, are given as even number measurements. So the percentage change in MPL will simply be given by:

$$\Delta PL / PL = (PL(B_n) - PL_{null}) / PL_{null}$$

where $PL_{null} = (\ PL(B_{n-1}) + PL(B_{n+1}\ ))\ /2$

Table 2.1: Measured magnetic field values for each MPL measurement

B_1=0mT	B_2=0.2mT	B_3=0mT	B_4=1.2mT	B_5=0mT
B_6=2.2mT	B_7=0mT	B_8=3.1mT	B_9=0mT	B_{10}=4.0mT
B_{11}=0mT	B_{12}=5mT	B_{13}=0mT	B_{14}=6.0mT	B_{15}=0mT
B_{16}=7.0mT	B_{17}=0mT	B_{18}=8.0mT	B_{19}=0mT	B_{20}=9.0mT
B_{21}=0mT	B_{22}=11.6mT	B_{23}=0mT	B_{24}=14.1mT	B_{25}=0mT
B_{26}=16.7mT	B_{27}=0mT	B_{28}=19.3mT	B_{29}=0mT	B_{30}=21.8mT
B_{31}=0mT	B_{32}=24.4mT	B_{33}=0mT	B_{34}=34.7mT	B_{35}=0mT
B_{36}=55.8mT	B_{37}=0mT	B_{38}=77.2mT	B_{39}=0mT	B_{40}=98.8mT
B_{41}=0mT	B_{42}=130.3mT	B_{43}=0mT	B_{44}=161.8mT	B_{45}=0mT
B_{46}=193.2mT	B_{47}=0mT			

2.3 Magnetoresistance

2.3.1 Introduction

In this section, we will introduce the processes for both the device fabrication and experimental methods. Device fabrication is composed of the preparation of the substrate and the organic and metallic deposition. A good substrate is vital for creating a useful OLED device and adheres to a strict preparation process, as described below. Once the device had been fabricated, we immediately measured its (current-voltage-light output) I-V-L characteristics to test the quality of the device. If the device was found to be of the operational standard required the OMR would need to be tested at different operating and temperature conditions, for the experimental purposes of Chapters 4 and 5. The I-V-L characteristics and OMR measurements are described later on in this section.

2.3.2 Device fabrication

Preparation of substrate

All OLED devices were fabricated on indium tin oxide (ITO) coated glass substrates purchased from Merck. The ITO is commonly used as electrodes for OLED devices as the work function of ITO matches the energy levels of the hole transport materials. In addition the ITO is transparent, enabling light output from the devices. The substrate size was 20mm×20mm with a sheet resistance of ~13Ω/Square. The ITO coated glass substrates were cleaned, patterned by photolithography and etching, and cleaned again before the device was fabricated. The processes are as follows.

Cleaning

The cleaning process was crucial, as any failure in the cleaning procedure results in poor performance of devices. To achieve the proper cleanliness required, the substrates were cleaned in detergent and solvents using an ultrasonic bath. The substrates were first washed with powered detergent in distilled water. They were then transferred to specially designed holders and inserted into a beaker containing a solution of detergent and distilled water. The beaker was then placed in an ultrasonic bath for about 20 minutes. This process is called ultrasonication. The sonicator induces a high frequency acoustic wave in the liquid, which leads to the formation of microscopic gas bubbles. When these bubbles collapse, the energy will transfer to the substrate surface to remove the microscopic impurities. Further ultrasonications were repeated three times, with the substrates being immersed in distilled water for five minutes per rinse. After this, the substrates were ultrasonicated in acetone and chloroform for five minutes; this was repeated twice. Finally the ITO substrates were dried with nitrogen gas.

Photolithography

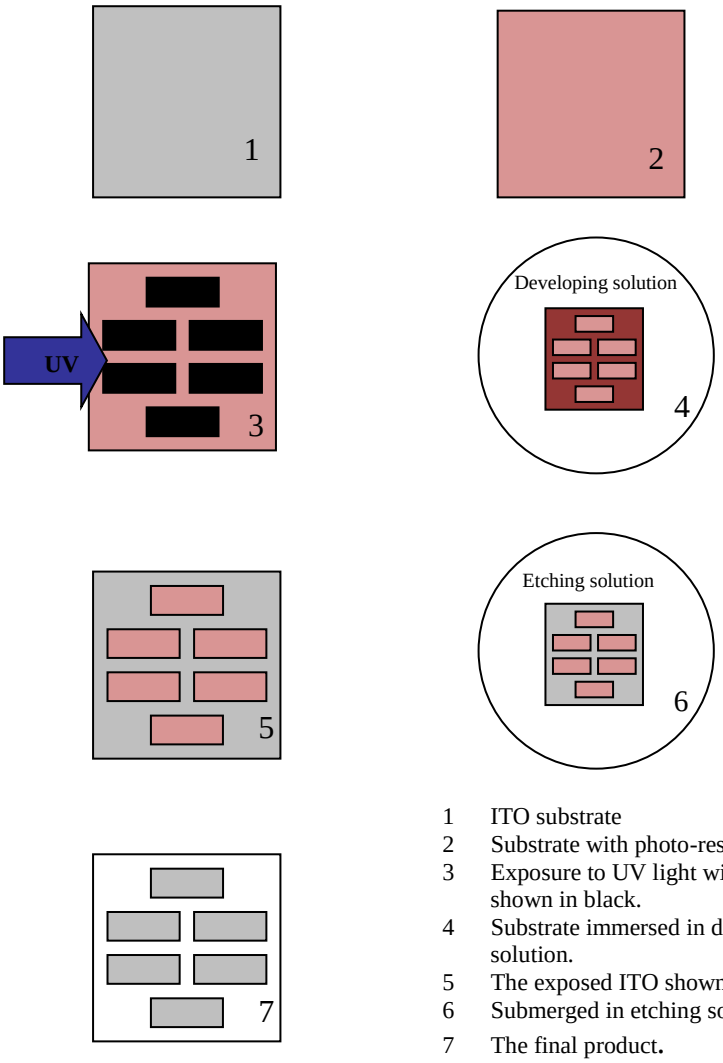

Figure 2.5: The flow diagram of the photolithography process.

The flow diagram of the photolithography process is presented in Figure 2.5. Once cleaned, the ITO substrates were subjected to a series of photo-chemical processes to remove unwanted ITO from the substrate, finally leaving behind the electrode pattern.

The first step of this process was to spin coat a layer of *Shipley 1818 sp16* photo-resist onto the surface of the ITO substrates. This was done to ensure a uniform layer of photo-resist. The substrate was mounted on the chuck of the spin coater with the

ITO surface facing upward. The vacuum generated by a vacuum pump was able to securely hold the substrate while it was spinning. Furthermore, about 12 drops of photo-resistant solution were dropped onto the ITO substrate using a pipette. The wetting of the substrate was carried out at 500rpm for 18 seconds and then accelerated up to 6000-7000rpm and maintained for 60 seconds. The substrate was then cured for 15 minutes in a 90^{o}C oven.

Next, the pattern of the electrodes needed to be exposed onto the photo-resist. The substrates were laid, photo-resistant solution side down, upon the mask in a UV light box. The substrates were then exposed to the light source for 60 seconds. Next, they were immersed in the developing solution, which consisted of a 1:3 NaOH solution and distilled water. The substrate was submerged for 60 seconds, then rinsed with distilled water in the sonic bath for five minutes and dried.

The final step was to remove the unwanted ITO not covered with photo-resistant solution. The etching solution was a mixture of 50% distilled water, 48% hydrochloric acid and 2% nitric acid. Using a beaker, it was heated in a water bath to between 48^{o}C and 50^{o}C, after which the substrate was soaked in the solution for 1 minute 45 seconds then immediately rinsed in distilled water in the sonic bath. To remove the remaining photo-resistant solution the sample was rinsed with acetone in the sonic bath for five minutes. The ITO substrates went through another cleaning process (as described earlier) and then dried in preparation for the plasma treatment, which is described below.

Plasma Treatment

The purpose of the plasma treatment is to remove impurities from the patterned ITO and increase the work function of the ITO. The cleaned ITO substrate was transferred into a *Diner Electronic Femto plasma system* with the ITO facing upwards. Oxygen gas was allowed to flow through this chamber and kept at a pressure of about 1.5 mbar for five minutes to ensure the system was oxygen rich. The power of the plasma system was adjusted to 30W, and the treatment time was set to 4 minutes. When the pressure of oxygen gas was lowered to about 0.2 mbar, the generator was switched on and the ITO substrates were treated for the desired time. Once the

treatment was completed, the ITO substrate had to be mounted on the sample holder, which has an aperture in the middle allowing materials to be deposited on the substrate. Finally, the sample holder was loaded into the load lock chamber of the evaporation system growth.

Organic and metallic deposition

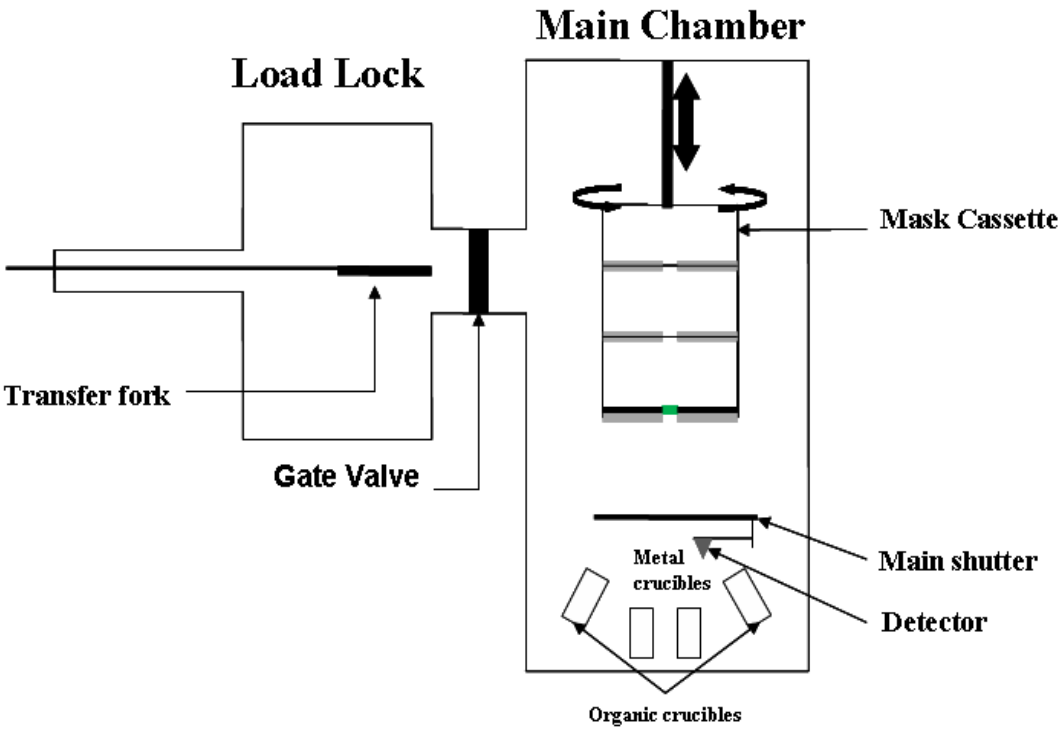

Figure 2.6: A schematic of a Kurt J. Lesker SPECTROS evaporation system.

A Kurt J. Lesker SPECTROS evaporation system is used for device growth. This system consists of two vacuum chambers: the load lock and the main chamber. Figure 2.6 shows a schematic for this evaporation system. The substrate holder is placed on the transfer fork in the load lock chamber, which is connected to a scroll pump and a turbo-molecular pump. Once the load lock chamber is pumped down to 10^{-5} mbar, the gate valve can be opened, allowing the substrate to transfer into the

main chamber. The main chamber is connected to a scroll and a helium cryo-pump. This chamber can be evacuated up to 10^{-8} mbar, reduced to ~10^{-7} mbar during evaporation. The mask cassette has four shelves and is designed to move vertically and rotate. There are two kinds of masks: a square one for the TPD, Alq_3 and LiF, and another rectangular one for the Al. The mask can be loaded onto different shelves by vertically moving the mask cassette. Furthermore, the sample holder has to be safely mounted on the plates over an aperture, which allows materials to be deposited on the substrate. Finally, the mask cassette can be lowered to a proper vertical distance from the material sources and rotated, to allow an even thickness film to be deposited.

The evaporation system in the main chamber consists of eight organic sources and two metal sources. The evaporation process is controlled by *SQS software* that regulates the power to heat the sources with a desired deposition rate to reach an expected thickness. The deposition rate of each source is monitored by the detector, which is a quartz crystal monitor. It is capable of measuring the thickness to an accuracy of 0.5%. The designs of organic source crucibles and metal source crucibles are different, since metals need higher temperatures to be sublimated, compared with the organic materails.

A standard device used for the purpose of this research was constructed by the following process. Firstly, a 50nm layer of TPD was deposited on the substrate using the square mask. The 50nm layer of Alq_3 was then deposited on top of the TPD, followed by approximately 1nm of LiF (see Figure 2.7a). The purpose of evaporating the LiF layer was to improve the charge injection into the device [13, 14]. This is because the LiF decreases the effective work function of the cathode and makes electrons from the cathode relatively easier to inject into the LUMO of the Alq_3 layer. The square mask was then replaced into the rectangular one to evaporate the Al cathode. For the first 10nm of Al, the deposition rate was kept at 0.1nm/s, after which it was increased to 0.4nm/s for the remaining 90nm. This resulted in a

100nm rectangular Al layer being deposited on the LiF layer, and sat vertically above the ITO to form the cathode (see Figure 2.7b). After the Al deposition was complete, the sample was ready for the following tests.

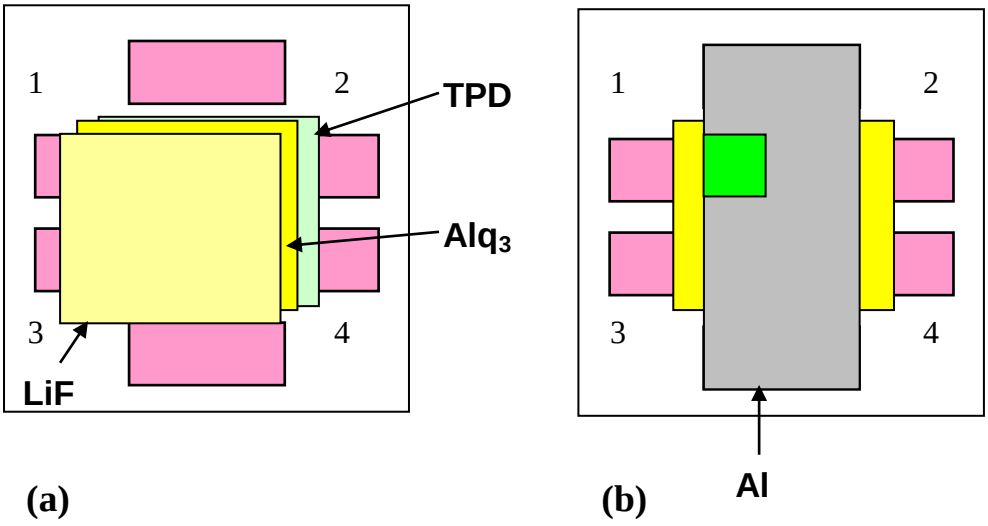

Figure 2.7: The areas the materials cover are a) a centred square for the TPD, Alq_3 and LiF, and b) rectangular for the Al cathode. The green square represents a single OLED (defined by the overlap area of the electrodes).

2.3.3 Experimental methods

I-V-L characteristics measurement

Before the OMR test, the quality of the devices needed to be assessed by measuring the I-V-L characteristics of the OLEDs. The efficiency of the OLEDs is the key factor when comparing the quality of different devices. The efficiency can be calculated by dividing the electrical power input by the light output. The equation for calculating the efficiency of the device is as follows:

$$\eta = \frac{L}{IV} \times 100\%$$

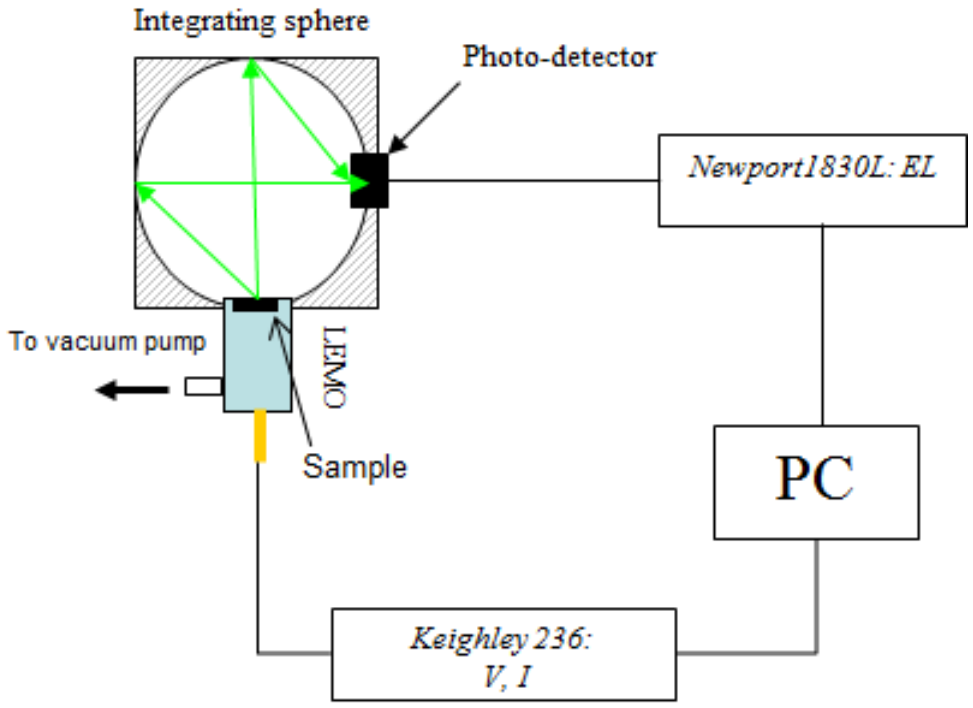

Figure 2.8: Schematic of the I-V-L characteristics assessment system.

Before testing our OLED device, a *Leybold PT50* pumping station was used to evacuate the sample environment, in order to prevent the device from oxidisation and contamination from the air. The schematic of the I-V-L characteristics assessment system is shown in Figure 2.8. A *Keithley 236 voltage/current source measure unit (Keithley 236:V.I)* was used to drive this device and measure the current passing through it. This device was placed into a sample holder, which was connected to the *Keithley 236:V.I* via a LEMO connector and a triax cable. This setup allowed for measurements of current from 10^{-12} to 10^{-1} A. The sample holder was placed on one side of the integrating sphere. The integrating sphere is designed to produce uniform light from the source by reflection and diffusion in the sphere's internal surface. A silicon photo detector was inserted into the other side of the integrating sphere. A silicon photo detector, also known as a photodiode, is usually made by a silicon P-N junction. When photos with efficient energy strike this detector it can generate a current and voltage. This process is attributed to the photovoltaic effect mechanism. The integrating sphere provides an even coverage over the silicon photo detector, allowing it to measure the light emitted from all angles, thus supplying accurate data of the total light emitted by the OLED. The silicon photo detector is connected to a *Newport1830 optical power meter (Newport1830 C: EL)* through a calibration module that accounts for different experimental arrangements of the silicon photo detector. In order to get a useful measurement, the power meter is set to the peak wavelength of the emission spectra of the OLED. The instruments are connected to a PC that records the I-V-L characteristics measurement simultaneously.

2.3.3.2 OMR measurement

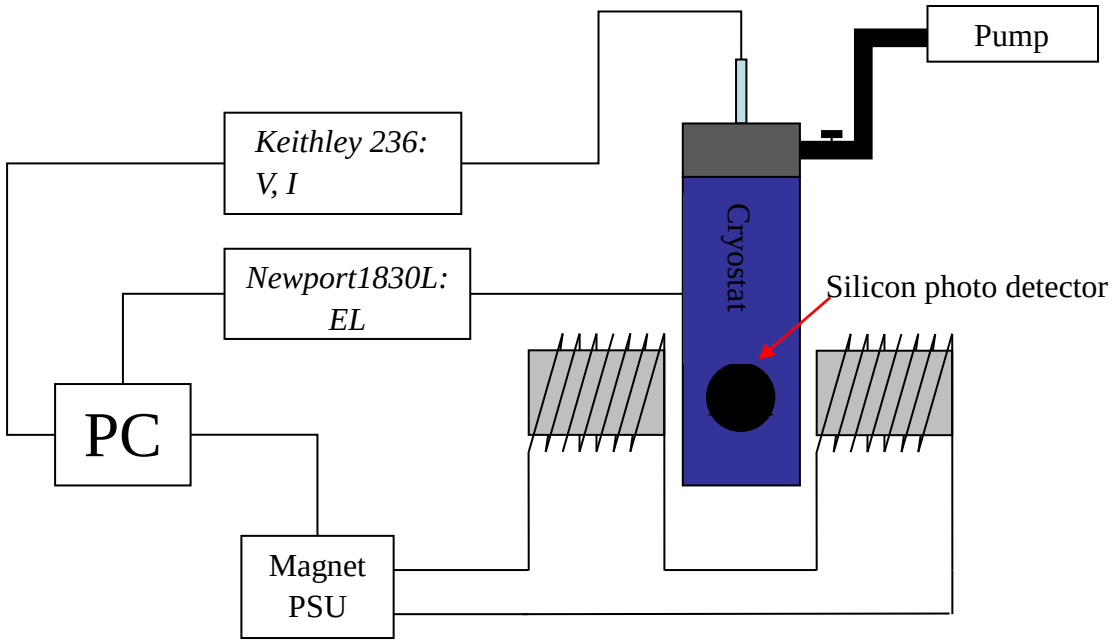

Figure 2.9: A schematic set up for organic magnetoresistance measurements for an Alq_3 based OLED device.

Figure 2.9 shows a schematic diagram for OMR measurements of devices. The device was mounted on a sample holder, and then placed into a continuous flow cryostat. In order to measure the OMR as a function of temperature, the temperature inside the cryostat could be adjusted between 80K and 300K. Furthermore, this cryostat was placed between the two poles of the electromagnet, with the magnetic field perpendicular to the direction of current flow in the device. A calibrated silicon photo detector of a *Newport1830 C: EL* is placed directly in front of one of the cryostat windows. In order to stop light pollution from outside, thick black tape was used to seal the other cryostat windows. The electromagnet set up for OMR was similar to that used in MPL.

Like the MPL measurement, the OMR test also needed to take into account the device degradation during device operation. Degradation could occur after the device had been operated for a long time, and causes small areas of the device to stop working, thus reducing the area of the device. Therefore, a drift in current through the device will occur at a given voltage. In order to remove any effects, due to drifting, in the device characteristics, the OMR was simply calculated using:

$$\Delta I / I = (I(B_n) - I_{null}) / I_{null}$$

where $I_{null} = (I(B_{n-1}) + I(B_{n+1})) / 2$

The value of $I(B_n)$ indicates the current through the device with a magnetic field B. The values of $I(B_{n-1})$ and $I(B_{n+1})$ denote the current through the device with null field. The I_{null} is the average value between $I(B_{n-1})$ and $I(B_{n+1})$.

Chapter 3:

Magnetic field effects on photoluminescence

3.1 Introduction

In Chapter 1, we introduced the basic principles of photoluminescence (PL). In 2004, Cölle *et al.* observed that the PL signal decreases to a constant equilibrium value, while using an intense rectangular laser pulse to excite an Alq_3 sample at low temperature [46]. The decay in the PL is analogous to the bleaching of laser dyes [47], and has previously been attributed to intersystem crossing (ISC) from the singlet to triplet states [46, 48]. They proposed a simple rate model to explain the decrease in the PL intensity and estimate the percentage of the molecules excited in the triplet state. At the beginning of this chapter, I will discuss this rate equation model. Next I will develop the rate equation model for the experimental results reported and use it to estimate the rate constant of ISC in Alq_3. In addition, the effect of a magnetic field on the PL intensity for Alq_3 will be discussed. Finally, I will study the change in the intersystem crossing rate caused by applying a magnetic field.

3.2 The decreased PL intensity for Alq_3

In 2001, Braun *et al*. proposed that it was possible to obtain significant triplet populations through optical excitation to an Alq_3 sample at low temperature [48]. The increase in the population of triplets was attributed to the intersystem crossing from the singlet to the triplet state. This work was extended in 2004 by Cölle's group [46]. This group proposed a simple rate model, as shown in Figure 3.1. This simple rate model can not only estimate the percentage of the molecules excited in the triplet state caused by the ISC, but can also explain the decrease in the PL intensity through an intense excitation pulse [49].

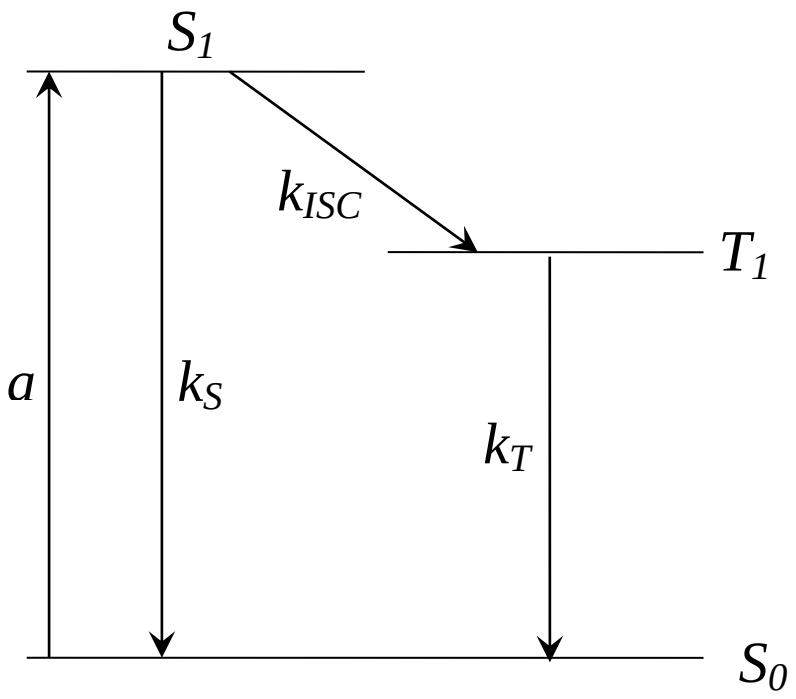

Figure 3.1: The simple rate model from the Cölle's group.

The equations for the simple rate model can be described as:

$$\frac{dS_0}{dt} = k_S S_1 + k_T T_1 - aS_0$$
$$\frac{dS_1}{dt} = aS_0 + k_{ISC} T_1 - k_S S_1 - k_{ISC} S_1 \qquad \text{Equation (3.1)}$$
$$\frac{dT_1}{dt} = k_{ISC} S_1 - k_T T_1 - k_{ISC} T_1$$

Where, S_0 and S_1 denote the non-excited ground state and the first excited singlet level, T_1 represents the lowest triplet level, k_S and k_T represent the recombination rates for singlet and triplet, a is the pump rate, which is proportional to the laser excitation intensity, and k_{ISC} is the rate constant for intersystem crossing.

The decrease in the PL intensity can be explained as follows. Before the excitation laser pulse is turned on the percentage of molecules in the S_0 is 100%, but both the S_1 and T_1 are not populated. When the Alq_3 sample is excited by a rectangular laser pulse, S_1 is directly populated by absorption of the laser pulse, and the ISC results in an increase in the population of the T_1 state. At a temperature of 80K, the lifetime for the singlet in Alq_3 is of the order of 10- 20ns [9], whilst that of the triplets is in the order of 10 ms [46]. This would suggest that the S_1 state can maintain a small population of molecules, because the recombination rate for the singlet is very fast ($\sim 10^8$ s^{-1}). In addition, the triplet states, being long lived, can't contribute to the fluorescence emission in this experiment. Therefore, the population of molecules is distributed mainly between the ground state and triplet state. This implies that the observed decrease in PL intensity is due to an increase in the percentage of molecules in the T_1 state is not able to emit the PL. The whole system will finally reach a dynamic equilibrium, resulting in the decrease in the PL intensity approaching an equilibrium value.

In this work, we used an intense laser pulse to excite the powdered Alq_3 sample at 80K. Figure 3.2 shows a typical absorption and emission spectra. The peak of the

emission spectrum (or PL), at sample temperatures of 80K is located at a wavelength of 520nm.

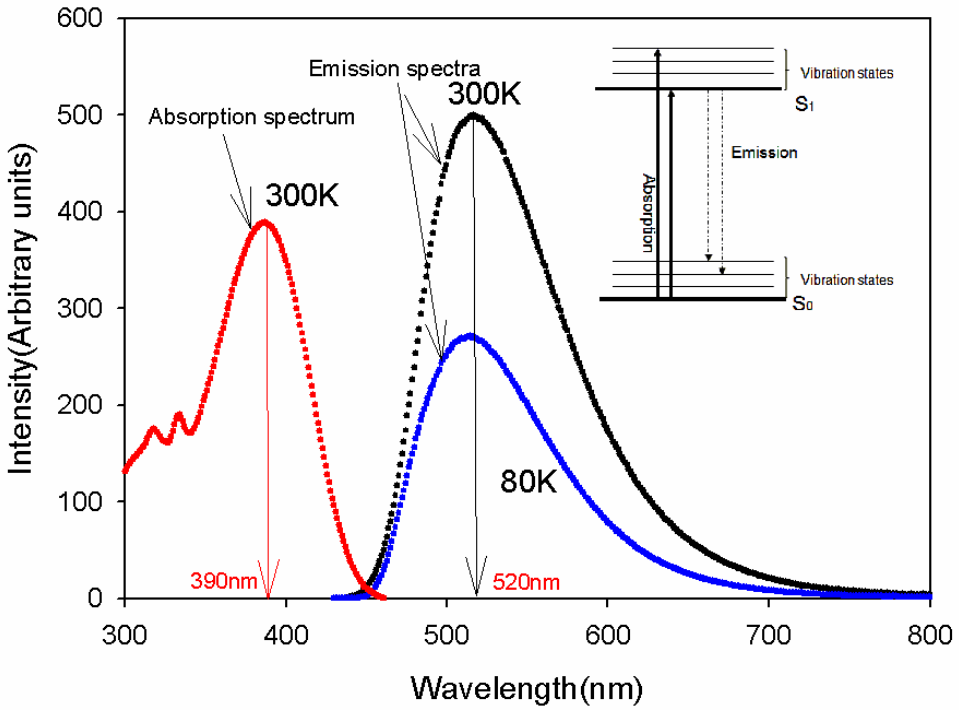

Figure 3.2: The typical absorption and emission spectrum. The inside figure is the energy diagram of absorption and emission spectrum.

Figure 3.3 shows the time dependence of the PL for Alq_3, recorded at a wavelength of 520nm, and at sample temperatures of 80K. Similarly to Cölle's group, we observed that after the excitation is switched on the PL intensity experiences a decrease and finally approaches an equilibrium value. The rise time of the PL for Alq_3 depends on the rise time of the laser pulse. The laser was mechanically modulated using an electromagnetically controlled switch. If the rise time of the laser is too large, then the decay process for the intensity of the PL can't be seen, even at intense excitations. This is due to the fact that the decay of the PL is convolved with the laser pulse. A very fast modulation can be achieved by using electrical modulation of the laser beam. However, this produces an oscillation in the laser intensity that made interpretation of the intensity decay difficult. It was observed that a modulated laser pulse with a rise

time of ~100 μs can be ideally used to produce a clean decay of the initial PL before it reaches a steady state value. In order to produce a rise time as fast as possible, a microscope objective has to be used to reduce the size of the laser beam and focus it at the switch of the relay. This is because the rise time of the laser is defined by the size of the laser when the speed of chopping the laser beam is constant. The frequency of laser beam was mechanically modulated by the switch of the relay at 5Hz. The relay was controlled by a function generator. This means the period of laser is 2×10^5 μs, which is long enough to observe the decay in the initial PL and achieve a continuous steady state PL.

Then, Neutral density filters were used to modify the laser intensity to excite the sample. As seen in Figure 3.3, the intensity of the PL is reduced by decreasing the intensity of excitation.

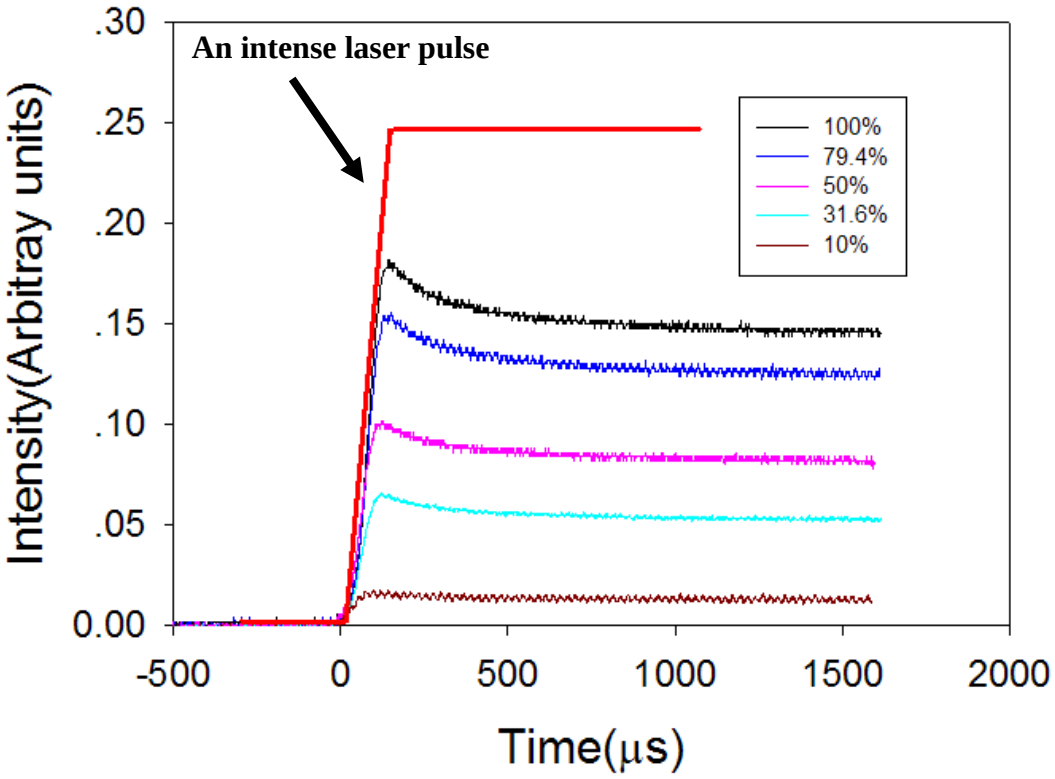

Figure 3.3: Time dependence of the 520nm PL from Alq_3 at a temperature of 80K at different laser intensities. The intense laser pulse with a frequency of 5Hz and a rise time of ~100μs.

Figure 3.4 shows the percentage change in PL intensity using various density filters of 100%, 79.4%, 50%, 31.6% and 10% of in front of the laser. The experimental data were measured using an 8-bit digital oscilloscope, which provides 256 digitising levels. Since only finite levels are available to represent the signal, the percentage change in PL intensity was difficult to observe with reduced excitation intensity (see Figure 3.4). First, these percentage change processes were fitted using a single exponential decay function of the form

$$I = I_0 + I_1 \exp(-t/\tau) \qquad \text{Equation (3.2)}$$

where, I_0 is the steady state intensity, I_1 is the initial intensity, and τ is the lifetime. Figure 3.4 shows that a single exponential decay function approximately fits the experimental data at long time range. Figure 3.5 shows the short time range of

Figure 3.4; the fast process observed experimentally could not be accurately fitted using a single exponential function.

Because the powdered Alq_3 sample has a large surface area, impurities such as water and oxygen can act as quenching centres at the surface of this sample. Therefore, there would be a distribution in lifetimes, with the bulk of this sample having long lifetimes, and those at the surface having short lifetimes due to the rapid quenching. As reasoned above, the powdered Alq_3 powder sample is regarded as a disordered system. In physics, the stretched exponential function is widely used as an empirical fit to the nonsingle-exponential decay process in the disordered systems [50]. Therefore, a stretched exponential function was used to fit these percentage change processes. The stretched exponential function takes the form

$$I = I_0 + I_1 \exp\left[-(t/\tau)^{\beta}\right] \qquad \text{Equation (3.3)}$$

where, I_0 is the steady state intensity, I_1 is the initial intensity, τ is the lifetime, and β is the stretching factor. β quantifies the variation in different τ *and its* value describes the characteristics of the experimental data. When β=1, the experimental process is regarded as a single exponential distribution. When β is between 0 and 1, the experimental process is characteristically stretched. Table 3.1 shows the individual β value of the stretched exponential fitting for each experimental data set in figure 3.4.

Using this stretched exponential function, it is possible to define an average relaxation time $\langle\tau\rangle$,

$$\langle\tau\rangle = \frac{\tau}{\beta}\Gamma\left(\frac{1}{\beta}\right) \qquad \text{Equation (3.4)}$$

Where $\Gamma\left(\frac{1}{\beta}\right) = \int_0^{\infty} t^{(\frac{1}{\beta})-1} e^{-t} dt$ is the Gamma function.

Figures 3.4 and 3.5 show that the quality of the free fits by the stretched exponential function is excellent in all cases. Table 3.1 shows the average relaxation times, the percentage changes in the PL, and the stretching factors derived from the stretched exponential fitting. Table 3.1 shows that the error for each of the parameters from the fitting increases when reducing the excitation intensity. This is due to the fact that, as the laser to excite the sample decreases, only a small population of molecules can transfer from singlet state to triplet state. This will result in a lower percentage change in the PL. Because an 8-bit digital oscilloscope was used, there is a lack of dynamic range and it is difficult to observe the small percentage change in the PL at low excitation to the sample. This explains why the error for each of the parameters from the fittings increases when reducing the excitation intensity. However, all of β values are within experimental errors, 3σ.

In Figures 3.4 and 3.5, it can be seen that the quality of the fits by fixing the stretching factor β= 0.68 is still excellent. The β= 0.68 is average number of the stretching factors for free fitting the percentage changes in PL with excitation percentage from 100% to 31.6%. The stretching factor for 10% excitation didn't account into average value, because it involves a large error. Table 3.1 shows the average relaxation times, the percentage changes in the PL, and the stretching factors derived from the stretched exponential fitting with β= 0.68. Table 3.1 shows very little effect on the average relaxation time observed in the PL for the free stretching factor case or for β= 0.68, with any changes being less than the experimental reproducibility of ~10%. Although the reduction in excitation intensity results in a dramatic reduction in the luminescence decay from its initial value when the laser is first switched on, table 3.1 illustrates that fixing the value of β to 0.68 does not affect this reduction. In the free stretching factor case, the percentage change in the PL is reduced from -9.9$\pm$0.01% to -2.9$\pm$0.35%, by reducing the excitation intensity from 100% to 10% of its initial value and these results have been published in Journal of Applied Physics[40]. Fixing β to 0.68, results in a percentage change in the PL from -9.8$\pm$0.02% to -2.54$\pm$0.3%, when the excitation intensity drops from 100% to 10% of its initial value. The difference

between free and fixed stretching factor for fitting the experimental data would be not significant.

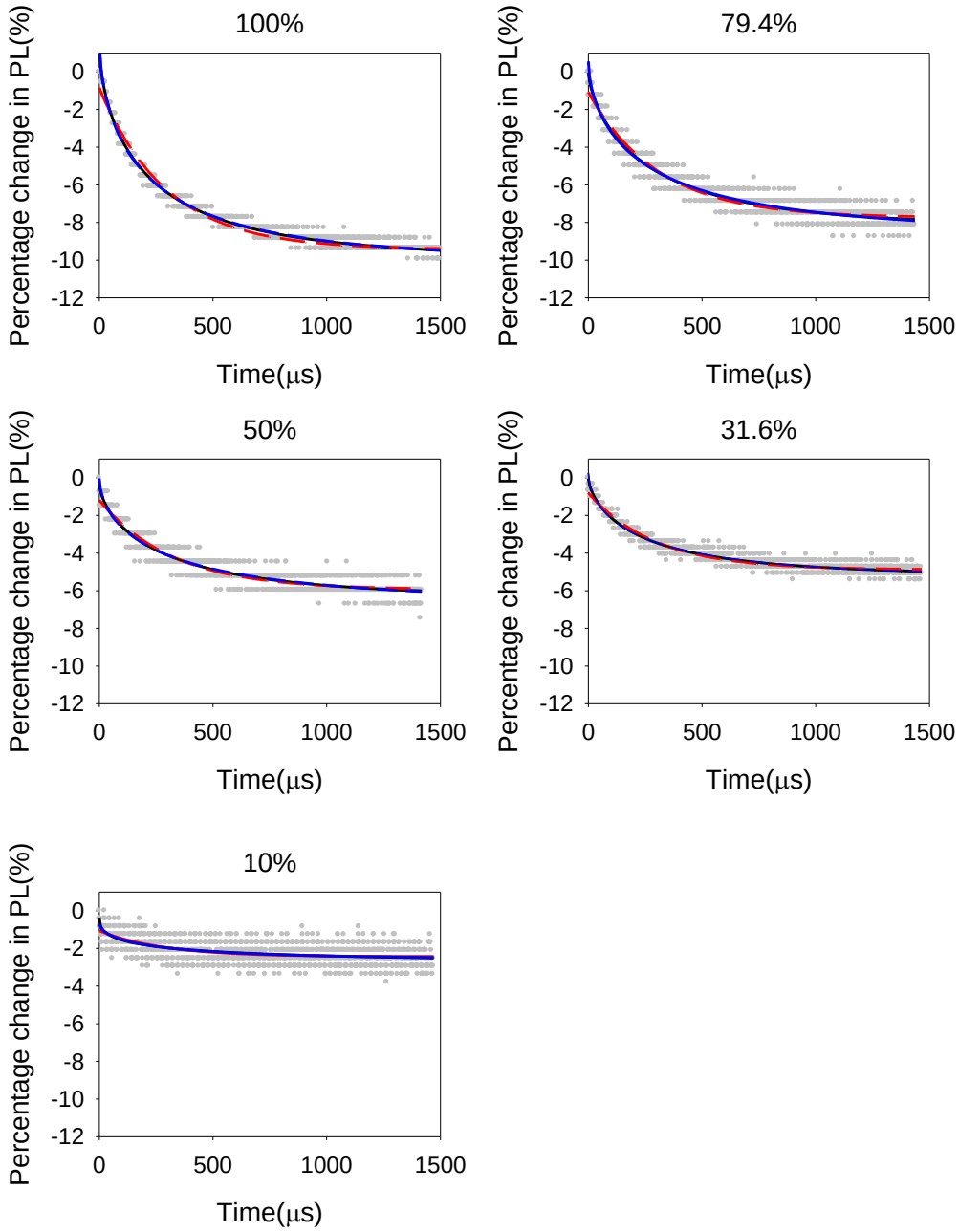

Figure 3.4: The percentage changes in PL intensity using various density filters of 100%, 79.4%, 50%, 31.6% and 10% in front of the laser. The red dashed lines are fits obtained using the exponential decay function, Equation (3.2). The black solid lines are fits obtained using the stretched exponential function, Equation (3.3). The blue solid lines are fits obtained using the stretched exponential function, Equation (3.3) and a fixed value of β=0.68.

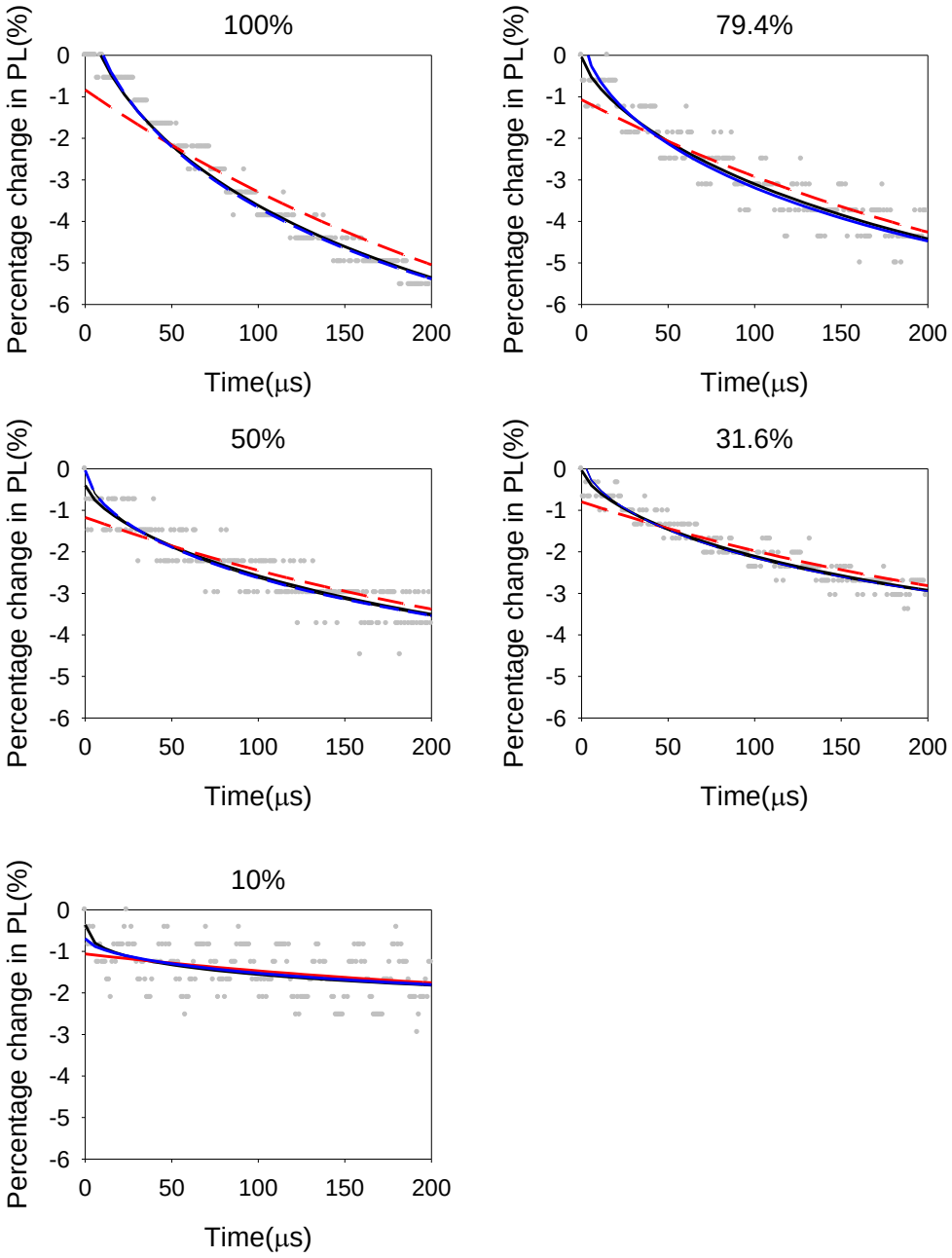

Figure 3.5: Each graph in Figure 3.4 corresponds to the detail of the short time region. The fits are as detailed in Figure 3.4.

Table 3.1: Experimental data for the PL relaxation lifetimes and the percentage change in PL intensity from the initial value as a function of initial intensity. β is the stretching factor for fitting each of the experimental decay curves. The errors are taken from the fits.

Percentage intensity	**100%**	**79.4%**	**50%**	**31.6%**	**10%**
Experimental $\langle\tau\rangle$	$(326 \pm 3.3)\,\mu s$	$(358 \pm 7.9)\,\mu s$	$(319 \pm 11.2)\,\mu s$	$(305 \pm 6.8)\,\mu s$	$(361 \pm 12.5)\,\mu s$
Experimental ΔI	$(-9.9 \pm 0.03)\%$	$(-8.2 \pm 0.08)\%$	$(-6.3 \pm 0.09)\%$	$(-5.2 \pm 0.1)\%$	$(-2.9 \pm 0.35)\%$
β	0.64 ± 0.01	0.71 ± 0.02	0.69 ± 0.03	0.68 ± 0.02	0.39 ± 0.12
Experimental $\langle\tau\rangle$	$(316 \pm 3.2)\,\mu s$	$(373 \pm 8.4)\,\mu s$	$(360 \pm 11.5)\,\mu s$	$(340 \pm 6.9)\,\mu s$	$(333 \pm 13.1)\,\mu s$
Experimental ΔI	$(-9.8 \pm 0.02)\%$	$(-8.3 \pm 0.09)\%$	$(-6.3 \pm 0.1)\%$	$(-5.2 \pm 0.14)\%$	$(-2.54 \pm 0.3)\%$
β	0.68	0.68	0.68	0.68	0.68

The decrease in the PL has previously been attributed to the ISC from the singlet to triplet states [48, 49]. In order to understand this phenomenon, Cölle's model (Equation 3.1) was used to try and simulate the percentage changes in PL intensity in Figure 3.4. The lifetime of the singlet state (τ_S) is 18ns, which is taken as a representative of the literature values [9] and used for all temperatures. In 2004, Cölle *et al.* measured the triplet lifetimes of Alq_3 powder by delayed PL as a function of temperature. Meanwhile, they also measured the triplet lifetimes in the Alq_3 based OLEDs by delayed electroluminescence (EL) as a function of temperature [46]. The values for the triplet lifetime (τ_T) for temperatures between 80K and 120K are summarised in Table 3.2.

Table 3.2: Temperature dependence of the triplet lifetime (τ_T) from 80K to 120K. (A) is the τ_T measured by the delayed PL of the yellowish-green Alq_3 powder. (B) represents the τ_T measured by the delayed EL of the Alq_3 based OLEDs.

Temperature	(A)	(B)
80K	8.5ms	5.6ms
100K	5ms	5ms
120K	4.5ms	6ms

Given that $k_S = 1/\tau_S$ and $k_T = 1/\tau_T$, the only variables in the simple rate model are k_{ISC} and a. As the triplet lifetime (τ_T) is much higher than the singlet lifetime (τ_S), the value of the rate constant of the singlet decay is far greater than that of the triplet ($k_S >> k_T$). The term k_{ISC} is introduced to denote the intersystem crossing from singlet to triplet. In this system, the k_{ISC} should be greater than k_T and less than k_S. Therefore, the range of k_{ISC} for simulating the percentage changes in PL intensity in Figure 3.4 should be chosen at between 10^3 and 10^8 s^{-1}. For each simulation, the k_{ISC} is kept constant and the pump rate (a) is reduced. Figure 3.6 shows the simulations of Cölle's model for the percentage changes in PL intensity. In order to simulate the experimental data at a temperature of 80K, as shown in Figure 3.4, we used the τ_T=8.5ms was used as the value for the triplet lifetime. This simulated data was fitted with the exponential decay function, Equation (3.2).

Table 3.3 presents the parameters from the fittings to simulated data in figure 3.6. By adjusting k_{ISC} and the pump rate (a), it is possible to approach the experimental magnitude of the decrease in the luminescence intensity (ΔI), but the simulated lifetime of the luminescence (τ) is far from the experimental relaxation lifetime, and *vice versa*. For example, while setting the $k_{ISC}=10^4 s^{-1}$ and $a=10^7/S_0(initial)$, ΔI is -7.8%, which approaches the experimental result of -9.9 ±0.01%. However, the τ ~7800 μs is rather far from the experimental relaxation lifetime ($\langle\tau\rangle$ =(326 ±3.3) μs).

Therefore, for simulations following Cölle's model, it was not possible to reproduce the percentage changes in PL intensity shown in Figure 3.4.

Furthermore, for simulations using Cölle's model, the effect of changing the excitation intensity by a factor of 10 not only changes the magnitude of the decrease in the luminescence intensity, but also dramatically alters the lifetime of the luminescence. For these experimental results presented in this thesis, as shown in Figure 3.4 and Table 3.1, by reducing the excitation intensity from 100% to 10% of its initial value, there is very little effect on the average relaxation time observed in the PL. The range of the average relaxation time is scattered from $305 \pm 6.8\,\mu s$ to $361 \pm 12.5\,\mu s$. However, the percentage change in PL intensity is reduced from $-9.9 \pm 0.01\%$ to $-2.9 \pm 0.35\%$. Hence it can be concluded that the reduction in the excitation intensity results in a dramatic reduction in the luminescence intensity, but has little effect on the average relaxation time. Therefore, the simulation based on Cölle's model does not correlate with the experimental results in Figure 3.4 and Table 3.1.

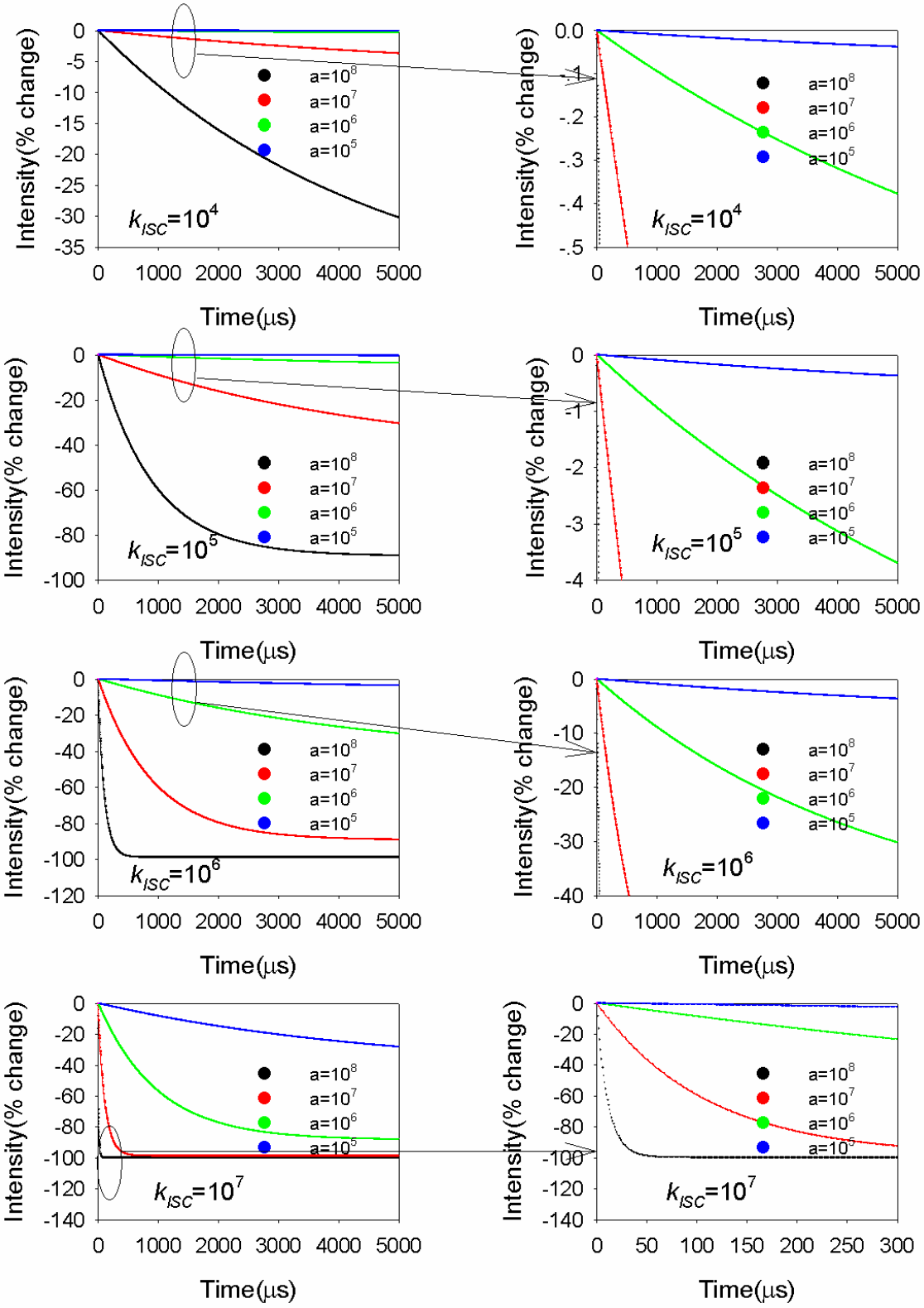

Figure 3.6: Simulations of Cölle's model for percentage changes in PL intensity at a temperature of 80K. A value of 8.5ms as the triplet lifetime (τ_T) is used. The unit of pump rate (a) is $1/S_0(initial)$, and the unit of intersystem crossing rate(k_{ISC}) is s^{-1}.

Table 3.3: The parameters from the fittings to the simulated data at a temperature of 80K, as shown in Figure 3.6. The unit of pump rate (*a*) is $1/S_0(initial)$, and the unit of intersystem crossing rate(k_{ISC}) is s^{-1}.

$k_{ISC}=10^4$	$a=10^8$	$a=10^7$	$a=10^6$	$a=10^5$
Fitted τ	4615.8 μs	7834.8 μs	8428.4 μs	9429.8 μs
Fitted ΔI	-45.7%	-7.8%	- 0.84%	-0.08%
$k_{ISC}=10^5$	$a=10^8$	$a=10^7$	$a=10^6$	$a=10^5$
Fitted τ	903.5 μs	4598.8 μs	7834.8 μs	8428.4 μs
Fitted ΔI	-89.4%	-45.9%	- 7.8%	-0.84%
$k_{ISC}=10^6$	$a=10^8$	$a=10^7$	$a=10^6$	$a=10^5$
Fitted τ	100.8 μs	903.5 μs	4615.8 μs	7840.2 μs
Fitted ΔI	-98.8%	-89.3%	-45.7%	-7.76%
$k_{ISC}=10^7$	$a=10^8$	$a=10^7$	$a=10^6$	$a=10^5$
Fitted τ	11.1 μs	108.7 μs	974.0 μs	4794.9 μs
Fitted ΔI	-99.9%	-98.7%	-88.5%	-43.6%

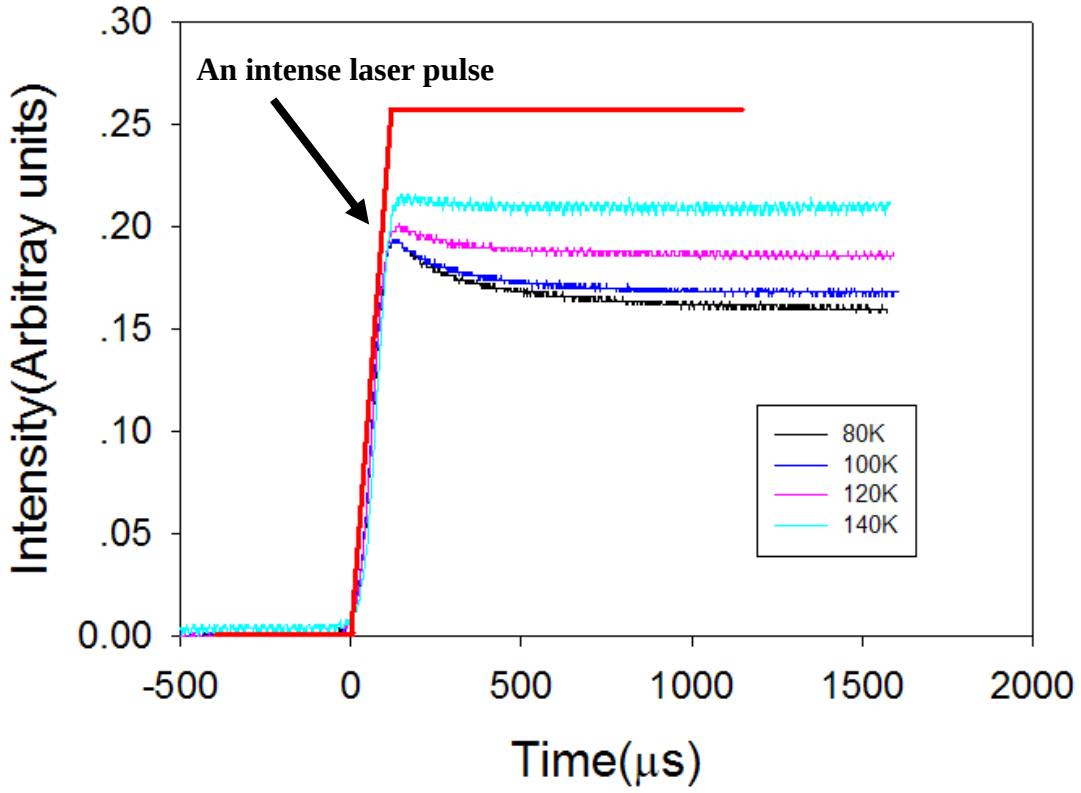

Figure 3.7: Time dependence of the 520nm PL from Alq_3, from 80K to 140K. The intense laser pulse with a frequency of 5Hz and a rise time of ~100 μs.

Figure 3.7 shows the PL signal for Alq_3 recorded at the peak of the PL spectrum at a wavelength of 520nm, as the temperature is changed from 80K to 140K. Figure 3.8 shows the temperature dependence of the percentage changes in PL intensity for Alq_3. It can be observed that it is very sensitive to temperature. At temperatures over 120K, the percentage change in PL was difficult to observe with the available excitation intensity. Similar to the experimental data as a function of excitation intensity, the fitting was compared with a single exponential decay function and a stretched exponential function. Figure 3.8 shows that the single exponential decay function approximately fits the experimental data. However, the fast process of the experimental data corresponding to the short time range (see Figure 3.9) could not be accurately fitted using a single exponential function. Therefore, these temperature dependent data had to be fitted with the stretched exponential function, Equation (3.3),

and the average relaxation times were calculated corresponding to the lifetime distribution function, Equation (3.4).

Table 3.4 shows the average relaxation times and the percentage changes in PL derived from the stretched exponential fitting in the case of using free stretching factor and fixed stretching factor. From Table 3.4 it is possible to see that, in the free stretching case, the percentage change in PL is reduced from -9.9±0.03% to -3.8±0.02% by increasing the temperature between 80K and 120K. At the same time, the average relaxation time is reduced from 326±3.3μs to 222±6.3μs. Fixing β to 0.68, results in a percentage change in the PL from -9.8±0.02% to -3.9±0.03% and the average relaxation time is reduced from 316±3.2μs to 229±6.7μs, when the temperature increases from 80K to 120K. Comparing the free stretching factor and fixed stretching factor cases, we do not consider these differences to be significant. In order to interpret this data, a temperature dependent rate equation model had to be introduced.

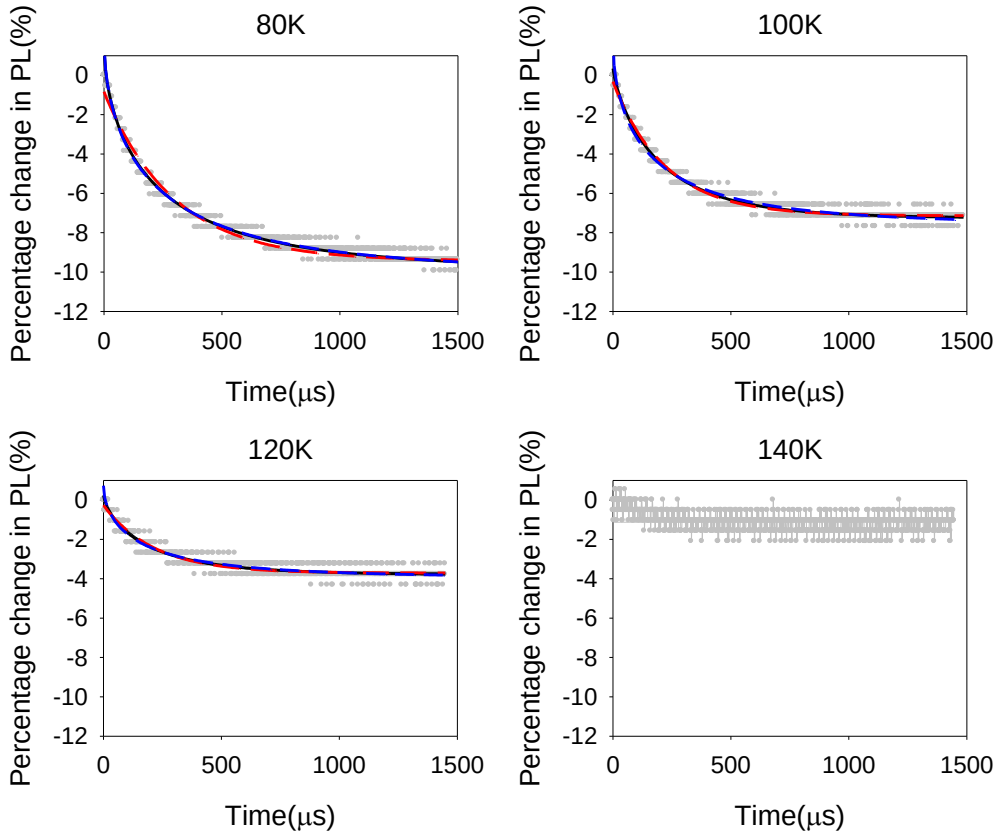

Figure 3.8: Percentage changes in PL intensity as a function of temperature. The red dashed lines are fits obtained using the exponential decay function, Equation (3.2). The black solid lines are fits obtained using the stretched exponential function, Equation (3.3). The blue solid lines are fits obtained using the stretched exponential function, Equation (3.3) and fixed β=0.68.

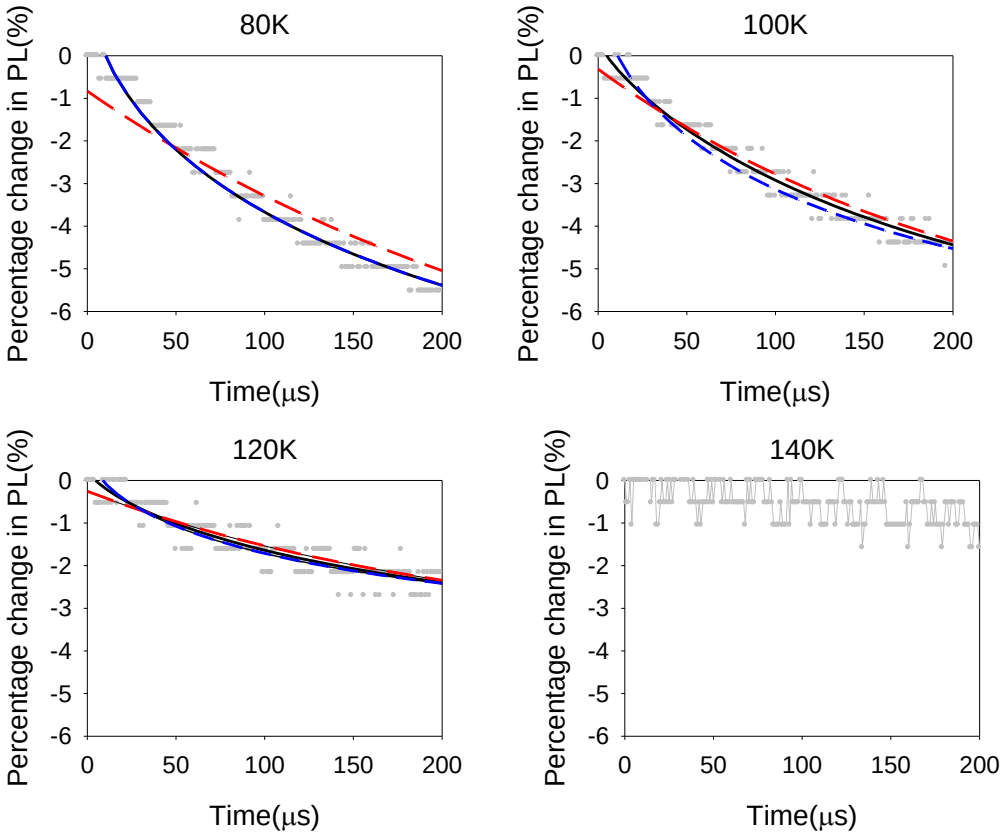

Figure 3.9: Each graph in Figure 3.8 corresponds to the detail of the short time region. The fits are as detailed in Figure 3.8.

Table 3.4: Experimental data for the PL average relaxation lifetimes and the percentage changes in PL intensity as a function of temperature. β is the stretching factor for fitting each of the experimental data.

Temperature	80K	100K	120K
Experimental $\langle\tau\rangle$	(326 ±3.3) μs	(225 ±2.8) μs	(222 ±6.3) μs
Experimental ΔI	(-9.9 ±0.03)%	(-7.3 ±0.02)%	(-3.8 ±0.02)%
β	0.64 ±0.01	0.82 ±0.01	0.75 ±0.03
Experimental $\langle\tau\rangle$	(316 ±3.2) μs	(237 ±3.2) μs	(229 ±6.7) μs
Experimental ΔI	(-9.8 ±0.02)%	(-7.4 ±0.02)%	(-3.9 ±0.03)%
β	0.68	0.68	0.68

It was mentioned earlier that Cölle's model does not fit the experimental data for the intensity dependence at a temperature of 80K. As in the previous simulation work at a temperature of 80K, Cölle's model was used with a temperature dependence of τ_t, as measured by Cölle (see Table 3.2) to simulate the percentage changes in PL intensity as a function of temperature. It was observed that τ_T is the only parameter in Cölle's model to be dependent on temperature. Figures 3.10 and 3.11 show the simulations of Cölle's model for percentage changes in PL intensity at temperatures of 100K and 120K, respectively. Table 3.5 and Table 3.6 present the parameters from the fittings to the simulated data in figure 3.10 and Figure 3.11, respectively.

Once again, like the simulation of Cölle's model at a temperature of 80K, this model was also unable to fit the experimental data at temperatures of 100K and 120K. By adjusting the k_{ISC} and the pump rate (a), it is possible to approach the experimental magnitude of the decrease in the luminescence intensity (ΔI), but the simulated lifetime of the luminescence (τ) is far from the experimental relaxation lifetime, and *vice versa*. Taking the simulation at 120K as an example, when $k_{ISC}=10^4 s^{-1}$ is set and $a=10^7/S_0(initial)$, ΔI is -4.3%, which approaches the experimental result of -3.8±0.02%. However, the τ ~3900 μs is far from the experimental relaxation lifetime ($\langle\tau\rangle$ = 222±6.3 μs). Therefore, Cölle's model cannot be used to fit this experimental data over a range of temperatures. As a result, Cölle's simple rate model should be modified. The modified rate model will be discussed in the following section.

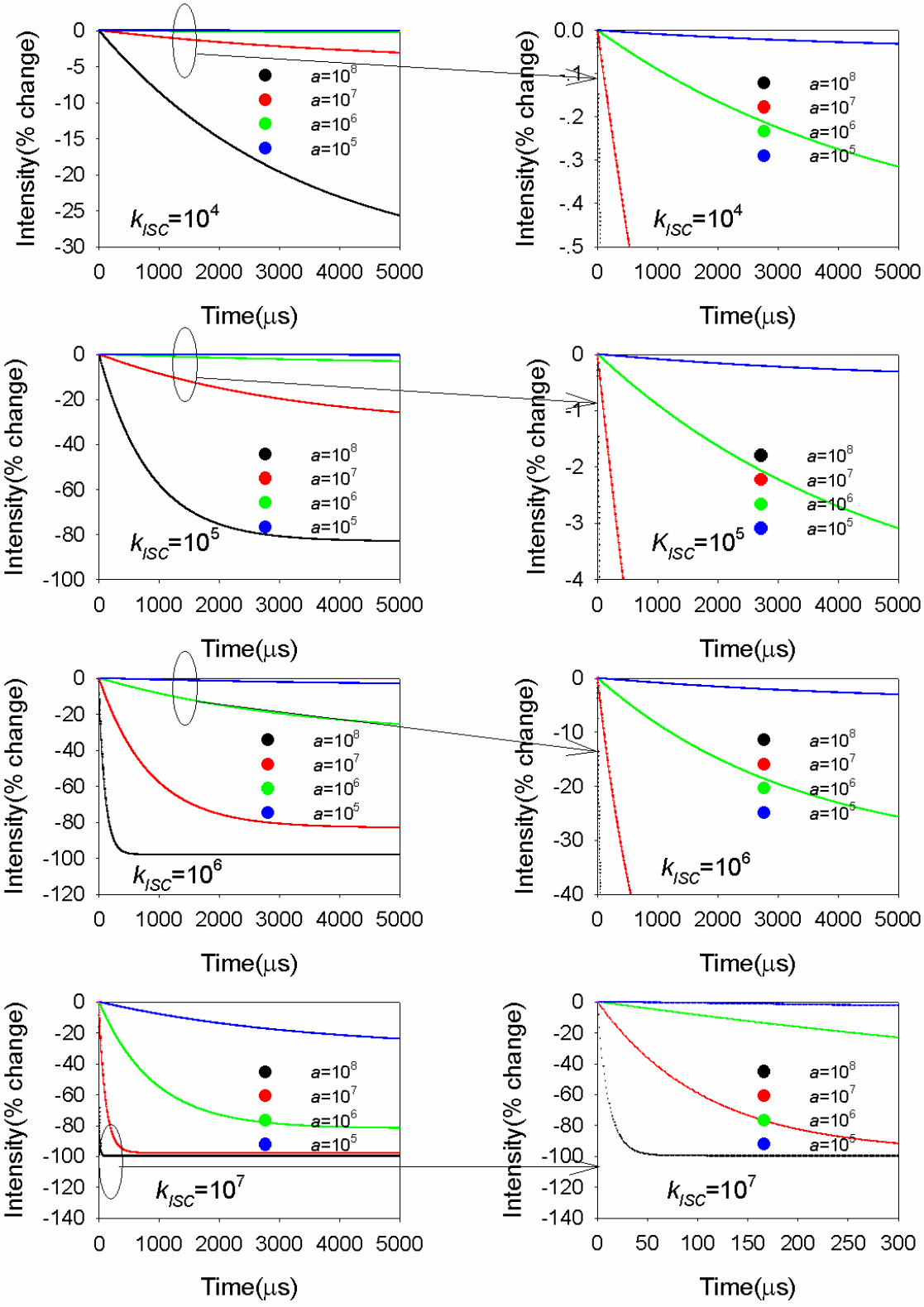

Figure 3.10: Simulations of Cölle's model for the percentage changes in PL intensity at a temperature of 100K. A value of 5ms is used as the triplet lifetime (τ_T). The unit of pump rate (a) is 1/S_0(initial), and the unit of intersystem crossing rate(k_{ISC}) is s^{-1}.

Table 3.5: The parameters from the fittings to the simulated data at a temperature of 100K as shown in Figure 3.10. The unit of pump rate (*a*) is $1/S_0$(initial), and the unit of intersystem crossing rate(k_{ISC}) is s^{-1}.

$k_{ISC}=10^4$	$a=10^8$	$a=10^7$	$a=10^6$	$a=10^5$
Fitted τ	3344.3 μs	4762.5 μs	4975.7 μs	5297.2 μs
Fitted ΔI	-33.1%	- 4.8%	- 0.5%	-0.05%
$k_{ISC}=10^5$	$a=10^8$	$a=10^7$	$a=10^6$	$a=10^5$
Fitted τ	841.6 μs	3335.5 μs	4762.2 μs	4975.1 μs
Fitted ΔI	-83.2%	- 33.3%	- 4.8%	-0.5%
$k_{ISC}=10^6$	$a=10^8$	$a=10^7$	$a=10^6$	$a=10^5$
Fitted τ	100.0 μs	841.0 μs	3344.5 μs	4764.2 μs
Fitted ΔI	-98.0%	- 83.2%	- 33.1%	-4.7%
$k_{ISC}=10^7$	$a=10^8$	$a=10^7$	$a=10^6$	$a=10^5$
Fitted τ	11.1 μs	107.7 μs	901.7 μs	3437.5 μs
Fitted ΔI	-99.8%	- 97.8%	- 81.9%	-31.2%

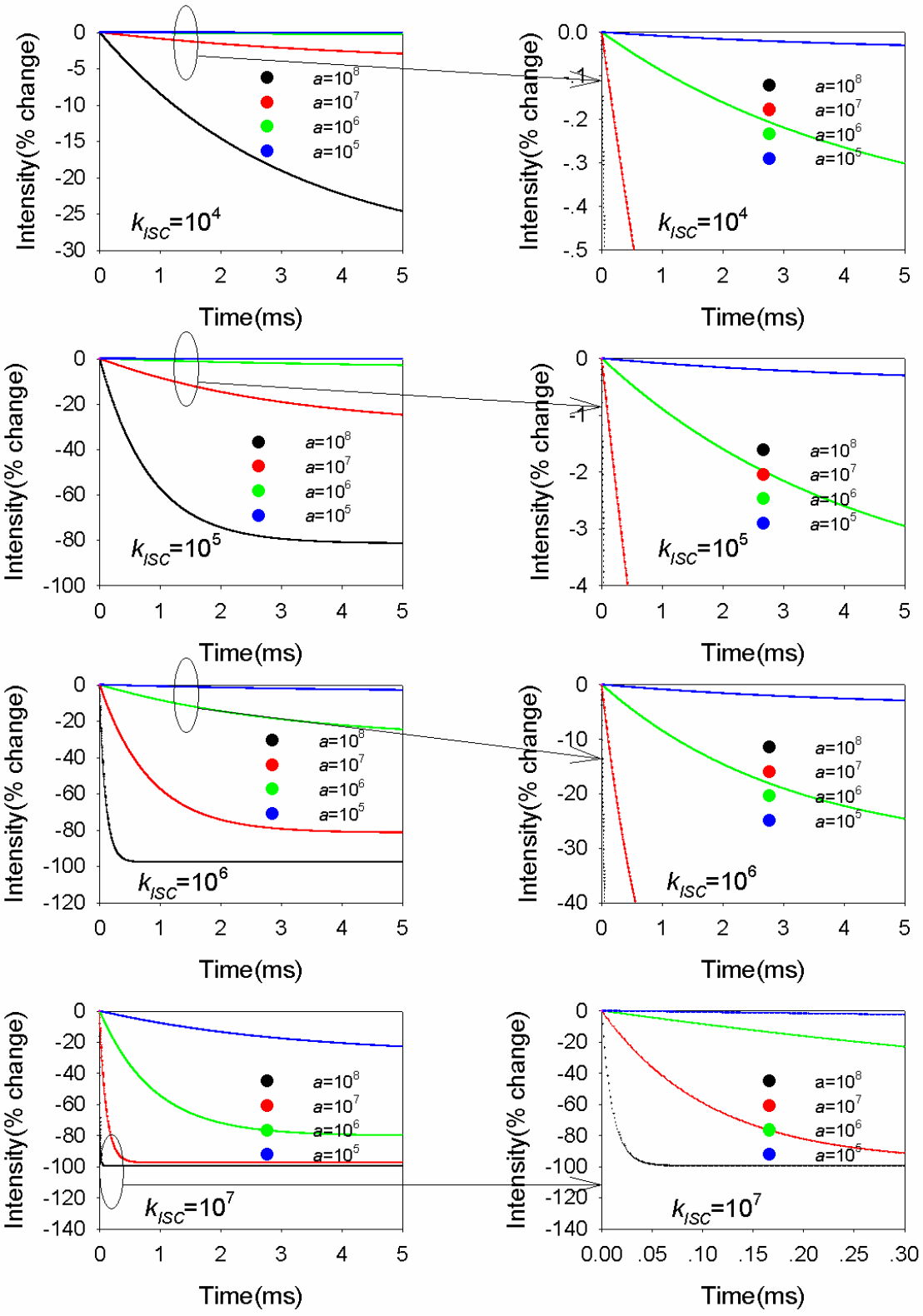

Figure 3.11: Simulations of Cölle's model for the percentage changes in PL intensity at a temperature of 120K. A value of 4.5ms is used as the triplet lifetime (τ_T). The unit of pump rate (a) is 1/S_0(initial), and the unit of intersystem crossing rate(k_{ISC}) is s^{-1}.

Table 3.6: The parameters from the fittings to the simulated data at a temperature of 120K, as shown in Figure 3.11. The unit of pump rate (a) is $1/S_0$(initial), and the unit of intersystem crossing rate(k_{ISC}) is s^{-1}.

$k_{ISC}=10^4$	$a=10^8$	$a=10^7$	$a=10^6$	$a=10^5$
Fitted τ	3113.1 μs	3906.4 μs	4379.8 μs	4898.0 μs
Fitted ΔI	-30.8%	- 4.3%	- 0.45%	-0.05%
$k_{ISC}=10^5$	$a=10^8$	$a=10^7$	$a=10^6$	$a=10^5$
Fitted τ	825.5 μs	3105.4 μs	4306.4 μs	4480.0 μs
Fitted ΔI	-89.6%	- 31.0%	- 4.3%	-0.45%
$k_{ISC}=10^6$	$a=10^8$	$a=10^7$	$a=10^6$	$a=10^5$
Fitted τ	99.7 μs	825.5 μs	3113.1 μs	4308.1 μs
Fitted ΔI	-97.8%	- 81.6%	- 30.8%	-4.26%
$k_{ISC}=10^7$	$a=10^8$	$a=10^7$	$a=10^6$	$a=10^5$
Fitted τ	11.1 μs	107.5 μs	884.0 μs	3193.6 μs
Fitted ΔI	-99.7%	- 97.6%	- 80.3%	-29.0%

3.3 Modified rate equations for the model

In Section 3.2 above, I showed how Cölle's model does not fit the PL intensity of Alq_3 as a function of excitation intensity, meaning that a modified rate model had to be introduced. In addition, a reflection of the temperature dependence in the rate model was needed, in order to explain why the PL intensity of Alq_3 is so temperature sensitive. In 2007, a modified rate model was proposed to explain related OMR phenomenon, such as the positive change in efficiency and current with applied field [39]. Compared to Cölle's model, this rate model includes the back transfer from the triplets to the singlet level, which is temperature dependent, as there is an energy barrier to overcome.

Figure 3.12 shows this modified rate equation model proposed by Desai *et al.*. I introduced the model in Chapter 1. In this chapter, I will use this model to simulate the above experimental data as a function of temperature and excitation intensity.

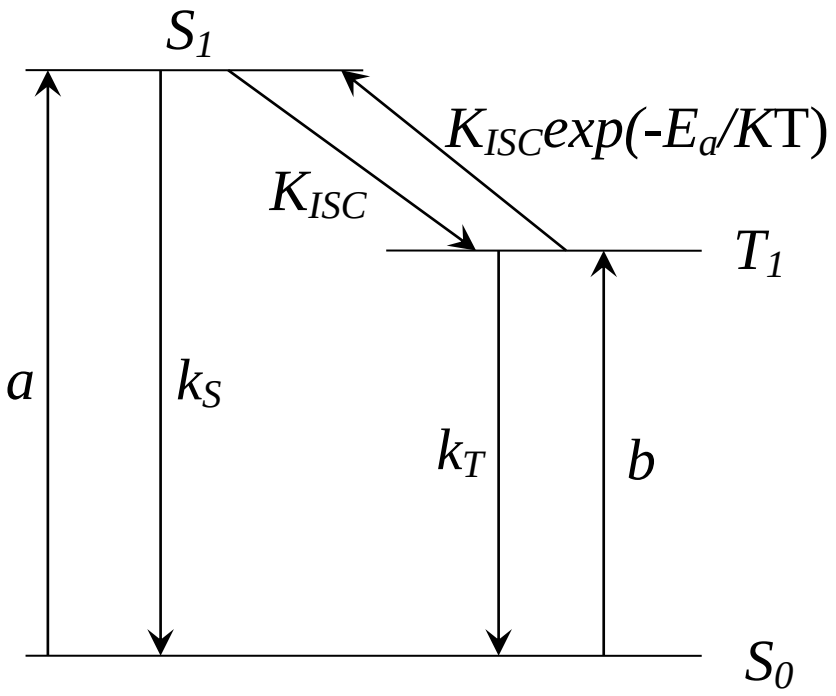

Figure 3.12: Schematic diagram of the modified rate equation model.

The modified rate equations can be written as

$$\frac{dS_0}{dt} = k_S S_1 + k_T T_1 - aS_0$$
$$\frac{dS_1}{dt} = aS_0 + k_{ISC} T_1 \exp\left(-E_a / k_B T\right) - k_S S_1 - k_{ISC} S_1 \qquad \text{Equation (3.5)}$$
$$\frac{dT_1}{dt} = k_{ISC} S_1 - k_T T_1 - k_{ISC} T_1 \exp\left(-E_a / k_B T\right)$$

where, S_0, S_1 and T_1 are the populations of the ground state, singlet state and triplet state respectively, k_S and k_T represent the recombination rates for singlet and triplet states, k_{ISC} is the rate constant for intersystem crossing, a is the pump rate, and E_a is the activation energy for the interchange from the triplet to the singlet.

The term k_{ISC} is introduced to denote the intersystem crossing from singlet to triplet. As there is an energy barrier E_a to undergo intersystem crossing from triplet to singlet, the intersystem crossing term is modified as $k_{ISC}\ exp\ (-E_a/k_BT)$ for a finite temperature,

T. k_B is Boltzmann's constant, which has the value 8.617343×10^{-5} eVK^{-1}. The modified rate equations for the model were solved numerically to determine the populations of the three levels as a function of time. In the system, if there is large population of triplets and the temperature is sufficient to overcome the energetic barrier, the interchange from the triplet to singlet state can occur.

Given that k_S, k_T, and k_B are defined, the only variables in the model are k_{ISC}, E_a and the pump rate (a). As mentioned previously, the percentage change in PL intensity is very temperature sensitive and is not visible at temperatures greater than 120K (see Figure 3.8). This fact shows that the activation energy (E_a) for back transfer from the triplet to the singlet state must be low. Figure 3.13 shows the simulations of the modified rate equation model for the temperature dependent percentage changes in PL intensity at a range of E_a from 5 meV to 25 meV. Table 3.7 shows a comparison between experimental data as a function of temperature, and the parameters from the fittings to the simulated data in Figure 3.13. As we have mentioned in the previous part that there is no significant difference using stretched exponential to fit the experimental data with free or fixed stretching factor. We used the fixed stretching factor case in here. Thus, the experimental data for the PL average relaxation lifetimes and percentage changes in PL were taken from Table 3.4. For each value of E_a the average relaxation times were firstly fitted for the PL and the percentage change in PL intensity at a temperature of 80K, in order to establish the k_{ISC} and pump rate (a). Next, for each value of E_a, the k_{ISC} and pump rate (a) were fixed to fit the experimental data with changing temperatures. As shown in Table 3.7, when $E_a <$ 10 meV, the modified rate model can fit the average relaxation times for the PL, but can't fit the percentage changes in PL intensity as a function of temperature. On the other hand, when $E_a >$ 20 meV, the modified rate model can fit the percentage change in PL intensity, but can't fit the average relaxation time for the PL as a function of temperature. Therefore, a value of 15 ± 5 meV was needed to fit the observed temperature dependence, while keeping all other fitting parameters constant.

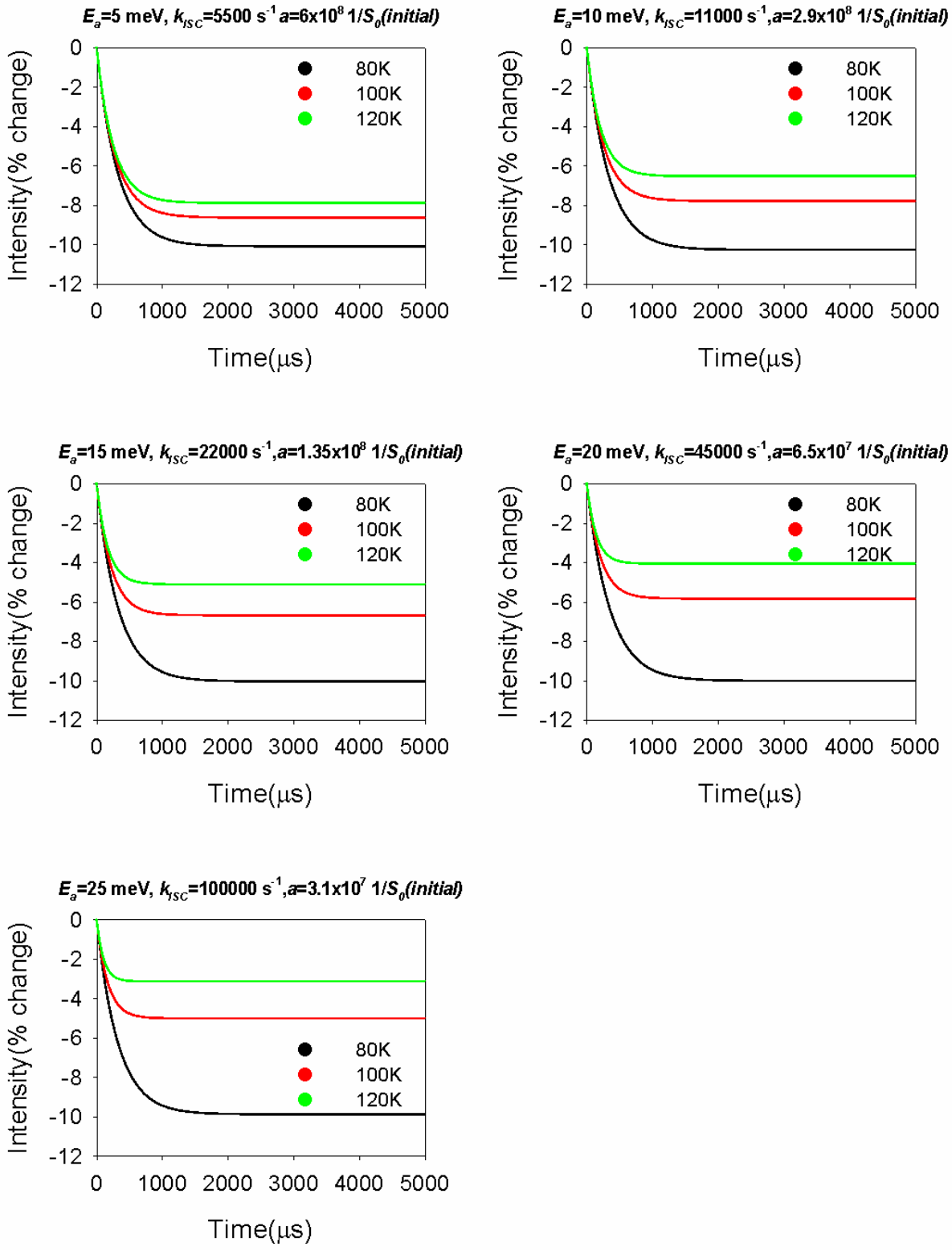

Figure 3.13: Simulations of the modified rate equation model for the percentage changes in PL intensity as a function of temperature. The lifetimes of the triplet (τ_T) used in this model are 8.5ms, 5ms and 4.5ms for 80K, 100K, and 120K, respectively.

Table 3.7: Experimentally determined and simulated average relaxation times for the PL, and the percentage change in PL intensity as a function of temperature. For each value of E_a, both K_{ISC} and pump rate (a) remain constant with changing temperatures.

Temperature	80K	100K	120K
Experimental $\langle\tau\rangle$	326 ± 3.3 µs	225 ± 2.8 µs	222 ± 1.9 µs
Experimental ΔI	-9.9 ± 0.01%	-7.3 ± 0.02%	-3.8 ± 0.02%
Simulated τ E_a=5 meV, K_{ISC}=5500 s^{-1}, a=6.0 x $10^8/S_0$ (initial)	323 µs	278 µs	255 µs
Simulated ΔI E_a=5 meV, K_{ISC}=5500 s^{-1}, a=6.0 x $10^8/S_0$ (initial)	-10%	-8.6%	-7.9%
Simulated τ E_a=10 meV, K_{ISC}=11000 s^{-1}, a=2.9 x $10^8/S_0$ (initial)	325 µs	251 µs	211 µs
Simulated ΔI E_a=10 meV, K_{ISC}=11000 s^{-1}, a=2.9 x $10^8/S_0$ (initial)	-10%	-7.7%	-6.5%
Simulated τ E_a=15 meV, K_{ISC}=22000 s^{-1}, a=1.35 x $10^8/S_0$ (initial)	329 µs	219 µs	170 µs
Simulated ΔI E_a=15 meV, K_{ISC}=22000 s^{-1}, a=1.35 x $10^8/S_0$ (initial)	-10%	-6.7%	-5.1%
Simulated τ E_a=20 meV, K_{ISC}=45000 s^{-1}, a=6.5 x $10^7/S_0$ (initial)	339 µs	203 µs	142 µs
Simulated ΔI E_a=20 meV, K_{ISC}=45000 s^{-1}, a=6.5 x $10^7/S_0$ (initial)	-9.8%	-5.8%	-4.0%
Simulated τ E_a=25 meV, K_{ISC}=100000 s^{-1}, a=3.1x $10^7/S_0$ (initial)	324 µs	167 µs	106 µs
Simulated ΔI E_a=25 meV, K_{ISC}=100000 s^{-1}, a=3.1x $10^7/S_0$ (initial)	-9.9%	-5.0%	-3.1%

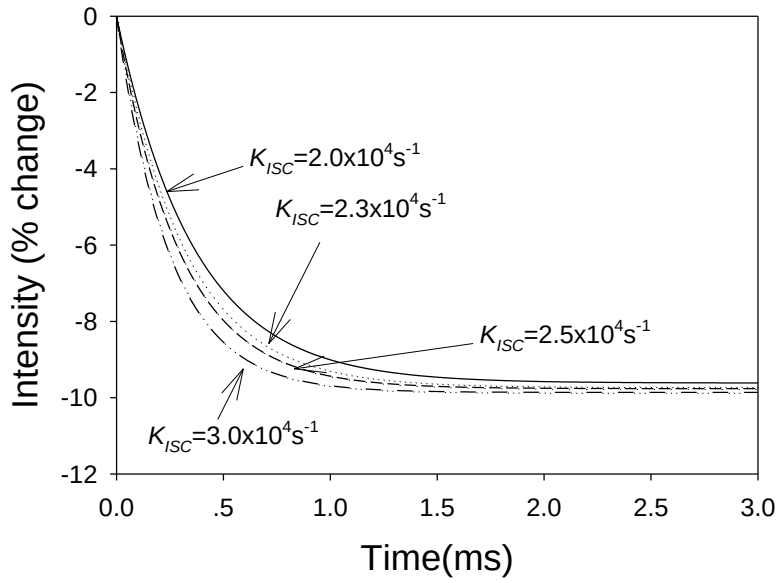

(a)

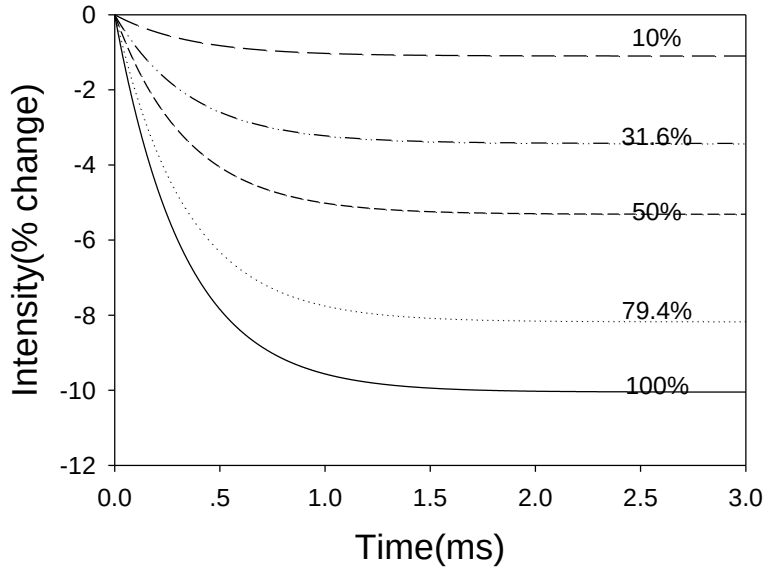

(b)

Figure 3.14: Calculated time dependence of the singlet population derived from the modified rate model presented in Equation 3.5. The data are presented as percentage changes in intensity from the initial value. In Figure (a) the pump rate (*a*) **is kept constant (1.35 x $10^8/S_0$ *(initial)*) and k_{ISC} is varied, whilst in Figure (b) k_{ISC} is kept constant (2.3 x 10^4 s^{-1}) and the intensity is reduced.**

Figure 3.14 shows the output from the rate equation model (at a temperature set to 80K and E_a= 15 meV), as either (a) k_{ISC} is changed whilst keeping the pump intensity constant, or (b) the pump rate (a) is changed whilst keeping k_{ISC} constant. Figure 3.14(a) shows that the values for k_{ISC} in the model primarily define the decay time in the observed PL. When the k_{ISC} is varied from $20000s^{-1}$ to $30000s^{-1}$, the lifetime of the decay decreases from 367 μs to 250 μs, with little change (<1%) in the magnitude of the steady state intensity. In Figure 3.14(b), however, it can be seen that the pump rate (a) principally determines the magnitude of the drop in PL. When the pump intensity reduces by 10%, there is a dramatic decrease of the magnitude of the steady state intensity, with a slight reduction in the lifetime of the decay by less than 10%. This is consistent with the experimental results shown in Section 3.2, in which the PL intensity percentage decreases when the pump rate (a) is reduced.

In order to observe a significant drop in the S_1 population with time, the pump rate (a) greater than singlet recombination rate (k_S) is required. A comparison between experimentally determined and simulated average relaxation times, and percentage changes in PL as a function of temperature, is shown in Table 3.8.

Table 3.8: Experimentally determined and simulated average relaxation lifetimes for the PL, and percentage changes in PL intensity from the initial value as a function of temperature. The parameters used for the fits were k_{ISC}=2.3 x $10^4 s^{-1}$, 1.35 x $10^8/S_0$ *(initial)* and E_a=15meV.

Temperature	**80K**	**100K**	**120K**
Experimental $\langle\tau\rangle$	(326 ±3.3) μs	(225 ±2.8) μs	(222 ±1.9) μs
Experimental ΔI	(-9.9 ±0.01)%	(-7.3 ±0.02)%	(-3.8 ±0.02)%
Simulated τ	329 μs	219 μs	170 μs
Simulated ΔI	-10%	-6.7%	-5.1%

Table 3.8 shows a comparison between experimental data as a function of temperature and the results from the rate equation model simulation using E_a=15meV, k_{ISC} = 2.3 x $10^4 s^{-1}$ and pump rate a=1.35 x $10^8/S_0$*(initial)*. It is evident that both the average relaxation time and the PL intensity reduction show a strong correlation between experimental and simulated data. In addition, the singlet recombination rate (k_S) is ~$10^8 s^{-1}$ [9] and the triplet recombination rate (k_T) is ~120 s^{-1} [46]. It was found that the k_{ISC} is ~200 times greater than the triplet recombination rate at 80K and ~5000 times less than the singlet recombination rate (k_S). This confirms that the value of k_{ISC} =2.3 x $10^4 s^{-1}$ is acceptable.

Section 3.2 shows that the percentage of PL intensity at a temperature of 80K decreases with a reduction in the excitation intensity. In order to test the modified rate model, the experimental data were compared with values obtained from the rate equation model using E_a=15meV, k_{ISC} = 2.3 x $10^4 s^{-1}$ and pump rate a=1.35 x $10^8/S_0$*(initial)*; these are the same parameters as used for the earlier simulation of temperature dependent data. Table 3.9 shows that both the average relaxation time and the reduction in intensity show very good consistency between experimental and simulated data.

Table 3.9 At a temperature of 80K, experimentally determined and simulated average relaxation lifetimes for the PL, and percentage changes in PL intensity from the initial value as a function of initial intensity. The parameters used for the fits were k_{ISC}=2.3 x $10^4 s^{-1}$, 1.35 x $10^8/S_0$ *(initial)* and E_a=15meV.

Percentage intensity	**100%**	**79.4%**	**50%**	**31.6%**	**10%**
Experimental $\langle\tau\rangle$	$(326 \pm 3.3)\,\mu s$	$(358 \pm 7.9)\,\mu s$	$(319 \pm 11.2)\,\mu s$	$(305 \pm 6.8)\,\mu s$	$(361 \pm 12.5)\,\mu s$
Experimental ΔI	$(-9.9 \pm 0.03)\%$	$(-8.2 \pm 0.08)\%$	$(-6.3 \pm 0.09)\%$	$(-5.2 \pm 0.1)\%$	$(-2.9 \pm 0.35)\%$
Simulated τ	329 µs	336 µs	347 µs	360 µs	362 µs
Simulated ΔI	-10%	-8.16%	-5.3%	-3.7%	-1.0%

In Section 3.2, it was shown that including the back transfer process from the triplet to singlet state is essential to describing the experimental data as a function of both the excitation intensity and temperature. This was achieved with the model by considering a simple Arrhenius process. In this chapter, I discussed that the range of the activation energy (E_a) should be between 10 meV and 20 meV for the modified rate model. However, the value of 15 ± 5 meV for the activation energy (E_a) is too small compared to the ~0.5eV difference in energy between the singlet and triplet energies [51]. In addition, given the very large difference in energy between the singlet and triplet levels, a simple thermal barrier from the triplet to singlet state does not appear to be possible. One possible mechanism for achieving the back transfer is the use of higher excited triplet states. In this situation, a scheme for the excited state absorption (ESA) should be proposed. A schematic of the back transfer process via excited state absorption (ESA) is illustrated in Figure 3.15. Transient state absorption spectroscopy of Alq_3 has shown the ESA from the first triplet state (T_1) to the second triplet state (T_2) occurs in Alq_3, and the triplet has an absorptive peak at a wavelength of ~510 nm [11,12]. This is coincidental with the singlet emission wavelength of Alq_3. Given the very high concentration of singlet recombination in the samples, the photons for the ESA can be provided by the singlet recombination

process. These photons can excite the molecule jumping from the T_1 to the T_2. Indeed the triplet to singlet interchange could occur via an intermediate higher energy triplet state. Therefore, this process would overcome the problem of the energy barrier and provide a route to convert triplets to singlet. In this scheme, the ESA is an allowed process, as is the relaxation from the T_2 to T_1 state. This would suggest that the instantaneous population of the T_2 level would be lower than that of the T_1 level. As a result, the presence of ISC into S_1 level would compete with relaxation to the T_1 level and provide a route to convert triplets to singlets. It is true that the actual system could be much more complicated. The simple Arrhenius expression that has been used in the modified rate model would only be an approximation of the actual system.

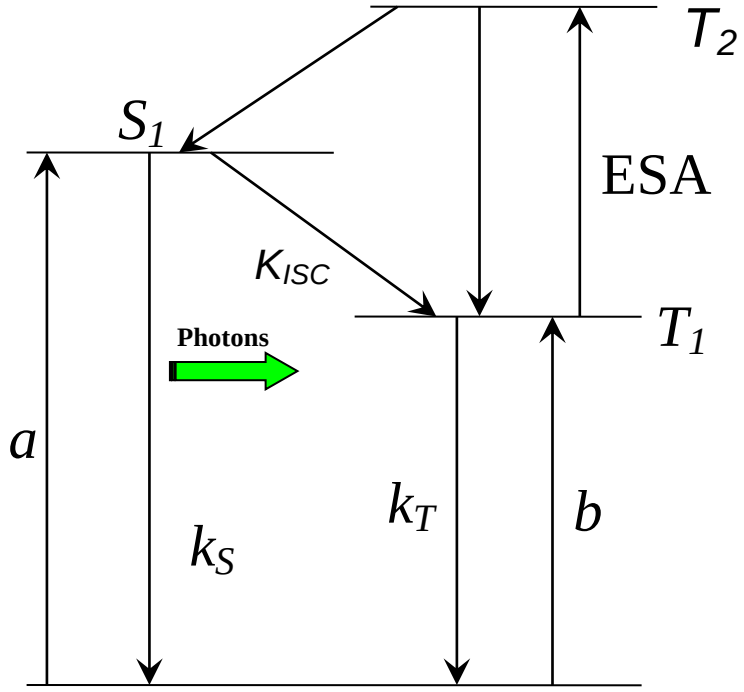

Figure 3.15: A schematic of the back transfer process via excited state absorption (ESA) from the first triplet state (T_1) to the second triplet state (T_2).

3.4 The effect of a magnetic field on the intersystem crossing rate

In 2008, Desai *et al.* observed an increase in efficiency of Alq_3 based OLEDs with the application of magnetic field [39]. In electrical excitation, due to spin statistics, one singlet is formed for every three triplets. The positive change in the efficiency was attributed to the ISC from the triplet to singlet state caused by the applied field. On the other hand, the singlet excitons are solely generated in the optical excitation. The role of the magnetic field is to increase the ISC between the singlet and triplet state, resulting in an increase in the triplet concentration and a decrease in the singlet concentration. As a result, a reduction in the steady state PL intensity with applied field should be observed. In Section 3.2, Figure 3.3 shows the time dependence of the 520nm PL for Alq_3 at a temperature of 80K. It can be seen that the PL experiences a decrease caused by the ISC, and finally approaches a constant saturated value, in which the whole system has reached a dynamic equilibrium, that is a non-equilibrium but time independent situation i.e. in this situation, the PL is regarded as being in the steady state.

In order to further understand the effect of magnetic field on the ISC, the percentage changes in the PL steady state were measured as a function of magnetic field. An intense laser pulse was used to excite the Alq_3 sample at a temperature of 80K. Based on the experimental conditions, this provides the best signal for the percentage changes in the PL. Figure 3.16 shows the percentage changes in PL intensity as a function of magnetic field.

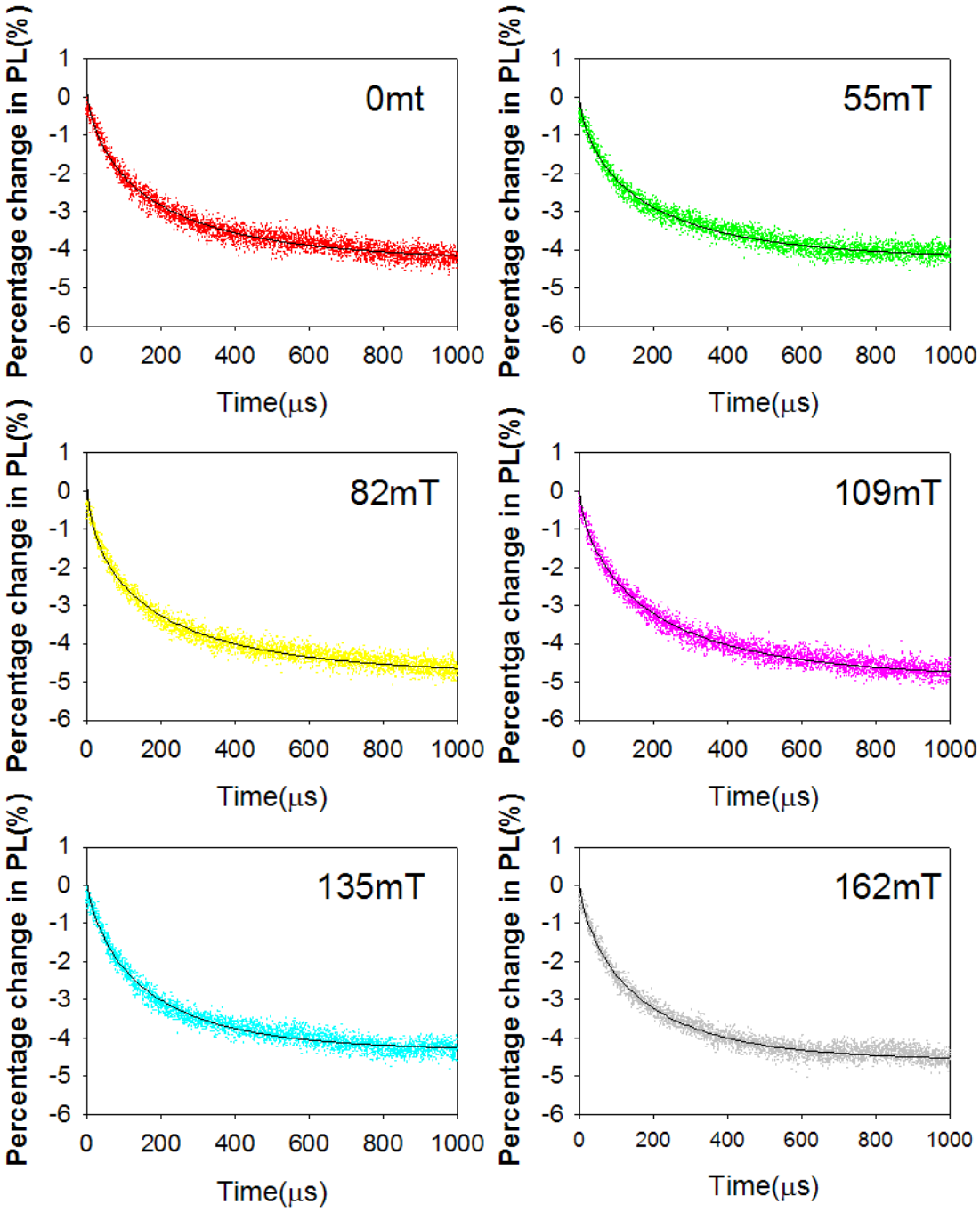

Figure 3.16: Percentage changes in PL intensity as a function of magnetic field. These processes in the PL intensity have been fitted by the stretched exponential function, Equation (3.3).

Table 3.10: Experimental data for the average relaxation times for the PL, and percentage changes in PL intensity as a function of magnetic field. β is the stretching function for fitting each of the experimental data.

Magnetic field	Experimental $\langle\tau\rangle$	Experimental ΔI	β
0mT	$(214 \pm 1.3)\,\mu s$	$(-4.3 \pm 0.004)\%$	0.68 ± 0.005
55mT	$(210 \pm 1.4)\,\mu s$	$(-4.3 \pm 0.003)\%$	0.70 ± 0.005
82mT	$(198 \pm 1.2)\,\mu s$	$(-4.7 \pm 0.005)\%$	0.62 ± 0.004
109mT	$(215 \pm 1.0)\,\mu s$	$(-4.8 \pm 0.004)\%$	0.70 ± 0.004
135mT	$(189 \pm 1.0)\,\mu s$	$(-4.3 \pm 0.003)\%$	0.75 ± 0.005
162mT	$(171 \pm 1.0)\,\mu s$	$(-4.5 \pm 0.002)\%$	0.76 ± 0.004

The experimental data in Figure 3.16 has been fitted with the stretched exponential function, Equation (3.3), in addition to which the average relaxation times can be extracted from a lifetime distribution function, Equation (3.4). Table 3.10 shows the average relaxation time and percentage change in PL intensity as a function of the magnetic field. In general, the average relaxation time is reduced by increasing the magnetic field. Although the data is scattered, a decrease of (at most) ~10% in the average relaxation time can still be observed. However, as found in Table 3.10, this can have very little effect on the percentage changes in PL intensity. According to the calculated time dependence of the singlet population derived from the rate model, it can be seen in Figure 3.14(a) that a ~10% drop in the lifetime will need a ~10% increase in k_{ISC}. Therefore, it could be suggested that the effect of a magnetic field is to increase k_{ISC}, in which the change in k_{ISC} is no more than ~10%.

As seen in the previous part of this section the transient method dose not give sufficient sensitivity to measure the change in the steady state of PL. Therefore, the use of a lock-in technique is necessary to improve sensitivity. The effect of a magnetic field on the percentage changes in steady state PL intensity for Alq_3 is abbreviated as MPL in the following context. The experimental set-up for the MPL

is as follows. The powered Alq_3 sample stimulated inside a cryostat, was placed between the poles of an electromagnet, in combination with a variable power supply. When the laser pulse excites this sample, the luminescence is dispersed in a spectrometer and detected using an S-20 photomultiplier. The lock-in amplifier needs to be used. This is because the MPL data is predominantly determined by the small shift in the steady state PL intensity. The lock-in amplification not only recovers signals from a noisy background, but can also enhance the resolution in the measurements of relatively clean signals over several orders of magnitude and frequency. The measurement time for each experimental point was set to 500ms in order to reduce the noise in the data.

Figure 3.17 shows the MPL as a function of temperatures ranging from 300K to 80K. It can be observed that the MPL data experiences a dramatic decrease at low magnetic fields, followed by saturation as the field is increased. The MPL experiment measures the small shift in the steady state PL intensity with applied field. In this case, the whole system in the modified rate model reaches a dynamic equilibrium. Therefore, the k_{ISC} is the only parameter in this system to decide the change in the steady state PL intensity. It can also be seen, in Figure 3.17, that there are no significant differences in the effect of the magnetic field over this temperature range from 300K to 80K. This would suggest that k_{ISC} is independent of the temperature and indeed, Sheng *et al.* (2007) have suggested that k_{ISC} is independent of temperature when extracting the k_{ISC} from the PL spectrum of $Ir(ppy)_3$ at different temperatures [35].

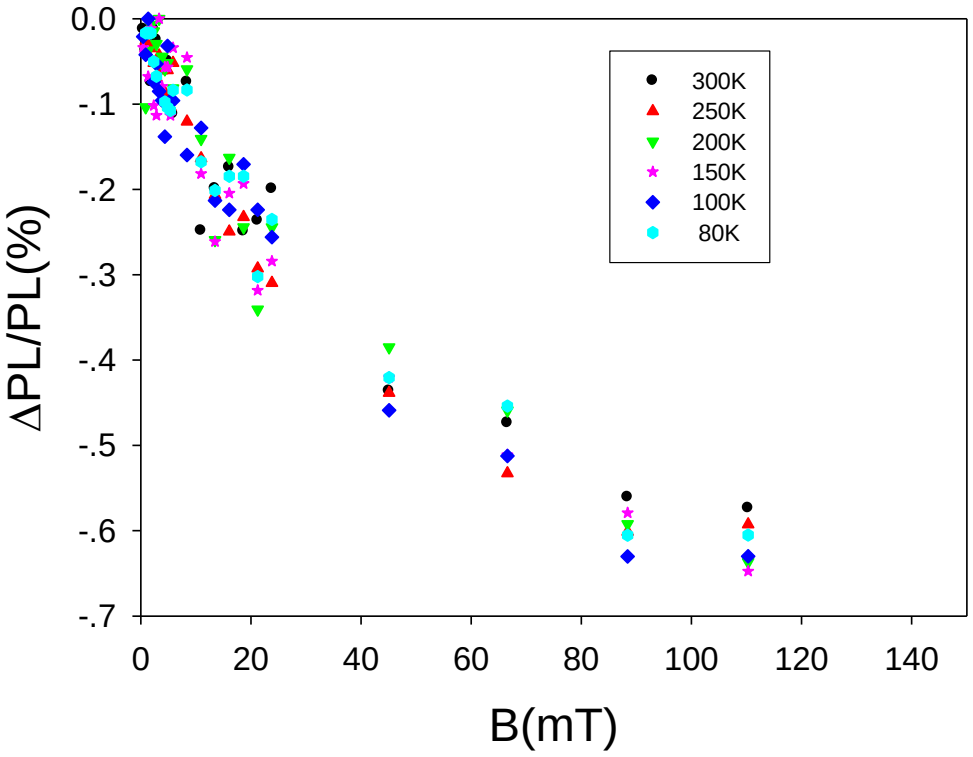

Figure 3.17: The MPL measured using lock-in amplification at temperatures ranging from 300K to 80K.

Figure 3.14(a) shows that, whilst k_{ISC} changes, there is very little change to the magnitude of the PL decay. Figure 3.14(a) shows that a 10% change in k_{ISC}, from $2.3 \times 10^4 s^{-1}$ to $2.5 \times 10^4 s^{-1}$, will produce a decrease in the saturated PL intensity of ~0.6%. From Figure 3.17, it is evident that the application of a magnetic field of ~100mT produces a decrease in the saturated PL intensity of <1%. This would, therefore, suggest that the effect of a magnetic field of ~100mT will result in the increase ~10% of the k_{ISC}. There is an internal consistency between the attempts to measure the changes in the lifetime for the decrease in PL intensity, and the MPL data obtained using lock-in detection. Therefore, both would suggest that the application of a magnetic field increases the ISC rate by ~10%.

3.5 Discussion of possible mechanisms for the changes in the intersystem crossing rate

It was previously mentioned that the positive change in efficiency of an OLED with applied field is due to the ISC from the triplet to singlet state, resulting in the increase of the singlet population. Figure 3.18 shows the effect of a magnetic field on the efficiency of a 50nm Alq_3 based OLED. An increase in the efficiency of an OLED at low magnetic fields can be seen, followed by saturation as the field is increased.

Mermer *et al.* [52] showed that some OMR data could be fitted empirically by a single Lorentzian function of the form

$$f(B) = B^2 / \left(B^2 + B_0^2\right) \qquad \text{Equation (3.6)}$$

where B is the applied field and B_0 is the saturation field.

Sheng *et al.* (2007) went on to show that this magnetic field dependence could be derived from either a Hyperfine [28] or spin-orbit [35] interaction. The fitting to the OMR data will be discussed in Chapters 4 and 5. Figure 3.18 illustrates that the change in efficiency of an OLED, with the applied magnetic field at low drive voltages, can be approximated by a single Lorentzian function, Equation (3.6). Figures 3.18 and 3.19 show that the efficiency data, at a driving voltage of 2.5V, can be fitted to a single Lorentzian function, Equation (3.6). The driving voltage of 2.5V is around the onset of light emission of this OLED. However, as driving voltage increases, a dual Lorentzian function

$$f(B) = A_1 \times B^2 / \left(B^2 + B_1^2\right) + A_2 \times B^2 / \left(B^2 + B_2^2\right) \qquad \text{Equation (3.7)}$$

is required to fit the efficiency data. For this dual Lorentzian function expression, B is the applied magnetic field, A_1 and A_2 are the prefactors for the Lorentzians, and B_1 and B_2 are the saturation fields for each of the components, respectively.

The values and associated errors for fitting the efficiency data of a 50nm Alq_3 based OLED are presented in Table 3.11. The errors for the saturation field B_2 are relatively significant; this is because our efficiency data only ranges up to ~200mT and we are not able to measure high enough fields to fully saturate the process.

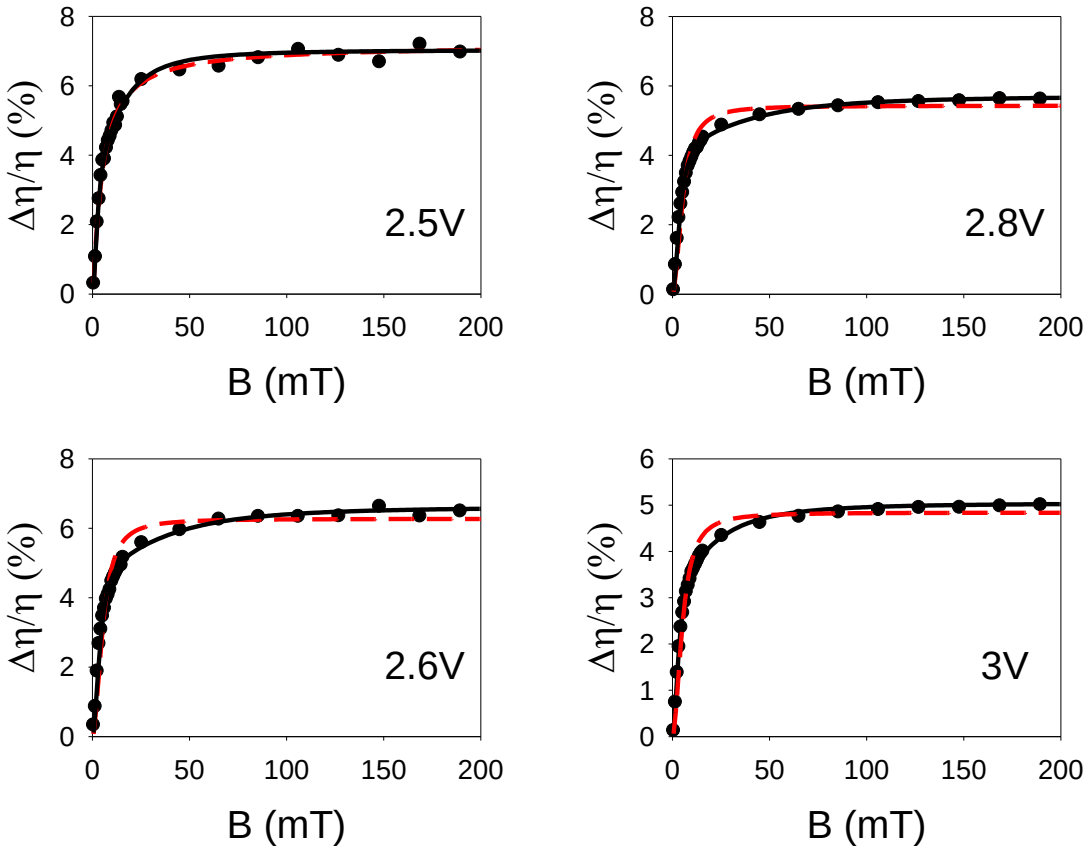

Figure 3.18: Change in efficiency of a 50nm Alq_3 based OLED with the applied field. The red dashed lines are fits obtained using the single Lorentzian function, Equation (3.6). The black solid lines are fits obtained using the dual Lorentzian function, Equation (3.7).

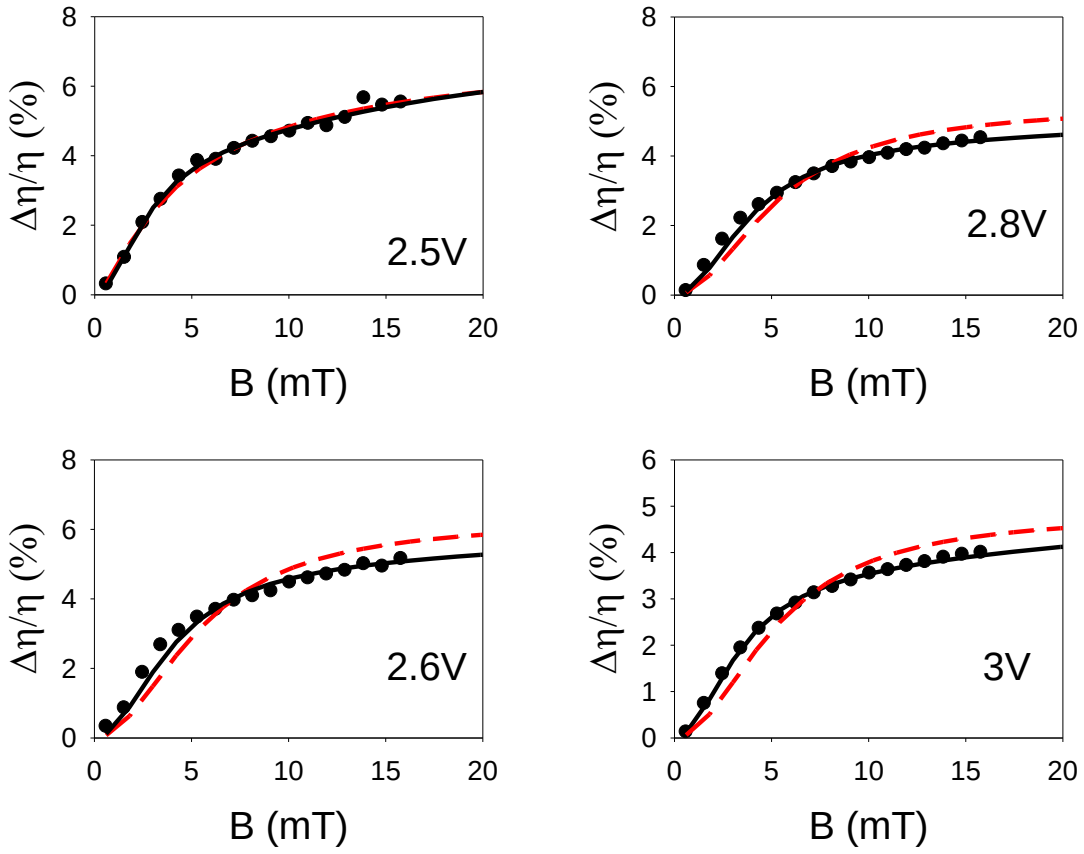

Figure 3.19: Each graph in Figure 3.18 corresponds to the detail of the low field region from 0 to 20mT. The red dashed lines are fits obtained using the single Lorentzian function, Equation (3.6). The black solid lines are fits obtained using the dual Lorentzian function, Equation (3.7).

Table 3.11: Fitting parameters obtained from the efficiency data as a function of the applied field for a 50nm Alq_3 based OLED over the full range of operating conditions.

Voltage	A_1	B_1 (mT)	A_2	B_2 (mT)	A_1/A_2
2.5V	4.4 ±0.32	2.7 ±0.26	2.7 ±0.31	17.0 ±2.66	1.6
2.6V	4.5 ±0.17	3.0 ±0.16	2.1 ±0.16	21.8 ±2.72	2.1
2.8V	4.2 ±0.10	3.3 ±0.12	1.49 ±0.10	25.0 ±2.95	2.8
3V	3.8 ±0.10	3.4 ±0.10	1.3 ±0.10	26.6 ±2.80	2.9
Average		3.1 ±0.16		22.6 ±1.74	

There are two contrasting approaches for explaining the OMR. One group has proposed a bipolaron-based model for the OMR, which predicts that the effect can be seen in unipolar structures [41, 53]. However, the majority of current models are primarily based on an excitonic mechanism to explain the OMR, although there is still no consensus for the excitonic mechanism. In 2003, Kalinowski *et al.* observed that, for Alq_3 devices, the increases in light output of ~5% could be obtained with the application of magnetic fields of ~500mT [23]. This increase in the light output was attributed to the increased mixing of electron-hole pair states prior to exciton formation. Prigodin *et al.* (2006) [26], and Hu *et al.*(2008) [27], have proposed that the ISC may occur at the level of pair states before the excitons are formed. On the other hand, Desai *et al.* have suggested that the effect of the magnetic field is to alter the ISC of the excitons [54].

In this work, it was found that a dual Lorentzian function, Equation (3.7), is required to fit the efficiency data. This would suggest that there are two independent processes occurring in the efficiency data. A proposed assumption is as follows: The low field component in Equation (3.7), parameters A_1 and B_1, would indicate that the process of the magnetic field may affect the ISC of pair states prior to exciton formation. On the other hand, the high field component in Equation (3.7), parameters A_2 and B_2, would present the process, in which the magnetic field may affect the ISC at the excitonic level. If the ratio is $A_1/A_2>1$, where the low field component dominates, this system is regarded as the magnetic field significant dependence of the ISC of pair states. If the ratio is $A_1/A_2<1$, where high field component plays a dominant role, we would expect it to be dominated by ISC at the excitonic level. For the electrical excitation system, the fitting parameters are presented in Table 3.11; in all cases the ratio is $A_1/A_2>1$, which suggests that the magnetic field may dominantly affect on the pair state prior to exciton formation. This is because the pair state can be formed before exciton formation in the electrical excitation, hence the magnetic field may dominantly affect on the pair state. This also corresponds to why the efficiency data at low driving condition can be fitted by a single Lorentzian function, Equation (3.6). As

the drive voltage is increased, a dual Lorentzian function, Equation (3.7), is required to fit for the efficiency data. At high driving condition, the magnetic field may affect the mixing of a pair state and excitonic level, but the effect on the pair state still plays a dominant role.

Figure 3.20 shows the MPL data as a function of temperature. The shape of the MPL data (see Figure 3.20) has a similar form to that obtained for the efficiency of an Alq_3 OLED (see Figure 3.18), but the sign is opposite. In the work relating to the OMR of an Alq_3 based OLED, it was observed that there is a positive change in the efficiency of OLEDs with applied field. This was attributed to an increased singlet formation rate, which could result in the conversion from triplet to singlet state with the ISC. In the work regarding the PL for Alq_3, it is only singlet excitons that can be generated. Hence, the magnetic field increases in the ISC to transfer the singlet into triplet states. According to the above factors, the MPL should have an opposite sign to the change in the efficiency of Alq_3 based OLEDs.

Similar to the efficiency data, the MPL data also has an approximately Lorentzian shape of the form, Equation (3.6), where B is the applied magnetic field and B_0 is the saturation field. In Section3.2, the MPL data was attributed to the reduction in the singlet exciton population, caused by the magnetic field on the ISC from the singlet exciton to triplet excitons. As a result, this approximate single Lorentzian process should indicate that the magnetic field may affect the ISC of excitons.

Figure 3.20 and 3.21 show the MPL data as a function of temperature from 300K to 80K. It can be seen that the fitting with a single Lorentzian is deviating with the PL data, especially in the low field. In this case, a dual Lorentzian function, Equation (3.7), has been used to fit for the MPL data.

It is obvious that the fitting with a double Lorentzian is better than the use of a single Lorentzian. These curves of the MPL as a function of temperature have been fitted

by the dual "Lorentzian" to the data producing saturation field values, which are shown in Table 3.12. Comparing the fitting results between the efficiency of Alq_3 based OLED and MPL (Table 3.11 and Table 3.12), it can be seen that the saturation fields for the two processes acting on the exciton are very similar. This would suggest that the same process is responsible for the change in intersystem crossing in the two situations. Similar to the efficiency data fittings, the standard errors for the saturation field B_2 of the MPL data are comparatively significant. This may be due to the limited data range. However, the difference in the relative strength of the two processes indicates important differences. For the optical excitation system, where the ratio is $A_1/A_2<1$, it can be suggested that the magnetic field may dominantly affect the exciton intersystem crossing rate. This is because the exciton is directly formed in the optical excitation, hence the magnetic field may dominantly affect on the exciton itself. However, some of excitons could be dissociate into the pair states. This also corresponds to why a double Lorentzian, Equation (3.7), is better than the use of a single Lorentzian, Equation (3.6), to fit the MPL data. In this case, the magnetic field may affect the mixing of a pair state and exciton itself, but the effect on the excitonic level still is dominant.

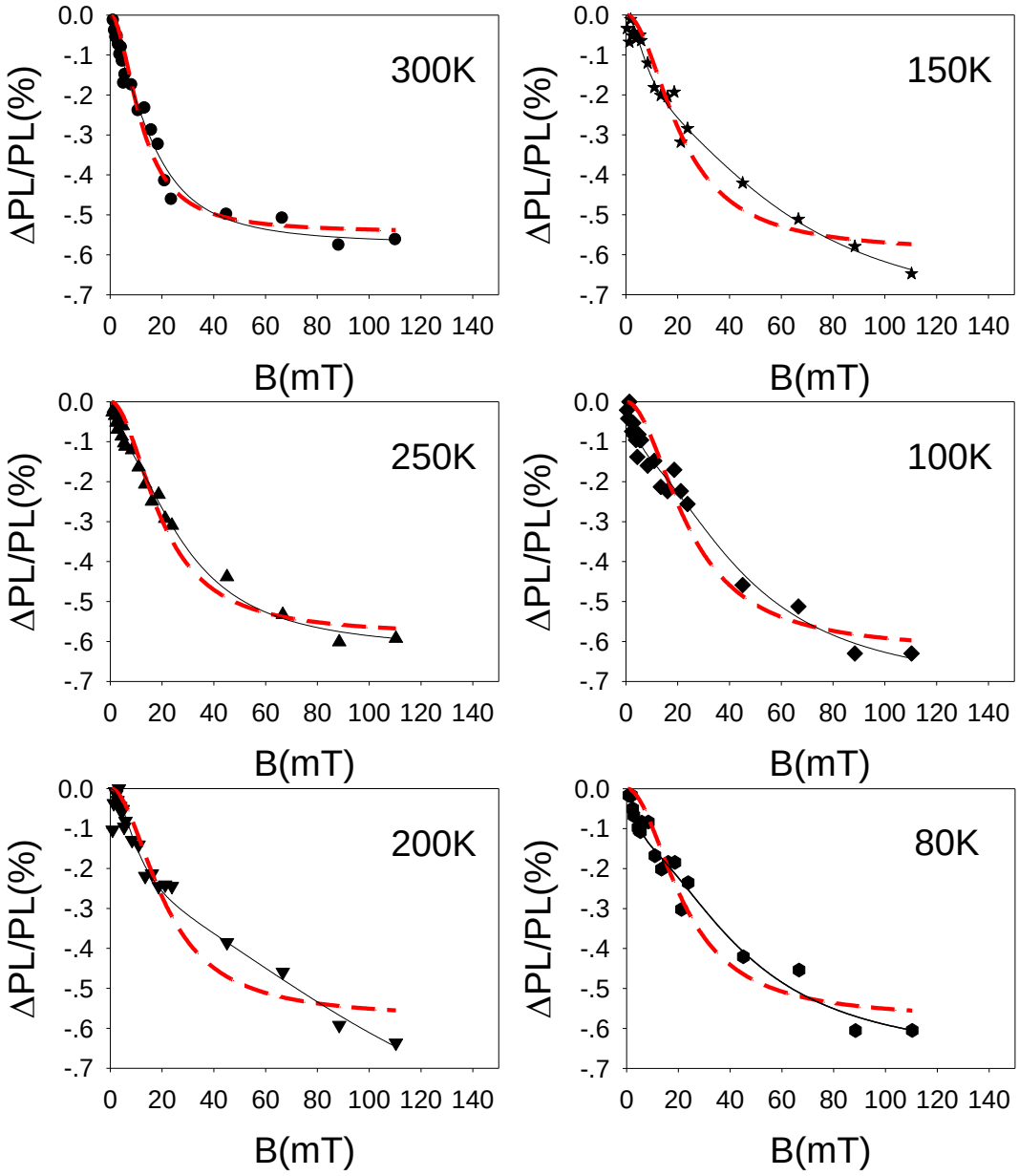

Figure 3.20: MPL data at temperatures ranging from 300K to 80K. The red dashed lines are fits obtained using the single Lorentzian function, Equation (3.6). The black solid lines are fits obtained using the dual Lorentzian function, Equation (3.7).

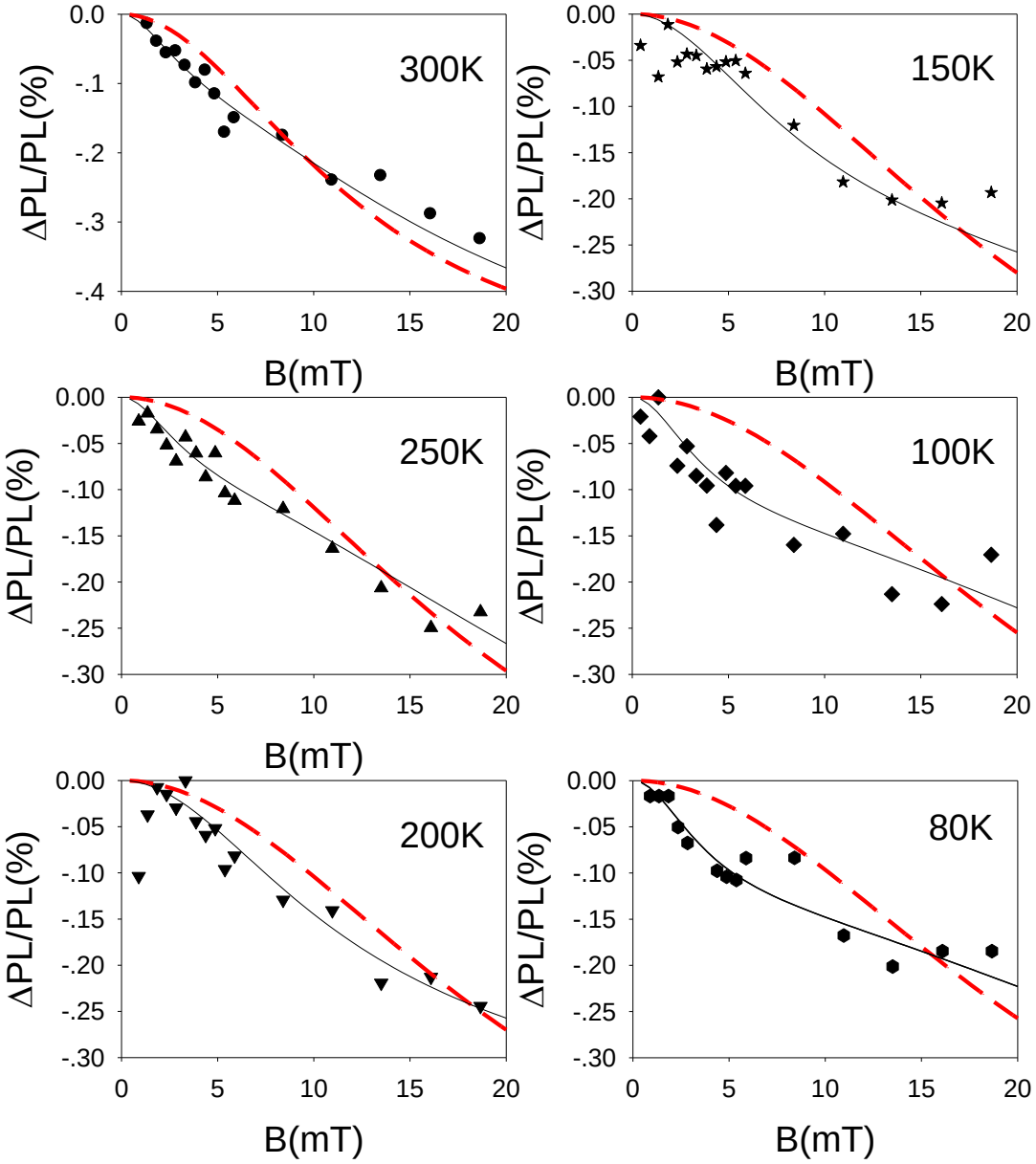

Figure 3.21: Each graph in Figure 3.20 corresponds to the detail of the low field region from 0 to 20mT. The red dashed lines are fits obtained using the single Lorentzian function, Equation (3.6). The black solid lines are fits obtained using the dual Lorentzian function, Equation (3.7).

Table 3.12: The fitting parameters obtained from the MPL data at temperatures ranging from 300K to 80K.

Voltage	A_1	B_1 (mT)	A_2	B_2 (mT)	A_1/A_2
300K	-0.12 ±0.05	3.1 ±1.5	-2.66 ±0.05	18.2 ±2.68	0.24
250K	-0.10 ±0.03	3.25 ±1.17	-0.53 ±0.03	28.9 ±3.15	0.19
200K	-0.31 ±0.07	11.0 ±2.96	-0.72 ±0.12	116.4 ±87.68	0.43
150K	-0.25 ±0.08	8.52 ±2.84	-0.52 ±0.11	62.94 ±29.31	0.48
100K	-0.14 ±0.04	3.60 ±1.30	-0.59 ±0.05	45.26 ±9.20	0.23
80K	-0.13 ±0.07	3.7 ±2.46	-0.55 ±0.09	45.5 ±19.4	0.24

3.6 Conclusion

In this chapter, it has been shown that in Alq_3 it is possible to estimate the ISC rate by modelling the time dependence of the PL under an intense laser pulse excitation. Using a modified rate model, an ISC rate, k_{ISC}, of $2.3 \times 10^4 s^{-1}$ can be deduced at a temperature of 80K. A value of 15 ± 5 meV was used as the activation energy (E_a) within the modified rate model, in order to explain the observed temperature dependence of the change in the PL intensity. However, the value of the E_a is too small when compared with the ~0.5eV difference in energy between the singlet and triplet levels. An ESA model has been proposed to amend this fault in the simple rate model. In addition, the ESA model also helps to understand that ISC can occur from higher excited triplet states to the singlet state, rather than just from the singlet to a lower lying triplet state.

It has also been shown that a magnetic field acts to increase the ISC by ~10% for fields up to ~100mT. Comparing the efficiency data under the effect of a magnetic field for an Alq_3 OLED with the MPL data would suggest that the magnetic field may affect the mixing of a pair state prior to exciton formation as well as the exciton itself. In the electrical excitation, the magnetic field may dominantly affect the pair state, and have less influence on the exciton itself. On the other hand, in the optical excitation, the magnetic field may induce significant modulation of the ISC at excitonic level, and less significant on the ISC for the pair state.

Chapter 4:

Modelling of OMR as a function of device thickness

4.1. Introduction

In 2003, Kalinowski *et al.* observed that the photoconductivity in organic devices can be perturbed by a magnetic field[55]; in addition, they showed that a weak magnetic field can affect the current and light emission from OLEDs, hence decreasing its efficiency [23]. The study of these phenomena has increased dramatically since then, [26, 36, 39, 56], however, there has not yet been a successful model that can fully explain OMR, nor predict the trends observed in the magnetic field effects as the operating conditions of the devices are changed. Such a model will be essential for understanding the fundamental mechanism of the OMR.

There are two contrasting approaches to explain the workings of OMR. One group proposed a bipolaron based model for the OMR, which predicts that the effect can be seen in unipolar structures [53]. However, the majority of the current models are primarily based on the effect of magnetic fields on excitons, or the pair states prior to exciton formation [23, 26, 36]. This is because the majority of experiments suggest that OMR can only be seen in devices above turn-on (an applied voltage above the built-in potential of the device). The exception to this is for devices that contain a poly(3,4,-ethylenedioxythiophene) poly(styrenesulfonate) (PEDOT:PSS) hole transport layer [29, 52], in which the OMR can be seen before the device turn-on.

PEDOT:PSS is a highly doped semi-conducting polymer, rather than an intrinsic semiconductor. The OMR below turn-on is probably due to PEDOT:PSS itself.

In this chapter, the triplet polaron interaction (TPI) model is proposed, which is based on the effect of excitons (primarily the long lived triplets) on charge transport [39]. Furthermore, it is demonstrated that for aluminium *tris*(8-hydroxyquinoline) (Alq_3) based devices with different layer thicknesses, the OMR can be accurately modelled using two Lorentzian processes that both scale linearly with exciton concentration over nearly six orders of magnitude [57]. Finally the model is extended to include the effect of exciton dissociation and it is demonstrated that for all Alq_3 devices of any thickness, the OMR can be modelled using just these three processes.

4.2. Exciton trapping and triplet polaron interaction (TPI)

4.2.1. Mechanism

In 2008, Desai *et al.* observed that there are no OMR effects for an Alq_3 based OLED before the onset of light emission [39] and concluded that the OMR is due to exciton formation in the device. Meanwhile, the TPI model was proposed to explain the positive OMR data, which refers to the percentage change in current with applied magnetic field in this context. In the electrical excitation, due to the spin statistics, one singlet is formed for every three triplets. In this case, a magnetic field enhances the transfer from triplets to singlet excitons with the ISC, resulting in a decrease in the population of triplets. The fewer remaining triplets can, therefore, still interact with free carriers. As a result, the mobility of the free carriers is increased and hence a positive OMR is obtained. The TPI model suggested that triplets can act to reduce the mobility through two independent processes: trapping excitons and TPI. The schematic of possible reactions between excitons and charge carriers is shown in Figure 4.1.

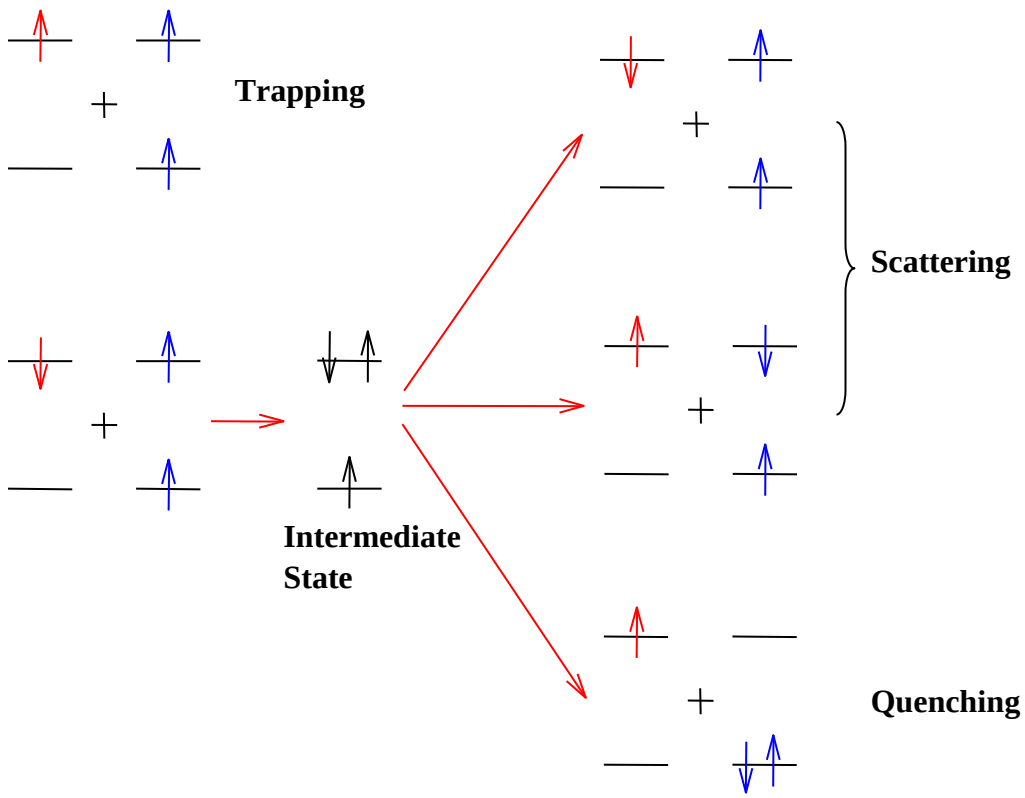

Figure 4.1: Schematic of possible reactions between excitons and charge carriers.

The first mechanism is the exciton trapping process. This process in the OMR is thought to be due to the simple trapping of charges at excitons, as predicted by Agranovich *et al.* [58]. They have demonstrated theoretically that excitons should act as shallow traps for polarons, either through Frenkel type trapping – where the exciton and polaron are on adjacent molecules – or through the formation of charged excitons. If a polaron has the same spin state as the corresponding charge carrier on the triplet, then this triplet will act as a blocked site for the transferring polaron, and reduce the mobility of the polaron. The simple exciton trapping mechanism has recently been demonstrated in the polymer system poly-(3-hexylthiophene) (P3HT) [42] and in the small molecule system TPD [8]. It was observed that, for a unipolar P3HT device, there is no change in mobility with DC bias. Otherwise, for the ambipolar device, a reduction in mobility（～15%) perfectly correlates with the turn-on voltage in I-V characterisation. This behaviour is not only observed in P3HT devices, but is also demonstrated in TPD devices. In TPD, the mobility

reduction is still around 15%, and it perfectly correlates with both the turn-on voltage in IV characterisation and light emission. This strongly suggests that excitons play a critical role in reducing the mobility in organic semiconductors. In addition, Song *et al.* measured the effect of a magnetic field on the mobility of holes in TPD under different bias conditions. A significant increase in mobility for the ambipolar device on the effect of magnetic field was observed, but not in the unipolar device. As mentioned above, for electronic excitation, the triplets can inter-convert to singlets with an applied field. According to this idea, a magnetic field can make the triplets generated inside the ambipolar device transfer to singlet states. This will result in the reduction of the triplet-polaron interaction, hence increasing the mobility of free carrier. No such mechanism is possible in unipolar devices. This experiment also strongly supports the triplet-polaron interaction mechanism.

The change in the triplet population can be directly measured by the change in the device efficiency with applied magnetic field, caused by the increase in the singlet population [39]. Therefore the simple trapping component should be identical to the change in efficiency. In Chapter 3, we explained that the efficiency data at low drive voltage can be fitted to a single Lorentzian function, Equation (3.6). Figure 4.2 shows the percentage change in efficiency for the 90, 70, and 50nm Alq_3 based OLEDs. The driving voltages are 3.5V, 3.4V and 2.4V, which are just above the onsets of light emission for the 90, 70, and 50nm Alq_3 based OLEDs, respectively. The efficiency data in Figure 4.2 was fitted with a single Lorentzian function and an average B_0 value of ~6mT was determined. It was shown that a dual Lorentzian function, Equation (3.7), is required to fit the efficiency data when increasing the drive voltage. It was suggested that the exciton trapping process probably has a contribution from ISC at both pair state and excitonic level. Chapter 3 also mentioned that, for an electrical excitation system, the ratio of $A_1/A_2>1$ indicates that the magnetic field may dominantly affect the pair state prior to exciton formation. Therefore, it could be suggested that the pair state is playing a more important role in the simple exciton trapping.

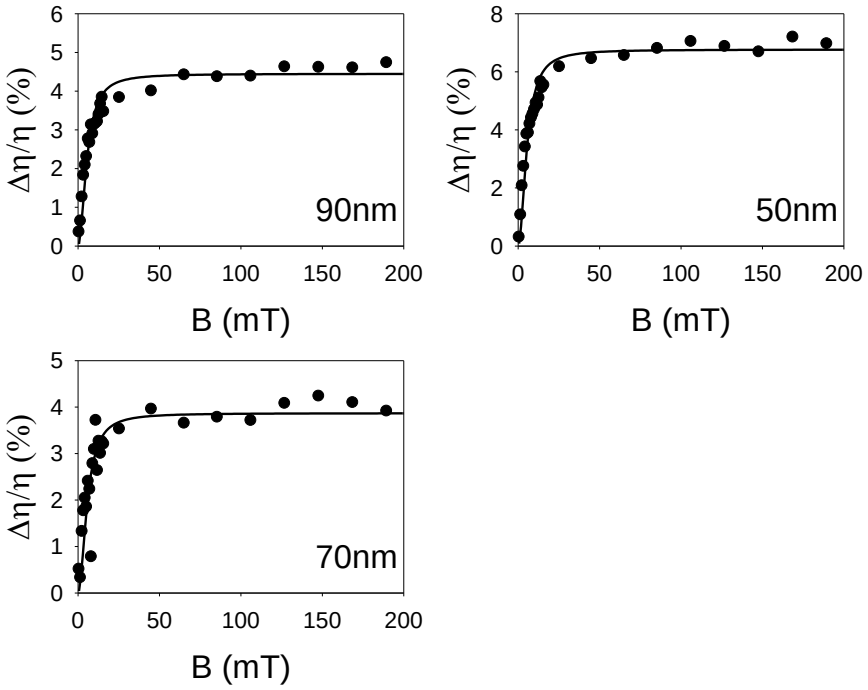

Figure 4.2: Percentage change in efficiency for the 90, 70, and 90nm Alq_3 based OLEDs. The fits are single Lorentzians, and B_0 values for the three fits are 5.9±0.3mT, 5.8±0.6mT, 5.5±0.5mT for 90nm, 70nm, and 50nm Alq_3 based OLEDs, respectively.

The second mechanism is the TPI, which is indicative of the higher field component in the OMR. The TPI process can be explained in detail as follows (see also Figure 4.1). If a polaron has an opposite spin state to the corresponding charge carrier on the triplet, then the polaron and triplet can interact to form a charged exciton. This results in two possibilities. The triplet can be quenched by the free carrier or can interact with it, but leaving a free carrier and triplet, resulting in an effective scattering event [21]. Both quenching and scattering would take some time and reduce the mobility of the polaron. These reactions will also have a magnetic field dependence that should distinguish them from the exciton trapping mechanism.

There is existing data for the effect of a magnetic field on TPI as a change in triplet lifetime, with magnetic field observed by Ern and Merrifield in anthracene [21]. The Ern and Merrifield data has been replotted in Figure 4.3 and is fitted with a single

Lorentzian function, Equation (3.6). The average B_0 for the TPI process was found to be ~70mT. It is obvious that the saturation field for the TPI process is at a much larger field scale than that for the ISC component.

In conclusion, the TPI model would suggest that triplets can act to reduce the mobility through two mechanisms, which should be distinguishable by their different magnetic field dependencies.

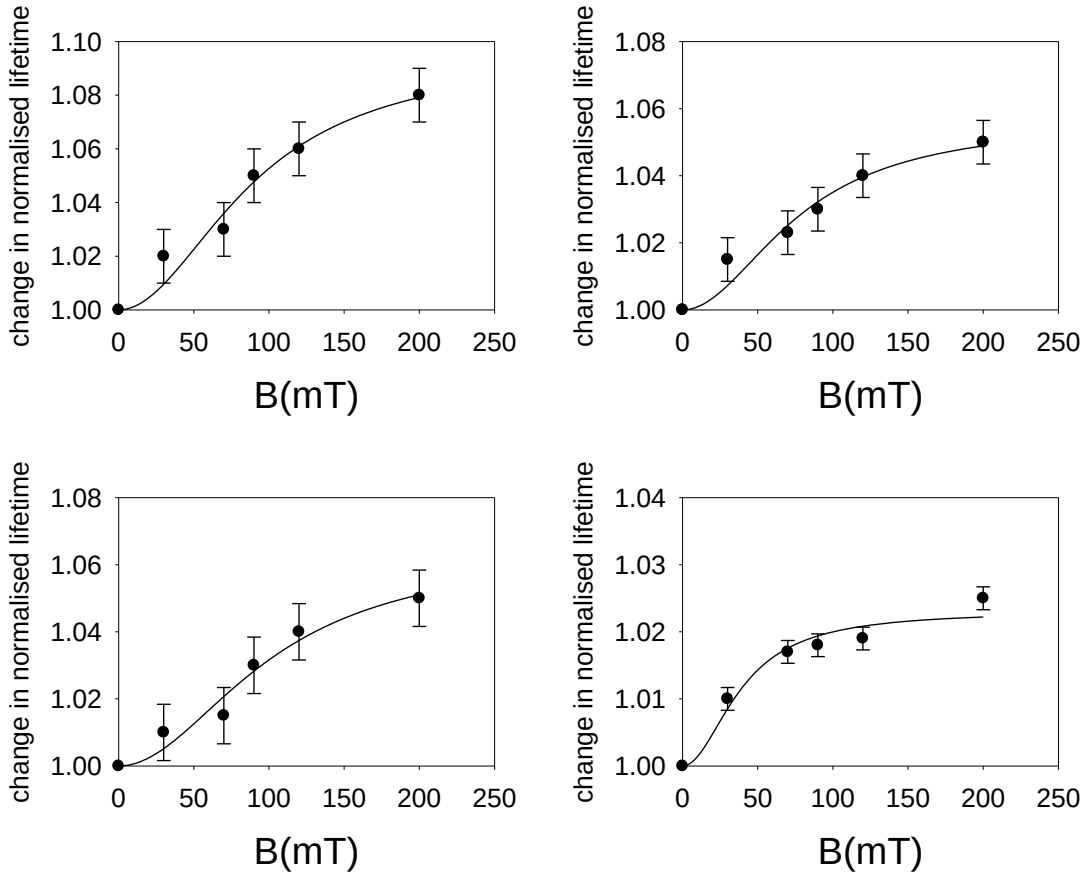

Figure 4.3: The magnetic field dependence of the normalised triplet lifetime in X-ray irradiated anthracene, extracted from the work of Ern and Merrifield [21]. The solid lines are a Lorentzian fit to the data.

4.2.2 Dual Lorentzian fits

Figure 4.4 shows the OMR curves (plotted as the relative change in current) for a 50nm Alq_3 device over a range of operating voltages. It can be seen in Figure 4.4 that the onset of OMR (~2.4V) coincides with the onset of light emission (~2.4V). This strongly suggests an excitonic cause behind the OMR. Mermer *et al.* [48] first proposed that the OMR has an approximately single Lorentzian shape of the form, Equation (3.6). As seen in Figure 4.4, the OMR data could not be accurately fitted using a single Lorentzian function. Mermer *et al.* [52] also suggested that a specific non-Lorentzian function

$$f(B) = B^2 / \left(|B| + B_0\right)^2 \qquad \text{Equation (4.1)}$$

could fit data that could not be accurately fitted using a single Lorentzian function.

For this specific non-Lorentzian function (Equation (4.1)) expression, B is the applied magnetic field and B_0 is the saturation field. This equation has therefore also been applied to the OMR data in Figure 4.4, but the specific non-Lorentzian function still cannot accurately fit the OMR data. Based on the OMR data fitting with the single Lorentzian function, Equation 3.6, or the specific non-Lorentzian function, Equation 4.1. Sheng *et al.* proposed a solution to theoretically explain the OMR data with the Hamiltonians for both hyperfine [28] and spin-orbit [35] interactions. This may be a generic expression for a spin interaction in the presence of a magnetic field in these systems.

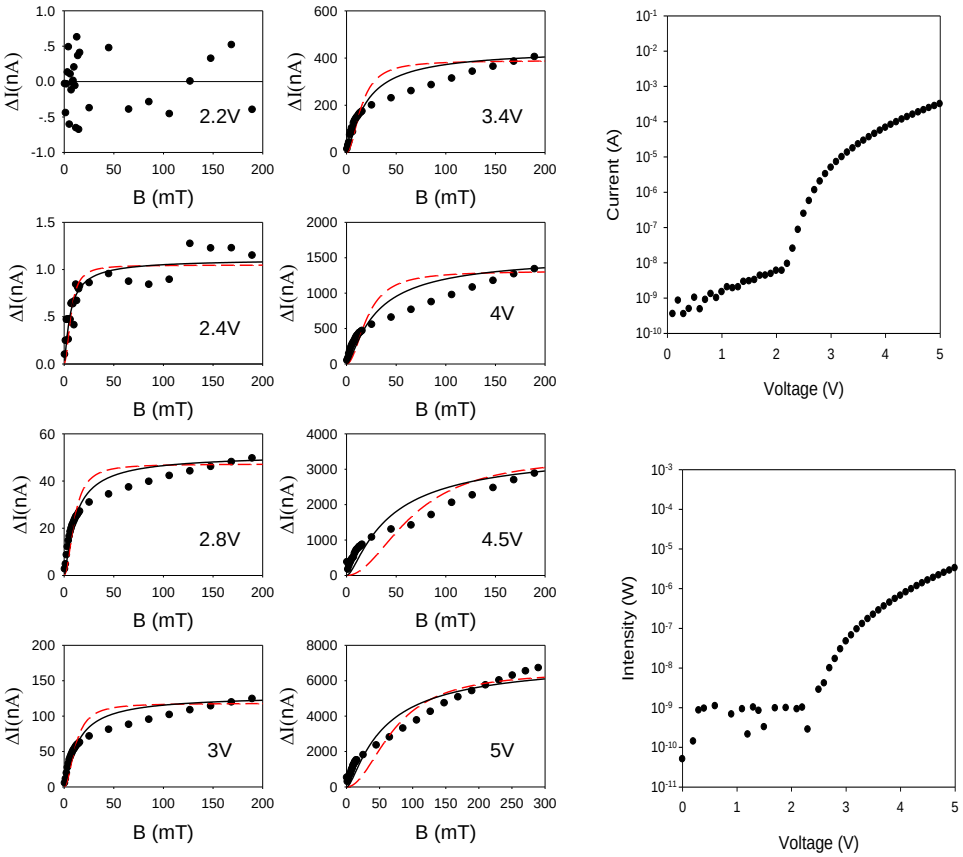

Figure 4.4: (a) The relative change in current in a 50nm Alq_3 OLED as a function of magnetic field for several drive voltages. The red dashed lines are fits obtained using the single Lorentzian function, Equation (3.6). The black solid lines are fits obtained using the empirical equation, Equation (4.1). (b) Shows the voltage against current and luminescence of the OLED device. The onset of light emission is ~2.4V, while the onset of OMR is ~2.4V.

Neither the single Lorentzian function, Equation (3.6), nor the specific non-Lorentzian function, Equation (4.1), can accurately fit the OMR data. In this case, a dual Lorentzian function is required, Equation (3.7), to fit the OMR data. Firstly a dual Lorentzian (Equation (3.7)) is used to free fit the OMR data for a 50nm Alq_3 based OLED, as seen in Figure 4.5. It shows that the fits were excellent and

produced a low and high field component. This would confirm that there are two independent processes occurring in the OMR. The values with error bars for fitting the OMR data of a 50nm Alq_3 based OLED are presented in Table 4.1. It was observed that these free fits give some variation in the values of the saturation fields at different voltages. For the low field component, the average saturation field was 5.6 ± 1.8mT. This was very similar to the saturation field value (~6 mT) obtained from a single Lorentzian fit to the efficiency data.

In Chapter 3, we have introduced a dual Lorentzian (Equation (3.7)) was introduced to better fit the efficiency data, as a magnetic field may affect the mixing of a pair state prior to exciton formation as well as the exciton itself. The low field component in Equation (3.7), parameters A_1 and B_1, would indicate that the magnetic field may affect the pair state. On the other hand, the high field component in Equation (3.7), parameters A_2 and B_2, would present the magnetic field may affect the exciton itself. The saturation fields, B_1 =3.1 ± 0.16 and B_2 =22.6 ± 1.74 are referred to the average values in Table 3.11. Therefore, the value (~6 mT) obtained from a single Lorentzian fit to the efficiency data is an approximation, indicating a magnetic field may affect the mixing of a pair state and the exciton itself. In addition, it is easy to understand that the saturation field obtained from a single Lorentzian fit to the efficiency data would increase with driving a higher voltage. This is because the high field component in Equation (3.7), $A_2 \times B^2 / \left(B^2 + B_2^2\right)$, could play more significant role when more excitons are formed at a higher driving condition.

The OMR data is less clear than the efficiency data, particularly in the low field. It is difficult to distinguish the pair state and exciton components. Therefore, it is necessay to present the combined two components as a single Lorentzian function expression, indicating a magnetic field may affect on the mixing of a pair state and the excitonic level. Agranovich *et al* [58] have proposed that both pair state and exciton itself would contribute to the trapping process.

For the high field component, the average saturation field was 131 ±48mT. The error bar for this component is relatively significant. This is because the OMR data obtained only ranges up to ~200mT and it is not possible to measure to high enough fields to fully saturate the process. However, it was found that at higher operating voltages, where the process becomes dominant, the value tended to saturate at ~160mT. Consequently, the error on this process was estimated to be at least ±40mT.

As has been already suggested, there are only two processes, namely the excitons trapping and TPI, that could effect the positive OMR data. The two B_0 fields should, therefore, be independent of operating conditions. Subsequently, the final function used for fitting the OMR data was

$$f(B) = a_t \frac{B^2}{\left(B^2 + B_t^2\right)} + a_i \frac{B^2}{\left(B^2 + B_i^2\right)} \qquad \text{Equation (4.2)}$$

where B is the applied magnetic field, a_t and a_i are the prefactors for the Lorentzians, and B_t and B_i are the saturation fields, while the subscripts t and i stand for trapping and interaction respectively. The constrains used in the fit were $a_t > 0$, $4 < B_t < 8$ mT, $a_i > 0$, and $B_i = 160$ mT.

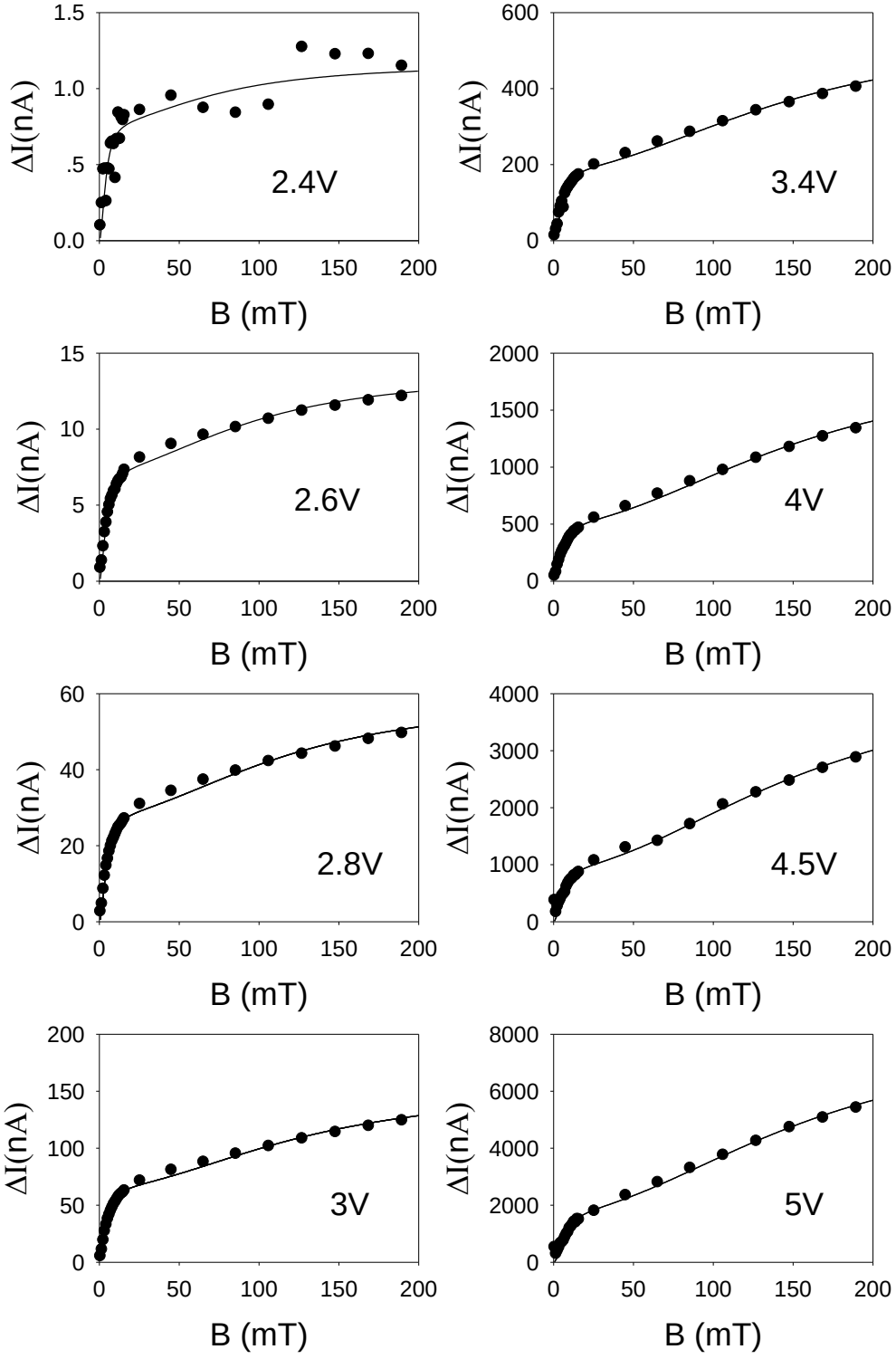

Figure 4.5: The relative change in current in a 50nm Alq_3 OLED as a function of magnetic field for several drive voltages. The black solid lines are fits using a dual Lorentzian function, Equation (3.7), to free fit the OMR data.

Table 4.1: The parameters obtained from the dual Lorentzian function (Equation (3.7)) free fittings for a 50nm Alq_3 based OLED, as seen in figure 4.5.

Voltage	A_1 (nA)	B_1 (mT)	A_2(nA)	B_2 (mT)
2.4V	0.8 ±0.1	4.3 ±1.4	0.4 ±0.1	76 ±45
2.6V	7.4 ±0.2	4.5 ±1.2	6.2 ±0.2	98 ±28
2.8V	28.6 ±0.7	4.9 ±1.2	30.6 ±1.1	118 ±38.
3V	66.7 ±1.5	5.1 ±1.2	87.7 ±2.7	129 ±28
3.4V	191.1 ±5.3	5.8 ±1.3	361.2 ±11.0	149 ±38
4V	519.1 ±15.9	6.0 ±1.3	1434.9 ±34.9	157 ±27
4.5V	967.2 ±54.5	6.3 ±1.6	1434.9 ±34.9	160 ±40
5V	1813.3 ±99.9	7.7 ±1.6	6397.0 ±186.6	162 ±39
Average		5.6 ±1.8		131 ±48

Figure 4.6 shows the OMR curves for a 90nm Alq_3 based OLED over a range of operating voltages. Similar to the 50nm Alq_3 device, it was found that the onset of OMR for a 90nm Alq_3 device (~3.5V) coincides with the onset of light emission (~3.5V). This could confirm an excitonic cause behind the OMR. As was already suggested, the OMR data should be fitted using Equation (4.2) with $4 < B_t < 8$ mT, B_i=160 mT. Also as shown, the quality of the fits is excellent in all cases. The values with error bars for fitting are presented in Table 4.2. It is observed that the relatively significant error bars for the B_i could be caused by the noisy data at low operating conditions.

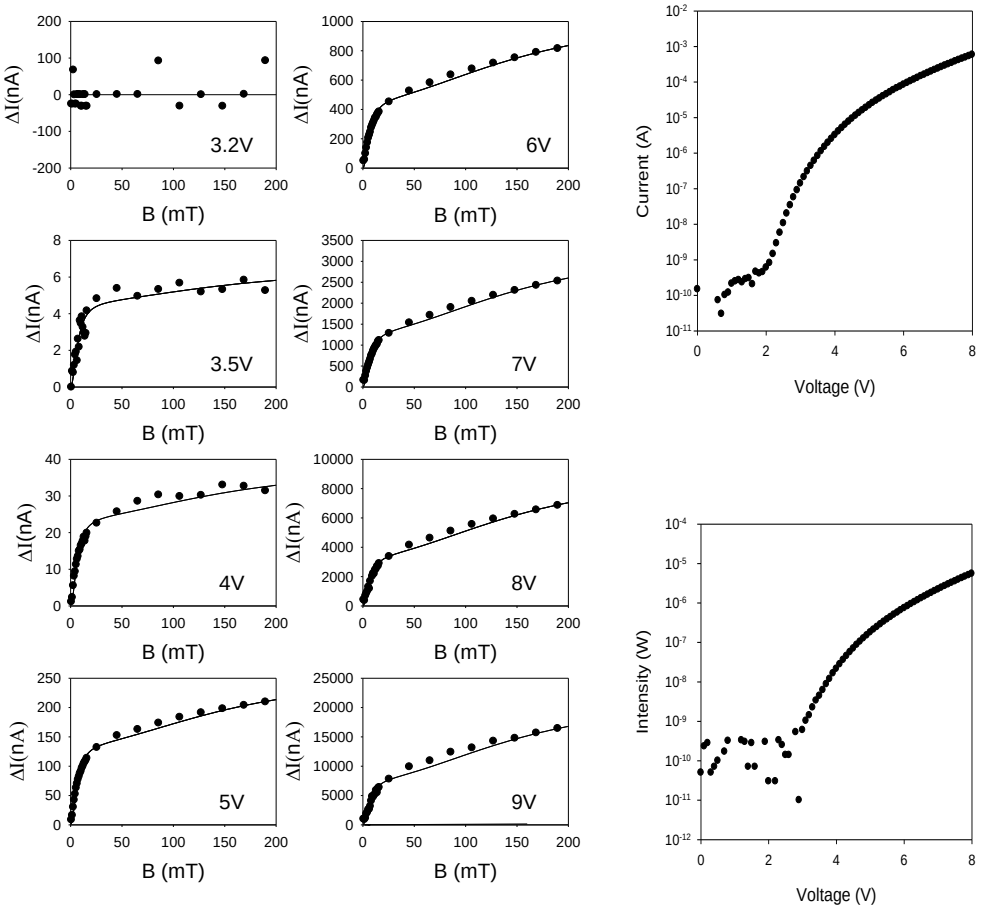

Figure 4.6: (a) The relative change in current in a 90nm Alq_3 OLED as a function of magnetic field for several drive voltages. The black solid lines are fits obtained using Equation (4.2) and the parameters in the text. (b) Shows the voltage against current and luminescence of the OLED device. The onset of light emission is ~3.5V, while the onset of OMR is ~3.5V.

Table 4.2: The parameters obtained from the constrained dual Lorentzians ittings for a 90nm Alq_3 OLED in figure 4.6.

Voltage	a_t(nA)	B_t(mT)	a_i(nA)	B_i(mT)
3.5V	4.7 ±0.4	5.6 ±0.8	1.9 ±0.7	160 ±76
4V	24 ±1	6.4 ±0.5	14 ±2	160 ±41
5V	138 ±5	6.5 ±0.4	124 ±9	160 ±21
6V	473 ±17	6.8 ±0.4	596 ±32	160 ±16
7V	1377 ±49	7.4 ±0.4	2012 ±89	160 ±13
8V	3680 ±151	7.6 ±0.5	5523 ±250	160 ±14
9V	8350 ±423	7.9 ±0.6	13867 ±707	160 ±18

In Figures 4.7 and 4.8, the OMR data for 70 nm and 50nm Alq_3 devices has been presented and fitted using Equation (4.2). The same constraints were used as for the 90nm Alq_3 devices. Again it can be seen that, over a wide range of operating voltages, the results for these devices can be fitted using just two processes: exciton trapping and TPI terms. For all data in all devices, including 90nm, 70nm, and 50nm Alq_3 based OLEDs, the saturation fields for the two processes were constrained; the only fitting parameters were the prefactors (a_t and a_i) for the two Lorentzians.

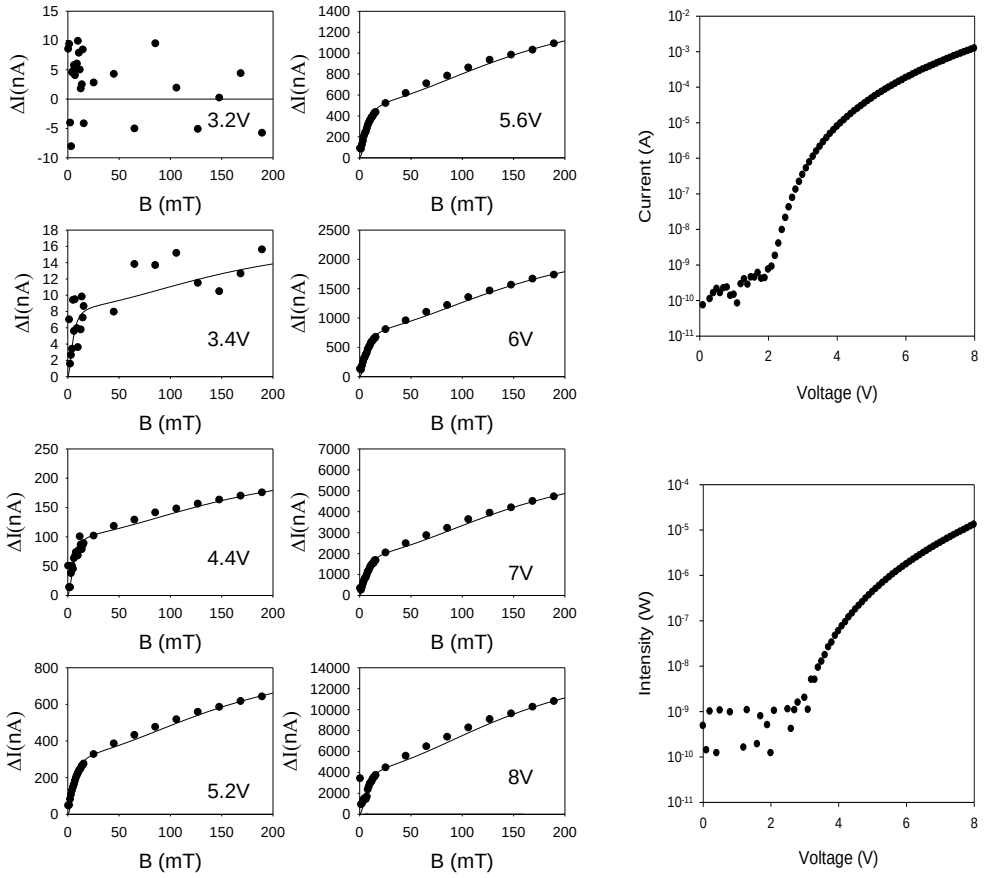

(a) **(b)**

Figure 4.7: (a) The relative change in current in a 70nm Alq_3 OLED as a function of magnetic field for several drive voltages. The fits to the curves were obtained using Equation (4.2), and the parameters are same as those used for 90nm Alq_3 devices. (b) Shows the voltage against current and luminescence of the OLED device. The onset of light emission is ~3.4V, while the onset of OMR is ~3.4V.

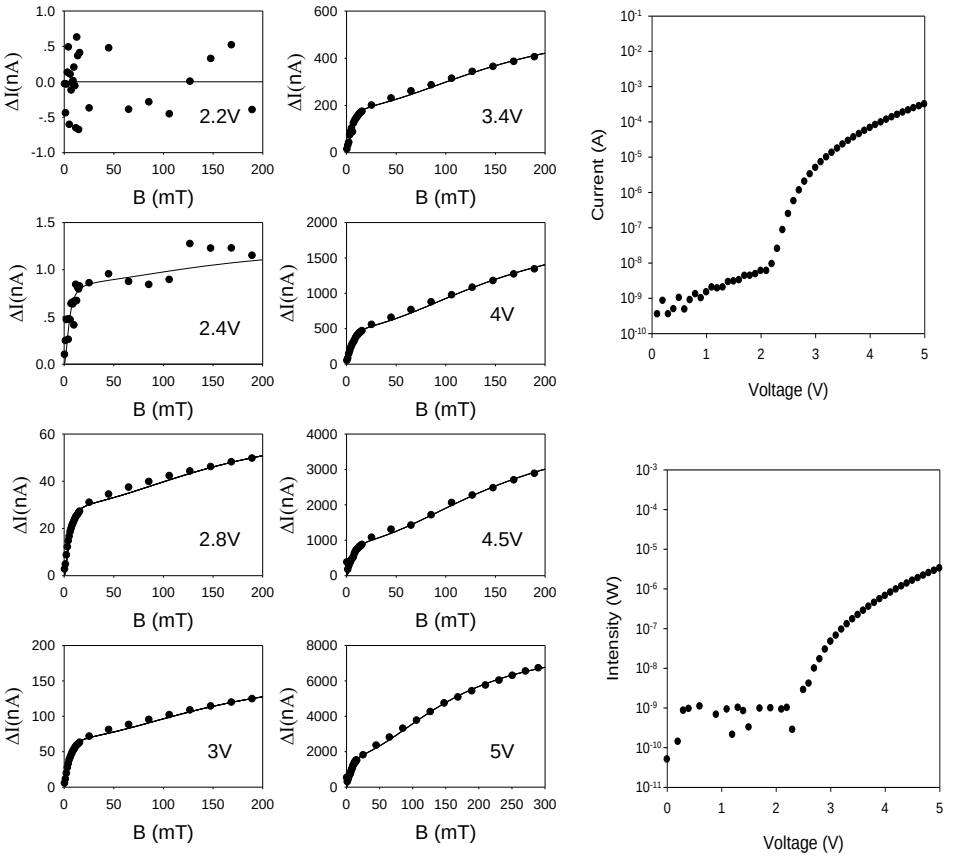

(a) **(b)**

Figure 4.8: (a) The relative change in current in a 50nm Alq_3 OLED as a function of magnetic field for several drive voltages. The fits to the curves were obtained using Equation (4.2) and the parameters are the same as those used for 90nm Alq_3 devices. (b) Shows the voltage against current and luminescence of the OLED device. The onset of light emission is ~2.4V, while the onset of OMR is ~2.4V.

Table 4.3: The parameters obtained from the constrained dual Lorentzian fittings for a 70nm Alq_3 OLED as shown in Figure 4.7.

Voltage	a_t(nA)	B_t(mT)	a_i(nA)	B_i(mT)
3.4V	8.1 ±1.7	3.8 ±1.9	9.5 ±4.3	160 ±60
4.4V	105 ±7	5.6 ±0.7	122 ±15	160 ±34
5.2V	335 ±13	6.6 ±0.5	537 ±26	160 ±14
5.6V	537 ±23	6.8 ±0.5	953 ±44	160 ±14
6V	829 ±34	7.1 ±0.5	1580 ±63	160 ±12
8V	2144 ±91	7.7 ±0.5	4471 ±155	160 ±11
9V	4738 ±556	7.9 ±0.7	10480 ±930	160 ±27

Table 4.4: The parameters obtained from the constrained dual Lorentzian fittings for a 50nm Alq_3 OLED as shown in Figure 4.8.

Voltage	a_t(nA)	B_t(mT)	a_i(nA)	B_i(mT)
2.4V	0.8 ±0.1	4.3 ±0.9	0.4 ±0.2	160 ±66
2.8V	30 ±1	5.0 ±0.3	34 ±2	160 ±15
3V	70 ±2	5.1 ±0.3	94 ±4	160 ±12
3.4V	196 ±6	5.5 ±0.3	370 ±13	160 ±9
4V	523 ±16	5.6 ±0.3	1444 ±36	160 ±7
4.5V	968 ±55	5.8 ±0.6	3346. ±118	160 ±10
5V	1801 ±100	7.1 ±0.6	6389 ±184	160 ±9

It was mentioned previously that the OMR data, over a range of device thicknesses and operating conditions, can be attributed to the magnetic field dependence of exciton trapping and TPI. The exciton trapping should be responsible for the change in concentration of triplets caused by ISC at either the excitonic or pair state level [40]. In addition to the exciton trapping, the change in concentration of triplets caused by

the ISC also could affect the TPI, and hence the mobility of free carriers. Therefore, it is necessary to observe the relationship between each of the prefactors (a_t and a_i) for the two processes and the exciton concentration.

The values for a_t and $a_{i,}$ with error bars for 90nm, 70nm and 50nm Alq_3 based OLEDs, are presented in Tables 4.2, 4.3 and 4.4, respectively. Given that the two processes proposed affecting the OMR, are both dependent on the triplet concentration in the device, the magnitude of the two processes (a_t and a_i) against the light output intensity was firstly plotted. In Figure 4.9, it can be seen that the prefactors of the two processes (a_t and a_i) scale linearly with light output for all devices over a range of device thickness from 90nm to 50nm and over driving voltages.

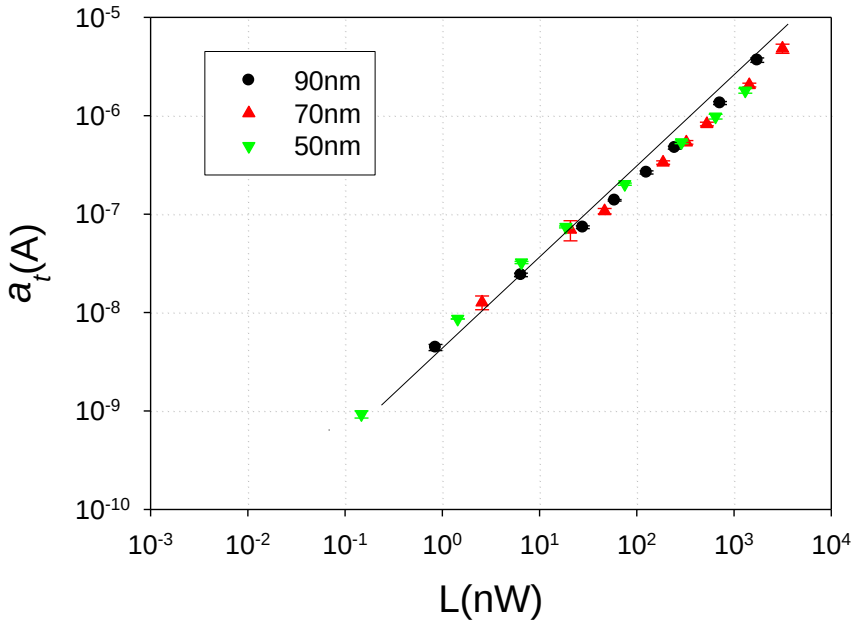

(a)

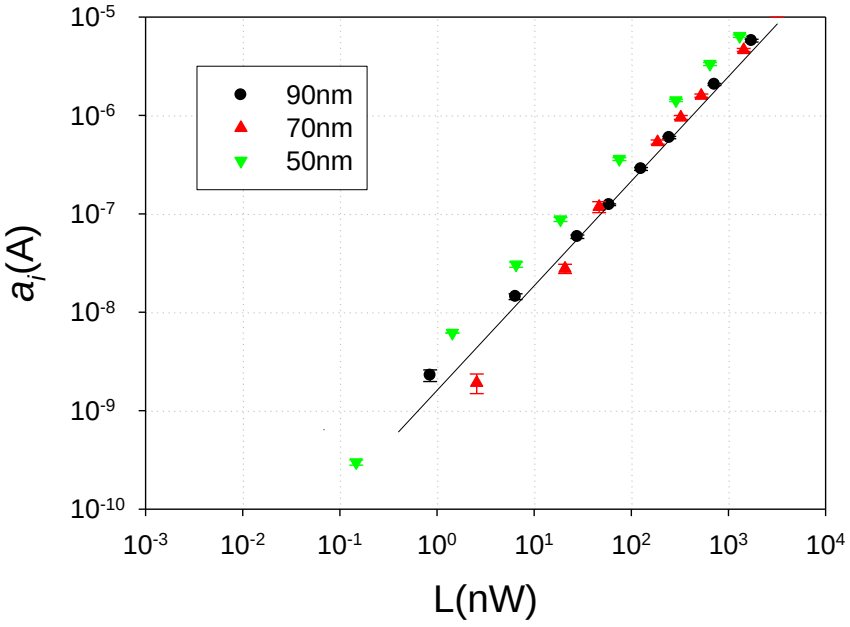

(b)

Figure 4.9: The prefactors from the fits plotted against the light output intensity. The thickness of Alq_3 devices ranges from 90nm to 50nm. (a) Shows the exciton trapping component, a_t, and (b) shows the TPI component, a_i. The straight lines are of slope 1.

In Chapter 1 the light output intensity of an OLED was introduced as being proportional to the number of singlets recombination. Figure 4.10 shows that the light out intensity changes with the device thicknesses at the same driving conditions. Therefore, the conversion from the light output intensity to singlet exciton concentration should be dependent on the device thickness.

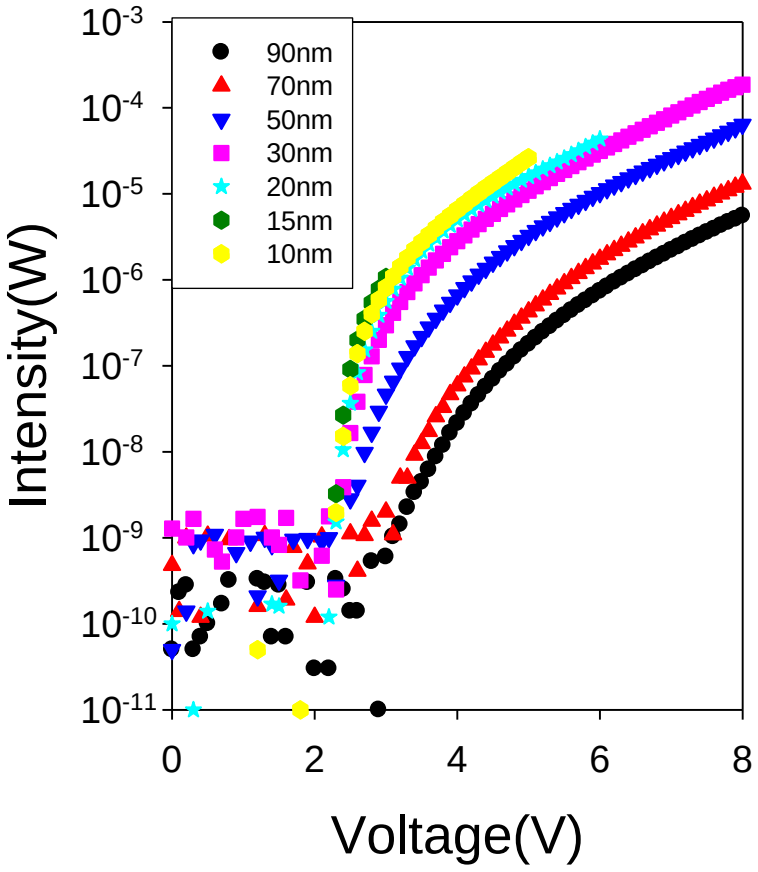

Figure 4.10: The voltage against the light output intensity for all Alq_3 devices, of thickness ranging from 90nm to 10nm.

According to this, the data was replotted against singlet concentration (Figure 4.11), where the singlet concentration is calculated by assuming a recombination wavelength of 520nm and a lifetime of 10ns for all singlets. The thickness of the singlet recombination layer was taken to be the thickness of the Alq_3 layer, and it was

assumed that the concentration was uniform throughout this layer. The assumption can be elucidated in the following equations:

$$Singlet\ concentration = \frac{Number\ of\ singlets}{Volume\ of\ diode} \qquad \text{Equation (4.3)}$$

$$Volume\ of\ diode = Area\ of\ diode \times device\ thickness \qquad \text{Equation (4.4)}$$

$$Number\ of\ singlets\ = \frac{E(Total)}{E(One\ singlet)} \qquad \text{Equation (4.5)}$$

where $E(Total)$ is the total energy of light emitted by the device in the lifetime of a singlet exciton, and $E(One\ singlet)$ is the energy emitted by one singlet.

$$E(Total) = P \times \tau \qquad \text{Equation (4.6)}$$

where P is the illumination power of the device, and τ is the lifetime of the singlet (~10ns) [9].

$$E(One\ singlet) = \frac{hc}{\lambda} \qquad \text{Equation (4.7)}$$

where h is the planck constant (6.626×10^{-34}J s), c is the speed of light(3.0×10^{8} m/s), and λ is the wavelength of the light emission of the device (520nm).

It can be seen in Figure 4.11 that the prefactors of the two processes (a_t and $a_{i,}$) scale linearly with the singlet concentration. Due to the ISC factors mentioned above, the singlet concentration is directly proportional to the triplet concentration in the OLED devices. Therefore, it could be suggested that the prefactors of the two processes (a_t and a_i) also scale linearly with the triplet concentration.

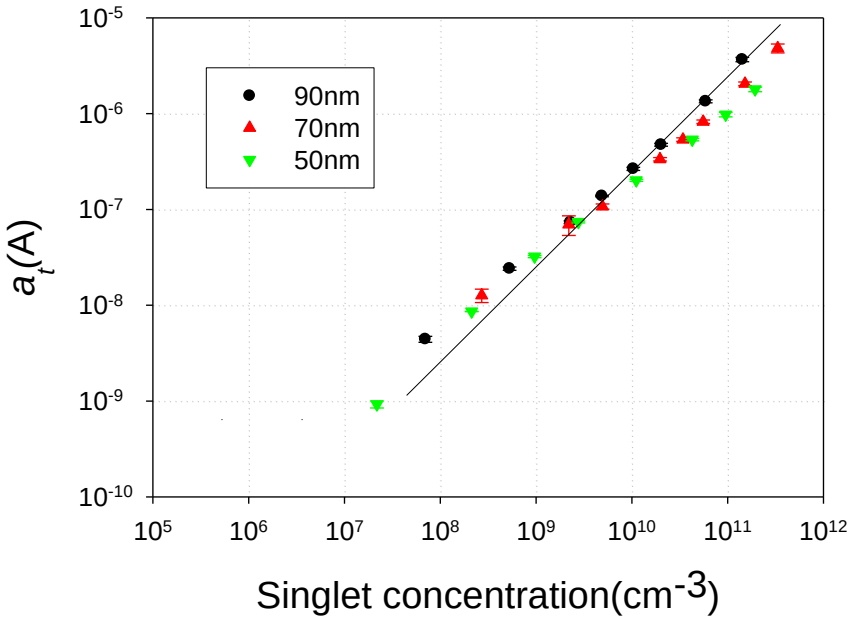

(a)

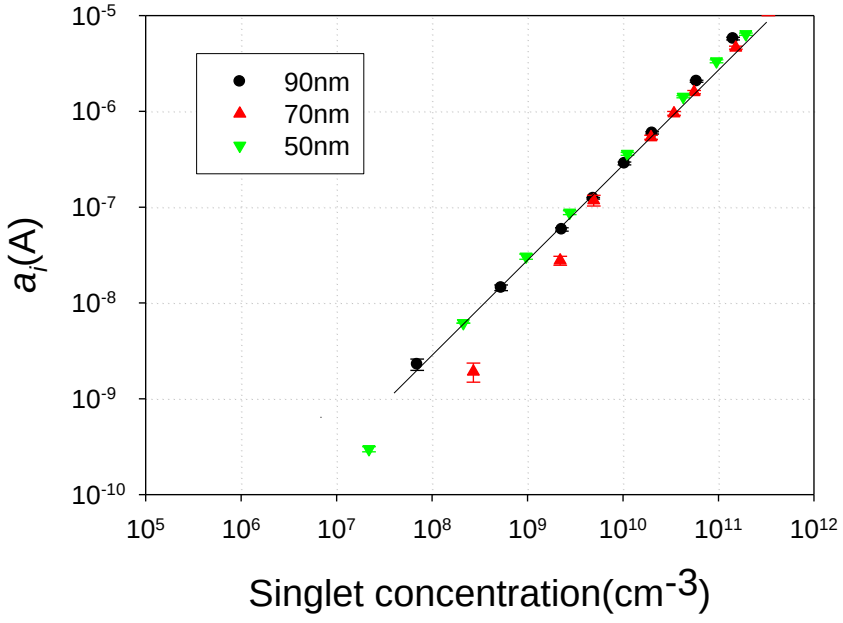

(b)

Figure 4.11: The prefactors from the fits plotted against singlet exciton concentration. The thickness of Alq_3 devices ranges from 90nm to 50nm. (a) shows the exciton trapping component, a_t, and (b) shows the TPI componenet, a_i. The straight lines are of slope 1.

4.3 Triplet dissociation component for negative OMR

4.3.1 Background

In the previous section, it was suggested that the positive OMR in Alq_3 based devices could be modelled using two Lorentzians that represent the exciton trapping and the TPI. However, negative OMR has been observed under certain circumstances. In 2008, Desai *et al.* demonstrated that, for a thin Alq_3 based OLED device, a negative OMR can be observed at low operating conditions [54]. For a very thin working OLED device, excitons can be formed at the TPD/Alq_3 interface, then diffuse towards the Alq_3/cathode interface where they can be quenched. This results in a hole entering the cathode and the electron being recycled. This process is regarded as exciton dissociation. The schematic diagram of the exciton dissociation mechanism is shown in Figure 4.12.

In electrical excitation, due to spin statistics, one singlet is formed for every three triplets. In addition, the lifetime of triplets is at least a factor of one thousand larger than the lifetime of singlet excitons. Therefore, the concentration of triplets should be considerably higher than singlet excitons in a working OLED device. It is necessary to address where the trapping and dissociation processes take place. Since any excitons (primarily the long lived triplets) in the layer can act as the trap for polarons, and hence reduce the mobility of the polaron, exciton trapping is regarded as taking place in the bulk of device. Otherwise, the excitons (primarily the long lived triplets) can dissociate at an energetically favourable interface, and the cathode is an ideal interface for dissociation. This is because there are available states for both electrons and holes to couple to the cathode. There is, therefore, a high probability that excitons present at the cathode will dissociate. With the effect of

magnetic field, the triplet concentration will be reduced due to the ISC, resulting in the decrease in the triplet concentration, and hence the current caused by the triplet dissociation is reduced. Therefore, the negative OMR could be attributed to a reduction in triplet dissociation, as triplets are converted to singlet excitons magnetically.

If BCP (2,9-dimethyl-4,7-diphenyl-1,10-phenanthroline), used as a blocking layer, is inserted into the interface between the Alq_3 and cathode, the negative OMR is suppressed [54]. The literature values of LUMO and HOMO for BCP are 3.2 and 6.7eV [59, 60], respectively. Comparing the value of LUMO for Alq_3 (3.1eV) [12], the BCP layer – with 3.2eV as the value of LUMO – can't restrict the electrons approach to the cathode. On the other hand, because the value of HOMO for BCP (6.7eV) is much higher than value of HOMO for Alq_3 (5.8eV) [12], the BCP layer would efficiently block holes entering the cathode. The energy gap (E_g) of BCP (3.5eV) is bigger than the E_g of Alq_3 (2.7eV), meaning that the triplets can not diffuse from Alq_3 to BCP, and hence triplet dissociation can not occur.

In this section the model will be extended to include the effect of exciton dissociation. For all Alq_3 devices of any thickness, the OMR can be modelled using just these three processes: exciton dissociation, exciton trapping and triplet polaron interaction. The approach also successfully models the negative peaks that are often seen in OMR data at high operating currents.

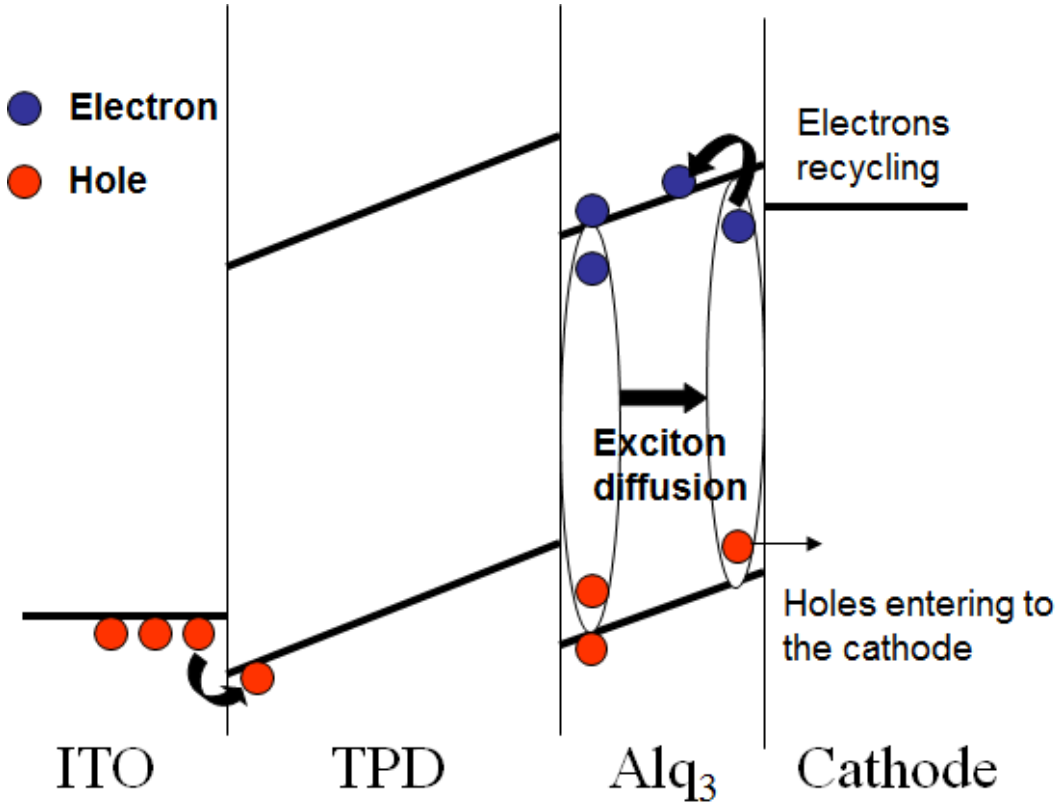

Figure 4.12: The schematic diagram of the exciton dissociation mechanism.

4.3.2 Triple Lorentzian fits

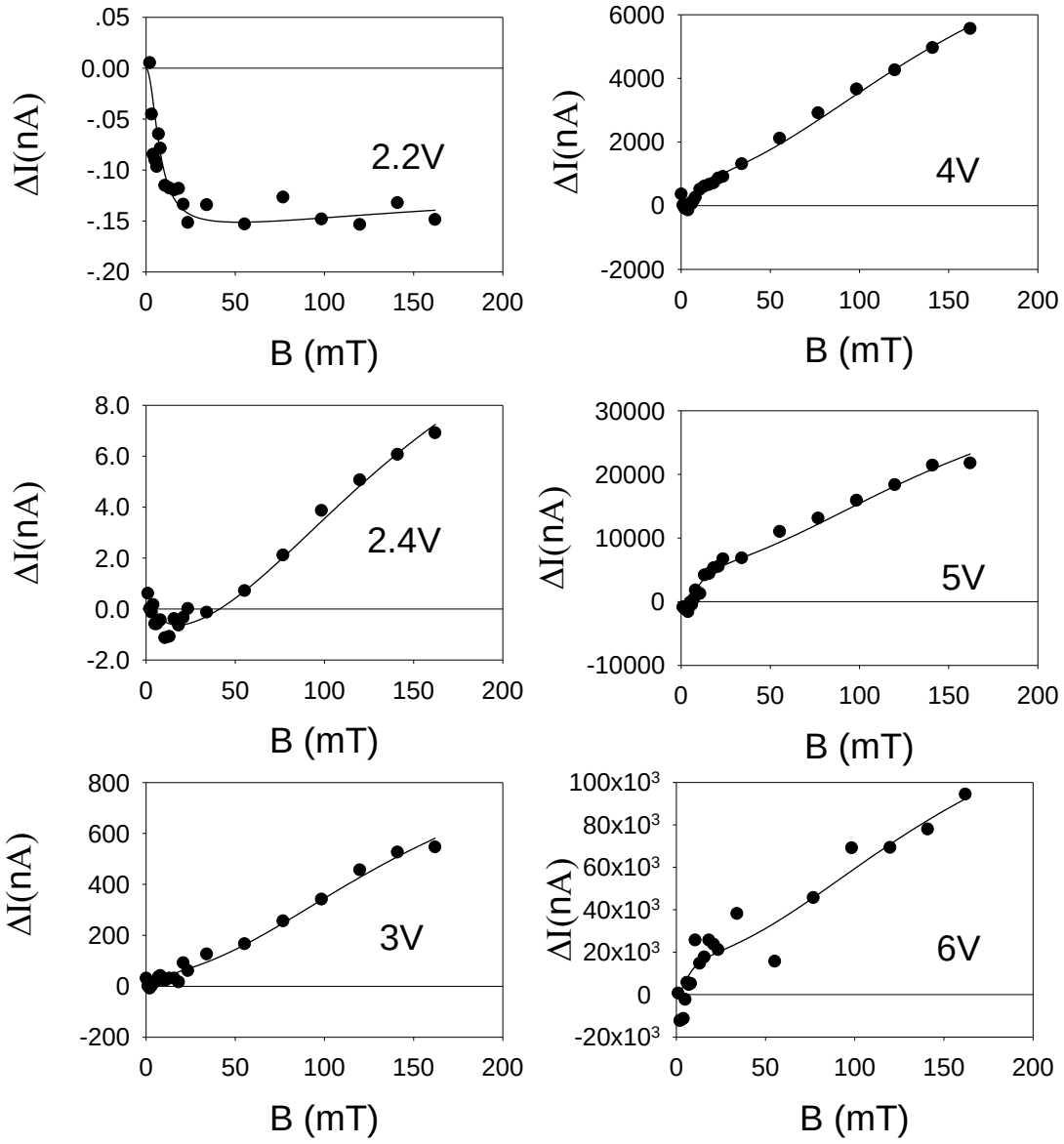

Figure 4.13: The relative change in current in a 30nm Alq_3 OLED, as a function of magnetic field for several drive voltages. The fits to the curves were obtained using Equation (4.8) and the parameters in the text.

Figure 4.13 shows the OMR curves for a 30nm Alq_3 device as a function of drive voltage. The negative change in current with applied field at low drive voltages is evident. Given that it has already been demonstrated above that in thick devices the OMR has a positive contribution from two processes, any negative contribution to the OMR will be in addition to these processes. As already suggested, the component that contributes to the negative OMR should be the triplet dissociation process. The data has therefore been fitted using a triple Lorentzian process of the form

$$f(B) = a_d \frac{B^2}{\left(B^2 + B_d^2\right)} + a_t \frac{B^2}{\left(B^2 + B_t^2\right)} + a_i \frac{B^2}{\left(B^2 + B_i^2\right)} \qquad \text{Equation (4.8)}$$

where B is the applied magnetic field, a_d, a_t and a_i are the prefactors for the Lorentzians, B_d, B_t and B_i are the saturation fields, and the subscripts d, t and i stand for dissociation, trapping and interaction respectively.

Any magnetic field effect on the dissociation component would be expected to scale as the triplet population at the interface. The change in efficiency of an OLED with applied magnetic field directly reflects the increase in the concentration of singlet excitons caused by the ISC from the triplet to singlet state [39]. This ISC between triplets and singlets can occur at either the pair state or the excitonic level [40]. Therefore, it would be expected that any contribution to the current due to the triplet dissociation component has the same magnetic field dependence as the measured change in efficiency. In Section 4.2, it was suggested that the exciton trapping component should also mirror the change in the concentration of triplets caused by the ISC. According to these reasons, both the dissociation and trapping components should have the same functional form, hence B_d should be equal to B_t. However, the dissociation component should have an opposite sign to the trapping component, since the dissociation component gives a negative OMR whilst the effect of trapping is positive; hence $a_d<0$ and $a_t>0$. For the values of the saturation fields we used the same approach was used as mentioned in Section 4.2 and the values were constrained to 4 mT < B_d < 8 mT, 4 mT < B_t < 8 mT and B_i=160 mT. In Figure 4.13, Equation

(4.8) was used with these constrains to fit the OMR data for a 30nm Alq_3 device as a function of drive voltage. It is evident that the fits were excellent.

Table 4.5 shows prefactors obtained from the constrained triple Lorentzians fittings for a 30nm Alq_3 based OLED as seen in Figure 4.13. It can be observed that the fitting prefactors (a_d and a_t), which represent the exciton trapping and dissociation components, inconstantly change with the quality of the fit. Because of the poor quality of OMR data at low field, the triple Lorentzian fitting does not provide unique values for each of these prefactors. It is necessary to note that the unique values for a_d and a_t obtained from the constrained triple Lorentzians fittings for a 30nm Alq_3 based OLED are unphysical. As a result, it is necessary to think about the sum of the prefactors for the dissociation and trapping components, which has physical significance as it corresponds to the magnitude of OMR.

Table 4.5: The parameters obtained from the constrained triple Lorentzian fittings for a 30nm Alq_3 based OLED as shown in Figure 4.13.

Voltage	a_d (nA)	B_d (mT)	a_t (nA)	B_t (mT)	a_i (nA)	B_i (mT)
2.2V	-1.5 ± 0.7	5.2 ± 7.1	1.5 ± 0.7	5.2 ± 0.01	$1.8 \times 10^{-10} \pm 0.03$	160.0 ± 2.4
2.4V	-1988 ± 13	4.0 ± 0.1	1987 ± 13	4.0 ± 0.1	15.9 ± 0.7	160.0 ± 24
3V	-87267 ± 930	7.9 ± 0.2	87326 ± 930	7.9 ± 0.2	1028 ± 176	160.0 ± 27
4V	$-8.54 \times 10^5 \pm 3.4 \times 10^9$	8.0 ± 15.7	$8.55 \times 10^6 \pm 3.4 \times 10^9$	8.0 ± 14.8	$8.9 \times 10^3 \pm 1.1 \times 10^3$	160.0 ± 34.9
5V	-11998 ± 54874	6.0 ± 30.0	19171 ± 54150	6.0 ± 30.0	30786 ± 6055	160.0 ± 35
6V	$-1.472 \times 10^8 \pm 1.1 \times 10^{11}$	5.0 ± 2.2	$1.473 \times 10^8 \pm 1.1 \times 10^{11}$	5.0 ± 2.5	$1.27 \times 10^5 \pm 7.5 \times 10^4$	160.0 ± 91.7

It is also noted in Table 4.5 that the there is almost no difference between the saturation field for dissociation and trapping components. However, when the value of (B_d - B_t) is calculated, the difference in saturation field for the two processes can still be observed in Table 4.6. This difference is remarkably small and increases

with the driving voltages. This reinforces the view that both dissociation and trapping components have the same origin. However, it is necessary to address the question of why there should be any difference between them at all. It was previously suggested that both the dissociation and trapping terms are proportional to the change in the triplet population in the device. The triplet dissociation occurs at the interface between the Alq_3 layer and the cathode. However, the trapping component is a bulk effect, as any triplet in the layer can act as a trap and hence reduce the mobility. Therefore, the small difference in saturation field for the two processes implies that the triplets close to the cathode are seeing a slightly different environment, which is affecting the local ISC rate. This effect was also noted by Wu *et al.* [36], who stated that the OMR is changed through shifting the exciton formation zone in organic semiconductor devices. This may be due to a change in the spin-orbit coupling induced by the metal cathode.

Table 4.6: The difference between the saturation field for dissociation and trapping components as a function of operating condition.

Voltage	**2.2V**	**2.4V**	**3V**	**4V**	**5V**	**6V**
$(B_d - B_t)$ (mT)	-2.8×10^{-6}	-8.6×10^{-4}	-1.9×10^{-3}	-7.5×10^{-3}	-8.7×10^{-3}	-9.3×10^{-3}

Similar behaviour of the negative OMR can be observed at 20nm and 15nm Alq_3 based devices. In Figures 4.14 and 4.15, the OMR data for 20nm and 15nm Alq_3 devices have been fitted by the triple Lorentzian functions. The same constraints were used as for the 30nm Alq_3 device. It also can be seen that the fitting is excellent.

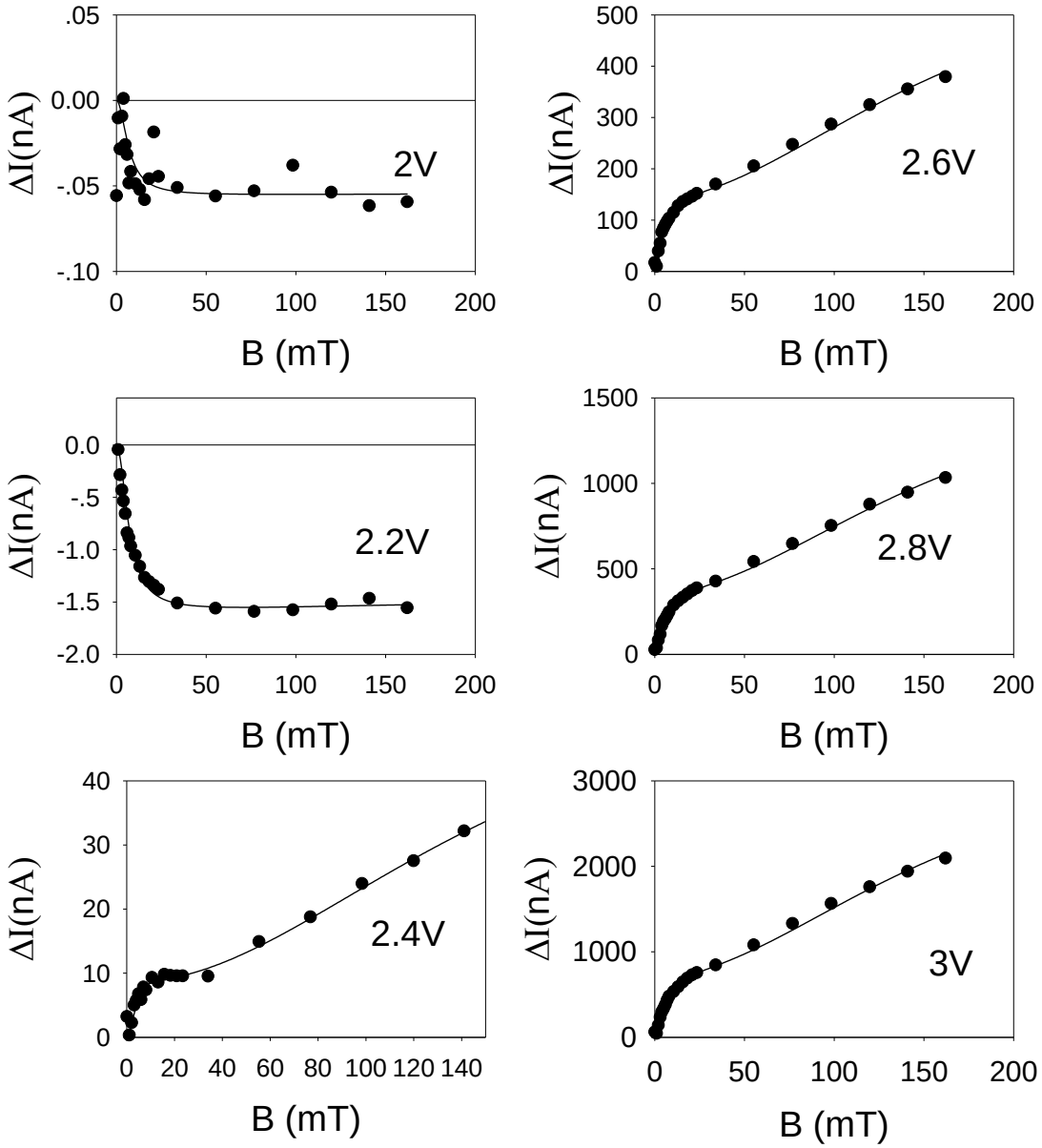

Figure 4.14: The relative change in current in a 20nm Alq_3 OLED as a function of magnetic field for several drive voltages. The fits to the curves were obtained using Equation (4.8) and the parameters are the same as those used for 30nm Alq_3 devices.

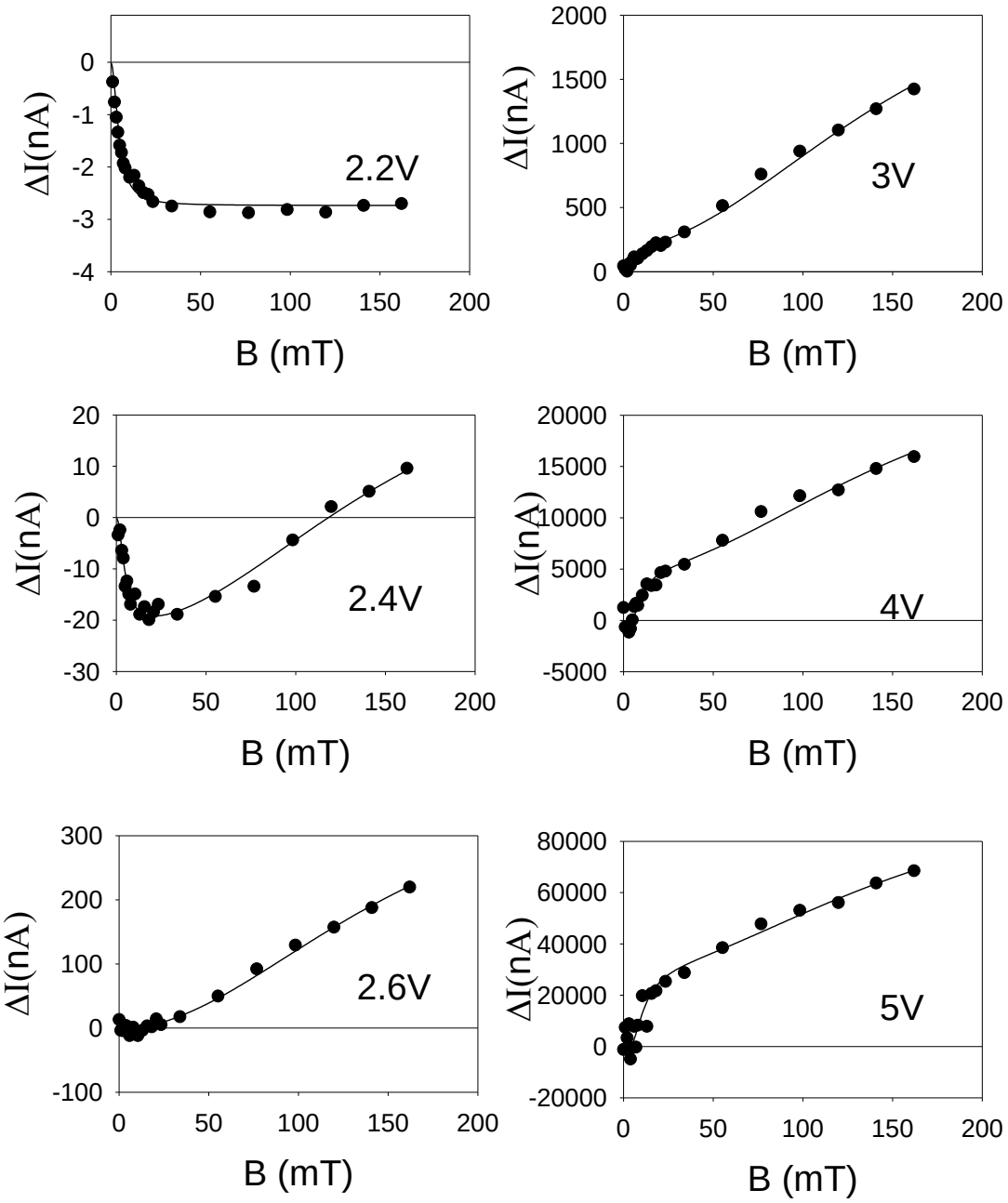

Figure 4.15: The relative change in current in a 15nm Alq_3 OLED at 300K as a function of magnetic field for several drive voltages. The fits to the curves were obtained using Equation (4.8) and the parameters are the same as those used for 30nm Alq_3 devices.

Once the thickness of the Alq_3 layer reaches 50nm or greater, there is no evidence of negative OMR at low voltages. The OMR data can be effectively modelled using just a dual Lorentzian. However, when the drive voltage is increased to very high, an additional feature can be observed at low magnetic field. Figure 4.16 shows the OMR data for a 50nm Alq_3 based OLED at the driving voltage from 6V to 9V. Figure 4.17 presents that each graph in Figure 4.16 shows the detail of the low field region from 0 to 20mT. Figures 4.16 and 4.17 show that there is a small negative peak in the low field component before it rises rapidly. In this case, the OMR data can no longer be fitted using just the exciton trapping and TPI components. This could suggest that the contribution from triplet dissociation is starting to become important. It can be seen that a triple Lorentzian function, Equation (4.8), can fit very well for the OMR data for a 50nm Alq_3 based OLED at high operating conditions.

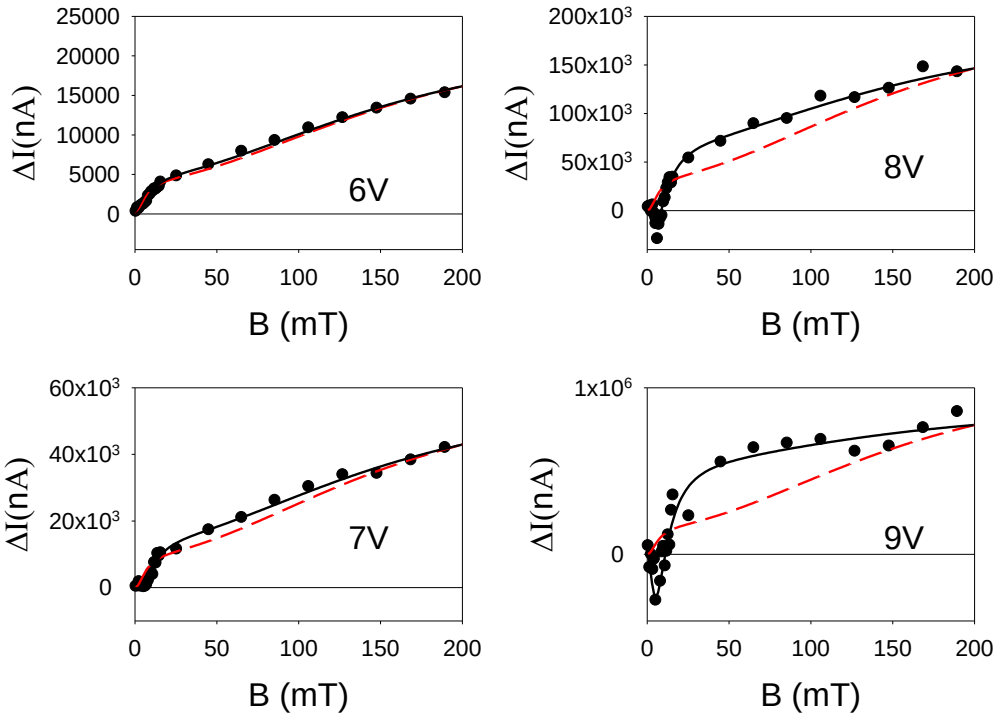

Figure 4.16: The relative change in current in a 50nm Alq_3 OLED as a function of magnetic field at the driving voltage from 6V to 9V. The red dashed lines are fits obtained using the dual Lorentzian function, Equation 4.1. The black solid lines are fits obtained using the triple Lorentzian function, Equation (4.8).

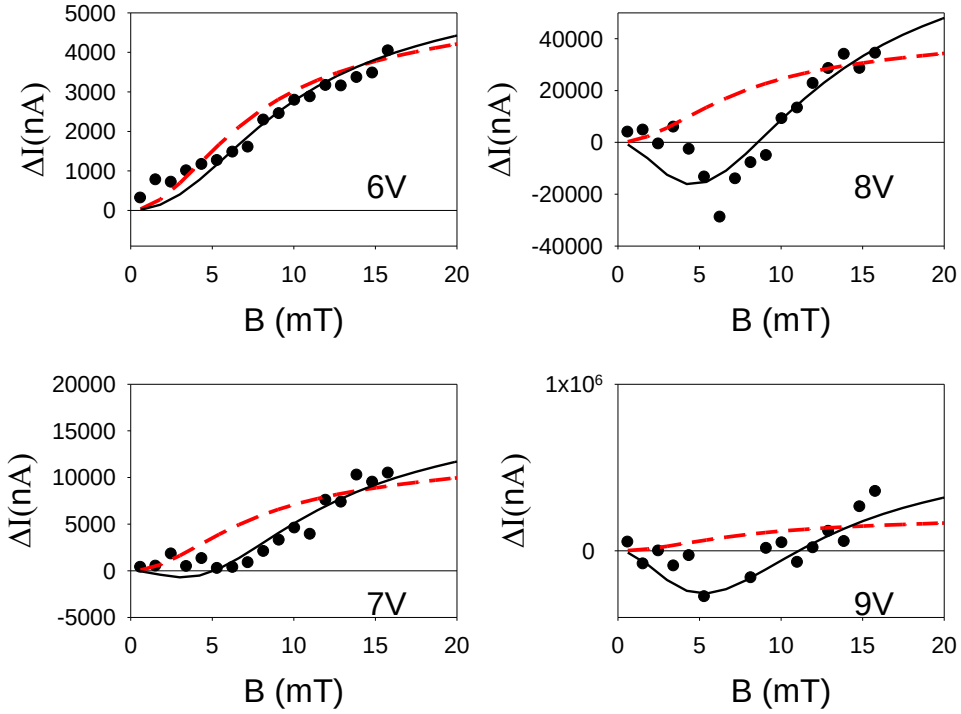

Figure 4.17: Each graph in Figure 4.16 shows the detail of the low field region from 0 to 20mT.

It can be seen in Figures 4.16 and 4.17 that there are clear negative peaks in the OMR data. Each of negative peaks occurs at ~6mT. Therefore, the exciton dissociation component should be taken into account for fitting the 50nm Alq_3 device OMR data at high driving voltages. Figures 4.16 and 4.17 also show the comparison between the double and triple Lorentzian fittings. It is obvious that the 50nm Alq_3 device OMR data at high driving voltages gets a better fitting using the triple Lorentzian, which takes the excitons dissociation component into account.

The reason for the appearance of excitons dissociation at higher drive voltages can be understood from the fact that exciton formation in TPD/Alq_3 devices is known to occur at the interface between the TPD and Alq_3 [10]. This is due to the fact that the TPD acts as an electron blocking layer. However, when the drive current and exciton concentration increases, the width of the recombination zone must also increase until it is wide enough for some of the excitons to be in the vicinity of the cathode, and hence liable to dissociate.

Figure 4.18 (a) shows the relative change in current in a 70nm Alq_3 OLED with a low field region from 0 to 20mT, while Figure 4.18 (b) is for the 90nm Alq_3 OLED case. For the thick devices, the onset of the triplet dissociation component can only be seen under very high drive conditions. This is consistent with the observation that it is correlated with the exciton recombination zone increasing with drive voltage.

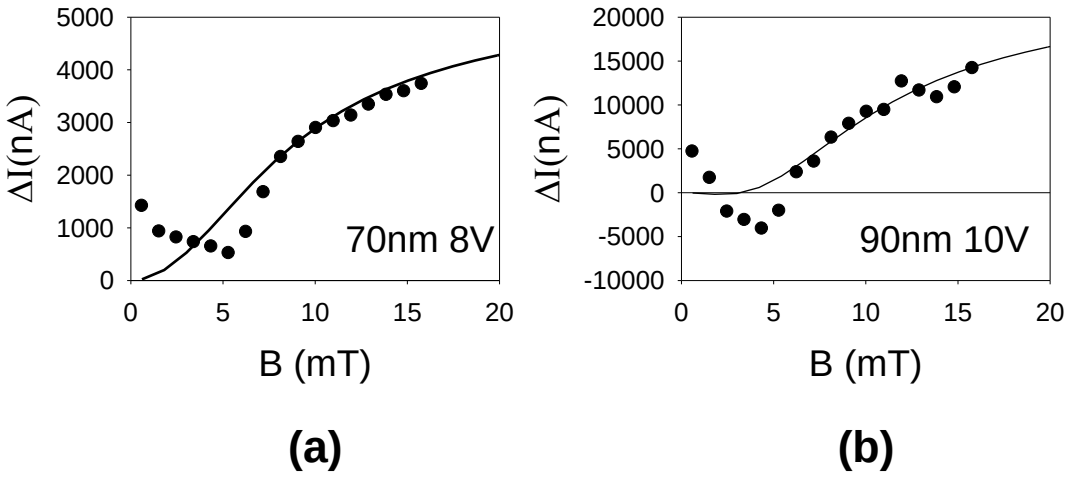

Figure 4.18: (a) shows the relative change in current in a 70nm Alq_3 OLED with low field region from 0 to 20mT, while (b) shows the 90nm Alq_3 OLED case. The black solid lines are fits obtained using the triple Lorentzian function, Equation (4.8).

In Section 4.2 discussing the OMR data of thick devices, it was mentioned that two prefactors (a_t and a_i), which indicate the exciton trapping and TPI, scale linearly with the luminance and the triplet population. In this section, it was found that a triple Lorentzian is required to fit the OMR data for the thin devices that exhibit a negative OMR at low voltage. Therefore, it is reasonable to observe the relationship between these prefactors ((a_d+a_t) and a_i) and the triplet population of thinner devices. A general summary about the relationship between the prefactors and the triplet population will be presented over a range of the device thicknesses and operating conditions.

In Figure 4.19, the sum of the prefactors for the dissociation and trapping components (a_d+a_t) was plotted against light out and singlet concentration over a range of device thicknesses and operating conditions. Figure 4.19 (a) shows, for Alq_3 devices with thickness ranges from 90nm to 10nm, the sum of the prefactors for the dissociation and trapping components obtained from the double or triple Lorentzian fits (a_t+a_d) plotted against the light output intensity from the devices. The dual Lorentzian, Equation (4.2) was used to fit for the OMR data of device thickness from 90nm to 50nm, while the triple Lorentzian, Equation (4.8), needed to be used to fit the OMR data of thin devices from 30nm to 10nm. Figure 4.19 shows that the data with a device thickness less than 30nm covers a smaller range of light out intensity and singlet concentration compared with the data for the thicker devices. This is because the value of (a_t+a_d) for the thinner device (Alq_3 layer less than 30nm) is negative (dissociation dominated) at low operating conditions, and the logarithmic plot only shows the positive data (trapping dominated).

Similar to the previous results relating to the thick devices, the (a_d+a_t) scales linearly with light out for all devices (see Figure 4.19 (a)). Furthermore, (a_d+a_t) was plotted against singlet concentration (See figure 4.19(b)). The conversion from the light out intensity to singlet concentration has already been discussed in Section 4.2. It was observed that the data overlapped for the thicker devices (Alq_3 layer greater than 50nm). However, for the thinner devices (thickness less than 30nm), the data for each device – whilst still linear and with a slope one – falls below those of the thicker devices. As mentioned previously, the triplet dissociation easily occurs near the cathode for the thinner devices and is proportional to the exciton population. The prefactor, a_d, for the dissociation component is negative and cannot be shown in the logarithmic plot. However, the negative prefactor, a_d, makes the value of (a_d+a_t) smaller. This would explain why the value of (a_d+a_t) for thinner devices (Alq_3 layer less than 30nm) falls below the thicker devices (thickness greater than 50nm).

In addition, it is interesting to see that, for the 70-30nm devices, there is a kink in each data set at a singlet concentration of ~10^9 cm^{-3}. The data for each device is linear both above and below that value, but the constant of proportionality changes. This change in the constant of proportionality is consistent with the onset of some dissociation, which would subtract from the sole exciton trapping process that occurs at low drive voltages. Therefore, the change in slope shown in Figure 4.19 (b) provides evidence that the onset of dissociation may be easily occurring in thinner devices with much lower operating voltages.

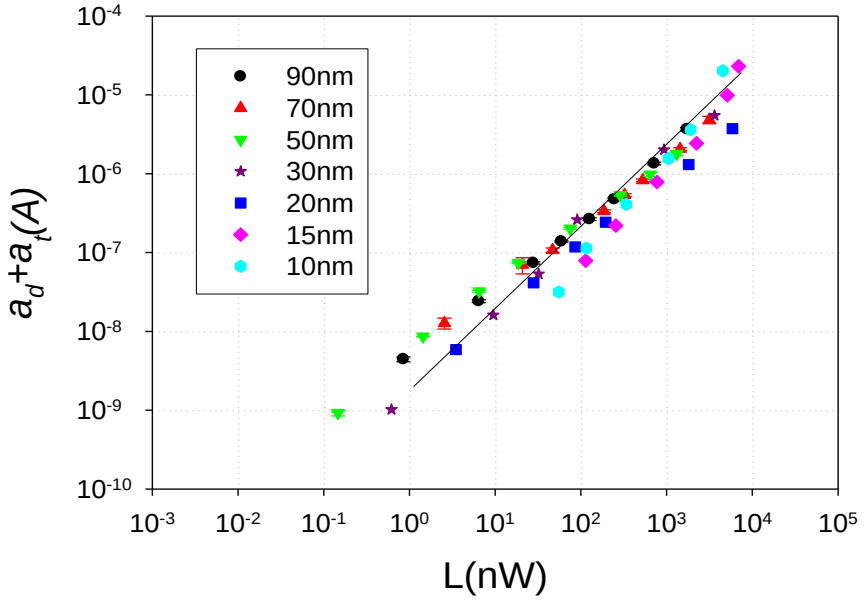

(a)

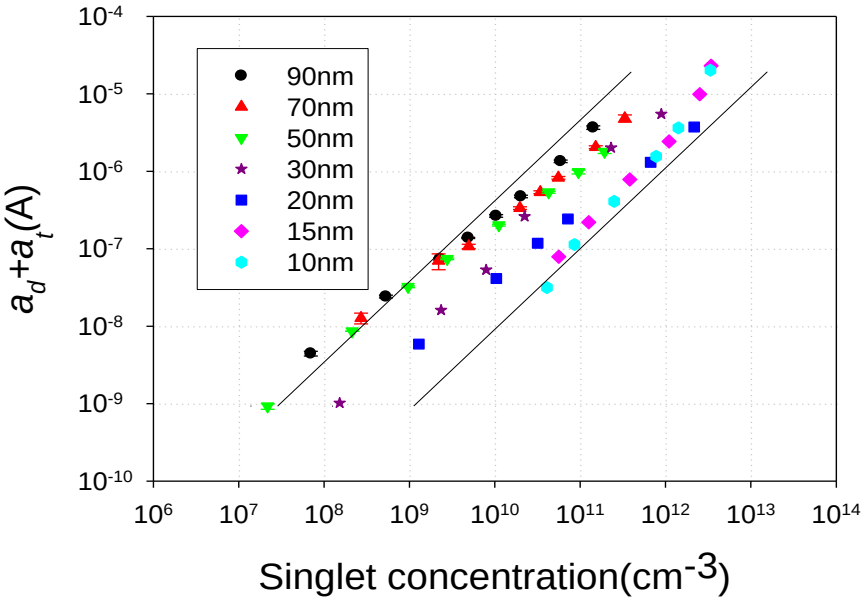

(b)

Figure 4.19: The sum of the prefactors for the dissociation and trapping components of the fit plotted against (a) light output and (b) singlet concentration. The thicknesses of Alq_3 devices range from 90nm to 10nm. The straight lines are of slope 1.

In Section 4.2, it was found that, for the thick devices, the prefactor for the TPI component, a_i, scales linearly with the luminance and the triplet concentration. Figure 4.20 (a) shows, for Alq_3 devices ranging in thickness from 90nm to 10nm, the prefactor for the TPI component, a_i, obtained from the double or triple Lorentzian fits and which is plotted against the light output intensity from the devices. Throughout the range of device thickness over the complete range of operating conditions, it can be seen that – even for the thin devices at low voltage – the magnitude of the TPI component, a_i, scales linearly with light output intensity (see Figure 4.20 (a)). A plot can also be produced to show that the TPI component scales linearly with the singlet concentration (see Figure 4.20 (b)). It is interesting to note that there is a great reduction in scattering of the data when plotting the prefactor for the TPI component, a_i, against the singlet concentration, rather than light output intensity. As already suggested, the singlet concentration is directly proportional to the triplet concentration in the OLED devices. Therefore, the result that the TPI component scales linearly with the triplet concentration is independent to the device thickness.

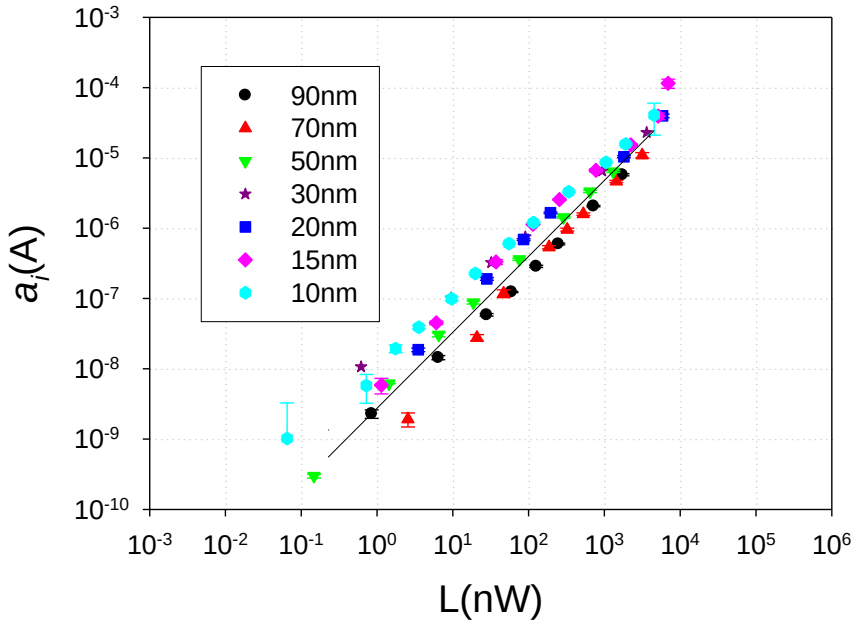

(a)

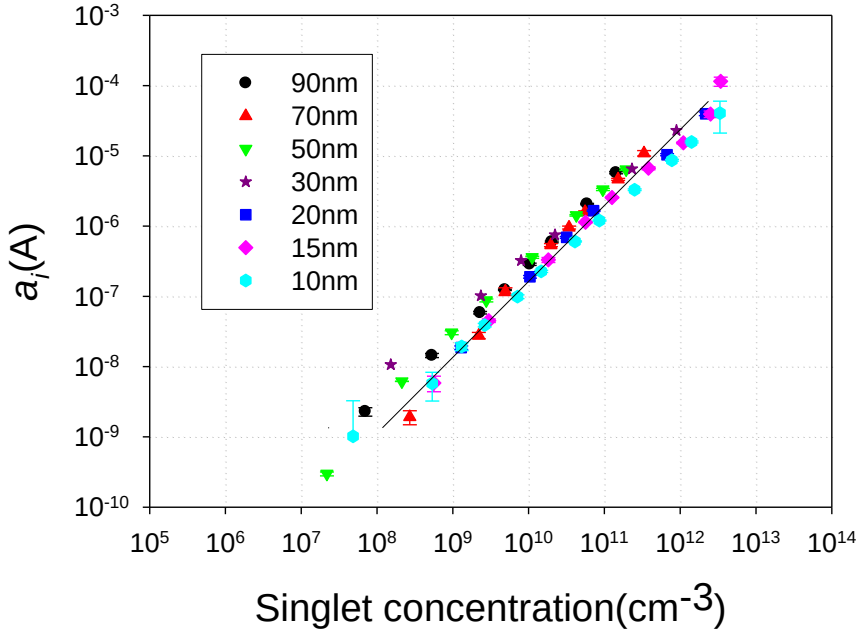

(b)

Figure 4.20: The prefactor for the interaction component of the fit against (a) light output and (b) singlet concentration. The thickness of the Alq_3 devices ranges from 90nm to 10nm. The straight lines are of slope 1.

4.4 Conclusion

In this chapter, a TPI model has been proposed to fit the OMR data as a function of thickness for Alq_3 based OLEDs. For the thick devices (Alq_3 layer greater than 50nm), it was observed that the data could be fitted using just these two processes: exciton trapping and TPI components. The exciton trapping mechanism has been theoretically predicted by the Agranovich group [58], while the TPI model was proposed by Ern and Merrifield's group [21]. Song *et al.* used the dark injection method and proved these two mechanisms [8, 42]. Meanwhile, it was also observed that the prefactors of these two processes (a_t and $a_{i,}$) scale linearly with the exciton concentration for all devices over a range from 90nm to 50nm and operating voltages.

By reducing the device thickness, or driving the device to very high voltage, a triple Lorentzian is required to fit the OMR data. It was shown that it is possible to model both the positive and negative OMR data of an Alq_3 based OLED using the TPI model coupled with triplet dissociation at the cathode. The relationship between these prefactors (a_d, a_t and $a_{i,}$) and the triplet concentration was also analysed and it was found that $(a_{d+} a_t)$ and $a_{i,}$ are respectively proportional to the exciton concentration within the device over the full range of operating conditions. Consequently, for all Alq_3 devices of any thickness, the OMR data can be modelled using just these three processes: triplet dissociation, exciton trapping and TPI.

Chapter 5:

Modelling of OMR as a function of temperature

5.1. Introduction

In Chapter 4, a triplet polaron interaction (TPI) model was proposed to fit the OMR data as a function of thickness for aluminium tris (8-hydroxyquinoline) (Alq_3) based OLEDs. A dual Lorentzian function, indicating exciton trapping and TPI, was used to fit the OMR data for thick devices (Alq_3 layer over 50nm). Furthermore, a triple Lorentzian function, combining triplet dissociation, exciton trapping and TPI components, was required to fit the OMR data of the thin device, or the device under a high driving condition. It was also found that the prefactors for the two or three processes scale linearly with the triplet concentration. In this chapter, this model has been used to fit the OMR data as a function of temperature and operating voltage for Alq_3 based OLEDs.

In addition, the work has been extended to investigate the temperature dependencies of the magnetic field effect on current and efficiency of Alq_3 based OLEDs. In 2007, Desai *et al.* found that the OMR is intimately linked to light emission from the devices at room temperature [39]. However, the delay between onset of light emission and onset of OMR has been observed at low temperature. The reasons have been analysed for this later on in this chapter. Furthermore, we also show that OMR at low temperatures can be observed only if this device is driven to a relatively

higher voltage. In this case, the population of triplets is too large, so the triplet-triplet annihilation (TTA) should be taken into account.

Xiong, *et al.* observed that the traces of electroluminescence at low temperature exhibit a dropping process at high field strength, which has been attributed to the magnetic field effects on the TTA process [61, 62]. A similar result was observed in the percentage change of efficiency in the Alq_3 OLED, which dropped when a high magnetic field was applied at low temperature. Moreover, this fall in percentage change of efficiency with applied magnetic field becomes more remarkable when increasing the driving voltage. This phenomenon is explained at the end of this chapter.

5.2 Temperature dependence of the magnetic field effect on Alq_3 based OLEDs

5.2.1 TPI model as a function of temperature

Figure 5.1 shows the OMR curves (plotted as the relative change in current) for a 50nm Alq_3 device over a range of temperatures and operating voltage. The OMR data for 50nm Alq_3 devices from 300K to 150K can be fitted using just two processes: exciton trapping and TPI terms. The same constraints were used as defined in Chapter 4 for 50nm Alq_3 devices at room temperature. However, when the temperature is decreased to 100K, OMR can only be observed at a high driving condition. This will be discussed in Section 5.3. In Chapter 4, it was mentioned that the triplet dissociation should play an import role at high driving conditions, even for the thick devices. With a high driving condition, it can be seen in Figure 5.1 that the low field component at 100K is no longer fitted using just the trapping and interaction components. Therefore, the triplet dissociation has been taken into account for the data fitting. It is obvious that the OMR data at low field can be fitted very well with a triple Lorentzian.

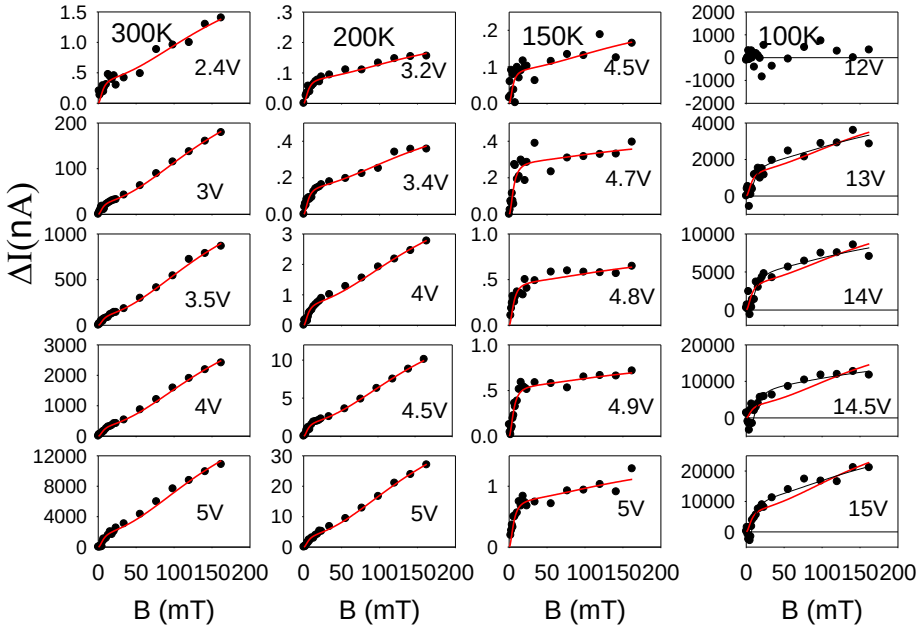

(a)

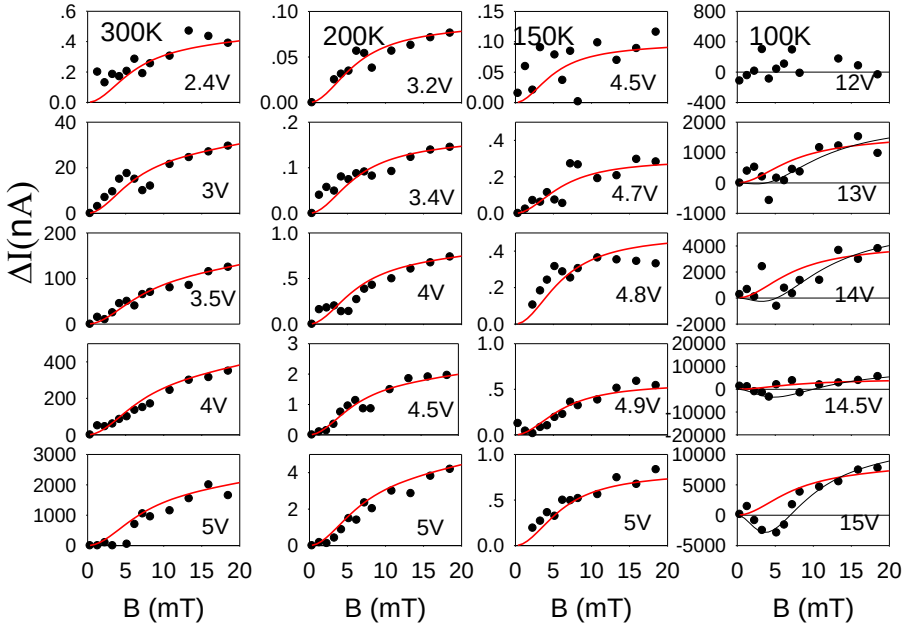

(b)

Figure 5.1: (a) The relative change in current in a 50nm Alq_3 OLED at 300K, 250K, 150K, and 100K with applied magnetic field for several drive voltages. (b) The detail of the low field region from 0 to 20 mT. The black line is the fitting by the triple Lorentzian, Equation(4.8) and the red line indicates the fitting by the double Lorentzian, Equation(4.2).

5.2.2 Dissociation, trapping, and TPI components (a_d, a_t and a_i)

In Chapter 4 it was mentioned that, for 50nm Alq_3 devices at room temperature, the two prefactors (a_t and a_i), which indicate the trapping and TPI, scale linearly with the triplet population. In this chapter, this work was extended to a range of temperatures. It was interesting to observe the relationship between the magnitudes of these processes and the singlet exciton concentration as a function of temperature.

From 300K to 150K, the magnitudes of the two processes, (a_d+a_t) and a_i, were plotted against the light out intensity in the device (see Figure 5.2). At a temperature of 100K, the OMR could only be observed at high driving voltages, and the OMR data required triple Lorentzian fits. As discussed in Chapter 4, due to the inconsistent change with the quality of the fit, fitting did not provide unique values for each of the prefactors for the dissociation and trapping components. Hence, the sum of the prefactors for the dissociation and trapping components of the fit were plotted versus the light out intensity of the device. In Figure 5.2, it can be seen that these prefactors scale approximately linearly with light output for all devices over a range of temperatures and operating voltages. It is interesting to note that (a_d+a_t), the sum of prefactors for the dissociation and trapping components, at a temperature of 100K looked likely to deviate from the straight lines of slope 1.

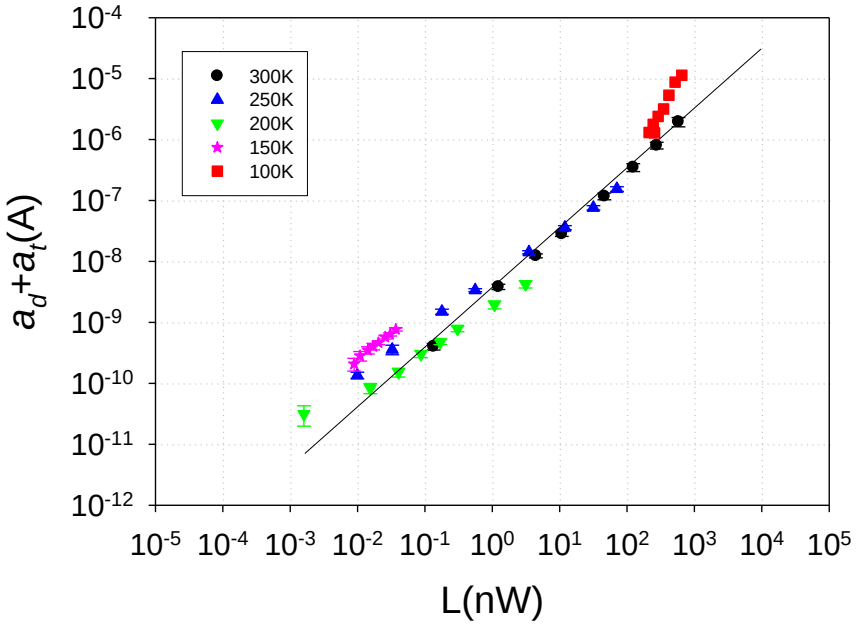

(a)

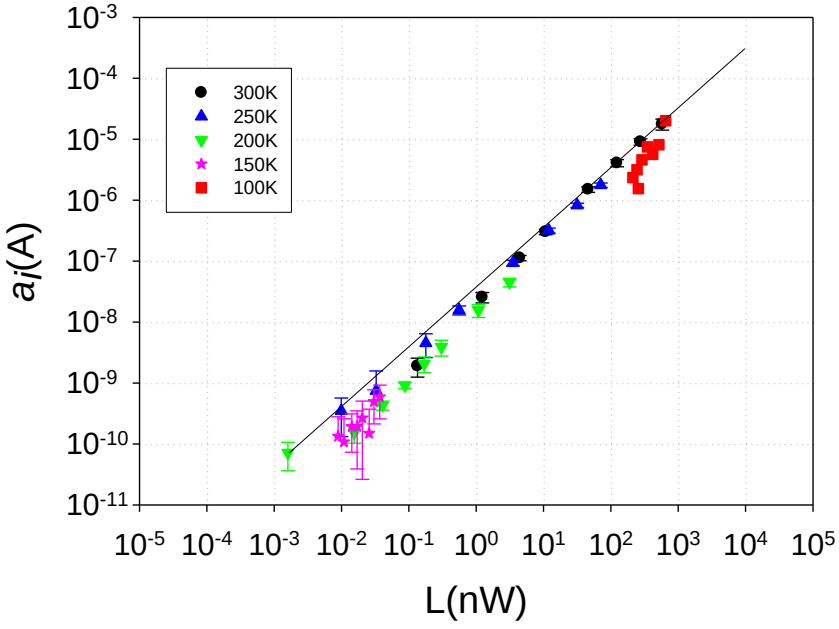

(b)

Figure 5.2: The prefactors from the fits plotted against light output. (a) shows the sum of the prefactors for the dissociation and trapping components (a_d+a_t) and (b) shows the TPI component, a_i . The straight lines are of slope 1.

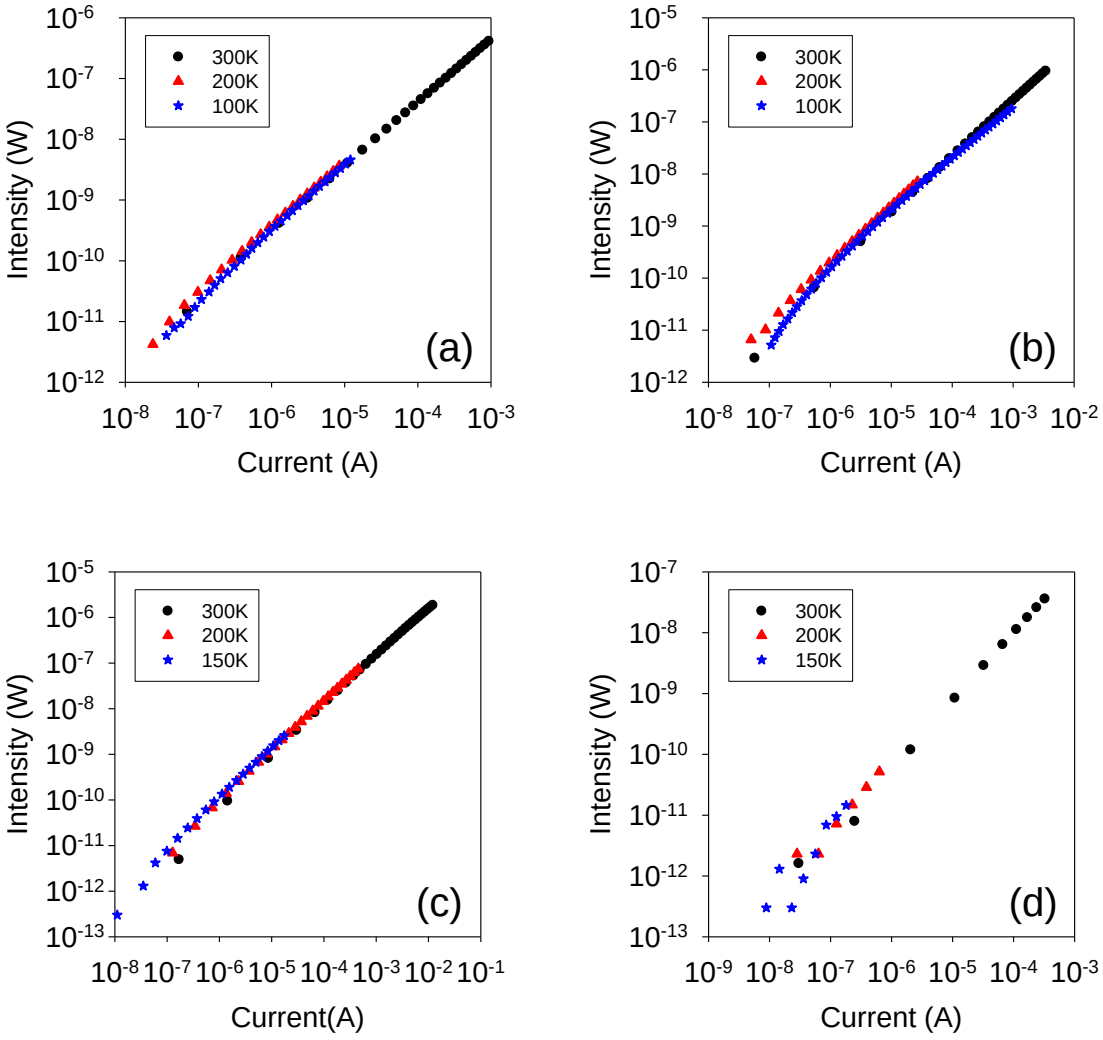

Figure 5.3: The light output intensity against current for (a) 50nm, (b) 30nm, (c) 20nm, and (d) 15nm Alq_3 based OLEDs over a range of temperatures.

Figure 5.3 shows the light output intensity against current at (a) 50nm, (b) 30nm, (c) 20nm, and (d) 15nm Alq_3 based OLEDs over a range of temperatures. It is interesting to note that there is no difference in light output intensity at a given current with temperature changes. The temperature dependence of the device's I-V-L characteristics is therefore due to the change in light output intensity against voltage. Figure 5.4 shows the light output intensity against voltage for (a) 50nm, (b) 30nm, (c) 20nm and (d) 15nm Alq_3 based OLEDs over a range of temperatures. Because the light out intensity changes with temperature, it was necessary to re-plot the magnitudes of these processes as a function of temperature against the singlet exciton

concentration in the device (see Figure 5.5). The conversion from the light out intensity to the singlet exciton concentration was introduced in Chapter 4. Figure 5.5 shows that the prefactors for these processes scale linearly with exciton concentration. Furthermore, changing the temperature of the sample had no effect upon that linearity.

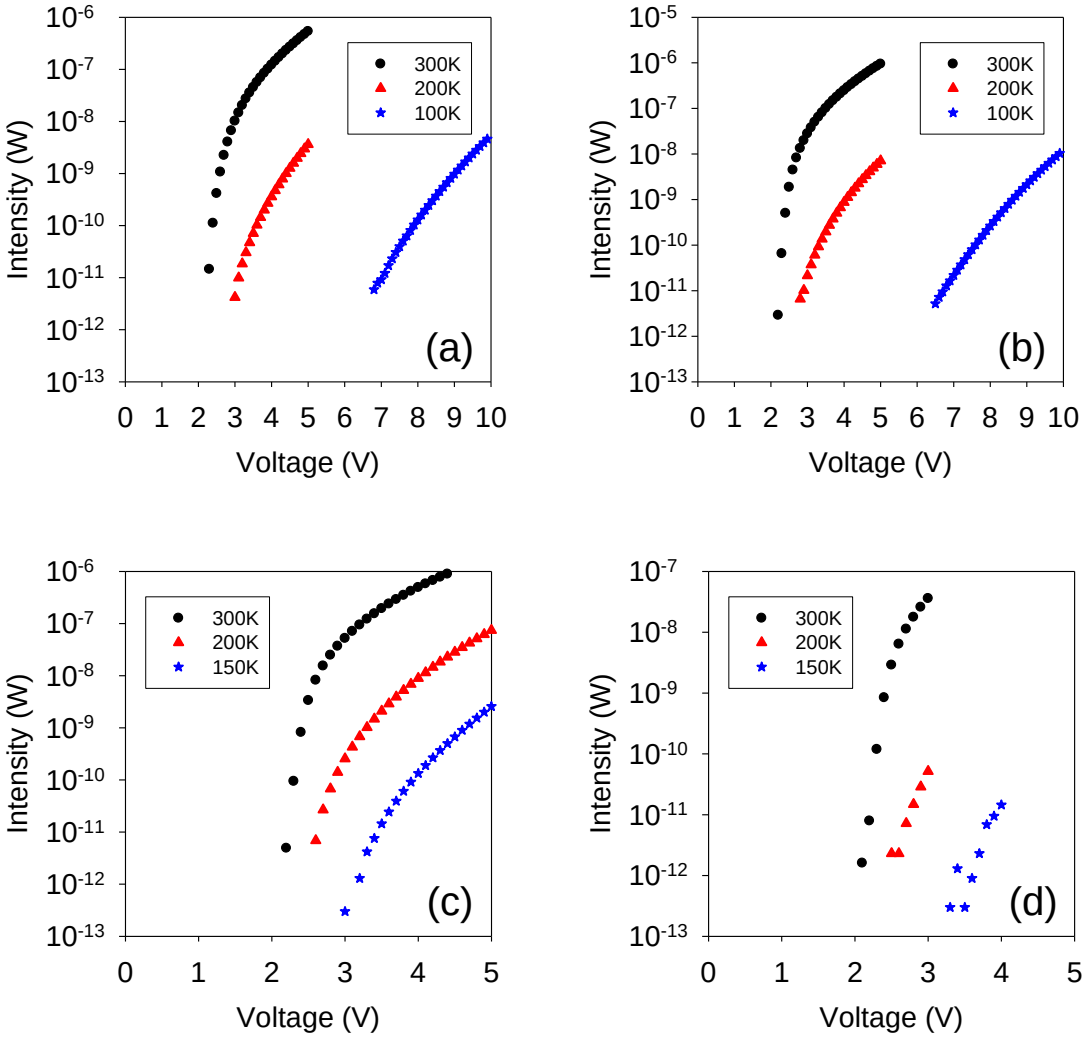

Figure 5.4: The light output intensity against voltage for (a) 50nm, (b) 30nm, (c) 20nm, and (d) 15nm Alq_3 based OLEDs over a range of temperatures.

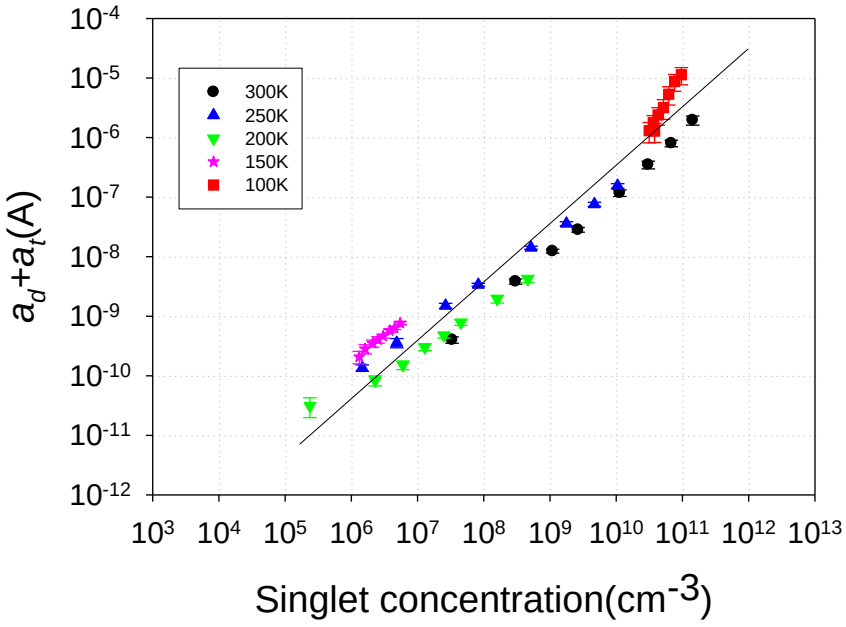

(a)

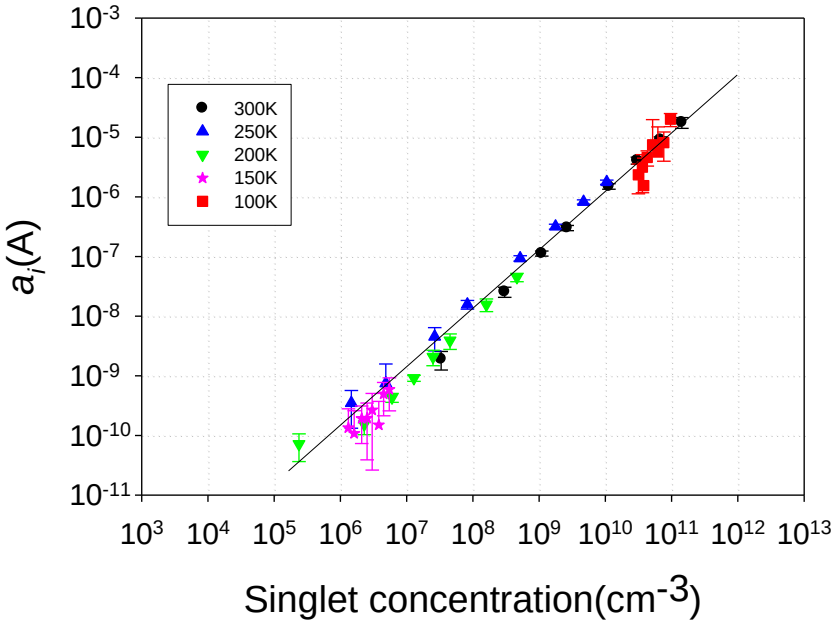

(b)

Figure 5.5: The prefactors from the fits plotted against singlet concentration. (a) shows the sum of the prefactors for the dissociation and trapping components (a_d+a_t) and (b) shows the TPI component, a_i . The straight lines are of slope 1.

This observation is interesting, as the triplet concentration only scales with singlet concentration if the ratio of their lifetimes is constant. There is little data about the triplet lifetime in Alq_3. Cölle *et al.* [46, 51, 63] measured the delayed photoluminescence and delayed electroluminescence to obtain the triplet lifetime at temperatures below 150K, and found a value of ~10ms that has a weak temperature dependence. At 300K, Baldo *et al.* [10, 46] estimated that the triplet lifetime in an Alq_3 based OLED is a value of ~25μs, which is calculated from the diffusion measurement. Given that interactions between polarons and triplets should act to quench the triplet lifetime, it is possible that the triplet lifetime obtained by Baldo is dominated by these polaron quenching interactions. Therefore the triplet lifetime in the absence of quenching must be much bigger than the ~25μs obtained by Baldo, although in our samples significant quenching is expected, so the Baldo figure is used, as explained in the following paragraph.

The actual lifetime of the triplet can be divided into two parts: the initial component and the quenching component. The equation can be written as:

$$\frac{1}{\tau_A} = \frac{1}{\tau_I} + \frac{1}{\tau_q} \qquad \text{Equation (5.1)}$$

where τ_A is the actual triplet lifetime, τ_I is the initial triplet lifetime, and τ_q is the quenching triplet lifetime. It is well known that the quenching triplet lifetime is very short [64]. Thus, if one thinks about the recombination rate from excited triplet state (T_1) to ground state (S_0), the quenching component ($k_q=1/\tau_q$) will be dominant. This suggests that the lifetime of a triplet at room temperature, 25±15μs, should be the quenching triplet lifetime, rather than the initial triplet lifetime. The fact that the data reported here suggests there is little change in a triplet lifetime from 300K to 100K, may be indicative that triplet-polaron quenching may dominate the triplet lifetime in operating devices over the whole temperature range[65].

It has been shown that both exciton trapping and TPI components are independent of the temperature changes. In addition, it was mentioned in Chapter 4 that the dissociation component should be taken into account for thinner devices and high driving conditions. It will now be discussed how the dissociation component changes with temperature.

Figure 5.6 shows the OMR curves for a 30nm Alq_3 device over a range of temperatures and operating voltages. At a temperature of 300K, negative OMR can be observed, which is due to the triplet dissociation mentioned in Chapter 4. Therefore, it was necessary to use a triple Lorentzian to fit the OMR data. The constraints are the same as used in Chapter 4, namely $a_d < 0$ and $a_t > 0$, 4 mT < B_d < 8 mT, 4 mT < B_t < 8 mT and B_i=160 mT. Figure 5.6 shows that the fits are excellent.

At temperatures of 250K and below, negative OMR could no longer be observed over a range of voltages. However, the dissociation component could still be seen in the low field. The fitting comparison between dual and triple Lorentzian was done at temperatures ranging from 250K to 100K. It was observed that the data fitting with triple Lorentzian, particularly in the low field, was better than the fitting with a dual Lorentzian. At a temperature of 100K, the OMR could only be observed at high driving voltage conditions and the OMR data needed to fit using a triple Lorentzian.

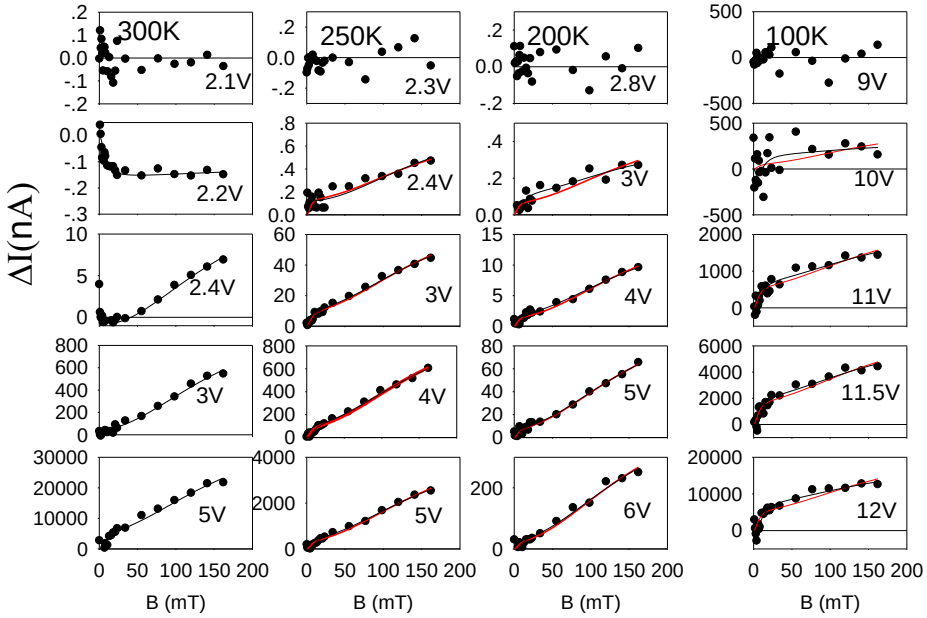

(a)

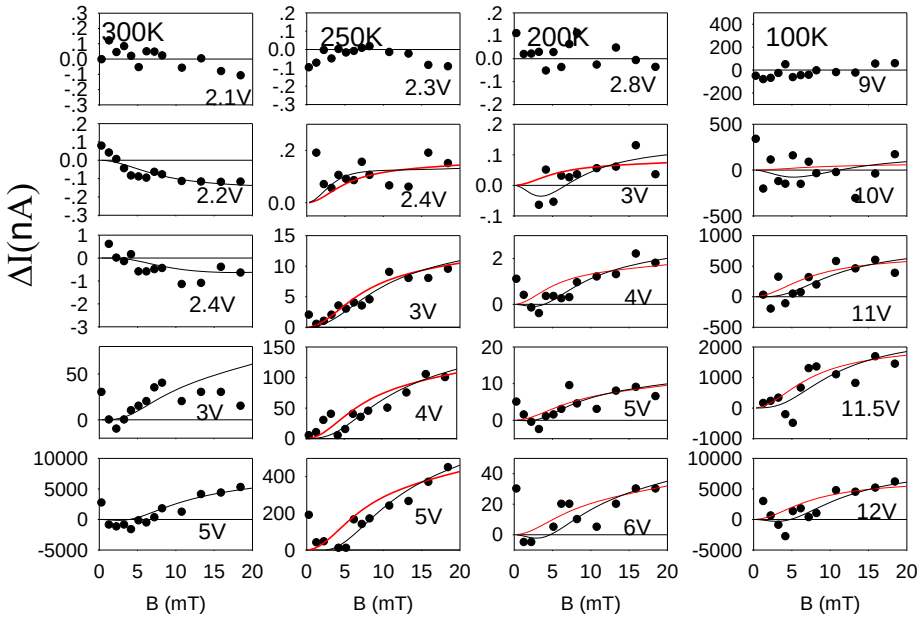

(b)

Figure 5.6: (a) The relative change in current in a 30nm Alq_3 based OLED at temperatures of 300K, 250K, 200K, and 100K, with applied magnetic field for several drive voltages. (b) The detail of the low field region from 0 to 20 mT. The black line is the fitting by the triple Lorentzian, Equation(4.8) and the red line indicates the fitting by the double Lorentzian, Equation(4.2).

Given that it has been proposed that these three processes – polaron trapping, TPI, and exciton dissociation – are all dependent on the exciton concentration, the sum of the prefactors for the dissociation and trapping components of the fit were plotted against the light out intensity in the device (see figure 5.7). The light out intensity was then converted into the singlet exciton concentration. Figure 5.8 shows the prefactors for these processes against the singlet exciton concentration in the device. Figure 5.8 shows that the prefactors for these processes scale linearly with exciton concentration. As with the 50nm Alq_3 device case at 100K, (a_d+a_t) for 30nm Alq_3 device at 100K also deviates from the straight lines of slope 1. This deviation suggests that a new process would take into account the effect on the OMR. This assumption will be analysed further on in this chapter.

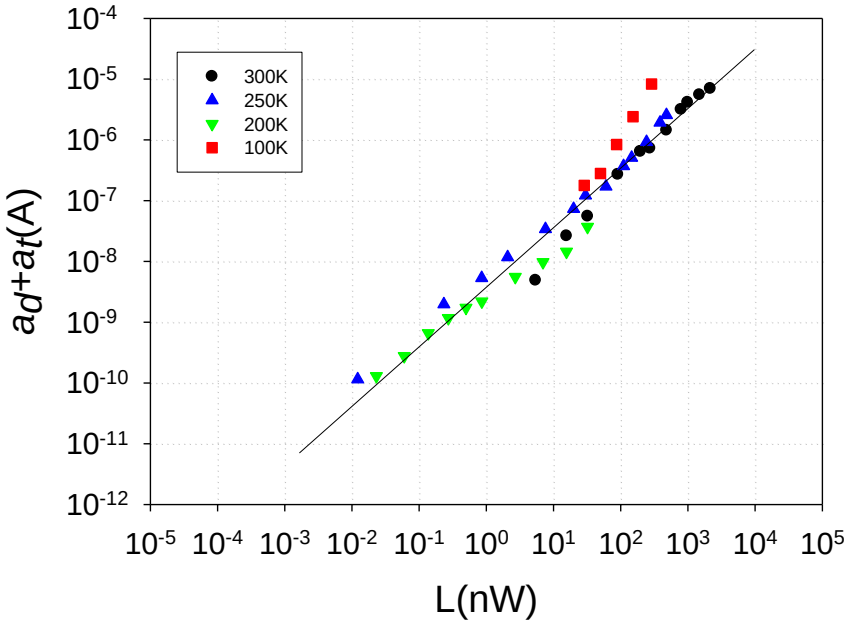

(a)

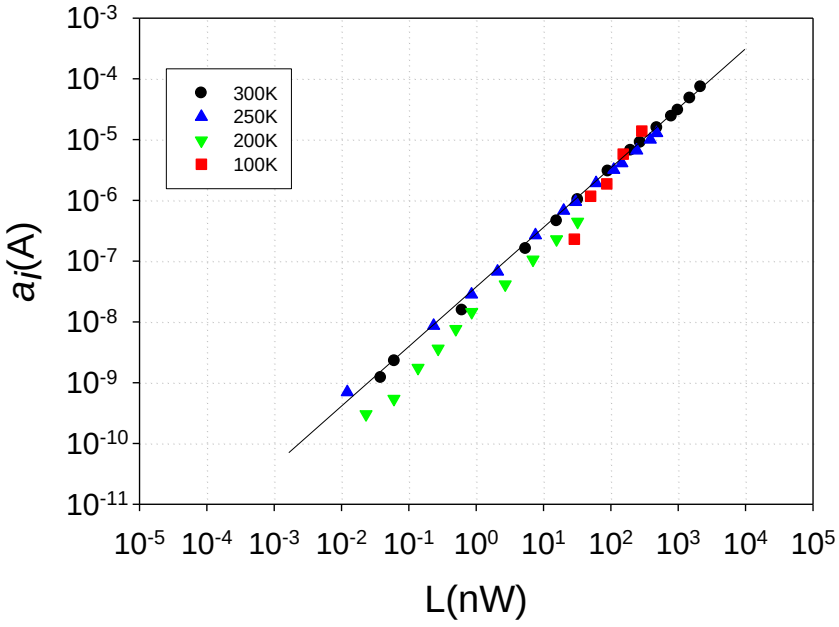

(b)

Figure 5.7: The prefactors from the fits plotted against light output for a 30nm Alq_3 based OLED. (a) shows the sum of the prefactors for the dissociation and trapping components (a_d+a_t) and (b) shows the TPI component, a_i. The straight lines are of slope 1.

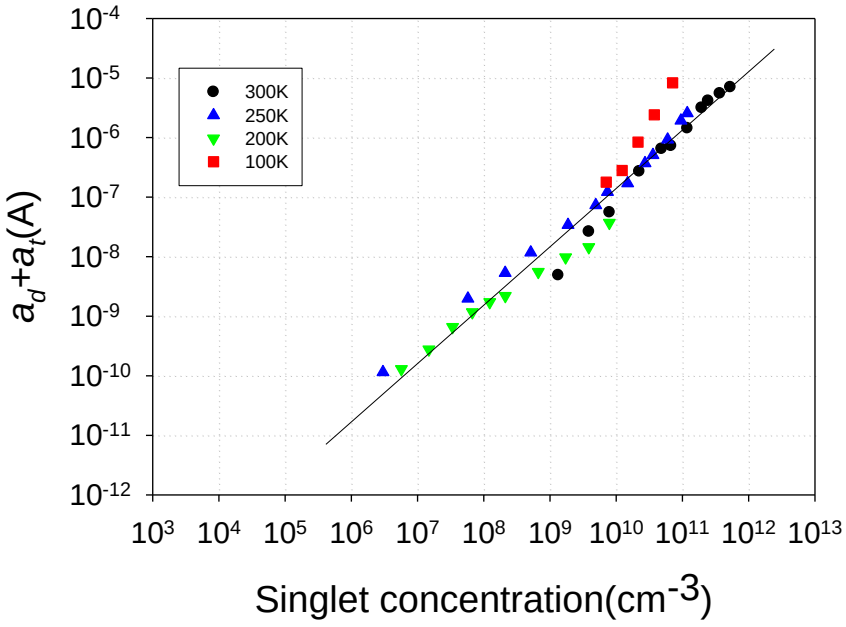

(a)

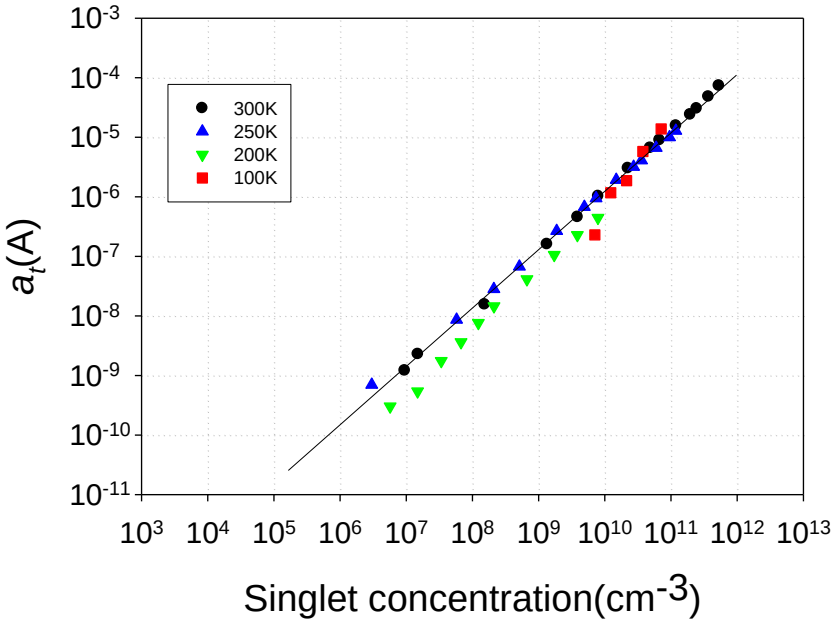

(b)

Figure 5.8: The prefactors from the fits plotted against singlet concentration for a 30nm Alq_3 based OLED. (a) shows the sum of the prefactors for the dissociation and trapping components (a_d+a_t) and (b) shows the TPI component, a_i. The straight lines are of slope 1.

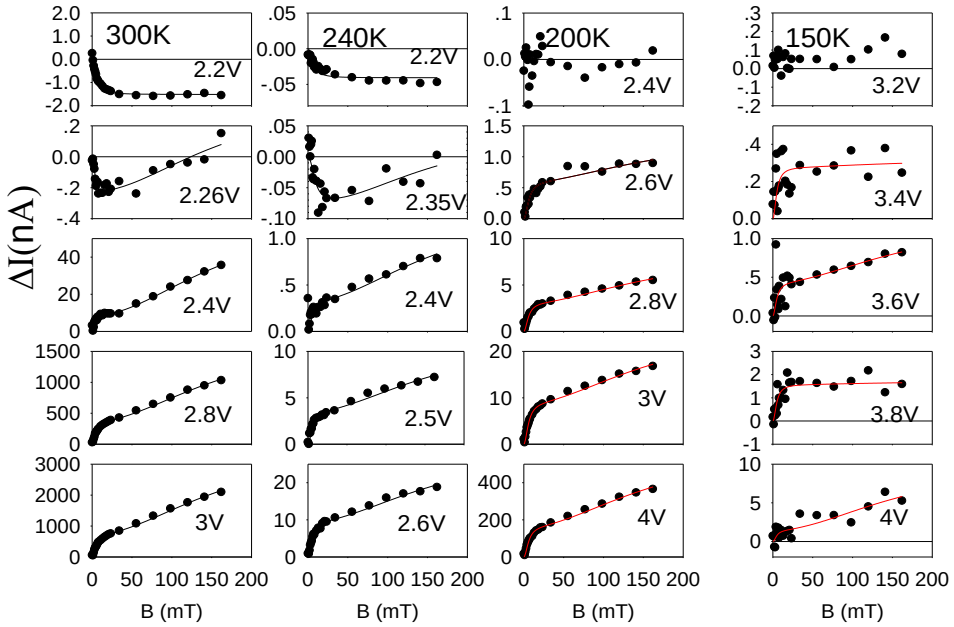

(a)

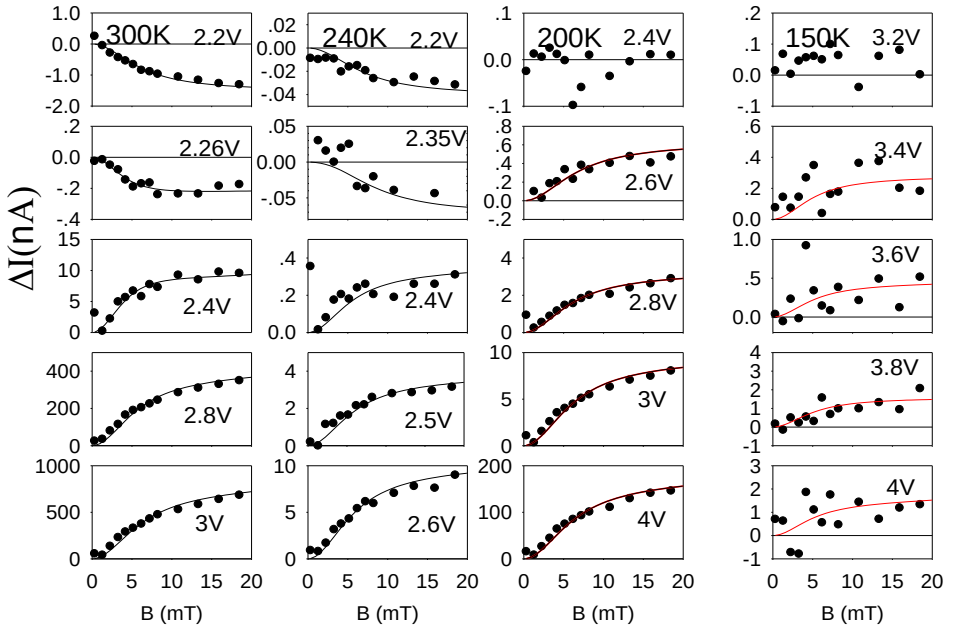

(b)

Figure 5.9: (a) The relative change in current in a 20nm Alq_3 based OLED at temperatures of 300K, 240K, 200K, and 150K with applied magnetic field for several drive voltages. (b) The detail of the low field region from 0 to 20 mT. The black line is the fitting by the triple Lorentzian, Equation(4.8) and the red line indicates the fitting by the double Lorentzian, Equation(4.2).

Figure 5.9 shows the OMR curves for a 20nm Alq_3 based device over a range of temperatures and operating voltages. At temperatures of 300K and 240K, the negative OMR was observed at low voltages. However, when the temperature is decreased to 240K, the negative OMR was no longer observed. At temperatures below 240K, the fits with a dual Lorentzian were excellent even for the low field region. Unlike for the 30nm Alq_3 based OLED at low temperatures, it was found that the exciton dissociation component could not be observed to have an effect on the OMR data. This could be because the device wasn't driven to a high voltage.

The magnitude of the three processes, (a_d+a_t) and a_i was plotted against the light out intensity in the device, as shown in Figure 5.10. Meanwhile, the magnitude of these three processes was also plotted against the singlet exciton concentration, as shown in Figure 5.11. Figure 5.11 also shows that, for these processes, the magnitude of the effect scales linearly with exciton concentration. Furthermore, changing the temperature from 300K to 150K of the sample had no effect upon that linearity.

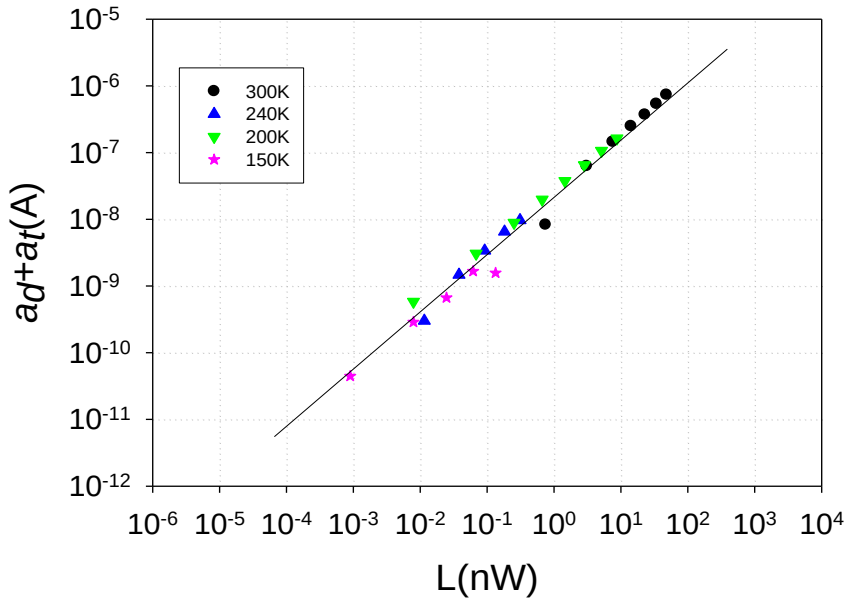

(a)

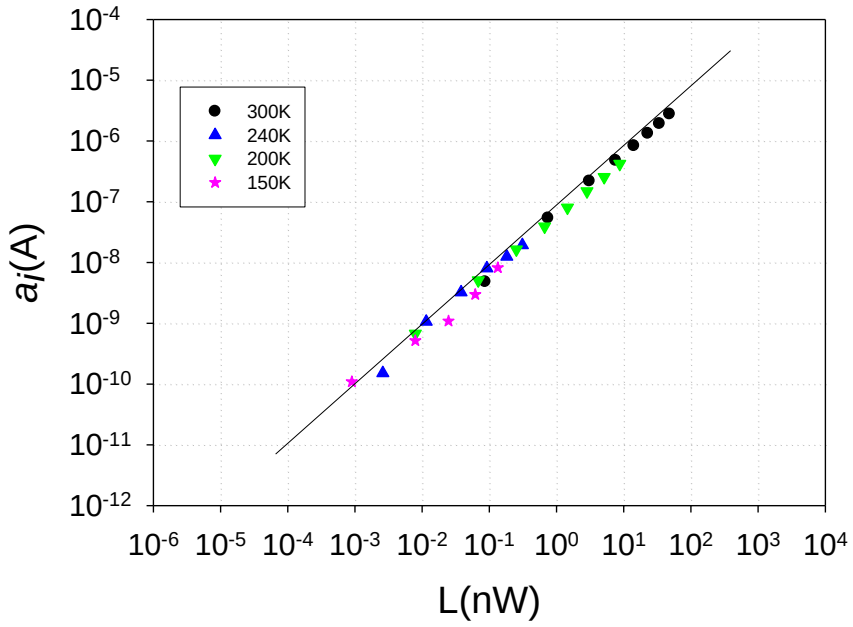

(b)

Figure 5.10: The prefactors from the fits plotted against light output intensity for a 20nm Alq_3 based OLED. (a) shows the sum of the prefactors for the dissociation and trapping components (a_d+a_t) and (b) shows the TPI component, a_i. The straight lines are of slope 1.

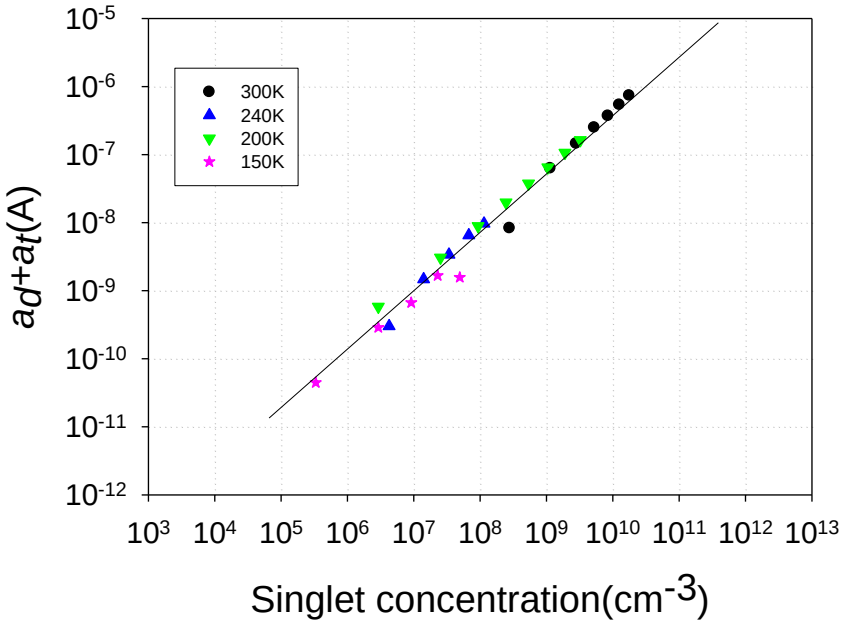

(a)

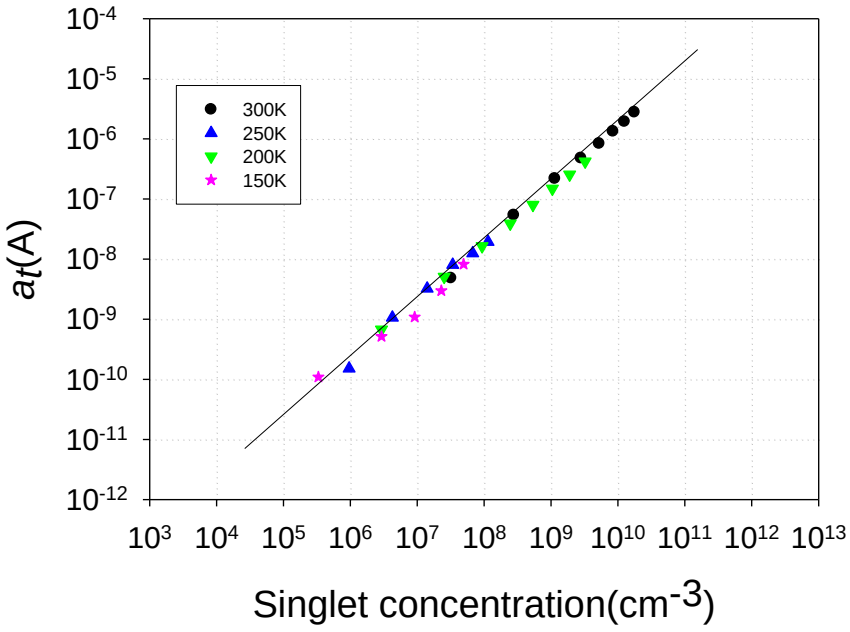

(b)

Figure 5.11: The prefactors from the fits plotted against singlet concentration for a 20nm Alq_3 based OLED. (a) shows the sum of the prefactors for the dissociation and trapping components (a_d+a_t) and (b) shows the TPI component, a_i. The straight lines are of slope 1.

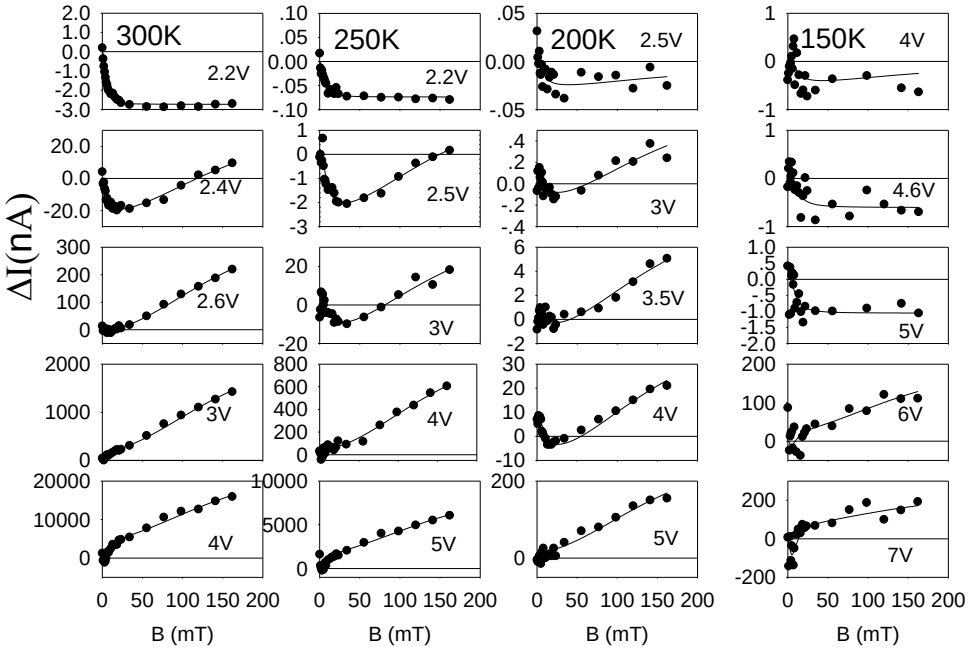

(a)

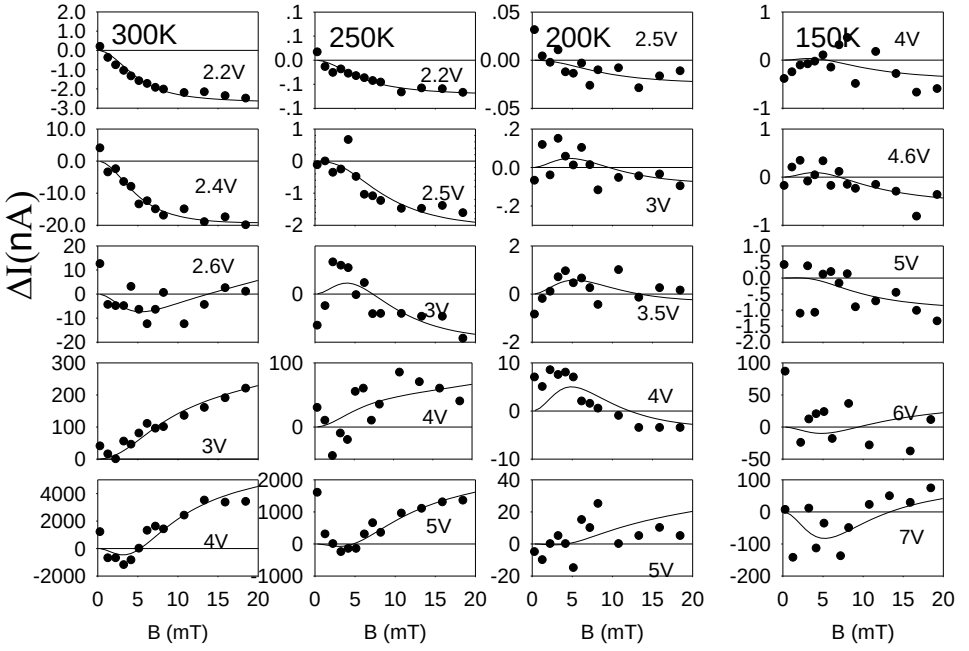

(b)

Figure 5.12: (a) The relative change in current in a 15nm Alq_3 OLED at temperatures of 300K, 240K, 200K, and 150K with applied magnetic field for several drive voltages. (b) The detail of the low field region from 0 to 20 mT. The OMR data are fits obtained using a triple Lorentzian, Equation (4.8).

Figure 5.12 shows the OMR curves for a 15nm Alq_3 device over a range of temperatures and operating voltages. Even when the temperature is decreased to 150K, the dissociation component could still be observed to affect the OMR data. In this situation, the triple Lorentzian was required to fit the OMR data. It can be seen that the fits are excellent. The magnitude of the three processes, (a_d+a_t) and a_i was plotted against the light out intensity in the device, as seen in Figure 5.13. The conversion from the light out intensity into the singlet exciton concentration was completed. Figure 5.14 shows that, for these processes, the magnitude of the effect scales linearly with exciton concentration. Furthermore, changing the temperature from 300K to 150K of the sample had no effect upon that linearity.

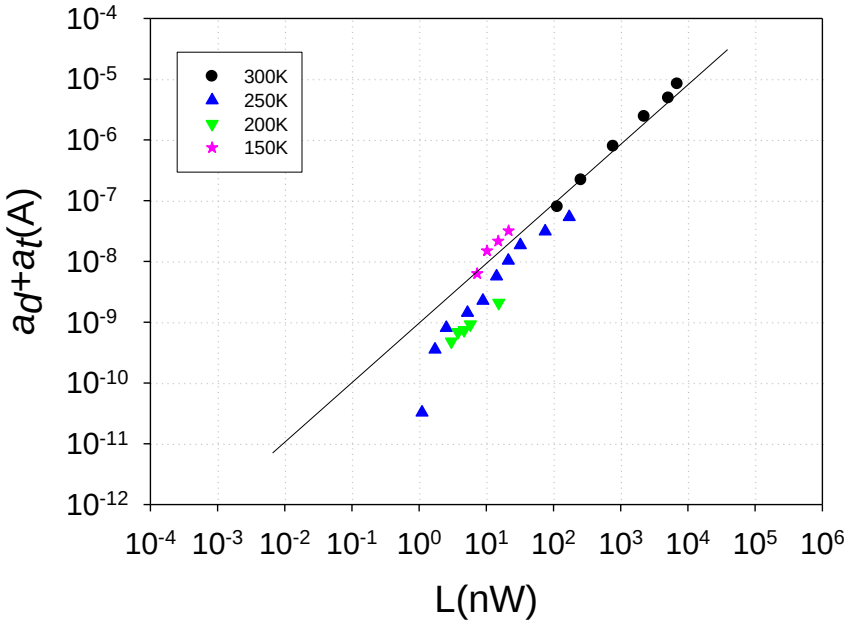

(a)

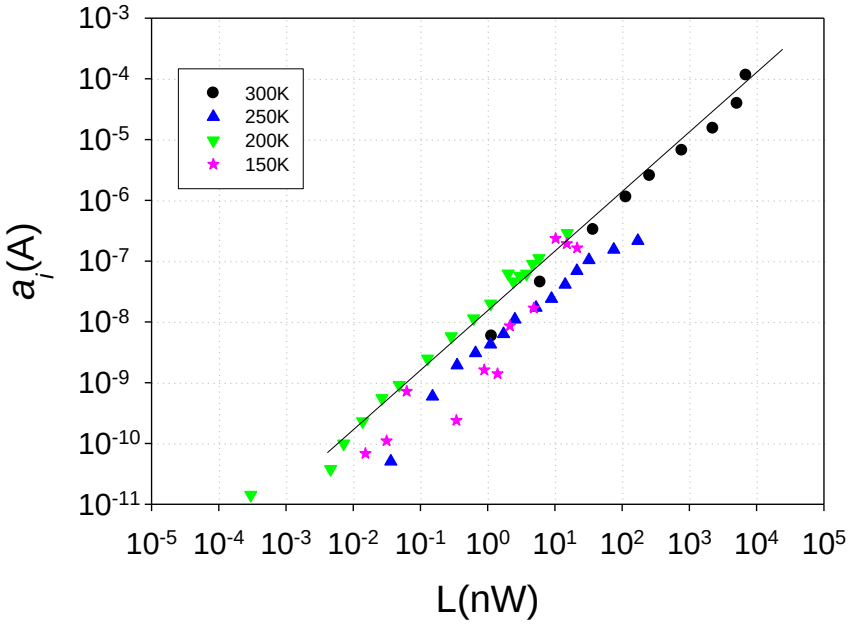

(b)

Figure 5.13: The prefactors from the fits plotted against light output intensity for a 15nm Alq_3 based OLED. (a) shows the sum of the prefactors for the dissociation and trapping components (a_d+a_t) and (b) shows the TPI component, a_i. The straight lines are of slope 1.

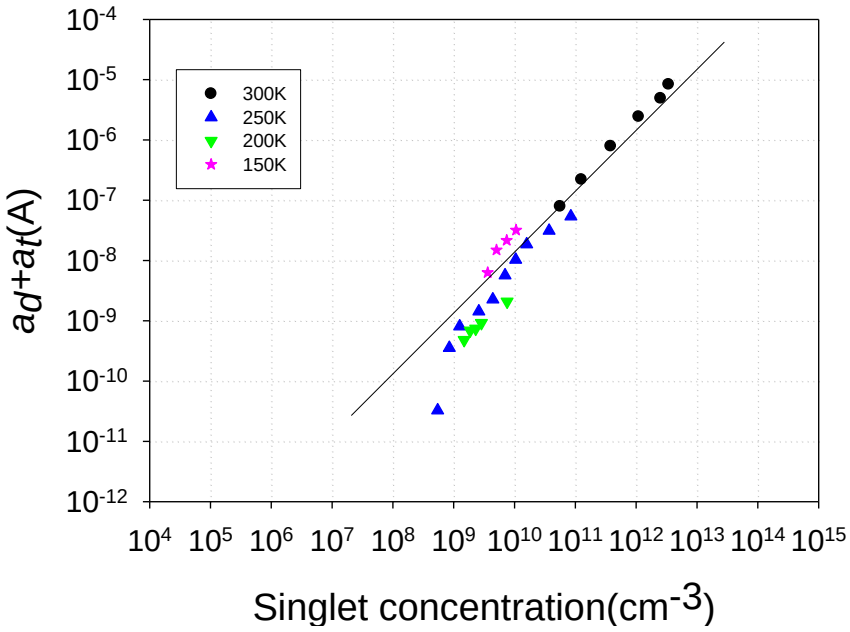

(a)

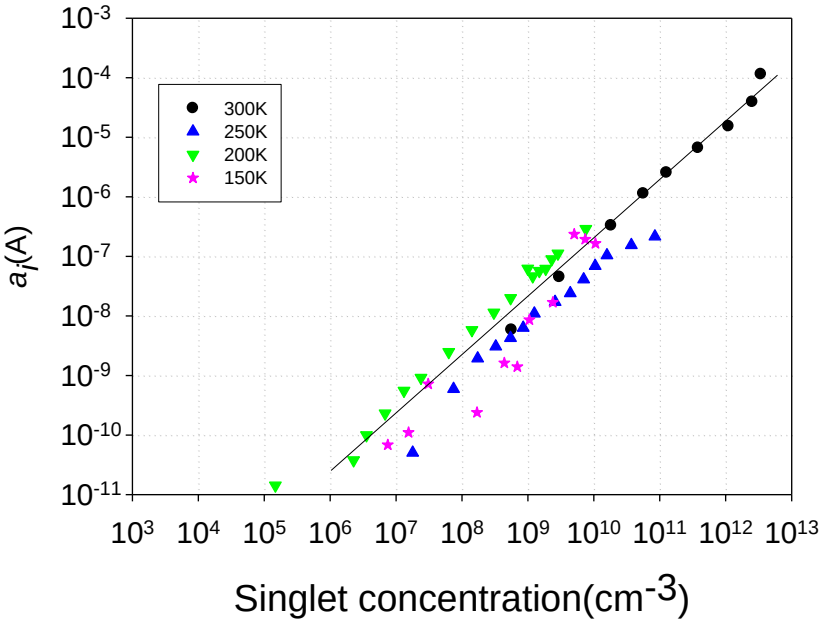

(b)

Figure 5.14: The prefactors from the fits plotted against singlet concentration for a 15nm Alq_3 based OLED. (a) shows the sum of the prefactors for the dissociation and trapping components (a_d+a_t) and (b) shows the TPI component, a_i. The straight lines are of slope 1.

Table 5.1: The temperature below which negative OMR vanishes for different devices.

Thickness of the Alq_3 layer in the device	**Temperature at which negative OMR vanishes**
30nm	250K
20nm	200K
15nm	<150K

Table 5.1 shows the summary of the negative OMR for different device thicknesses with temperatures. It is evident that, by decreasing the temperature, the exciton dissociation component would be weakened. This phenomenon can be explained by considering triplet diffusion at different temperatures. The triplet diffusion length is dependant on the temperature. By decreasing the temperature, both diffusion length and mobility of the exciton would be reduced [66, 67]. In this case, a small population of excitons could reach the interface between the Alq_3 and the cathode. This results in a weakness of the exciton dissociation component for the negative OMR. Therefore, this assumption would be reasonable.

5.3 The delay between onset of light emission and onset of OMR at low temperature

Desai *et al.* [39] found that magnetoresistance is intimately linked to light emission from the devices at room temperature. Figure 5.15(a) shows the luminescence against voltage for a 50nm Alq_3 OLED at temperatures ranging from 300 to 100K. The light emission onset voltages for these curves are 2.4V (300K), 3.2V (200K) and 7V (100K), respectively. These are obtained by the first data-point where the luminescence exceeds 10^{-11}W.

Figure 5.15(b) shows (for the 50nm Alq_3 based OLED) the onset of the percentage changes in light emission and current with magnetic field at temperatures ranging from 300K to 100K. It can be observed that the onsets of OMR at temperatures of 300K and 200K are 2.4V and 3.2V respectively, which coincide with the onsets of light emission. This strongly suggests an excitonic cause behind the OMR. However, the delay between onset of light emission and onset of OMR at a temperature of 100K can be observed (see Figure 5.15). At a temperature of 100K, a magnetic change in light emission was measured at 7V, with corresponding onsets of light emission. The onset of light emission was due to the formation of singlets. The magnetic field effects on light emission mean that the ISC from triplet to singlet had been occurring. However, a weak OMR could only be detected by the equipment used when the device was driven up to 13V. A lot of averaging was undertaken to improve signal to noise, but any effect was below the detection limit.

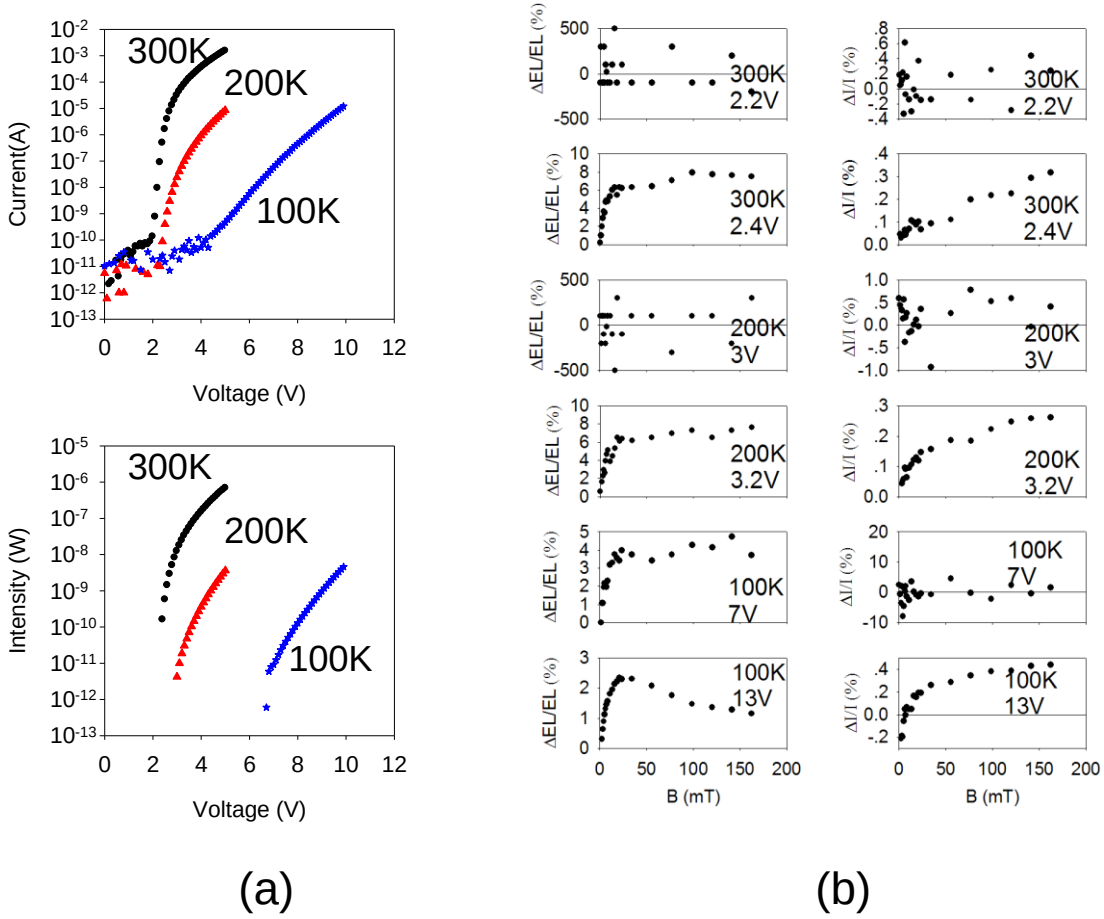

(a) (b)

Figure 5.15: (a) The voltage against current and luminescence for a 50nm Alq_3 based OLED at temperatures of 300K, 200K, and 100K, respectively. (b)The onset of the percentage changes in the light emission and current with magnetic field from 300K to 100K.

In an earlier paper, Desai *et al.* [39] suggested that the OMR may be due to the interaction of free carriers with triplets within the device, through the mechanism proposed by Ern and Merrifield. According to this mechanism, any process that reduced the concentration of triplets would have the effect of increasing the mobility of free carriers within the device, hence increasing the current. The singlets can form when this device is driven at the turn-on voltage stage and hence the light emission can be observed. However, the mobility of the polaron is decreased at low temperatures [68, 69], so that it doesn't efficiently affect the magnetic field. The OMR could only be detected by the equipment used if the driving voltage was high

enough to increase the possibility of the triplet polaron interaction. Therefore, the delay between onset of light emission and onset of OMR could be observed at low temperatures.

A similar result to the delay between onset of light emission and onset of OMR at low temperature could also be found in the 30nm Alq_3 OLED. Figure 5.16(a) shows the voltage against luminescence for a 30nm Alq_3 OLED at temperatures ranging from 300 to 100K. The onsets of light emission voltage for corresponding curves are 2.3V (300K), 3V (200K) and 7V (100K), respectively. Figure 5.16(b) shows that, for the 30nm Alq_3 based OLED, the onset of the percentage changes in the light emission and current with magnetic field occur at temperatures ranging from 300K to 100K. It can be observed that the onsets of OMR at temperatures of 300K and 200K are 2.3V and 3V respectively, which coincide with the onsets of light emission. However, the delay between onset of light emission and onset of OMR could be observed when the temperature was decreased to 100K (see Figure5.16). Figure 5.16 shows that the onset of luminescence at a temperature of 100K was 7V; a weak OMR could only be detected by the equipment when the device was driven up to 10V.

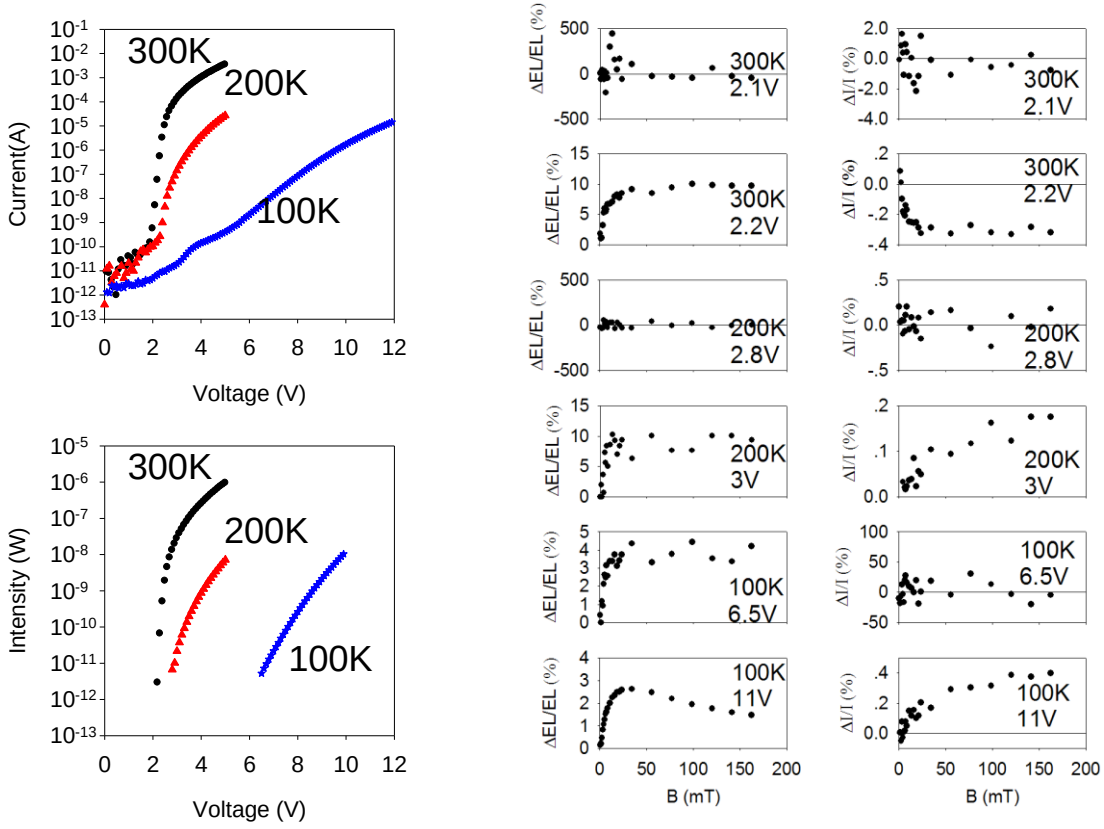

Figure 5.16 (a) The voltage against light output intensity for a 30nm Alq_3 based OLED at temperatures of 300K, 200K, and 100K, respectively. (b)The onset of the percentage changes in the light emission and current with magnetic field from 300K to 100K.

5.4 Magnetic field dependent TTA at low temperatures

5.4.1 Low temperature changes in efficiency

Figure 5.17 shows the percentage change in efficiency of a 50nm Alq_3 OLED at 300K, 200K and 100K, with applied magnetic field for several drive voltages. It was reported by Desai *et al.* that the percentage change in efficiency at room temperature appears to almost saturate with the effect of magnetic field above 50mT, while the percentage in current continues to increase [39]. Due to the saturation of the change in efficiency, it was previously suggested that the TTA is unlikely to play a significant role in the magnetic field effect on efficiency at room temperature [33]. In figure 5.18, a linear rise in efficiency is seen with magnetic field superimposed on the saturation from 300K down to 200K.

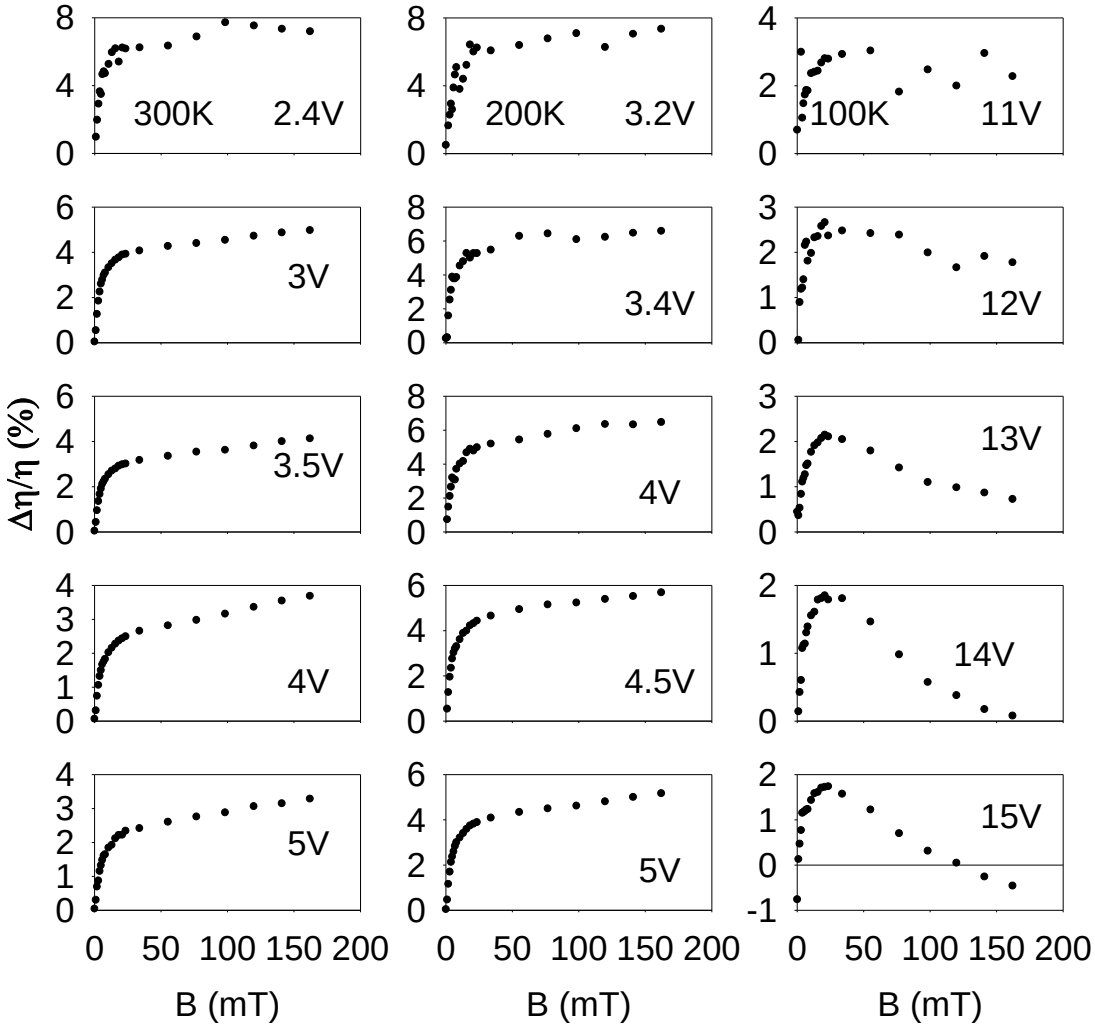

Figure 5.17: The percentage change in efficiency in a 50nm Alq_3 OLED at temperatures of 300K, 200K and 100K with applied magnetic field for several drive voltages.

However, when the temperature is decreased to 100K, the percentage change in efficiency starts to drop at high field under high voltage driving conditions. This coincides with the onset of the OMR. An identical result was observed in a 30nm Alq_3 OLED at a temperature of 100K (see figure 5.18). Similar phenomena have also been reported by different research groups. Johnson *et al.* [20] observed a small increase in delayed fluorescence of anthrancene at low field, followed by a decrease as the magnetic field increases. This was attributed to the magnetic field effects on the TTA process. In following years, other similar results were observed in delayed

EL of Alq_3 OLEDs [70] and delayed PL of PtOEP-doped DPA films [71]. In the latest published paper to report the magnetic effects on the TTA, Xiong, *et al.* observed that the traces of electroluminescence at low temperature exhibit a dropping process at high field strength [61, 62].

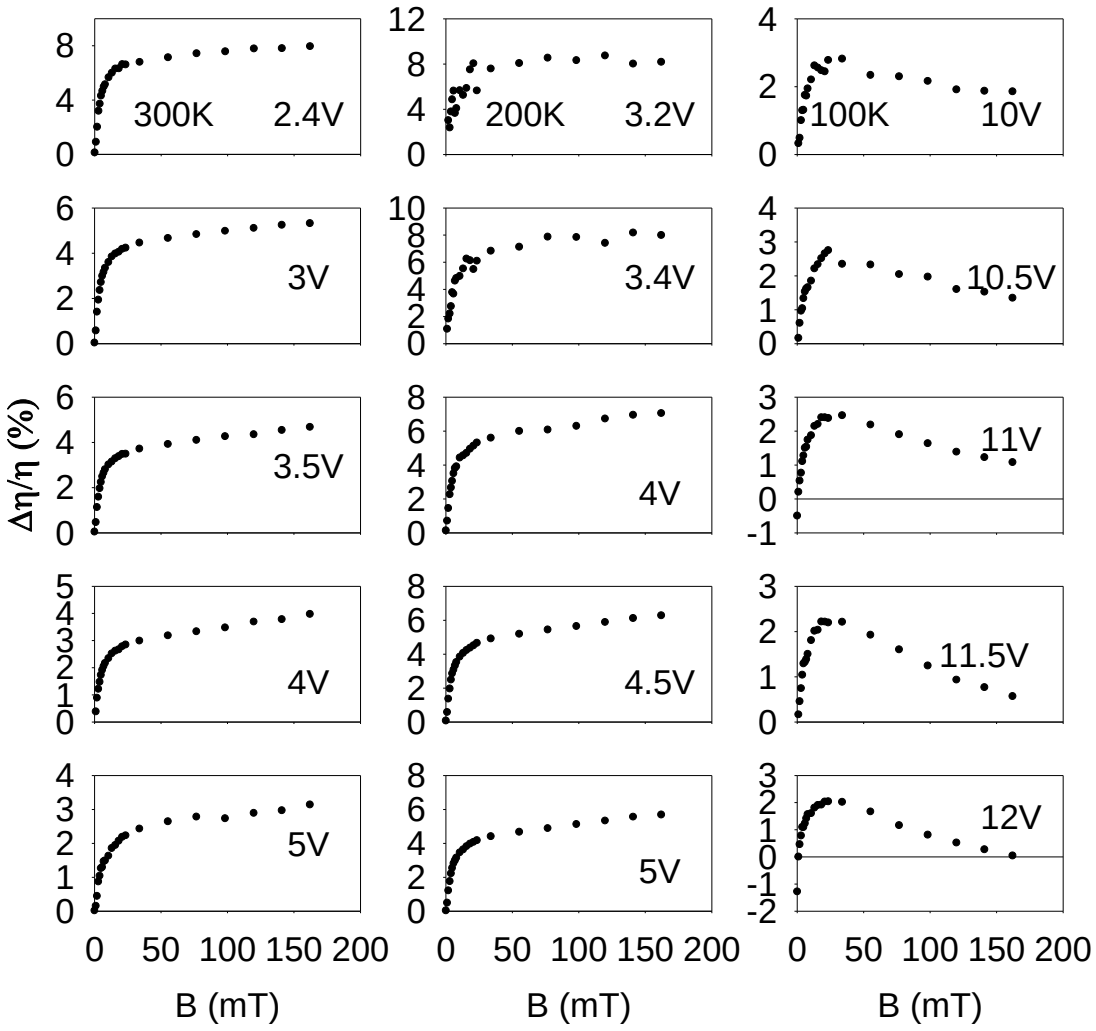

Figure 5.18: The percentage change in efficiency in a 30nm Alq_3 OLED at temperatures of 300K, 200K and 100K with applied magnetic field for several drive voltages.

5.4.2 The mechanism of percentage change in efficiency dropping at high field

Figure 5.19 shows the percentage efficiency change in the 50nm Alq_3 based OLED at a temperature of 100K and as a function of the magnetic field. The drive voltage for this device is 15V. It was suggested that the percentage change in efficiency from 300K to 200K experiences a dramatic increase at low field, followed by saturation at high field strength. As discussed in Chapter 3, the efficiency data could be fitted by a dual Lorentzian function, Equation (3.7). This behaviour was attributed to the ISC at both pair state and excitonic level [40]. However, it was observed that the percentage data at a temperature of 100K performed a dropping process at high field strength. Therefore, another process, other than the ISC between triplets and singlets, should be taken into account. To explain this process, we tried to deconvolve this curve into two parts: H(B)=F(B)-G(B). The F(B) is due to the ISC between triplets and singlets. This process was simulated by a dual Lorentzian function, Equation (3.7). The saturation fields, B_1 =3.1±0.16and B_2 =22.6±1.74, are referred to as the average values in Table 3.11.

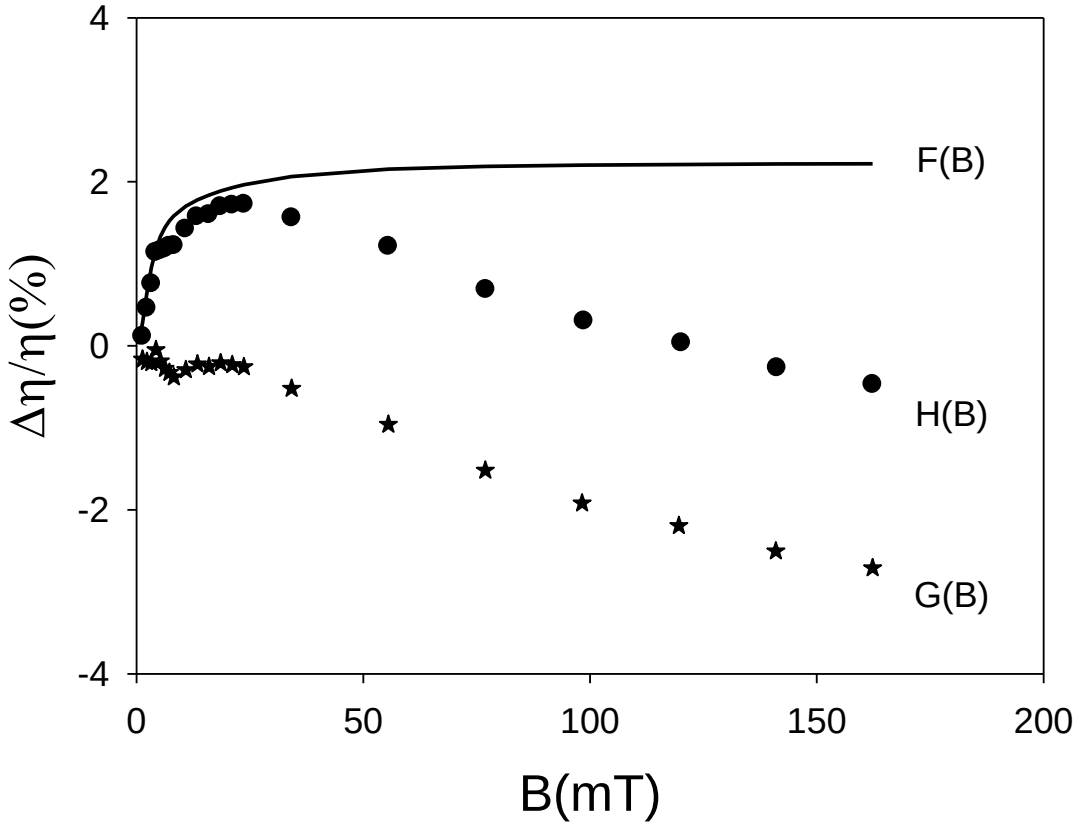

Figure 5.19: The percentage efficiency change in a 50nm Alq_3 OLED at a temperature of 100K as a function of the magnetic field (solid circle H(B)). The drive voltage for this device is 15V. The solid line F(B) and asterisks G(B) correspond to ISC between singlet and triplet and TTA, respectively.

Both TTA and quenching of triplets have been considered to be mechanisms of the efficiency drop, G(B). Firstly, it was assumed that the phenomenon could be due to triplet quenching. In 1968, Merrifield *et al.* reported that the triplet lifetime could be increased with the application of a magnetic field [21]. This triplet quenching process is magnetic field dependent and this route is suppressed by increasing the field. In addition, a decrease in the efficiency of quenching is accompanied by an increase in the exciton lifetime [21]. Once the efficiency of quenching is decreased, the triplets can possibly transfer to singlets and hence raise the efficiency of the device by increasing the magnetic field. This supposition conflicts with the results obtained here, in which the efficiency of the device decreased upon the application of

a magnetic field. Therefore, the effect of triplet quenching can be ruled out when explaining the mechanism of the efficiency drop, G(B).

Secondly, we supposed that the mechanism of the efficiency drop, G(B), was caused by the TTA. The curve, G(B), in Figure 5.19 has a similar form to that obtained for Johnson's works in molecular crystals [20], which has been explained by the triplet-triplet annihilation. According to Merrifiled's theory, the TTA process can be modulated by a magnetic field, producing a small rise of EL at low field and a subsequent fall at high field. This similar behavior in the Alq_3 based OLEDs was also explained by the TTA mechanism [61, 62, 70, 71]. As a result, this leaves the magnetic modulation of the triplet-triplet annihilation rate as the only viable cause to explain the mechanism of the efficiency drop.

5.4.3 Dependence of the TTA process on the population of triplet excitons

In the previous section, we observed a decrease of the percentage efficiency change in the 50nm Alq_3 based OLED at 100K as a function of the magnetic field. The driving voltage for this device is 15V. The cause of a drop in the percentage efficiency change was explained by the TTA process. Figure 5.20 shows that the fall in the percentage efficiency change becomes more remarkable by increasing the driving voltage. This means that the portion of light emission caused by the TTA is more significant at larger current density through the device. The reason could be explained by the fact that the TTA is proportional to the density squared of the triplet excitons [51].

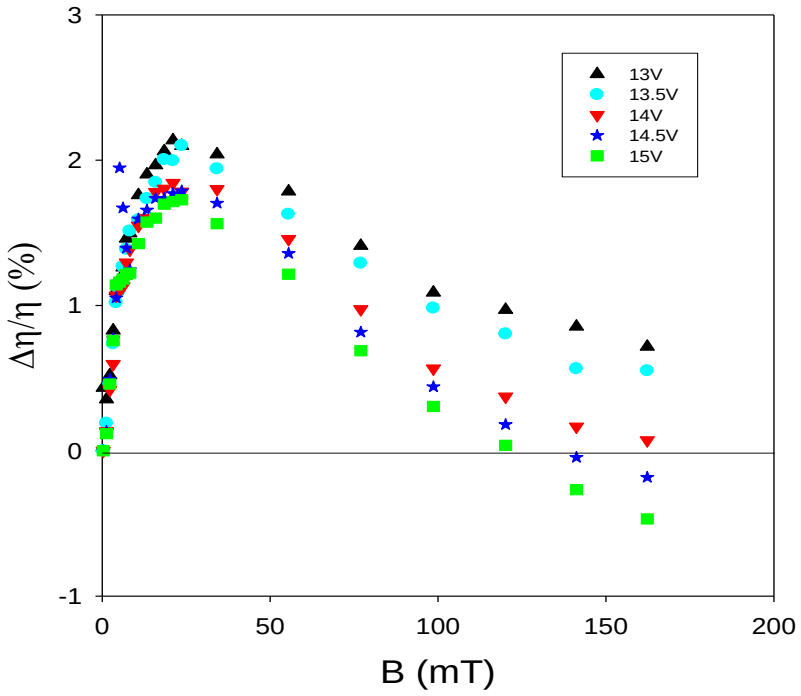

Figure 5.20: The percentage efficiency change in the 50nm Alq_3 based OLED at 100K as a function of the magnetic field. The drive voltages for this device range from 13V to 15V.

Another example supporting the observation that the TTA process is dependent on the population of triplet excitons can be seen in Figure 5.21. As we can see, the onset of efficiency dropping at 100K corresponds to the onset of the TTA process in devices of differing thickness. Figure 5.21 also shows that the onsets of efficiency dropping for 80nm, 50nm, 30nm, and 20nm Alq_3 based OLEDs are 18V, 11V, 8V, and 7V, respectively. Even though these (varied thickness) devices were placed at the same temperature, 100K, the driving voltages for the onset of the TTA process differ.

Table 5.2 presents a summary of the relationships among the device thickness, the onset of TTA, the current density, and light-out intensity. It can be seen that, even for the varied thickness devices, the densities of current through the devices for the onset of the TTA process are all around 1 Am^{-2}. Furthermore, it is also worth noting that the intensities of luminance emission are also similar. The onset of drop in EL with a magnetic field corresponds to a given current density, hence a given population of triplet excitons. Therefore, it can be concluded that the TTA process is dependent on the population of triplet excitons.

As described in the previous section, the onset of OMR for the 50nm Alq_3 OLED at 100K is 13V (see Figure 5.1), while the onset of OMR for the 30nm Alq_3 OLED at 100K is 10V (see figure 5.6). Comparing the data shown in Table 5.2, it is found that 13V for the 50nm Alq_3 OLED and 10V for the 30nm Alq_3 OLED were over the onset of the TTA. In addition, it also previously mentioned that the (a_d+a_t), the sum of prefactors for the dissociation and trapping components, at a temperature of 100K, look like they deviate from the straight lines of slope 1 (See Figures 5.5 and 5.8). It could therefore be suggested that the TTA is a new possible process that affects the OMR.

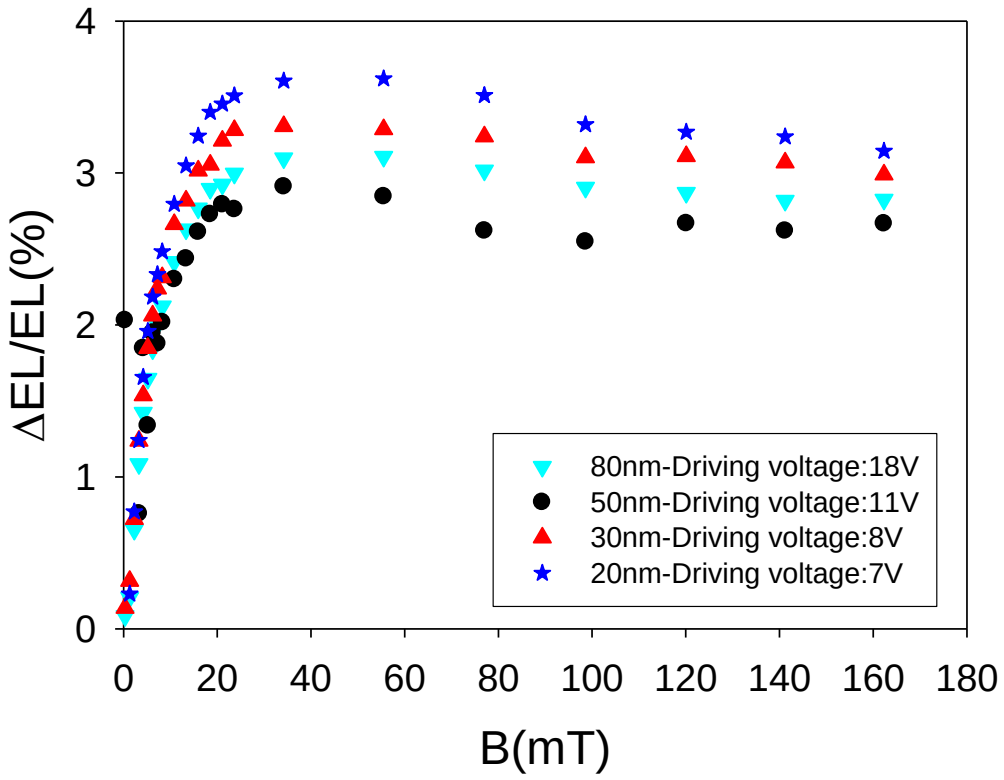

Figure 5.21: At temperature of 100K, the onsets of efficiency dropping for 80nm, 50nm, 30nm, and 20nm Alq_3 based OLEDs are 18V, 11V, 8V and 7V, respectively.

Table 5.2: Summary of the relationships between the device thickness, the onset of TTA, the current density, and light-out intensity.

Thickness of Alq_3 layers of the devices	**Driving voltage for the onset of TTA**	**Current density** (Am^{-2})	**Light-out intensity** (W)
80nm	18V	0.86	4.5×10^{-9}
50nm	11V	0.61	7.5×10^{-9}
30nm	8V	1.37	9×10^{-9}
20nm	7V	1.5	1.2×10^{-9}

5.4 Conclusion

In this chapter the triplet polaron interaction model has been extended to fit the OMR data as a function of temperatures and operating voltages for Alq_3 based OLEDs. It was observed that in all cases, at different temperatures, the data could be fitted using just three processes: triplet dissociation, exciton trapping and TPI components. Meanwhile, it was found that both trapping and TPI components are independent to temperature changes, but the dissociation component changes with temperatures.

In addition, the temperature dependencies of the magnetic field effect on the current and efficiency of Alq_3 based OLEDs where investigated. The delay between onset of light emission and onset of OMR was observed at low temperatures. This phenomenon is abnormal, because the OMR was attributed to the exciton formation in the device [39]. It was discussed that the reason for this could be the decrease in mobility at low temperatures. In the later part of this chapter, the TTA mechanism was used to explain the percentage change in efficiency dropping at low temperatures. Furthermore, it was reported that the TTA process is dependent on the population of triplet excitons.

Chapter 6:
Conclusions and Future Work

The aim of my PhD work has been to understand the modelling of OMR. My work has been divided into two parts: the magnetic field effects on the intersystem crossing (ISC) in organic semiconductors, and the modelling of OMR, including triplet polaron interactions (TPI).

In Chapter 3, the effect of a magnetic field on the ISC in organic semiconductors was studied. Chapter 3 showed that, in an Alq_3 device, it is possible to estimate the ISC rate by modelling the time dependence of the PL under an intense laser pulse excitation. A modified rate model was introduced in order to derive an ISC rate: k_{ISC}, of 2.3 x $10^4 s^{-1}$ at a temperature of 80K. The only difference between the simple rate model, as proposed by Cölle's group, and our modified rate model is that there is an intersystem crossing back from the triplet to the singlet state. It was proven that the back transfer is necessary. In order to explain the observed temperature dependent on the change in the PL intensity, a value of 15±5 meV as the activation energy (E_a) was found within the modified rate model. However, the value of the E_a is too small when compared with the ~0.5eV difference in energy between the singlet and triplet levels. Furthermore, an ESA model was proposed to amend this discrepancy. The ESA model also reasonably explains how the triplet back transfer to singlet states occurs. In addition, Chapter 3 discussed how a magnetic field acts to increase the k_{ISC} by ~10% for fields up to ~100mT. Comparing the efficiency data under the effect of a magnetic field for an Alq_3 OLED with the MPL data, it was possible to suggest that the magnetic field may affect the mixing of a pair state prior to exciton formation, as well as the exciton itself. In the electrical excitation, the magnetic

field may dominantly affect the pair state, and have less influence on the exciton itself. On the other hand, during optical excitation, the magnetic field may cause significant modulation of the ISC at excitonic level, and is less significant on the ISC for the pair state.

In Chapter 4, the TPI model was proposed to fit the OMR data. The TPI model incorporates just three processes: triplet dissociation, exciton trapping and TPI. In Chapter 4, this TPI model was used to fit the OMR data as a function of thickness for Alq_3 based OLEDs. Each of the three processes has a Lorentzian function shape. As both triplet dissociation and exciton trapping mirror the change in the concentration of triplets caused by the ISC, the saturation fields for triplet dissociation and exciton trapping are very similar to the saturation field value (~6 mT) obtained from a single Lorentzian fit to the efficiency data.

For efficiency data, the saturation field, B_1 =3.1±0.16, indicating the magnetic field dependence of the pair state, and the saturation field, B_2 =22.6±1.74, referring to the magnetic field dependence of the exciton itself can be found. Therefore, the value (~6 mT) obtained from a single Lorentzian fit to the efficiency data is just an approximation. However, the OMR data is less clear than the efficiency data, particularly in the low field. It is difficult to distinguish the pair state and exciton components. If the OMR data quality can be improved at low field in the future, it will be possible to distinguish between the pair states and excitons being affected. The magnetic field dependence of the TPI is also a Lorentzian function shape, in which the fixed saturation field (160 mT) is consistent with Merrifield's work on triplet quenching in anthracene. In future work it will be of interest to measure the OMR at high fields, for example over 1000 mT, and explore any possible new phenomena. In Chapter 4, it was also found that the sum of prefactors for dissociation and trapping, $(a_{d+} a_t)$, and the prefactor for TPI, a_i, are both proportional to the exciton concentration within the device over the full range of operating conditions. This work demonstrates that the magnitude and shape of the OMR can

be predicted, and is therefore very useful for understanding the fundamental mechanisms behind OMR.

In Chapter 5, the OMR measurements were extended as a function of temperature. It was shown that, in an OLED device of any thickness, and at different temperatures, the data can be fitted by the TPI model. Meanwhile, it was found that both trapping and TPI components are independent of temperature changes, but the dissociation component changes with temperature. It is worth noting that the OMR data at low temperatures is noisier than the data at room temperature, particularly in the low field region. This will provide motivation to think of ways of improving the quality of OMR data for future low temperature measurements. It was observed that the prefactor of the TPI component obtained from the fits, a_i, is proportional to the exciton concentration over the range of device thicknesses and temperatures.

At any thickness of device, the sum of prefactors for dissociation and trapping $(a_{d+} a_t)$ is proportional to the exciton concentration from 300K to 150K. However, it was observed that $(a_{d+} a_t)$ at a temperature of 100K looked likely to deviate from the straight line of slope 1. The OMR data at 100K was only obtained in the 50nm and 30nm Alq_3 based OLEDs. This was because the OMR at 100K can only be observed by applying a high driving voltage, and the thinner devices (20nm, 15nm, and 10nm Alq_3 based OLEDs) were easily damaged at such high driving conditions. Future work will attempt to look at how to protect the operating devices at high driving conditions. In addition, some surprising results were found when the magnetic field effect on the current and efficiency of Alq_3 based OLEDs was measured at low temperature.

There is a delay between onset of light emission and onset of OMR at low temperatures. This phenomenon is abnormal compared with the OMR data at room temperature. It was discussed that the reason for this could be that the decrease in carrier mobility at low temperatures masks the effects of any trapping or interaction at

low fields. In Chapter 5, the TTA mechanism was discussed to explain how the percentage change in efficiency with a magnetic field drops at low temperatures. It was that the TTA process is dependent on the population of triplet excitons.

In future work, this study will be extended to OLEDs that use PEDOT:PSS as a hole transport layer. According to Mermer's observation, the OMR can be seen before the device turn-on for a PEDOT:PSS/Alq_3 device. This is different from the observation in the TPD/Alq_3 devices. PEDOT:PSS is a doped semi-conducting polymer, rather than an intrinsic semiconductor. The OMR below turn-on is probably due to PEDOT:PSS itself. Another member of the group has found that the percentage change in the efficiency of a PEDOT:PSS/Alq_3 device with a magnetic field drops at room temperature (see Figure 6.1). This could suggest that the TTA mechanism may occur at room temperature. Future work should continue to explore the effect of TTA on the OMR of a PEDOT:PSS/Alq_3 OLED device.

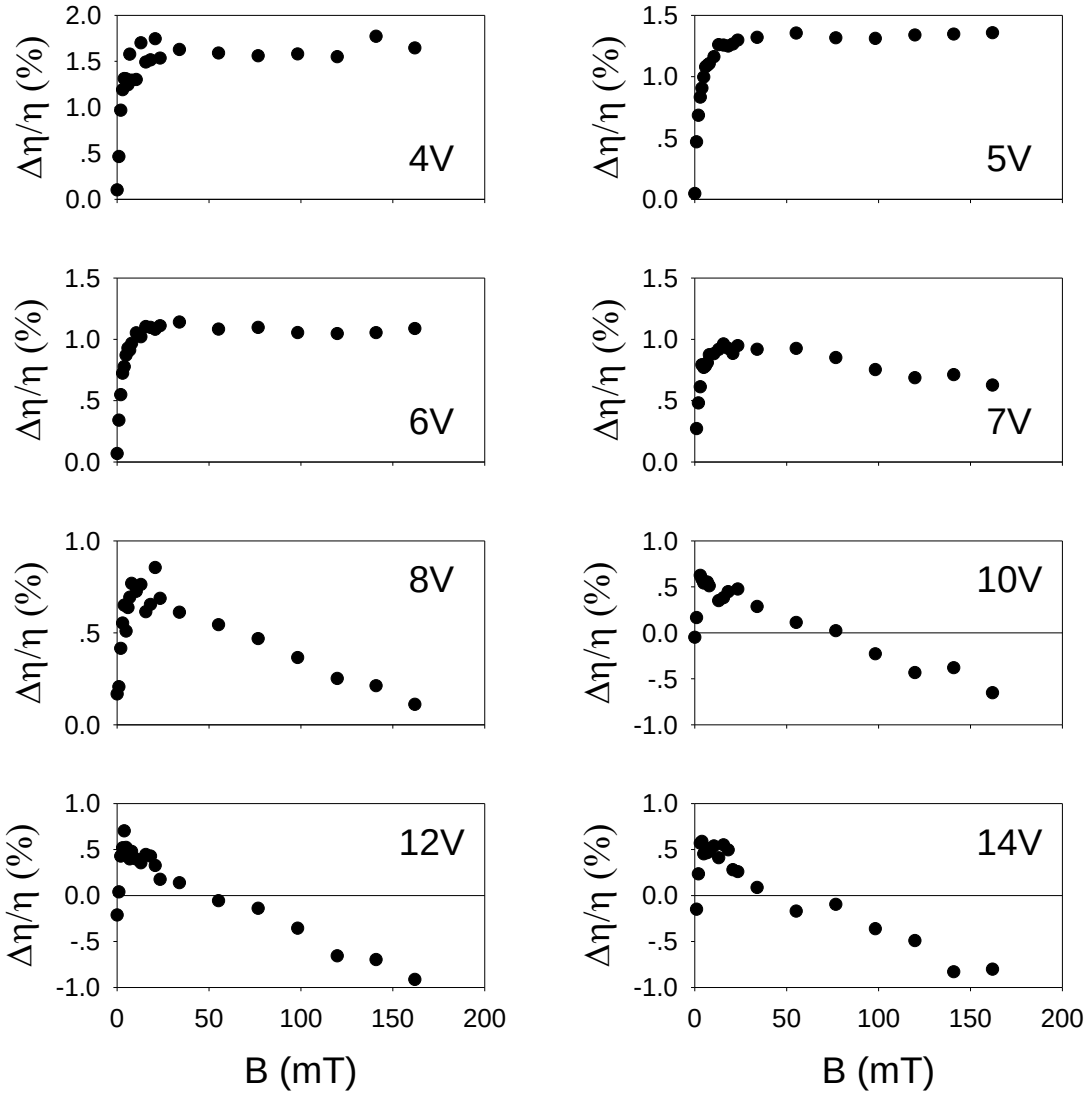

Figure 6.1: The percentage change in efficiency of a PEDOT:PSS/Alq_3 OLED at room temperatures with a magnetic field for several drive voltages.

References

1. C. W. Tang, and S.A. Vanslyke, Appl. Phys. Lett. **51,** 913 (1987).
2. J. H. Burroughes, D. D. C. Bradley, A. R. Brown, R. N. Marks, K. Mackay, R. H. Friend, P. L. Burns and A. B. Holmes, Nature, **347,** 539 (1990).
3. T. R. Hebner, C. C.Wu, D.Marcy, M. H. Lu, and J. C.Sturm, Appl. Phys. Lett.**72,** 519 (1998).
4. Y. Shirota and H. Kageyama, Chemical Reviews, **107,** 953 (2007).
5. C. E. Swenberg and M. Pope, Electronic Processes of Organic Crystals and Polymers (Oxford University Press, Oxford, 1999).
6. S. Barth, P. Muller, H. Riel, P. F. Seidler, W. Rieb, H. Vestweber and H. Bassler, J. Appl. Phys. **89,** 3711 (2001).
7. M. Stolka, J. F. Yanus and D. M. Pai, J. Phys. Chem. **88,** 4707 (1984).
8. J. Y. Song, A. J. Drew, N. Stingelin, W. P. Gillin and T. Kreouzis, Phy. Rev. B **82,** 085205, (2010).
9. A. D. Walser, R. Priestley and R. Dorsinville, Synth. Met. **102,** 1552 (1999).
10. M. A. Baldo, S. R. Forrest, Phy. Rev. B **62,** 10958 (2000).
11. J. S. Kim, M. Granstorm, R. H. Friend, N. Johansson, W. R. Salaneck, R. Daik, W. J. Feast and F. Cacialli, J. Appl. Phys. **84,** 6859 (1998).
12. I.G. Hill, D. Milliron, J. Schwartz, A. Kahn, Applied Surface Science, **166,** 354 (2000).
13. T. M. Brown, R. H. Friend, I. S. Millard, D. J. Lacey, J. H. Burroughes and F. Cacialli, Appl. Phys. Lett. **79,** 174 (2001).
14. T. M. Brown, D. J. Lacey, J. H. Burroughes, F.Cacialli, Synth. Met. **124,** 15 (2001).
15. M. A. Baldo, C. Adachi, and S.R. Forrest, Phy. Rev. B **60,** 14422 (1999).
16 J. S.Wilson, A.S.Dhoot, A. J. A. B.Seeley, A.Kohler and R.H.Friend, Nature, **413**, 6858 (2001).
17 A.Köhler and J.Wilson, Organic Electronics,**4**,179(2003).
18 M.Wohlgenannt and Z.V.Vardeny, Journal of Physics-Condensed Matter,**15**,83(2003).
19 S.P.Yang,X.F.Zhang,S.L.Zhao,Z.Xu,F.J.Zhang,Y.R.Yang,Q.Liand X.X.Pang,Spectroscopy and Spectral Analysis,**28**,512(2008).

20. R.C. Johnson and R. E. Merrifield, Phy Rev. B **1,** 896 (1970).
21. V. Ern and R. E. Merrifield, Phy. Rev. Lett. **21,** 609 (1968).
22. E. L. Frankevich, A. A. Lymarev, I. Sokolik, F. E. Karasz, S. B,R. H. Baughman and H. H. Hörhold, Phys. Rev. B **46,** 9320 (1992).
23. J. Kalinowski, M. Cocchi, D. Virgili, P. D. Marco and V. Fattori, Chem. Phys.Lett. **380,** 710 (2003).
24. J. D. Jackson. Classical Electrodynamic Third Edition. John Wiley & Sons, Inc., 1999.
25. P. Atkins and R. Friedman. *Molecular Quantum Mechanics Fourth Edition*. Oxford University Press, 2008.
26. V. N. Prigodin, J. D. Bergeson, D. M. Lincoln and A. J. Epstein, Synth. Met. **156,** 757 (2006).
27. B. Hu, and Y. Wu, Nature Materials. **6,** 985 (2007).
28. Y. Sheng, T. D. Nguyen, G. Veeraraghavan, Ö. Mermer,M. Wohlgenannt, S.Qiu, U.Scherf, Phy. Rev. B **74,** 045213(2006).
29. T. D. Nguyen, Y. Sheng, J. Rybicki, G. Veeraraghavan, and M. Wohlgenannt, J.Mater. Chem. **17,** 1995 (2007).
30. T.D. Nguyena, Y.S., M. Wohlgenannta, and T.D. Anthopoulosb, Synth. Met., **157**,930 (2007).
31. N. J. Rolfe, M. Heeney, P. B. Wyatt, A.J.Drew, W.P.Gillin and T.Kreouzis,, Phy. Rev. B **80,** 241201 (2009).
32. P. A. Bobbert, Nature Materials, **9,** 288 (2010).
33. T.D. Nguyen, G.H. Markosian, FujianWang, Leonard Wojcik, Xiao-Guang Li, Eitan Ehrenfreund and .Z.V. Vardeny, Nature Materials, **9**,345(2010).
34. N.J. Rolfe, M. Heeney, P.B. Wyatt, A.J. Drew, T. Kreouzis, and W.P. Gillin, Synth. Met. **161,** 608 (2011).
35. Y. Sheng, T. D. Nguyen, G. Veeraraghavan, Ö. Mermer and M. Wohlgenannt,Phy. Rev. B **75,** 035202 (2007).
36. Wu, Y. and B. Hu, Appl. Phys. Lett. **89,** 203510 (2006).
37. P. Shakya, P. Desai, M. Somerton, G. Gannaway, T. Kreouzis and W. P. Gillin,J. Appl. Phys. **103,** 103715 (2008).
38. P. Shakya's PhD thesis. 2008.

39. P. Desai, P. Shakya, T. Kreouzis and W. P. Gillin, Phys. Rev. B, **75,** 094423 (2007).

40. Sijie Zhang, J.Y.Song, T. Kreouzis, and W. P. Gillin, J. Appl. Phys. **106**, 043511(2009).

41. P. A. Bobbert, T. D. Nguyen, F. W. van Oost, B. Koopmans and M. Wohlgenannt, Phys. Rev. Lett. **99,** 216801 (2007).

42. J.Y. Song, N. Stingelin, W.P. Gillin, T. Kreouzis, Appl. Phys. Lett. **93,** 2333306(2008).

43. M.Schaer, F.Nuesch, D.Berner, W.Leo, L.Zuppiroli, Advanced Functional Materials, **11,**158(2001).

44. J.James, Spectrograph Design Fundamentals.(Cambridge University Press, (2007).

45. C.H.Robison, American Journal of Physics, **39**(6), (1971).

46. M. Cölle, C. Gärditz and M. Braun, J. Appl. Phys. **96,** 6133 (2004).

47. B.B.Snavely, Proc. IEEE, **57,** 1374, (1969).

48. M.Braun, J.Gmeiner,M.Tzolov, M. Cölle, F. D.Meyer, W.Milius, H.Hillebrecht, O.Wendland,J. U.von Schutz and W.Brutting, J. Chem. Phys. **114,** 9625 (2001).

49. M. Cölle and W. Brutting, Physica Status Solidi a-Applied Research, **201,** 1095(2004).

50. C.P.Lindsey and G.D. Patterson, J. Chem. Phys. **73,** 3348 (1980).

51. M. Cölle and C. Gärditz, Appl. Phys. Lett. **84,** 3160 (2004).

52. Ö. Mermer, G. Veeraraghavan, T. L. Francis, Y. Sheng, D.T. Nguyen, M. Wohlgenannt, A. Kohler, M. K. Al-suti and M. S. Khan, Phys. Rev. B, **72,** 205202 (2005).

53. P. A. Bobbert, W.Wagemans, F. W. A.van Oost, B.Koopmans, M.Wohlgenannt,Phys. Rev. Lett. **102,** 156604 (2009).

54. P. Desai, P. Shakya, T. Kreouzis and W. P. Gillin, J. Appl. Phys. **102,** 73710 (2007).

55. J.Kalinowski, J.D. Szmytkowski, and W. Stampor, Chem Phys. Lett, **378,** 380 (2003).

56. Ö. Mermer, G. Veeraraghavan, T. L. Francis and M. Wohlgenannt, Solid State Commun **134,** 631 (2005).
57. W. P. Gillin, Sijie Zhang, N.J. Rolfe, P. Desai, P. Shakya, A.J. Drew and T. Kreouzis, Phys. Rev. B **82,** 19520856.
58. V. M. Agranovich, D. M. Basko,K.Schmidt,G.C.LaRocca,F.Bassani,S.Forrest, K. Leo, D. Lidzey, Chemical Physics, **272,**159 (2001).57.
59. M. A. Baldo, S. Lamansky, P. E. Burrows, M. E. Thomson and S. R. Forrest, Appl. Phy. Lett. **75,** 4 (1999).
60. H. C. Yeh, L. H. Chan, W. C. Wu and C. T. Chen, J. of Mater. Chem. **14,** 1293 (2004).
61. Y.Zhang, R.Liu, Y. L.Lei, Z. H.Xiong, Appl. Phys. Lett. **94**, 083307 (2009).
62. R.Liu, Y.Zhang, Y. L.Lei, P.Chen, Z. H.Xiong, J. Appl. Phys. 105**,** 093719 (2009).
63 M. Cölle and C. Garditz, Journal of Luminescence, **10**, 200, 2004.
64. C. G.Hubner, A.Renn,I.Renge,U. P.Wild, J. Chem. Phys. **115,** 9619 (2001).
65 Sijie Zhang, A.J. Drew, T. Kreouzis and W. P. Gillin, Synthetic Metals,**161**,628,2011.
66. S.Athanasopoulos1, E.V. Emelianova1,A. B. Walker, and D.Beljonne, Phys. Rev. B, **80**, 195209 (2009).
67. S. J.Martin, A. B.Walker, A. J.Campbell, and D. D. C.Bradley, J. Appl. Phys. **98**, 063709 (2005).
68. H.Bassler, Adv Mater, **5,** 662 (1993).
69. H.Mu, D.Klotzkin, A.de Silva, H. P.Wagner, D.White,B.Sharpton, Journal of Physics D-Applied Physics, **41,** 235109 (2008).
70. C.Garditz, A.G. Muckl, and M. Cölle, J. Appl. Phys. **98,** 104507 (2005).
71. J. Mezyk, R. Tubino, A. Monguzzi, A. Mech, and F. Meinardi, Phys. Rev. Lett. **102,** 087404 (2009).